Universidade do Minho
Escola de Ciências

Bruna Machado da Silva

Naturally Layered Perovskite Heterostructures

July 2025

Bruna Machado da Silva **Naturally Layered Perovskite Heterostructures**
UMinho | 2025

Universidade do Minho
Escola de Ciências

Bruna Machado da Silva

Naturally Layered Perovskite Heterostructures

Doctoral Thesis
Doctoral Program in Physics

Work supervised by:
Prof. Doctor Bernardo Gonçalves Almeida
Prof. Doctor Armandina Maria Lima Lopes
Prof. Doctor João Pedro Esteves Araújo

July 2025

COPYRIGHT AND TERMS OF USE OF THIS WORK BY A THIRD PARTY

This is academic work that can be used by third parties as long as internationally accepted rules and good practices regarding copyright and related rights are respected.

Accordingly, this work may be used under the license provided below.

If the user needs permission to make use of the work under conditions not provided for in the indicated licensing, they should contact the author through the RepositoriUM of Universidade do Minho.

License granted to the users of this work



Atribuição
CC BY

https://creativecommons.org/licenses/by/4.0/

ACKNOWLEDGMENTS

First, I want to acknowledge the University of Minho and Portuguese Foundation for Science and Technology (FCT) for the Ph.D. grant with reference 2021.07277.BD. This work was also supported by the FCT, through the projects POCI-01-0145-FEDER-029454, NORTE-01-0145-FEDER-028538, PTDC/NAN-MAT/0098/2020, NORTE-01-0145-FEDER-022096 and POCI-01-0145-FEDER-032527.

I would like to express my sincere gratitude to Professor Bernardo Almeida. His trust and encouragement were key to embarking on this Ph.D. His attentive guidance, constant search for answers, and ability to challenge me were fundamental. The combination of scientific rigor, professionalism, and his human nature made working under his supervision truly enriching. Moreover, his support in enabling my participation in conferences broadened my perspective. For all, I extend my sincere thanks.

I am deeply grateful to Prof. Armandina Lopes and Prof. João Pedro Araújo, my co-supervisors, for accepting this challenge. Their expertise, perceptiveness, and constructive suggestions were essential to the development of this work and its related publications, shaping its direction and progress.

I thank Prof. Silvino Marques, Alexandre Silva and Veniero Lenzi for Density Functional Theory calculations and paper reviews. Also, Prof. Michael Belsley and Manuel Rodrigues for second harmonic analyses and text reviews. Their collaboration has been precious to the development of this work.

To my colleagues at the University of Minho - João Oliveira, Tiago Rebelo, Daniela Santos, Tiago Rodrigues and Vahideh Isfahani - thank you for your support in various tasks, from manuscript revisions to measurement assistance and knowledge sharing. A special thanks to researcher Rosa Batista, whose genuine encouragement left a significant mark on this journey. I am truly deeply grateful for your support.

From the University of Porto, I am thankful to Pedro Rodrigues, Neenu Lekshmi and João Belo for their support, particularly in target production, magnetic measurements and paper reviews.

I am grateful to the organizing committee of CMD31 - General Conference of Condensed Matter, especially Prof. Joaquim Agostinho, for the opportunity to join and learn so much from this experience.

I also acknowledge the Centro de Física for all the resources and support, especially Eng. José Santos, Mr. Jaime, and Ms. Elisabete, who were always ready to solve issues with remarkable solutions.

Finally, I sincerely thank my parents, my brother and partner for their unconditional support and patience throughout my academic journey. This work is also a product of your love and dedication.

This journey has shaped me into someone motivated to achieve more. To everyone who contributed to this stage of my academic life, my deepest thanks. This thesis carries a piece of each of you.

fct Fundação para a Ciência e a Tecnologia
REPÚBLICA PORTUGUESA CIÊNCIA, TECNOLOGIA E ENSINO SUPERIOR
COMPETE 2020
PORTUGAL 2020
Cofinanciado pela União Europeia

STATEMENT OF INTEGRITY

I hereby declare having conducted this academic work with integrity. I confirm that I have not used plagiarism or any form of undue use of information or falsification of results along the process leading to its elaboration.

I further declare that I have fully acknowledged the Code of Ethical Conduct of the University of Minho.

RESUMO: Heteroestruturas de perovskite em camadas naturais

Os compostos magnetoelétricos (ME) à temperatura ambiente (TA) são promissores para aplicações em eletrónica eficiente, no entanto, a sua produção em multicamadas é difícil e dispendiosa. As perovskites em camadas naturais, como as fases Ruddlesden-Popper, oferecem uma alternativa promissora. A sua manipulação em filmes finos depositados em substratos cristalinos permite ajustar as interações magnéticas e elétricas, para possíveis aplicações em eletrónica energeticamente eficiente.

Nesse sentido, esta tese estuda a preparação e caracterização de filmes finos de $Ca_3Mn_2O_7$ depositados em substratos de $SrTiO_3$ por ablação laser. Os filmes foram sintetizados sob diversas condições e difração de raios X e espectroscopia Raman, confirmando a coexistência das fases *Acaa* e *A2₁am* à TA. As propriedades dielétricas de filmes com 300 nm de espessura foram estudadas e a função de Havriliak-Negami ajustada à permitividade dependente da frequência, revelando dois regimes: abaixo de 107 K (onde os filmes se tornam antiferromagnéticos) e acima de 121 K. A função de Kohlrausch-Williams-Watts (KWW) indicou uma queda abrupta a ~110 K, sugerindo interações magnetoelétricas e um aumento das correlações dipolares magneticamente induzido com a diminuição da temperatura.

As propriedades estruturais, magnéticas e dielétricas de filmes finos de $Ca_3Mn_2O_7$ com diferentes espessuras em substratos de (100) $SrTiO_3$ também foram estudadas. Os filmes mais finos apresentaram maior tensão induzida pelo substrato e variações significativas no espaçamento interplanar, enquanto os mais espessos exibiram um relaxamento mais próximo do material em volume. As medidas magnéticas indicaram temperaturas de transição (T_N) antiferromagnética (AFM) aumentando de 90 K nos filmes mais finos para 110 K nos mais espessos, próximo do valor em volume (112.5 K). As análises da permitividade dielétrica revelaram relaxações de não-Debye, indicando correlações dipolares. O parâmetro KWW exibiu alterações abruptas próximas da T_N AFM, sugerindo fortes interações magnetoelétricas. Esses comportamentos dependem a espessura, com os filmes mais finos exibindo valores menores de T_N.

Foram também estudados substratos de $SrTiO_3$ com outras orientações. A análise dielétrica de filmes de $Ca_3Mn_2O_7$ em substratos (110) $SrTiO_3$:Nb revelou valores mais elevados da T_N AFM (124 K e 145 K), superando a T_N em volume. Isto indica que a orientação do substrato (110) aumenta a estabilidade das fases ferrelétrica e AFM. Além disso, foram encontrados comportamentos térmicos anômalos entre 180 K e 242 K, dependentes da espessura, possivelmente associados à fase não polar *Acaa*. Os cálculos baseados na teoria do funcional da densidade indicam efeitos magnetoelétricos e magnetoelásticos.

Este estudo demonstra que a tensão induzida pelo substrato pode ajustar os comportamentos magnéticos e dielétricos dos filmes de $Ca_3Mn_2O_7$, para aplicações em eletrónica e spintrónica.

Palavras-chave: óxido de cálcio e manganês, filmes finos, multiferróicos, espectroscopia de impedâncias

ABSTRACT: Naturally Layered Perovskite Heterostructures

Room temperature (RT) magnetoelectric (ME) compounds are of great interest for efficient electronic devices applications. However, high-quality multilayered ME compounds are difficult and costly to produce. Naturally layered structures, such as Ruddlesden-Popper phases, offer a promising alternative. The manipulation of these structures in thin films on crystalline substrates allows for the tuning of magnetic and electric interactions, opening pathways to energy-efficient electronic applications.

Building on this, this thesis focuses on the preparation and characterization of $Ca_3Mn_2O_7$ thin films on $SrTiO_3$ substrates using pulsed laser deposition. $Ca_3Mn_2O_7$ dense films were synthesized under diverse preparation conditions. X-ray diffraction and Raman spectroscopy confirmed the coexistence of *Acaa* and *A2₁am* phases at room temperature. 300 nm-thick film's dielectric properties were studied and a Havriliak-Negami function fitted to the frequency-dependent permittivity revealed two regimes: below 107 K (where the films become antiferromagnetic) and above 121 K. The Kohlrausch-Williams-Watts (KWW) function indicated an abrupt decrease below ∼110 K, suggesting magnetoelectric interactions and magnetically induced enhancement of dipolar correlations with decreasing temperature.

The structural, magnetic, and dielectric properties of $Ca_3Mn_2O_7$ thin films with varying thicknesses on (100) $SrTiO_3$ substrates were also investigated. Thinner films showed higher substrate-induced strain, and significant interplanar spacing variations, while thicker films showed relaxation towards bulk material characteristics. Magnetic measurements indicated antiferromagnetic transition temperatures (T_N) increasing from 90 K in the thinnest films to 110 K in thicker films, approaching the bulk value (112.5 K). Dielectric permittivity analyses revealed non-Debye relaxation behaviors and indicating dipole correlations. The KWW parameter exhibited abrupt changes near the antiferromagnetic transition temperatures, suggesting strong magnetoelectric interactions. These behaviors displayed clear thickness dependence, with thinner films showing lower T_N. Building on these findings, $SrTiO_3$ substrates with other orientations were also studied. The dielectric analysis of $Ca_3Mn_2O_7$ thin films on (110) $SrTiO_3$:Nb substrates revealed antiferromagnetic T_N at higher temperatures (124 K and 145 K), exceeding the bulk material value. This indicates that the (110) substrate orientation enhances the stability of the ferroelectric and antiferromagnetic phases. Furthermore, anomalous temperature behaviors between 180 K and 242 K were found and exhibited thickness dependence, potentially related to the onset of the nonpolar *Acaa* phase. Density functional theory calculations indicate magnetoelectric and magnetoelastic effects.

This study reveals that substrate-induced strain can serve to tune magnetic and dielectric $Ca_3Mn_2O_7$ thin film behaviors, enhancing multiferroicity for advanced electronic and spintronic applications.

Keywords: calcium manganese oxide, thin films, multiferroics, impedance spectroscopy

LIST OF CONTENTS

ACKNOWLEDGMENTS ..... **II**

STATEMENT OF INTEGRITY ..... **III**

RESUMO ..... **IV**

ABSTRACT ..... **V**

LIST OF CONTENTS ..... **VI**

LIST OF ABBREVIATIONS AND ACRONYMS ..... **IX**

LIST OF FIGURES ..... **XI**

LIST OF TABLES ..... **XX**

1. INTRODUCTION **1**

1.1. Objectives 3

1.2. Thesis structure 4

2. FUNDAMENTAL CONCEPTS **6**

2.1. Perovskite 6

2.1.1. Layered perovskites 7

2.1.2. Ruddlesden-Popper Phase Series 8

2.1.3. $Ca_3Mn_2O_7$: Structure and Properties 10

2.2. Ferroelectricity 12

2.2.1. Hybrid Improper Ferroelectricity 16

2.3. Dielectric materials 19

2.3.1. Polarization in dielectric materials 20

2.3.2. Dielectric properties under alternating electric field 22

2.3.3. Variation of $\boldsymbol{\tau}$ with temperature 27

2.4. Magnetic materials 28

2.5. Multiferroicity 32

3. THIN FILM PRODUCTION AND CHARACTERIZATION TECHNIQUES **35**

3.1. Pulsed laser deposition 35

3.1.1. Procedure 36
3.1.1.1. Vaporization of the Target Material 36
3.1.1.2. Transport of the Vapor Plume 37
3.1.1.3. Growth of the Thin Film 38
3.1.2. Factors that influence deposition 39
3.1.2.1. Laser parameters 39
3.1.2.2. Target 40
3.1.2.3. Laser spot size 42
3.1.2.4. Atmosphere 43
3.1.2.5. Pressure 44
3.1.2.6. Substrate 44
3.1.2.7. Substrate temperature 46
3.1.3. Advantages and disadvantages 47
3.1.4. Setup used in this work 48
3.2. Post-thermal annealing treatment 50
3.3. X-Ray Diffraction 51
3.4. Scanning Electron Microscopy 54
3.5. Energy-dispersive X-ray Spectroscopy 58
3.6. Raman Spectroscopy 60
3.7. Magnetic characterization by a Superconducting Quantum Interference Device magnetometer 62
3.8. Dielectric characterization by Impedance Spectroscopy 64
3.9. Optic characterization by Second Harmonic Generation 70
3.10. Density Functional Theory 72
4. CALCIUM MANGANESE OXIDES THIN FILMS: INFLUENCE OF DEPOSITION PARAMETERS ON MAGNETIC AND DIELECTRIC PROPERTIES 75
4.1. Thin film synthesis 75
4.2. Structural and morphological characterization 77
4.3. Raman Spectroscopy 84
4.4. Second Harmonic Generation 85
4.5. Magnetic Characterization 86
4.6. Dielectric Characterization 87
4.7. Density-functional theory calculations 95

5. CALCIUM MANGANESE OXIDES: STRAIN-DEPENDENT MAGNETIC AND DIELECTRIC PROPERTIES 98

5.1. Structural and Morphological Characterization 98

5.2. Magnetic Characterization 105

5.3. Dielectric characterization 110

5.3.1. Antiferromagnetic transition temperature analysis 110

5.3.2. Anomalous temperature region analysis 117

5.3.3. Relaxation times analysis 121

5.4. Density-functional theory calculations 122

6. CALCIUM MANGANESE OXIDES: INFLUENCE OF SUBSTRATE ORIENTATION 124

6.1. Structural Characterization 124

6.2. Dielectric characterization 126

7. CONCLUSIONS 133

8. CRITICAL ANALYSIS AND FUTURE PERSPECTIVES 136

9. APPENDIX: FITTING PARAMETERS FROM DIELECTRIC MEASUREMENTS 138

10. REFERENCES 143

LIST OF ABBREVIATIONS AND ACRONYMS

AFM - Antiferromagnetic

AFM-G - Antiferromagnetic G-type

BCC - Body-Centered Cubic

BSE - Backscattered electrons

$Ca_3Mn_2O_7$ - Tricalcium dimanganese heptaoxide

CCD - Charge-Coupled Device

CMO - Calcium Manganese Oxide

DC - Direct Current

DFT - Density Functional Theory

DJ - Dion-Jacobson (layered perovskite structure)

E_a - Activation Energy

E - Electric Field

EDS - Energy-Dispersive X-ray Spectroscopy

FCC - Face-Centered Cubic

f - Frequency

FE - Ferroelectric

FIB-SEM - Focused Ion Beam - Scanning Electron Microscopy

GGA - Generalized Gradient Approximation

HIF - Hybrid Improper Ferroelectricity

HN - Havriliak-Negami (model for non-Debye relaxations)

IS - Impedance Spectroscopy

KWW - Kohlrausch-Williams-Watts (function for stretched exponential decay)

M - Magnetization

ME - Magnetoelectric

NLP - Naturally Layered Perovskites

P - Polarization

PM - Paramagnetic

PVD - Pulsed Laser Deposition

RP - Ruddlesden-Popper (layered perovskite structure)

RT - Room Temperature

SE - Secondary Electrons

SEM - Scanning Electron Microscopy

SHG - Second Harmonic Generation

SQUID - Superconducting Quantum Interference Device

SQS - Special Quasirandom Structures

$SrTiO_3$ - Strontium titanate (STO)

T - Temperature

T_c - Curie Temperature

TEM - Transmission Electron Microscopy

T_N - Néel Temperature

VASP - Vienna Ab initio Simulation Package

V - Voltage

XRD - X-Ray Diffraction

ε **(Epsilon)** - Permittivity

τ **(Tau)** - Relaxation Time

LIST OF FIGURES

Figure 2-1: Ideal cubic perovskite crystal structure: cation B is surrounded by six oxygen ions in an octahedral configuration. A site is surrounded by 12 oxygen ions (not shown). Adapted from reference [31]. 6

Figure 2-2: Schematic diagrams of phase transitions for pure $BaTiO_3$ in the temperature range from −90 °C to 130 °C (183,15 K to 403,15 K). Taken from reference [34]. 7

Figure 2-3: Set of perovskites naturally arranged in layers, originating from the cubic ABO_3 structure. In the Dion-Jacobson phases, A′ is typically an alkali cation, although it can alternatively be a transition metal halide complex such as $(MnCl)^+$. In A-site ordered double perovskites, A′ exhibits a distinct chemical composition compared to A. The perovskite blocks are arranged between layers of $[Bi_2O_2]^{2+}$ in the Aurivillius phases. Taken from reference [43]. 8

Figure 2-4: $Ca_3Mn_2O_7$ structure and rotation distortions. (a) The *A2₁am* ferroelectric ground state structure. Large (blue) spheres correspond to Ca ions. (b) Schematic of the atomic displacements corresponding to the X^+_2 rotation. The dashed square denotes the unit cell of the *I4/mmm* parent structure. (c) Schematic of the X_3 tilt mode. All axes refer to the coordinate system of the *I4/mmm* parent structure [67]. 10

Figure 2-5: Schematic description of the $Ca_3Mn_2O_7$ structure in the undistorted aristotypical *I4/mmm* symmetry and alongside the MnO_6 octahedral rotation and tilting modes corresponding to the experimentally observed *Acaa* $X1-$ and *A2₁am* $X2-, X3-$ structural phases [55]. The respective Glazer notations are also specified. Blue spheres represent Ca atoms, while Mn atoms occupy the center of the octahedra, with an O atom at each apex. Green/blue arrows illustrate the orientation of rotation and tilting of the MnO_6 octahedra that are enclosed by the green/blue dashed circles. The $X1-$ out-of-phase and the $X2+$ in-phase rotation of MnO_6 octahedra present in the *Acaa* and *A2₁am* symmetries, and the orientation of the $X3-$ tilting mode as well are highlighted. In the *A2₁am* section, at the right bottom corner, the antiferroelectric displacement of Ca ions along the [100] direction, associated with the condensation of the polar mode of irrep $\Gamma 4+$, established as a secondary order parameter of the HIF transition, driven by the condensation of the two nonpolar primary lattice instabilities, MnO_6 rotation $X2+$ and tilting $X3-$ modes [67] are depicted. Taken from reference [18]. 11

Figure 2-6: Symmetry hierarchy for piezoelectricity materials. Taken from reference [74]. 13

Figure 2-7: Interrelationship among piezoelectric, ferroelectric, pyroelectric, and dielectric materials. 14

Figure 2-8: Ferroelectric domains: (a) set of domains with random orientation in their natural state; (b) domains aligned in a specific direction due to an applied external electric field; (c) most domains remain ordered after removing the initially applied electric field. Taken from reference [79]. 15

Figure 2-9: The $Ca_3Mn_2O_7$ ferroelectric hysteresis loops measured at 5 K with different peak voltages. Taken from reference [17]..... 15

Figure 2-10: Fundamental configuration of a ferroelectric capacitor. The polarization is shielded by free charges residing on the capacitor plates. When the polarization orientation is switched, a current must flow to supply free charges with a polarity opposing that of the capacitor plates. Taken from reference [80]. 16

Figure 2-11: Energy surface about paraelectric *I4/mmm* in $Ca_3Mn_2O_7$. Change in energy per formula unit as a function of the amplitude of (a), the $X2+$ rotation and $X3-$tilt modes and (b), the polar $\Gamma 5-$distortion. (c), (d) Polarization in the presence of a hybrid order parameter, $QX23 = \lambda QX3 - QX2+$. Taken from reference [67]..... 18

Figure 2-12: Four main polarization types: (a) electronic, (b) atomic-ionic, (c) dipolar and (d) ionic-interfacial. Adapted from reference [88]..... 21

Figure 2-13: Frequency dependencies of four polarization types: interfacial, dipolar, ionic, and electronic. Taken from reference [89]. 22

Figure 2-14: Alignment of spin/magnetic moments in different types of magnetic materials: (a) diamagnetic, (b) paramagnetic, (c) ferromagnetic, (d) antiferromagnetic and (e) ferrimagnetic. Taken from reference [93]..... 30

Figure 2-15: Variation of magnetic susceptibility with temperature. Taken from reference [93]..... 31

Figure 2-16: (a) Unit magnetic cell of antiferromagnetic MnO compound, (b) dependence of antiferromagnetic material susceptibility with temperature (material below Neel temperature) and (c) the correspondent configurations (parallel and transverse). Taken from reference [93]. 31

Figure 2-17: (a) Correlation between multiferroic and magnetoelectric materials, outlining the necessary conditions for their coexistence in a material. (b) Diagram illustrating different coupling types found in materials, with a specific focus on those exhibiting coupling between electric and magnetic orders, referred to as magnetoelectric materials. Taken from reference [95]. 34

Figure 3-1: Schematic of a PLD system. A pulsed laser impinges on a target, removing material that deposits on a substrate, forming a thin film. 36

Figure 3-2: Diagram illustrating the sequential processes involved in laser ablation leading to material expulsion from the target: (a) melting and instantaneous vaporization, (b) shockwave formation, and (c) plume expansion following the cessation of the laser pulse. Taken from reference [109]..... 37

Figure 3-3: Temporal evolution of visible plasma emission from the $LaMnO_3$ laser ablation plume under varying oxygen background pressures. All images are normalized to their maximum intensity. The cross in each image indicates the point of impact of the laser beam on the target surface. Taken from reference [115]. 38

Figure 3-4: Description of simultaneous rotation and translation of the target with frequencies ωr and ωt, respectively [136]. 42

Figure 3-5: Diagram depicting variations in the opening angle of the plasma plume concerning the dimensions of the spot size for (a) a small laser spot and (b) a large laser spot. Taken from reference [109]..... 43

Figure 3-6: Schematic illustrating two potential growth scenarios for films with lattice parameters distinct from the substrate. (a) Coherent growth under strain, where the in-plane lattice parameter aligns with the substrate, and (b) incoherent growth in a relaxed state, maintaining the film's original lattice parameter. Taken from reference [109]. 45

Figure 3-7: List of cubic (pseudo-cubic) substrates and thin films within the lattice constant range from 3.70 to 4.00 Å. Taken from reference [149]. 46

Figure 3-8: Model with the different types of grain structure that occur on vapor-deposited metal films [153]. 47

Figure 3-9: The laser beam is directed and focused on the camera window using a set of mirrors and a lens. 49

Figure 3-10: View of the interior of the camera showing the path taken by the laser beam from the window to the target. 49

Figure 3-11: Photograph of the interior of the chamber during deposition where it is possible to see the plume formed after the laser beam reaches the target. 50

Figure 3-12: Carbolite Digital Tube Furnace utilized for thin films post-annealing thermal treatment. 51

Figure 3-13: Schematic representation of Bragg diffraction in a crystalline lattice, which describes the condition for constructive interference. This interference depends on the X-ray wavelength (λ), the diffraction angle (θ), and the perpendicular interplanar spacing between the lattice planes ($dhkl_i$). The integer n represents the order of the interference. Taken from reference [159]..... 52

Figure 3-14: Schematic diagram of XRD. Taken from reference [160]..... 53

Figure 3-15: Schematics of the incidence vector $K0$, the reflected vector $K$and the scattering vector Q in $\theta = 2\theta$ XRD measurements..... 54

Figure 3-16: Schematic diagram outlining the core components of an SEM microscope. Taken from reference [166]..... 56

Figure 3-17: The electron beam interaction with the specimen, leading to the emission of signals from the sample [168]..... 58

Figure 3-18: Working principle of EDS where a sample of interest is bombarded with a focused beam of electrons, which can excite and eject an inner shell electron, leaving behind a vacancy that is filled by an electron from an outer shell. Taken from reference [172]..... 59

Figure 3-19: Working principle of Raman spectroscopy. Taken from reference [172]..... 61

Figure 3-20: Standard configuration of a Raman spectrometer featuring a microscope coupled with a near-infrared laser. Taken from reference [191]..... 61

Figure 3-21: The dual-junction DC (direct current) SQUID loop incorporates a capacitor, which symbolizes the self-capacitance of the junction. Taken from reference [194]..... 63

Figure 3-22: (a) Bias point (I_b) for the Josephson junction. (b) Voltage in the function of externally applied flux at constant bias current. Taken from reference [194]..... 63

Figure 3-23: Diagram of the MPMS3 SQUID system illustrating key components. Taken from reference [195]..... 64

Figure 3-24: Parallel plate capacitor illustrating its components: dielectric material, electrodes, area (A), and thickness of the film capacitor (L)..... 66

Figure 3-25: Representation of the dielectric constant as a vector in the complex plane..... 66

Figure 3-26: Real ε' and imaginary part ε'' of the complex dielectric function vs normalized frequency for a Debye relaxation process. Taken from reference [85]..... 67

Figure 3-27: Cole-Cole plots for different model functions with $\Delta\varepsilon$ = 1, $\varepsilon\infty$ = 1 and τ = 1 s: (a) Debye-function; (b) Cole-Cole-function with β = 0.5; (c) HN-function with β = 0.7 and γ = 0.6. Taken from reference [85]..... 68

Figure 3-28: (a) Real part ε' (circles) and imaginary part ε''(squares) of poly(propylene glycol) at T = 213.7 K. (b) Cole-Cole representation of the data in a. Taken from reference [85]..... 69

Figure 3-29: Low-temperatures dielectric spectroscopy test stand: 1 – helium cryostat head, 2 – vacuum chamber with sample holder - cryostat, 3 - precision component analyzer, 4 - digital voltmeter, 5 - temperature controller, 6 - compressor of helium cryostat, 7 – rotary vacuum pump, 8 —

turbomolecular vacuum pump, 9 – pressure vacuum gauge, 10 – computer with software controller. Adapted from reference [198]. 70

Figure 3-30: Layout of the second harmonic microscope. PBS represents the polarized beam splitter, and λ/2 denotes the half-wave plate. 72

Figure 3-31: Schematic representations of the Mn spin arrangements in the (a) FM, (b) the AFM-G, and (c) AFM-C states of $Ca_3Mn_2O_7$. Dark blue and white open spheres refer to up- and down-spin alignments, respectively. Adapted from reference [218]. 73

Figure 4-1: X-ray diffraction spectra measured on the samples prepared with different oxygen pressures and deposition temperatures. The peaks marked with "S" are from the substrate. The green lines mark the reference diffraction peaks of the $CaMnO_3$ *Pnma* phase. 78

Figure 4-2: X-ray diffraction spectra measured in the samples prepared with different oxygen pressures and deposition temperatures, but with higher laser pulse energies (high fluences) and with an annealing step after deposition. The peaks marked with "S" are from the substrate. The red and blue patterns were obtained on bulk $Ca_3Mn_2O_7$ powder samples with *Acaa* or *A2₁am* phases, respectively. The blue arrows mark the corresponding peaks observed in the films. 79

Figure 4-3: Scanning electron microscopy (SEM) micrographs of the surface of the samples: (a) CMO10 deposited at room temperature and annealed at 730 °C and (b) CMO14 deposited at 700 °C and annealed at 900 °C. (c)-(d) Corresponding FIB-SEM cross-section micrographs of sample CMO14, which was presented in (b). 80

Figure 4-4: Energy-dispersive X-ray spectroscopy (EDX) spectrum measured in samples (a) CMO10 and (b) CMO14. 81

Figure 4-5: (a) Ca/Mn atomic ratio represented as a function of the laser fluence applied during the film deposition. (b) The corresponding stabilized phases as a function of the laser fluence and annealing temperature, as obtained from the XRD and EDX results. 82

Figure 4-6: Raman spectrum of the CMO14 sample showing the *A2₁am* (marked with P) and *Acaa* (marked with B) modes. 84

Figure 4-7: Second Harmonic Generation response of $Ca_3Mn_2O_7$ 300 nm-thick thin film over Si substrate. 85

Figure 4-8: Temperature-dependent magnetization of CMO11, CMO12 and CMO14 samples, under an applied magnetic field of 2500 Oe. 86

Figure 4-9: Temperature-dependent magnetization of sample CMO14, under 2500 Oe, showing an AFM transition with T_N = 112 K in CMO14 sample, obtained through the derivative of magnetization as a function of temperature (dM/dT graph) (inset). 87

Figure 4-10: SEM cross-section micrographs of sample CMO-305. 88

Figure 4-11: (a) Temperature-dependent real part of the permittivity at 500 Hz (red curve), 5 kHz (green curve) and 10 kHz (blue curve). (b) The temperature-dependent imaginary part of the permittivity at the same frequencies for the CMO-305 sample. 90

Figure 4-12: (a) Real and (b) imaginary parts of the permittivity as a function of frequency at temperatures between 68 and 242 K with the HN equation fit for the CMO-305 sample. 92

Figure 4-13: Nyquist plot of the imaginary part as a function of the real part of the complex permittivity at temperatures between 68 K and 242 K with the HN equation fit for the CMO-305 sample. 93

Figure 4-14: Logarithm of the relaxation times as a function of the inverse of temperature with linear fits to the two different regimes, for temperatures below 107 K (blue fit) and temperatures above 121 K (red fit). 94

Figure 4-15: Parameter β and γ values obtained for the main relaxation. 94

Figure 4-16: Temperature dependence of the stretched exponential parameter, β_{KWW} marked by an abrupt decrease around $\sim$ 100 K, close to the antiferromagnetic transition temperature $T_N \sim$ 112 K, found from temperature-dependent magnetic measurements (section 4.5). 95

Figure 4-17: Sequence of phase transitions in $Ca_3Mn_2O_7$ from the paraelectric *I4/mmm* phase to the ferroelectric *$A2_1am$* phase. (c) Antiferromagnetic to paramagnetic transition temperatures as a function of biaxial strain. The line is a guide to the eye. 96

Figure 4-18: Ferroelectric polarization switching barrier as a function of magnetic ordering for $Ca_3Mn_2O_7$. 97

Figure 5-1: SEM micrographs of the cross-section of the samples over $SrTiO_3$ substrate: (a) CMO-34, (b) CMO-42, (c) CMO-96, (d) CMO-165 and (e) CMO-293. 100

Figure 5-2: SEM micrographs of the cross-section of the samples over $SrTiO_3$:Nb substrate: (a) cCMO-53, (b) cCMO-57, (c) cCMO-107, (d) cCMO-183, (e) cCMO-305 and (f) cCMO-346. 101

Figure 5-3: X-ray diffraction spectra measured on the samples with different thicknesses deposited over $SrTiO_3$ substrates. The peaks marked with "S" are from the substrate. The blue vertical lines mark the reference diffraction peaks (111), (206) and (222) of the $Ca_3Mn_2O_7$ *$A2_1am$* phase. The

blue and red curve lines (shown in the bottom line of the graph) mark the reference diffraction diffractograms of the $Ca_3Mn_2O_7$ *A2₁am* and *Acaa* phases. 102

Figure 5-4: Zoom-in of the X-ray diffraction spectra measured on the samples with different thicknesses around the (222) peak. 103

Figure 5-5: Percentage of strain calculated from the (222) *A2₁am* peak position. 104

Figure 5-6: Temperature dependence of the moment measured in $Ca_3Mn_2O_7$ thin films with 100 Oe applied. In the figure, the samples are presented in increasing order of CMO layer thickness, from top to bottom. In the same direction, the AFM transition temperature also increases. 106

Figure 5-7: Transition temperature as a function of deposition time. The dashed green line marks the AFM transition temperature of bulk $Ca_3Mn_2O_7$ [70]. 107

Figure 5-8: Plot of the logarithm of T_N versus the logarithm of thickness for $Ca_3Mn_2O_7$ thin films. The linear fit is shown, with the slope corresponding to $\lambda = 0.90588$. 108

Figure 5-9: Antiferromagnetic hysteresis curves measured in samples (a) CMO-42 and (b) CMO-96. 109

Figure 5-10: Sample cCMO-53. (a) Real and (b) imaginary parts of the permittivity as a function of the HN equation fit. (c) Nyquist plot of the imaginary part as a function of the real part of the complex permittivity at temperatures with the HN equation fit. (d) Parameter β and γ values obtained for the main relaxation. (e) Temperature dependence of the stretched exponential parameter, βKWW, marked by an abrupt decrease near 85 K and by another regime shift between 206 K and 252 K (marked by the filled area). (f) Logarithm of relaxation times as a function of the inverse of temperature. 111

Figure 5-11: Sample cCMO-107. (a) Real and (b) imaginary parts of the permittivity as a function of the HN equation fit. (c) Nyquist plot of the imaginary part as a function of the real part of the complex permittivity at temperatures with the HN equation fit. (d) Parameter β and γ values obtained for the main relaxation. (e) Temperature dependence of the stretched exponential parameter, β_{KWW}, marking an abrupt decrease near 105 K and a new increase at 222 K. (f) Logarithm of the relaxation times as a function of the inverse of temperature with linear fit corresponding to the AFM region. 112

Figure 5-12: Sample cCMO-183. (a) Real and (b) imaginary parts of the permittivity as a function of the HN equation fit. (c) Nyquist plot of the imaginary part as a function of the real part of the complex permittivity at temperatures with the HN equation fit. (d) Parameter β and γ values obtained for the main relaxation. (e) Temperature dependence of the stretched exponential parameter, β_{KWW}, marking an abrupt drop across de AFM near 112 K and a second drop near 246 K. (f) Logarithm of the relaxation times as a function of the inverse of temperature with linear fits for the three different identified regions. 113

Figure 5-13: AFM transition temperature as a function of the thickness obtained through the dielectric measurements. The thickest sample (305 nm) presented here comes from a study carried out in reference [50]. The dashed red line is a guide to the eye. The dashed green line marks the AFM transition temperature of bulk $Ca_3Mn_2O_7$ [70]. 115

Figure 5-14: Comparison of AFM transition temperatures obtained through magnetic measurements (blue) with dielectric measurements (red). The thickest sample (305 nm) presented here comes from a study carried out in reference [50]. The dashed red and blue lines shall guide the eye. The dashed green line marks the AFM transition temperature of bulk $Ca_3Mn_2O_7$ [70]. The upper axis displays the strain scale, which allows for a direct association with the thickness. 116

Figure 5-15: Sample cCMO-57. (a) Real and (b) imaginary parts of the permittivity as a function of the HN equation fit. (c) Nyquist plot of the imaginary part as a function of the real part of the complex permittivity at temperatures with the HN equation fit. (d) Parameter β and γ values obtained for the main relaxation. (e) Temperature dependence of the stretched exponential parameter, β_{KWW} with a peak at 183 K. (f) Logarithm of the relaxation times as a function of the inverse of temperature with linear fits for two distinct regions, for temperatures above and below 212 K. 118

Figure 5-16: Sample cCMO-346. (a) Real and (b) imaginary parts of the permittivity as a function of the HN equation fit. (c) Nyquist plot of the imaginary part as a function of the real part of the complex permittivity at temperatures with the HN equation fit. (d) Parameter β and γ values obtained for the main relaxation. (e) Temperature dependence of the stretched exponential parameter, β_{KWW}, marking an abrupt increase near 212 K. (f) Logarithm of the relaxation times as a function of the inverse of temperature with a linear fit, marking an abrupt increase between 266 and 212 K. 119

Figure 5-17: Anomalous temperature as a function of the thickness. The dashed red line is a guide to the eye. 120

Figure 5-18: Variation of the antiferromagnetic to paramagnetic transition temperature ΔT_N as a function of the calculated substrate-imposed in-plane strain for $Ca_3Mn_2O_7$ thin films. Here, $\Delta T_N = 0$ K represents the zero-strain transition temperature, introduced to emphasize the relative changes in T_N due to strain rather than absolute values. 123

Figure 6-1: X-ray diffraction spectra measured on the samples prepared on $SrTiO_3$ substrates with orientations (a) (110) and (b) (111). The vertical green lines mark the reference diffraction peaks of the respective substrates (marked with "S"). The vertical red and blue lines indicate the peak positions of $Ca_3Mn_2O_7$ with the orthorhombic structure [228] and of the ferroelectric *A2₁am* orthorhombic structure [229], respectively 125

Figure 6-2: SEM micrograph of the cross-section of the sample (110)STOcCMO-100 prepared over (110) $SrTiO_3$:Nb substrate. 127

Figure 6-3: SEM micrograph of the cross-section of the sample (110)STOcCMO-112 prepared over (110) $SrTiO_3$:Nb substrate. 127

Figure 6-4: Sample (110)STOcCMO-100. (a) Real and (b) imaginary parts of the permittivity as a function of the HN equation fit. (c) Nyquist plot of the imaginary part as a function of the real part of the complex permittivity at temperatures with the HN equation fit. (d) Parameter β and γ values obtained for the main relaxation. (e) Temperature dependence of the stretched exponential parameter, β_{KWW}, marking an abrupt decrease near 124 K and a new increase at 242 K. f) Logarithm of the relaxation times as a function of the inverse of temperature with linear fit corresponding to the AFM region. 130

Figure 6-5: Sample (110)STOcCMO-112. (a) Real and (b) imaginary parts of the permittivity as a function of the HN equation fit. (c) Nyquist plot of the imaginary part as a function of the real part of the complex permittivity at temperatures with the HN equation fit. (d) Parameter β and γ values obtained for the main relaxation. (e) Temperature dependence of the stretched exponential parameter, β_{KWW}, marking an abrupt decrease near 124 K and a new increase near 198 K. f) Logarithm of the relaxation times as a function of the inverse of temperature with linear fit corresponding to the AFM region. 131

Figure 6-6: Phases diagram and space groups of the regimes observed for the (110)STOcCMO-112 sample. At low temperatures, the material exhibits a coexistence of ferroelectric (FE) and antiferromagnetic (AFM) orders within the *A2₁am* phase. A transition occurs at 145 K, leading to a purely FE state, followed by the appearance of the *Acaa* phase at 198 K, which coexists with the *A2₁am* phase at higher temperatures..... 132

LIST OF TABLES

Table 2-1: Crystallographic data of the $Ca_3Mn_2O_7$ sample. Taken from reference [18]. 12

Table 2-2: List of layered perovskite and perovskite-like crystals, synthesized experimentally, exhibiting the emergence of a polar structure through a hybrid improper or trilinear coupling mechanism. Taken from reference [84]. 18

Table 4-1: Deposition laser conditions of the thin films on (100) $SrTiO_3$ substrates and the respective post-deposition annealing conditions at atmospheric pressure. 77

Table 4-2: Lattice parameters of the CMO14 thin film with the $Ca_3Mn_2O_7$ phase. Reference values taken from reference [18]. 83

Table 5-1: Details of the substrates used, the samples produced and the corresponding thicknesses of the $Ca_3Mn_2O_7$ thin films. *Sample cCMO-305 was studied in the previous chapter. 99

Table 5-2: Activation energies (eV) obtained through dielectric characterization of the different samples and considering the distinct temperature regions determined. 121

Table 6-1: Details of the substrate used, produced samples and the corresponding thicknesses of the $Ca_3Mn_2O_7$ thin films 126

Table 9-1: Fitting parameters obtained from the Havriliak–Negami model for the dielectric response of sample cCMO-305 at various temperatures. 138

Table 9-2: Fitting parameters obtained from the Havriliak–Negami model for the dielectric response of sample cCMO-53 at various temperatures. 138

Table 9-3: Fitting parameters obtained from the Havriliak–Negami model for the dielectric response of sample cCMO-107 at various temperatures. 139

Table 9-4: Fitting parameters obtained from the Havriliak–Negami model for the dielectric response of sample cCMO-183 at various temperatures. 140

Table 9-5: Fitting parameters obtained from the Havriliak–Negami model for the dielectric response of sample cCMO-57 at various temperatures. 140

Table 9-6: Fitting parameters obtained from the Havriliak–Negami model for the dielectric response of sample cCMO-346 at various temperatures. 141

Table 9-7: Fitting parameters obtained from the Havriliak–Negami model for the dielectric response of sample (110)STOcCMO-100 at various temperatures. 141

Table 9-8: Fitting parameters obtained from the Havriliak–Negami model for the dielectric response of sample (110)STOcCMO-112 at various temperatures 142

1. Introduction

In multiferroic magnetoelectric (ME) materials, the integration and control of electric and magnetic ferroic orders offer pathways to novel device architectures, particularly in fields such as information storage, sensors, actuators, and low-power, energy-efficient electronics [1–6]. However, achieving single-phase multiferroics with strong ME coupling at room temperature has proven challenging [1, 7, 8] needing the exploration of alternative approaches.

Conventional single-phase multiferroic oxides such as $BiFeO_3$ and $YMnO_3$ are renowned for their high spontaneous polarization [9, 10], yet they exhibit limited ME coupling. Enhanced couplings are anticipated in electronic ferroelectrics, such as charge-ordered materials [9–11], but their small polarization values and low Curie temperatures hinder practical applications. As an alternative, artificial ME multiferroics combining ferroelectric and ferromagnetic phases have been developed, showing potential to enhance ME performance [7, 8, 12–14]. However, these multilayer heterostructures require demanding and costly production techniques, and their interfaces often exhibit leakage, while their elastic coupling is constrained by the speed of sound due to the propagation speed of ferroelectric domain walls.

While significant in the field of sensors and actuators, such materials are unlikely to serve as effective ME systems for microelectronics, which typically require single-crystal or single-phase ME epitaxial films [6, 12, 15]. A simpler alternative approach involves embedding multiferroics into naturally layered structures. Recent advancements in creating non-centrosymmetry through the layering of perovskites or perovskite-like blocks have demonstrated that combinations of octahedral rotations and cation ordering can induce polar structures [16–18].

Naturally Layered Perovskites (NLP) do not rely on electric polarization as the primary order parameter; instead, polarization emerges from the coupling of two or more non-polar lattice instabilities [19], such as BO_6 octahedral rotations, thereby creating hybrid improper ferroelectricity [16]. In these materials, ferromagnetism and ferroelectricity are coupled by the same lattice instability, offering an indirect but very strong magnetoelectric effect. Examples include double perovskites ($AA'BMnO_6$) [20], Ruddlesden-Popper phases (e.g., $Ca_3(Mn,Ti)_2O_7$) [18, 21, 22], and Aurivillius phases [23, 24]. However, their study in the form of nanostructured multiferroic thin films has been poorly explored.

To advance practical applications of NLP, pathways are needed to enhance their multiferroic properties towards room temperature. Leveraging the high sensitivity of complex oxides to lattice distortions [17, 18] and employing interface and strain engineering [15, 19, 25–27] enables the development of new functionalities. For instance, strain-induced nonpolar-to-polar transitions, predicted

through density functional theory calculations, with a critical tensile strain beyond which the polar nature suddenly turns on, were proposed for $Ca_3(Mn,Ti)_2O_7$ and $Sr_3Zr_2O_7$ thin films over crystalline substrates [26]. The fabrication of film-on-substrate structures allows for precise control and enhancement of magnetization and polarization [26, 27]. Due to their straightforward structural characteristics (well-defined strain states and interfaces such as geometries are particularly suited for practical device implementation). Thus, NLP thin films need to be synthesized and tested, in order to understand their magnetic and electric properties at the nanoscale, their polar and magnetic cooperative behavior and the effect of interfacial strain, towards developing strategies for attaining room temperature magnetoelectric properties.

In this context, the study presented here will focus on the study of the synthesis and characterization of thin films of calcium manganese oxide ($Ca_3Mn_2O_7$) on strontium titanate ($SrTiO_3$) substrates, prepared by using pulsed laser deposition. The conditions for stabilizing the $Ca_3Mn_2O_7$ Ruddlesden-Popper phase (n = 2), with improper ferroelectricity and magnetic order, will be systematically studied. Specifically, the effects of varying oxygen pressures, laser fluences, substrate temperatures, and post-deposition annealing will be examined. The corresponding structural, morphological, and spectroscopic properties will be correlated with the stabilized phases and preparation conditions. To further understand the cooperative polar behavior, the analysis of polar order/disorder and the onset of multiferroic correlations in the $Ca_3Mn_2O_7$ films will be present by measuring their dielectric properties through impedance spectroscopy. Also, optic characterization by Second Harmonic Generation will be shown to investigate the non-centrosymmetric properties of the $Ca_3Mn_2O_7$ thin films.

Additionally, to enhance the multiferroic properties towards room temperature via substrate-induced strain, the influence of film thickness on the multiferroic properties of $Ca_3Mn_2O_7$ will be explored. This approach will allow for the study of the impact of thickness and strain on the magnetic and dielectric properties of the $Ca_3Mn_2O_7$ layer and its correlation. Density functional theory calculations will be presented to support the experimental findings.

By systematically investigating these parameters, this research aims to advance the understanding of how substrate-induced strain can optimize the multiferroic properties of $Ca_3Mn_2O_7$. This work paves the way for the development of next-generation magnetoelectric materials tailored for applications in microelectronics, memory devices, and magnetic field sensors.

1.1. Objectives

This thesis aims to produce NLP thin films based on Ruddlesden-Popper $Ca_3Mn_2O_7$, prepared over crystalline substrates. The primary objective is to obtain thin films of $Ca_3Mn_{2-x}Ti_xO_7$ by determining the optimal deposition conditions for their stabilization. The next step involves studying the structural properties of the thin films under the influence of the substrate, aiming to induce strain tuning and control of octahedral rotations and lattice distortions. Understanding the properties of these NLP oxides aims to develop guidelines to promote combined enhanced magnetization and polarization at room temperature. The role of strain as a parameter for tuning the NLP ME responses will be explored, targeting energy-efficient devices with magnetic-electric multifunctionalities. The specific main objectives are as follows:

- Synthesis: Produce laser-ablated nanoscopic (10-400 nm) epitaxial $Ca_3Mn_2O_7$ thin films composed over crystalline substrates. Systematically characterize their structural, chemical, and morphological properties.
- Magnetic Characterization: Characterize the magnetic properties as a function of temperature and magnetic field. Study the influence of strain on the magnetic ordering temperatures induced by varying the layer thicknesses.
- Electric Characterization: Characterize the electric properties (impedance spectroscopy) of the films. Determine the influence of strain on $Ca_3Mn_2O_7$ thin film octahedral rotations.
- Implementation of Density Functional Theory calculations to support and validate the experimental findings, providing deeper insight into the strain effects on magnetic and electric properties.

1.2. Thesis structure

This thesis is divided into nine chapters. The first chapter introduces the importance of controlling electric and magnetic ferroic orders in multiferroic magnetoelectric materials, specifically focusing on naturally layered perovskites and their potential for advanced practical applications. It highlights the pathways needed to enhance their multiferroic properties. The objectives of the thesis are also presented.

Chapter two covers the theoretical groundwork necessary for understanding the research. It delves into fundamental concepts related to perovskites, including their structural and functional properties. The chapter also explains the principles of ferroelectricity and ferromagnetic materials and discusses multiferroic materials. A detailed explanation of dielectrics is provided, along with an exploration of the concept of polarization.

The third chapter details the film production techniques used in this research, namely pulsed laser deposition and post-thermal annealing treatment. Also, this chapter describes the characterization techniques employed, covering structural studies as well as dielectric and magnetic characterization.

Chapter four presents the detailed study of the synthesis conditions to obtain $Ca_3Mn_2O_7$ thin films on $SrTiO_3$ substrates. In-depth structural characterization, spectroscopic and dielectric property studies are also shown to investigate magnetoelectric interactions. Part of the information covered in this chapter has been published in reference [28].

The fourth chapter deepens the study of the previous chapter by exploring the effect of film thickness on the structure, dielectric, and magnetic properties of the films, and understanding their correlation. In this chapter, density functional theory calculations are developed to support the experimental findings.

Chapter five examines the strain-dependent magnetic and dielectric properties of $Ca_3Mn_2O_7$ thin films grown on (100) $SrTiO_3$ substrates. This chapter explores how substrate-induced strain affects multiferroicity by varying the film thickness. Structural, magnetic, and dielectric properties are systematically characterized, alongside density functional theory calculations, to establish the relationship between strain and the enhancement of magnetoelectric interactions.

Chapter six investigates the influence of substrate orientation on the properties of $Ca_3Mn_2O_7$ thin films. This chapter explores alternative substrate orientations, such as (110) and (111), to understand their effect on strain configurations and their potential to enhance the multiferroic behavior of $Ca_3Mn_2O_7$ thin films, making them more suitable for technological applications.

The seventh chapter summarizes the main conclusions of this work, highlighting the significant advancements in the synthesis, characterization, and understanding of the multiferroic properties of $Ca_3Mn_2O_7$ thin films.

To conclude, the eighth chapter provides a critical analysis of the results obtained, contextualizing them within the current state of research in the field. It also explores future directions, proposing strategies for further enhancing the properties of $Ca_3Mn_2O_7$ thin films and addressing existing challenges. The final chapter lists all references cited throughout the thesis.

2. Fundamental concepts

2.1. Perovskite

Perovskite was the name initially called to calcium titanium oxide, $CaTiO_3$, in 1839 by Gustav Rose, and received this name in honor of Russian mineralogist Lev A. Perovski [29]. Later, a perovskite structure was defined as a material with the crystal structure ABX_3, where A and B are positively charged ions, and X is a negatively charged ion. The crystal structure of cubic ABO_3 perovskite can be described as consisting of a corner sharing BO_6 octahedra with the A cation occupying the 12-fold coordination site formed in the middle of the cube of eight such octahedra [30], as shown in Figure 2-1.

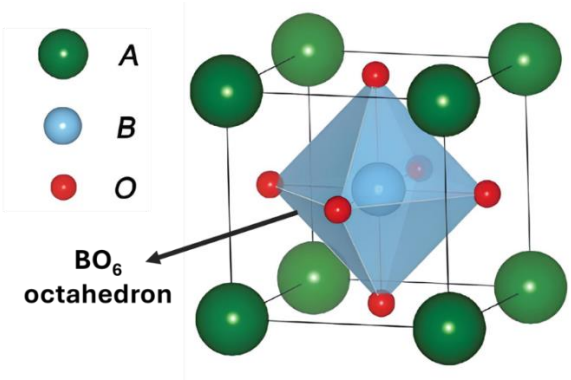


Figure 2-1: Ideal cubic perovskite crystal structure: cation B is surrounded by six oxygen ions in an octahedral configuration. A site is surrounded by 12 oxygen ions (not shown). Adapted from reference [31].

The standard cubic perovskite structure, as seen in compounds like $CaRbF_3$ and $SrTiO_3$, is not frequently encountered, and perovskite minerals themselves show slight distortion [32]. The natural perovskite shows a displacement of both Ca and O relative to Ti that reduces the symmetry to orthorhombic (space group Pbnm) [32]. This structure can be viewed as a lattice of tilted Ti-O octahedra with the Ca situated between these octahedra. The degree of tilt or twist of the octahedra allows many other elements to be incorporated within this structure in both natural and synthetic perovskites [33].

Numerous compounds with the general formula ABO_3 share the perovskite structure. Ca can be partially or entirely substituted by elements like Na, Mn, Ce, Sr, Pb, and Ti, while Fe, Nb, Zr, and Mg can replace Ti, with valency adjustments facilitated through paired substitutions, such as the replacement of Ti^{3+} by Fe^{3+} + Nb^{5+}. Size effects, deviations from the ideal composition, and the Jahn–Teller effect can contribute to the distortion and several factors influence the structure [33]. As an example of the complexity, $BaTiO_3$ has four phase transitions on heating: rhombohedral (R3m), orthorhombic (Amm2), tetragonal (P4mm) and cubic ($Pm\bar{3}m$) [34], as shown in Figure 2-2.

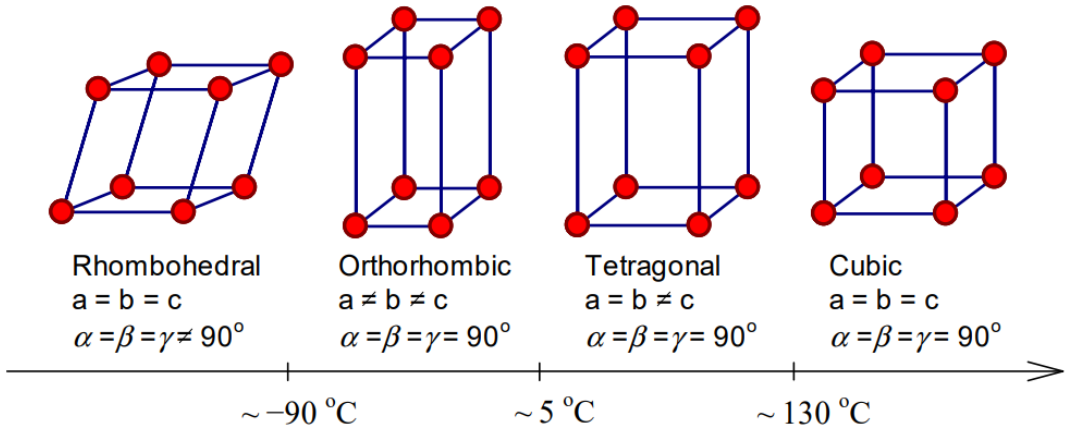


Figure 2-2: Schematic diagrams of phase transitions for pure $BaTiO_3$ in the temperature range from –90 °C to 130 °C (183,15 K to 403,15 K). Taken from reference [34].

Perovskites containing transition metal ions in the B site exhibit a wide range of attractive electronic and magnetic properties [33]. Multiferroicity, characterized by the simultaneous presence of spontaneous ferroelectric and ferromagnetic moments, is a rare occurrence due to the limited number of low-symmetry magnetic point groups, allowing spontaneous polarization [35]. However, in situations involving competing interactions, canted moments, or composite materials, substantial magnetoelectric couplings have been documented [33, 36]. Depending on the atoms present in the structure and octahedron distortions, perovskites can exhibit other impressive properties, such as magnetoresistance, superconductivity, ferroelectricity, charge ordering, spin-dependent transport, high thermopower, and the interplay of structural, magnetic, and transport properties. Therefore, perovskites offer exciting prospects for potential applications in microelectronics [32, 37–40].

2.1.1. Layered perovskites

The layered perovskite is formed by a regular perovskite doped with a chemically different element, such as an A' atom intercalated with an A atom, B' atom intercalated with B, or both, leading to structures such as double perovskites ($AA'B_2O_6$). Additionally, layered perovskites can also be constituted by the natural layering and intergrowth of AO rock salt layers. Different forms of layered perovskites can be considered depending on their crystal structure (see Figure 2-3), the most common being:

- Ruddlesden-Popper (RP) phase, $A_{n+1}B_nO_{3n+1}$ where A and B are cations, X is an anion (e.g., oxygen), and n is the number of octahedral layers in the perovskite-like stack. This structure consists of two-dimensional perovskite-like structures interleaved with cations. The intruding layer occurs either between every individual layer (n = 1) or multiple layers (n > 1) of the ABO_3 lattice. The

Ruddlesden–Popper (RP) phase (A'_2BO_4 for n=1) forms when monovalent organic spacer cations arrange into a bilayer [41];

- Aurivillius phase, represented by the general formula $A_2O_2A_n{-}1B_nO_{3n+1}$; where A is a large 12-coordinate cation, and B is a small 6-coordinate cation [42];
- Dion-Jacobson phase, $A'A_{n-1}B_nO_{3n+1}$; the intruding layer is composed of an alkali metal (M) every n ABO_3 layer.

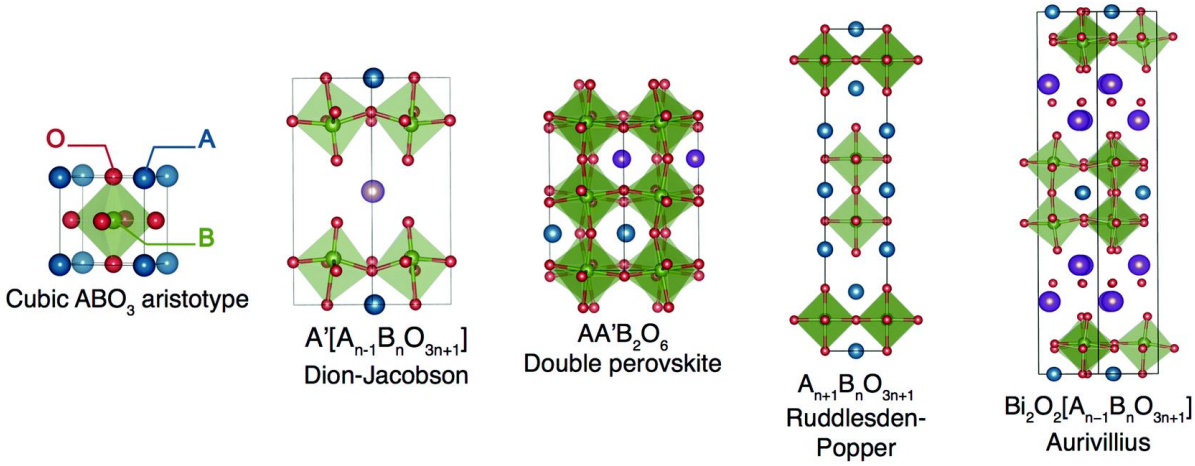


Figure 2-3: Set of perovskites naturally arranged in layers, originating from the cubic ABO_3 structure. In the Dion-Jacobson phases, A′ is typically an alkali cation, although it can alternatively be a transition metal halide complex such as $(MnCl)^+$. In A-site ordered double perovskites, A′ exhibits a distinct chemical composition compared to A. The perovskite blocks are arranged between layers of $[Bi_2O_2]^{2+}$ in the Aurivillius phases. Taken from reference [43].

Unlike bulk ABO_3 perovskites, the group of layered perovskite-like phases includes several polar and ferroelectric materials. Specifically, the Ruddlesden-Popper phases $Ca_3Ti_2O_7$, $Ca_3Mn_2O_7$, and $Ca_3Ru_2O_7$ are polar, even though their parent materials ($CaTiO_3$, $CaMnO_3$, and $CaRuO_3$) are not. The polarization of these Ruddlesden-Popper phase applications and the ability to manipulate and control this property opens opportunities for the development of new technologies that harness these unique properties. Considering the need to understand this property, the Ruddlesden-Popper phases will be explored in the following section.

2.1.2. Ruddlesden-Popper Phase Series

Ruddlesden-Popper (RP) Phase structures are characterized by a unique layering arrangement within the crystal lattice, introducing intriguing properties and potential applications. RP phases are a type of perovskite structure with a general formula of $A_{n+1}B_nO_{3n+1}$, where A and B are cations, X is an anion (e.g., oxygen), and n is the number of octahedral layers in the perovskite-like stack [43]. The value of *n*

determines the number of perovskite-like layers in each unit cell. In these materials, layers of perovskite-like units alternate with spacer layers, creating a distinct architecture [44]. Several RP structures with varying A and B atoms are documented in the literature. Examples include for A elements such as Ca, Sr, La and for B elements such as Ti, Mn, V, Fe, Ru, or Ir [18, 45–50].

These spacer layers are often comprised of organic or inorganic components (such as $R_2A_{n-1}B_nX_{3n+1}$, where R is the organic cation spacer with a long side chain to separate the inorganic layers, A is the organic cation in octahedral structures, B is the metal ion and X is the halide [51, 52] play a key role in determining the physical and chemical properties of RP phases. The incorporation of spacer layers introduces a new level of tunability, enabling researchers to fine-tune material characteristics such as magnetoresistance, superconductivity, optical properties and ferroelectricity [21, 44, 49, 53–56]. Ruddlesden-Popper phase structures exhibit a rich array of properties that make them highly promising for various applications in fields ranging from catalysis and energy storage to electronic devices [49, 57, 58].

Ruddlesden-Popper materials exhibit a distinctive lattice structure where the BO_6 octahedra are connected in only two dimensions, specifically along the *a* and *b* axes. This unique lattice topology, characterized by octahedral connections in two dimensions instead of three, plays a crucial role in determining various functional properties of RP phases [43]. These properties [59, 60] include fast low-temperature oxide ion mobility [61, 62], superconductivity [63, 64], and ferroelectricity induced by rotations of the BO_6 octahedra. In RP phases with a single A-site cation, the A-site can be occupied by cations with 2+ and 3+ valences (such as Ba_{2+}, Sr_{2+}, Ca_{2+}, and rare earth cations), while the B-site typically features a transition metal with 2+ or 4+ valence (for example, Ti_{4+}, Ni_{2+}, Mn_{4+}, or Mn_{2+}, Ru_{4+}). Research findings suggest that it is possible to achieve epitaxial growth of RP phases on perovskite substrates, enabling precise control over the thickness of the perovskite block [65–67]. This development opens avenues for epitaxial strain engineering within this class of compounds.

Octahedral rotations in perovskites are activated by various factors, including the coordination preferences of the A-site cation or external influences such as pressure and epitaxial strain. In certain space groups exhibiting octahedral rotations, the A-site cation may experience displacement from its original position to enhance its coordination environment, resulting in an observable polarization within the perovskite layers. For instance, Benedek and Fennie observed that the energy barrier for switching the sign of octahedral rotation/tilting can be tuned under (biaxial) compressive/tensile strain, respectively [67]. In general, the octahedral layer can exhibit at least two distortion modes: a rotational mode and a tilting mode. Each of these modes condenses into a distinct space group symmetry.

Therefore, considering that $Ca_3Mn_2O_7$ is known to exhibit distortion modes and octahedral rotations that can be activated by various factors, such as substrate-induced strain, it was selected for study in this work. This material will be further described in the following section.

2.1.3. $Ca_3Mn_2O_7$: Structure and Properties

The Hybrid Improper Ferroelectric (HIF) compound $Ca_3Mn_2O_7$ n = 2 RP has a crystal structure that presents layers of corner-sharing MnO_6 octahedra, with two layers of $CaMnO_3$ for every sheet of CaO (Figure 2-4 (a)). At high temperatures, $Ca_3Mn_2O_7$ is paraelectric, assuming the centrosymmetric *I4/mmm* structure [18]. As the temperature decreases, the paraelectric state of $Ca_3Mn_2O_7$ can change to a ferroelectric $A2_1am$ structure due to the combination of rotations and tilt distortions of oxygen octahedra [67], as shown in Figure 2-4. Additionally, a displacive mode may also be present, and it is the coupling of these three modes that gives rise to ferroelectricity and stabilizes the $A2_1am$ phase. The same lattice tilt distortions can modify the magnetic structure and the same rotations can produce a linear magnetoelectric coupling [67, 68].

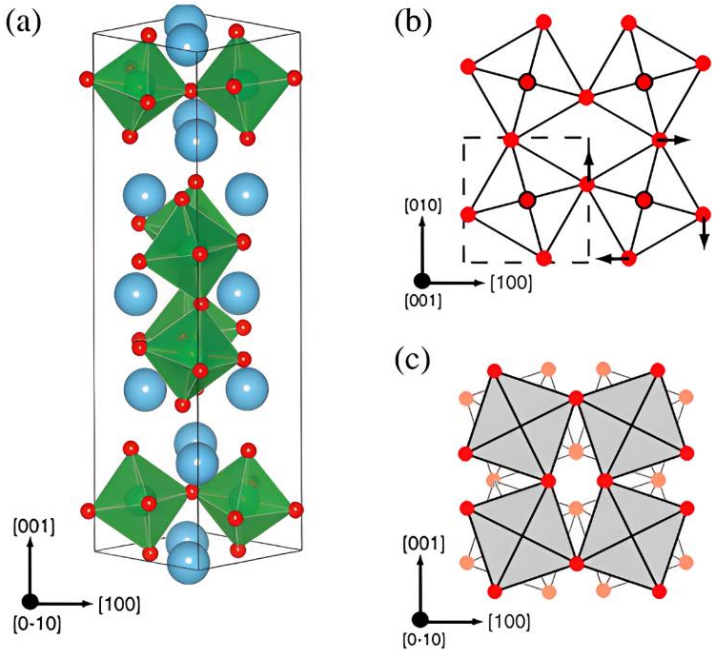


Figure 2-4: $Ca_3Mn_2O_7$ structure and rotation distortions. (a) The $A2_1am$ ferroelectric ground state structure. Large (blue) spheres correspond to Ca ions. (b) Schematic of the atomic displacements corresponding to the X^+_2 rotation. The dashed square denotes the unit cell of the *I4/mmm* parent structure. (c) Schematic of the X_3 tilt mode. All axes refer to the coordinate system of the *I4/mmm* parent structure [67].

Previous studies on the microscopic nature of the ferroelectricity mechanisms in $Ca_3Mn_2O_7$ (refined at 300 K) indicate that the $A2_1am$ phase occurs in the temperature range of 0 K to 350 K and the *Acaa*

phase between 200 K and 500 K [55, 69]. This indicates that in this temperature window, ~200 - 350 K, a mixture of multiple structures *A2₁am* and *Acaa* phase is possible. More recently, another study investigated the structural phase transition path from the low-temperature polar structure up to the highest symmetric phase in the hybrid improper ferroelectric $Ca_3Mn_2O_7$ compound at the atomic scale using the perturbed angular correlation local probe technique and ab initio electronic structure calculations [18]. The study revealed that $Ca_3Mn_2O_7$ undergoes a transition from the low-temperature *A2₁am* polar phase to the high-temperature *I4/mmm* predicted phase, with an intermediate phase characterized by the *Acaa* symmetry. Also, the combined experimental and ab initio study confirms that the phase *I4/mmm* stabilizes at the highest temperatures, also establishing the critical temperature for this second-order phase transition to be around 1163 K. Moreover, the presence of a HIF *A2₁am* phase up to 500 K at local scale was reported in contrast with previous macroscopic results that showed a near full conversion to the *Acaa* phase already at around 350 K [18]. In Figure 2-5 a schematic representation of the structural phases observed in $Ca_3Mn_2O_7$ is depicted. The undistorted aristotypical *I4/mmm* symmetry and the experimentally observed *Acaa* and *A2₁am* structural phases are also illustrated.

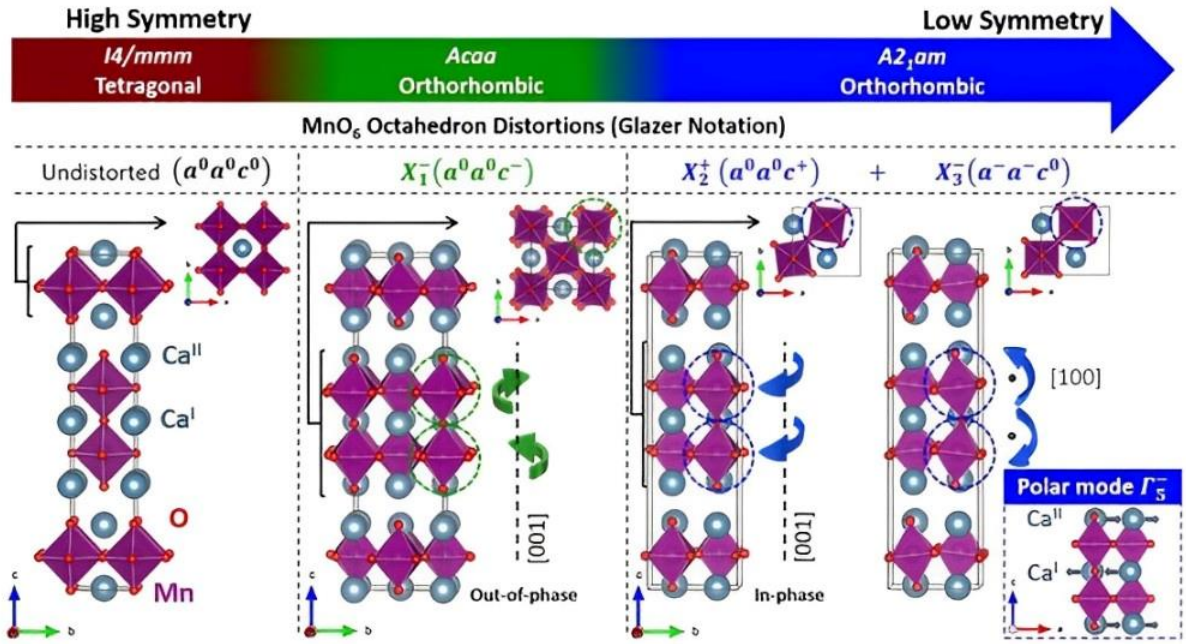


Figure 2-5: Schematic description of the $Ca_3Mn_2O_7$ structure in the undistorted aristotypical *I4/mmm* symmetry and alongside the MnO_6 octahedral rotation and tilting modes corresponding to the experimentally observed *Acaa* (X_1^-) and *A2₁am* (X_2^-, X_3^-) structural phases [55]. The respective Glazer notations are also specified. Blue spheres represent Ca atoms, while Mn atoms occupy the center of the octahedra, with an O atom at each apex. Green/blue arrows illustrate the orientation of rotation and tilting of the MnO_6 octahedra that are enclosed by the green/blue dashed circles. The X_1^- out-of-phase and the X_2^+ in-phase rotation of MnO_6 octahedra present in the *Acaa* and *A2₁am* symmetries, and the orientation of the X_3^- tilting mode as well are highlighted. In the *A2₁am* section, at the right bottom corner, the antiferroelectric displacement of Ca ions along the [100] direction, associated with the condensation of the polar mode of irrep Γ_4^+ , established as a secondary order

parameter of the HIF transition, driven by the condensation of the two nonpolar primary lattice instabilities, MnO_6 rotation (X_2^+) and tilting (X_3^-) modes [67] are depicted. Taken from reference [18].

Table 2-1 presents the structural parameters for the *A2₁am* and *Acaa* phases obtained by Profile matching fit to data collected by Cu-Kα radiation x-ray diffraction for polycrystalline $Ca_3Mn_2O_7$ at 300 K obtained from reference [18].

Table 2-1: Crystallographic data of the $Ca_3Mn_2O_7$ sample. Taken from reference [18].

T (K)	Space group	a (Å)	b (Å)	c (Å)
300	*A2₁am*	5.23954	5.23840	19.42711
	Acaa	5.21189	5.21189	19.59600

The $Ca_3Mn_2O_7$ magnetic order develops at low temperatures, $T_N \sim 112.5$ K [70], making it difficult to incorporate NLP into devices [68]. Therefore, for practical applications of these NLP, a pathway to obtaining multiferroic properties at room temperature is needed. In this regard, the high sensitivity of complex oxides to lattice distortions [17, 18] combined with interface and strain engineering [15, 19, 25–27] leads to new functionalities. For example, theoretical calculations predict that a strain-induced nonpolar-to-polar transition, with a critical tensile strain beyond which the polar nature suddenly emerges, might be observed in $Ca_3Mn_2O_7$ and $Sr_3Zr_2O_7$ thin films through epitaxial strain [26]. Then, the formation of film-on-substrate structures permits controlling and enhancing the film's magnetization and polarization [26, 27]. Due to its simple structural characteristics (well-defined strain states and well-defined interfaces), this geometry is particularly suited for device implementation. However, so far, the production of thin films of $Ca_3Mn_2O_7$ has not been properly explored. Thus, the preparation conditions to obtain the envisaged $Ca_3Mn_2O_7$ thin films need to be studied and optimized, and their electrical properties need to be characterized.

2.2. Ferroelectricity

Crystal lattices exhibit a diverse array of geometries, with their classification extending across 32 crystallographic groups [71]. Within this classification, 21 are characterized by structures devoid of a center of symmetry, giving rise to non-centrosymmetric architectures, while the remaining 11 boast a center of symmetry, rendering them centrosymmetric and consequently devoid of polar properties [72].

Among the 21 non-centrosymmetric structures, 20 possess the ability to induce electrical polarization when subjected to mechanical stresses, earning them the designation of piezoelectric classes [73, 74]. Within this subset, 10 classes emerge as polar, distinguished by the presence of a polar axis and a

temperature-dependent, spontaneous electrical polarization. This specific subset is referred to as pyroelectric [74]. Figure 2-6 represents the symmetry hierarchy for piezoelectric and pyroelectric materials [74].

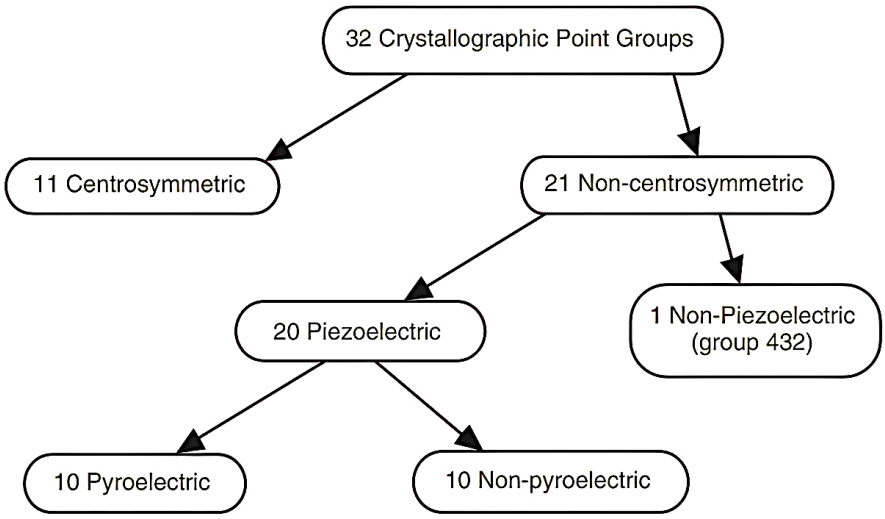


Figure 2-6: Symmetry hierarchy for piezoelectricity materials. Taken from reference [74].

The relationship between piezoelectric, pyroelectric, and ferroelectric materials illustrates a complexed interplay within dielectric materials [44]. Piezoelectric materials respond to external stimuli by altering strain or stress under an electric field or changing polarization due to mechanical excitation, while pyroelectrics exhibit polarization changes in response to temperature fluctuations [75]. Ferroelectric materials encompass both piezoelectric and pyroelectric properties, offering versatility in functionality [44]. Notably, all ferroelectric materials display piezo and pyroelectric behavior, distinguishing them from other dielectrics [75]. This multifaceted nature enables the integration of diverse functionalities through meticulous material design, underscoring the significance of understanding and leveraging the connections among these material classes [76–78]. Figure 2-7 summarizes the interrelationship among piezoelectric, pyroelectric, and ferroelectric materials, together with general dielectrics.

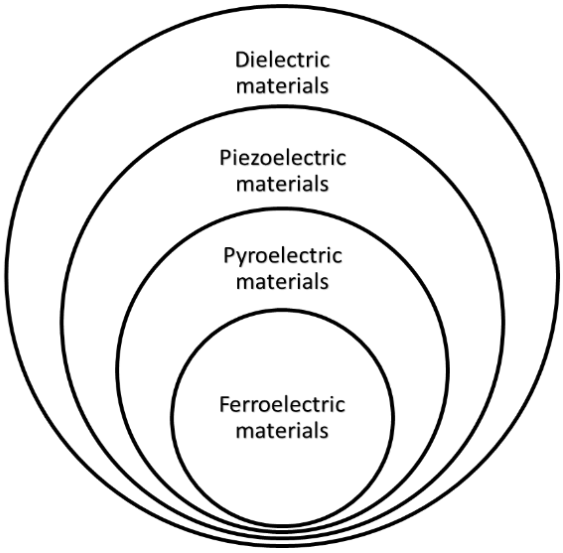


Figure 2-7: Interrelationship among piezoelectric, ferroelectric, pyroelectric, and dielectric materials.

The class of ferroelectric materials falls within dielectric materials, also possessing piezoelectric and pyroelectric properties. These materials exhibit spontaneous and reversible electrical polarization when exposed to external electric fields [44]. Below a critical temperature (known as the Curie temperature), charges within the unit cell shift in such a way that the center of positive charges does not coincide with the center of negative charges, consequently resulting in an electrical polarization.

At the Curie temperature, ferroelectric materials undergo a phase transition from the paraelectric to the ferroelectric phase. In this process, there is a symmetry-breaking, and it is observed that as the temperature rises during the transition from the ferroelectric phase to the paraelectric phase, the electrical polarization disappears. This transition is termed first order when the electrical polarization vanishes abruptly and second order when it occurs continuously [44].

In a ferroelectric crystal, during the transition from the paraelectric phase to the ferroelectric phase, the electric dipoles align in the same direction to minimize the lattice energy. With the formation of the ferroelectric phase, the electric energy of dipoles arranged in parallel accumulates. Consequently, to minimize the accumulated electrostatic energy, sets of unit cells with dipoles oriented parallelly within each set but, on average, oppositely between different sets are formed. These sets of unit cells with parallelly oriented dipoles are termed domains and are illustrated in Figure 2-8.

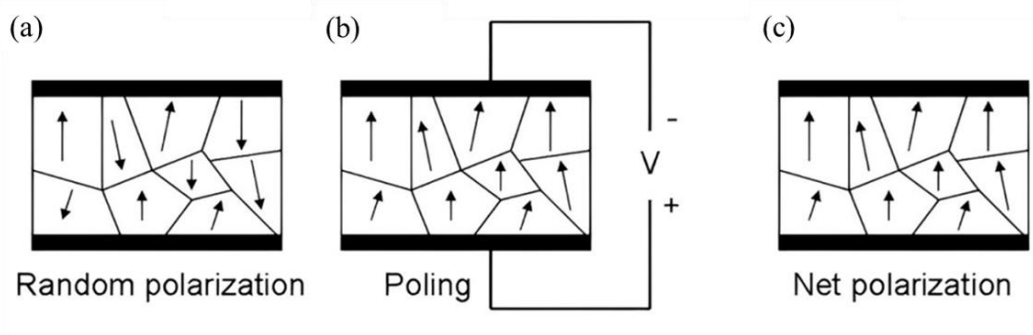


Figure 2-8: Ferroelectric domains: (a) set of domains with random orientation in their natural state; (b) domains aligned in a specific direction due to an applied external electric field; (c) most domains remain ordered after removing the initially applied electric field. Taken from reference [79].

Ferroelectric materials tend to retain their electrical polarization even in the absence of an applied electric field, resulting in hysteresis cycles of polarization versus an applied electric field [43, 80]. From these cycles, it is possible to extract some important characteristic parameters. Saturation polarization is the maximum polarization the material reaches as dipoles align parallelly due to the applied electric field. Remnant polarization represents the polarization that remains when the applied electric field is zero. The externally applied field, in the opposite direction to the initial field, used to eliminate the material's polarization, is known as the coercive field. As an example, Figure 2-9 illustrates the hysteresis cycle of a bulk sample of $Ca_3Mn_2O_7$, as provided by the study referenced in [17].

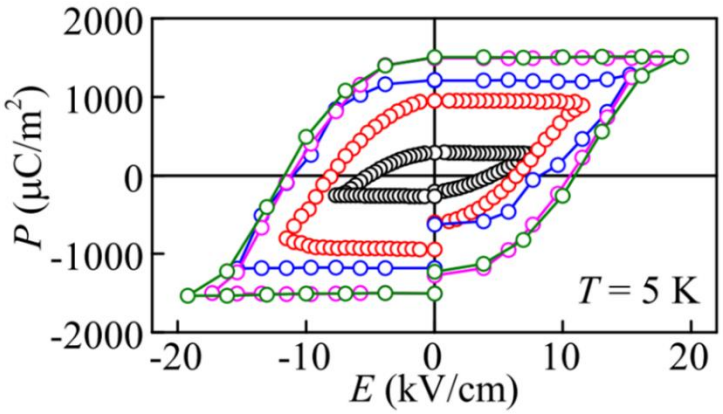


Figure 2-9: The $Ca_3Mn_2O_7$ ferroelectric hysteresis loops measured at 5 K with different peak voltages. Taken from reference [17].

Ferroelectric materials offer an unique capability for information storage and this is achieved by defining the upward or downward orientation of the dipoles as binary “1” or “0” [80]. The orientation of the dipoles can be manipulated by applying a voltage pulse exceeding the coercive voltage, aligning the internal dipoles in the direction of the electric field as shown in Figure 2-10. Various device setups have been devised to read out the polarization orientation [81].

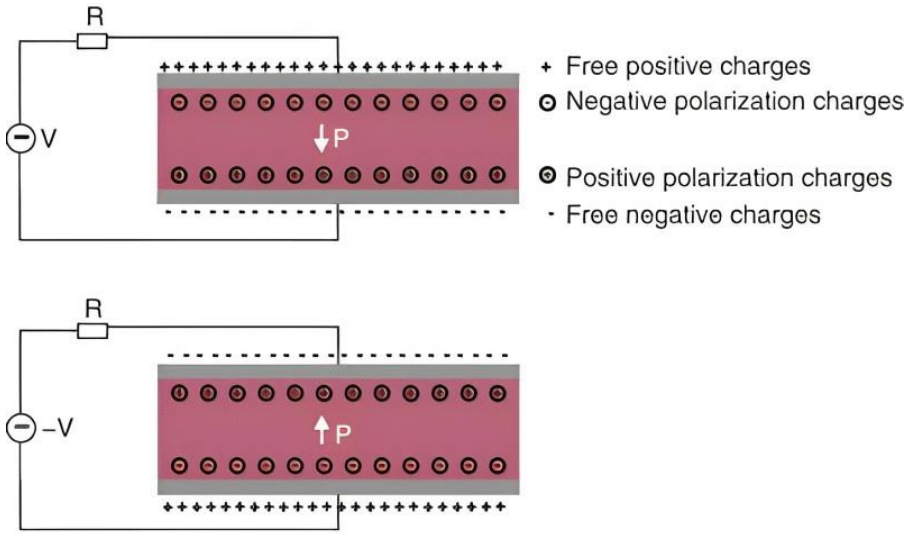


Figure 2-10: Fundamental configuration of a ferroelectric capacitor. The polarization is shielded by free charges residing on the capacitor plates. When the polarization orientation is switched, a current must flow to supply free charges with a polarity opposing that of the capacitor plates. Taken from reference [80].

2.2.1. Hybrid Improper Ferroelectricity

Hybrid Improper Ferroelectrics (HIFs) represent a class of materials that exhibit ferroelectric properties despite a lack of a primary order parameter typically associated with ferroelectricity [67]. Unlike traditional ferroelectrics where the ferroelectric order is driven by a single dominant order parameter, HIFs derive their ferroelectricity from the cooperative interplay of multiple order parameters. This distinctive feature distinguishes them from conventional ferroelectric materials.

The term 'hybrid' in Hybrid Improper Ferroelectrics refers to the coupling of different lattice distortion modes, such as oxygen octahedral rotations and tilts, which induce ferroelectric polarization as a secondary effect. In these materials, ferroelectricity does not originate from a conventional displacement of ions in response to an electric field, but rather from a combination of structural distortions that break inversion symmetry. The concept of hybrid improper ferroelectricity was first introduced by Benedek and Fennie [67], presenting a mechanism for enabling the electric field switching of magnetization in multiferroic materials. The potential significance of a trilinear coupling among different order parameters in polar materials had been recognized in references [82, 83] prior to this.

The Ruddlesden–Popper phases $Ca_3Ti_2O_7$ and $Ca_3Mn_2O_7$ were recognized as hybrid improper ferroelectrics by Benedek and Fennie [67]. The origin of their polar structures posed a problem since their parent perovskites, $CaTiO_3$ and $CaMnO_3$, are nonpolar (crystallizing in the nonpolar *Pnma* space

group). Both $Ca_3Ti_2O_7$ and $Ca_3Mn_2O_7$ exhibit tetragonal *I4/mmm* symmetry at elevated temperatures and eventually arrive at the polar space group *A2₁am* at lower temperatures.

In the same study [67], the contribution of each X_3^-tilt, X_2^+ rotation, and Γ_5^- distortion modes to the $Ca_3Mn_2O_7$ *A2₁am* ground state structure was isolated, and the $T = 0$ energy surface around the *I4/mmm* reference structure was calculated from first principles. The total energy as a function of distortion amplitude for individual rotation ($Q_{X_2^+}$), tilt ($Q_{X_3^-}$), and polar ($Q_{\Gamma_5^-}$) distortions was depicted in Figure 2-11 (a). Significant energy gains were evident within a characteristic double-well potential for rotation and tilt distortions, while the polar contribution remained stable, as shown in Figure 2-11 (b). Figure 2-11 (c) and Figure 2-11 (d) illustrate how polarization arises from coupling to a hybrid order parameter $Q_{X_{23}} = Q_{X_2^+}Q_{X_3^-}$. In the omission of rotation and tilt distortions$\left(Q_{X_{23}} = 0\right)$, polarization had a single minimum at $P = 0$. As $Q_{X_{23}}$ increased, the polarization remained stable, with the minimum shifting to a nonzero value. Increasing $Q_{X_{23}}$ had an effect similar to turning on a finite electric field, analogous to classic improper ferroelectricity. It was observed that the combination of $Q_{X_2^-}$ plus $Q_{X_3^-}$ lowers the energy, even without the $Q_{\Gamma_5^-}$ distortion, resulting in a ground state with four structural domains [67]. These observations suggested that the rotation mode and tilt mode primarily drive the transition to the ferroelectric *A2₁am* phase. This single distortion pattern, $Q_{X_{23}}$, serves as the hybrid improper mode. Unlike proper and conventional improper ferroelectrics, where only one lattice distortion may switch polarization, in a hybrid improper ferroelectric, more than one lattice distortion can do so [67]. Symmetry implies, and calculations confirm, that polarization reverses by either switching an X_2^+ distortion or an X_3^- distortion, resulting in two polar domains.

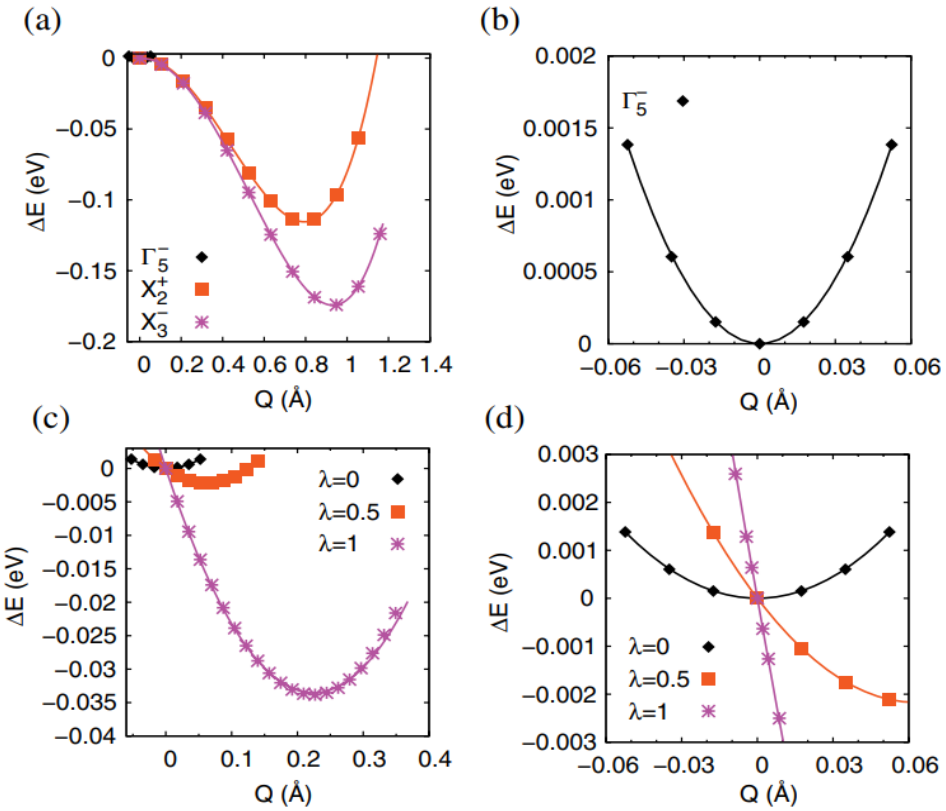


Figure 2-11: Energy surface about paraelectric *I4/mmm* in $Ca_3Mn_2O_7$. Change in energy per formula unit as a function of the amplitude of (a), the X_2^+ rotation and X_3^-tilt modes and (b), the polar Γ_5^-distortion. (c), (d) Polarization in the presence of a hybrid order parameter, $Q_{X_{23}} = \lambda Q_{X_3^-} Q_{X_2^+}$. Taken from reference [67].

Materials with hybrid improper ferroelectricity that uses nonpolar rotational/tilting distortions to create polarization, offer an attractive route to the discovery of new ferroelectric and multiferroic materials [67, 82], thus they will be deeper explored below. Table 2-2 lists several layered perovskites that have been experimentally synthesized, wherein a polar structure emerges through a hybrid improper mechanism [84].

Table 2-2: List of layered perovskite and perovskite-like crystals, synthesized experimentally, exhibiting the emergence of a polar structure through a hybrid improper or trilinear coupling mechanism. Taken from reference [84].

Material
Cation-ordered perovskites
$NaLnMnWO_6$ (Ln = La, Nd, Tb, Y)
$NaLmFeWO_6$ (Ln = La, Nd, Pr, Sm)
$NaLmCoWO_6$ (Ln = Sm-Er, Y, Yb)
$NaLmNiWO_6$ (Ln = La-Tb, Y, Dy, Ho, Yb)
n = 2 Aurivillius phases
$SrBi_2Nb_2O_7$

$SrBi_2Ta_2O_7$
n = 2 Ruddlesden-Popper phases
$Ca_3Mn_2O_7$
$Ca_3Ti_2O_7$
$(Ca,Sr)_3Ti_2O_7$
$Sr_3Zr_2O_7$
$(Ca,Sr)_3Sn_2O_7$
$Li_2AB_2O_7$ (A=Sr, Ca; B=Nb, Ta)
$LiNdB_2O_7$ (B = Nb, = Ta)
$(Ca,Sr,Tb)_3(Fe/Ti)_2O_7$
$Li_2La(TaTi)O_7$
n = 2 Dion-Jacobson phases
$CsBiNb_2O_7$
$RbBiNb_2O_7$
$CsNdB_2O_7$ (B = Nb, Ta)
$RbNdB_2O_7$ (B=Nb, Ta)
$CsLaNb_2O_7$

2.3. Dielectric materials

Polarization refers to the separation of charges within a material, resulting in the formation of electric dipoles. This phenomenon can occur naturally in certain materials, where permanent dipoles exist due to the intrinsic structure of the molecules, or it can be induced by external factors, such as an electric field [44]. At a microscopic level, the electric dipoles arise from the displacement of charges within atoms, molecules or in crystalline unit cells. In some materials, such as those with permanent dipoles, polarization exists even without the application of an external electric field. However, in most dielectrics, polarization is primarily induced by the action of an external field, which causes a redistribution of charges. This results in the alignment of the dipoles along the direction of the field [44].

When a dielectric material is subjected to an external electric field, the induced electric polarization (P) is the result of the alignment or displacement of the positive and negative charges. This polarization can be expressed as [44]:

$$P = N\alpha E \tag{2-1}$$

given N as the number of dipoles per unit volume, E as the electric field, and α as the polarizability.

2.3.1. Polarization in dielectric materials

The total polarizability combines contributions from different polarization mechanisms, including electronic, atomic-ionic, dipolar, and ionic-interfacial, as illustrated in Figure 2-12.

- Electronic polarization, also known as optical polarization, refers to the rearrangement of electrons within an atom or molecule in response to an external electric field [85]. It occurs when the electric field induces deformation or displacement of the symmetrical distribution of electron clouds around atoms or molecules [86]. This involves the shifting of outer electron clouds relative to the inner positive atomic cores.
- Atomic or ionic polarization, also known as vibrational polarization, occurs when the electric field displaces the atoms or ions within a polyatomic molecule/compound relative to each other [86]. This results in the distortion of the normal lattice vibration. It's especially important for their electrical properties across a range of frequencies, from direct current (DC) to infrared [87]. This type of polarization significantly influences the materials' dielectric constants.
- Orientational polarization occurs exclusively in materials comprising molecules or particles possessing a permanent dipole moment [86]. When subjected to an electric field, these dipoles reorient themselves toward the direction of the field.
- Interfacial polarization refers to a phenomenon that occurs primarily at lower frequencies and involves the movement of ions that is limited by the presence of interfaces or dielectric boundaries inside the material [87]. Since the ions can move over long-distances, the polarization arising from this effect can be significant.

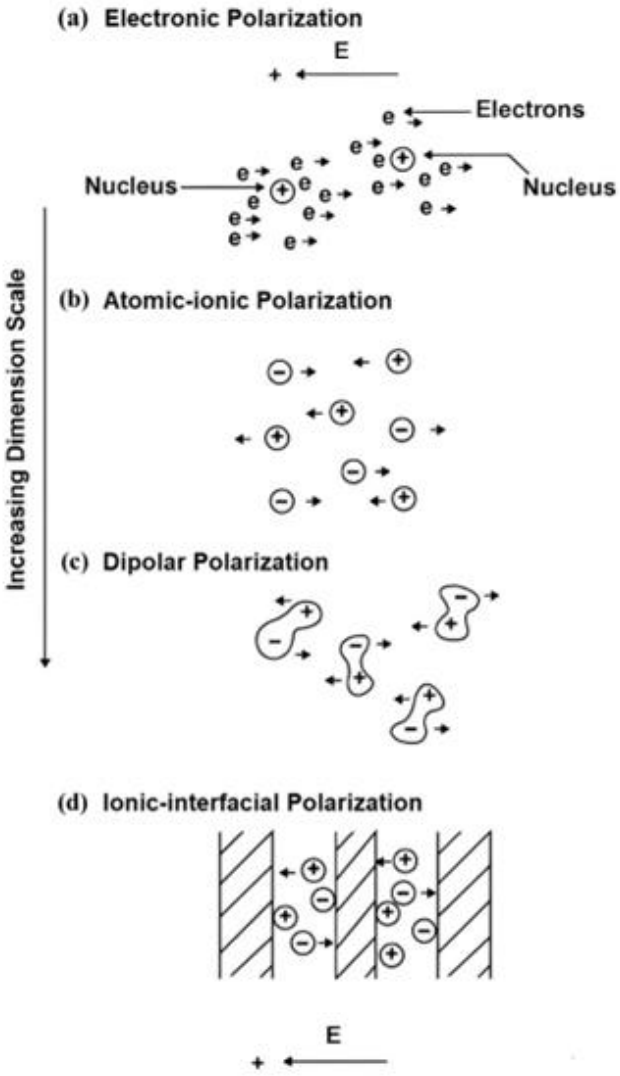


Figure 2-12: Four main polarization types: (a) electronic, (b) atomic-ionic, (c) dipolar and (d) ionic-interfacial. Adapted from reference [88].

For a linear dielectric:

$$\vec{D} = \varepsilon \vec{E} \tag{2-2}$$

where ε is the permittivity of the dielectric material, $\vec{E}$ is the electric field, and $\vec{D}$ is the electric displacement field.

Microscopically:

$$\varepsilon = \varepsilon_0 + N\alpha \tag{2-3}$$

where ε_0 is the vacuum permittivity, N is the number of dipoles per unit volume, and α is the polarizability.

The electric displacement, D, can be expressed in terms of the electric field, E and polarization, P:

$$\vec{D} = \varepsilon_0 \vec{E} + \vec{P} \tag{2-4}$$

Using Equation (2-5):

$$\varepsilon\vec{E} = \varepsilon_0\vec{E} + \vec{P} \Leftrightarrow \vec{P} = \varepsilon\vec{E} - \varepsilon_0\vec{E} \Leftrightarrow N\alpha\vec{E} = (\varepsilon - \varepsilon_0)\vec{E} \quad (2\text{-}5)$$

the relative permittivity is given by:

$$\varepsilon_r = \frac{\varepsilon}{\varepsilon_0} = \left(1 + \frac{N\alpha}{\varepsilon_0}\right) = 1 + \chi \quad (2\text{-}6)$$

where χ is the electric susceptibility.

2.3.2. Dielectric properties under alternating electric field

In dielectric materials, distinct polarization mechanisms exhibit varied response times. Consequently, their behavior at specific frequencies of the external alternating electric field may not contribute to dielectric polarization. The reduction in dielectric polarization varies with increasing frequency, and this behavior differs for each polarization mechanism, as depicted in Figure 2-13.

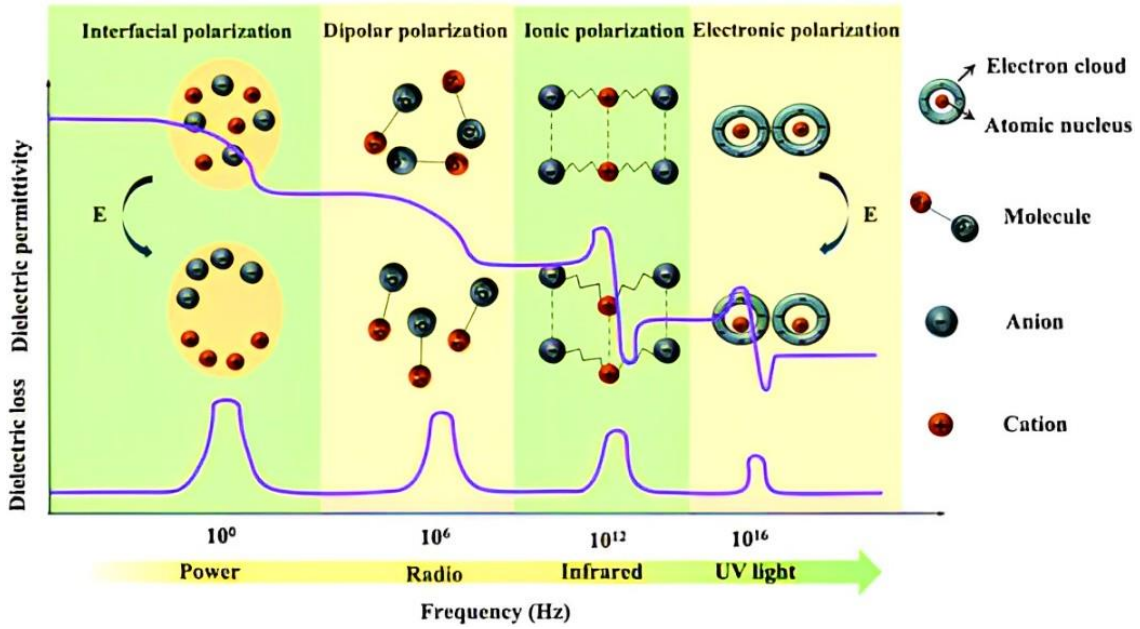


Figure 2-13: Frequency dependencies of four polarization types: interfacial, dipolar, ionic, and electronic. Taken from reference [89].

For electronic and atomic polarizations, the characteristic times are related to the vibration frequencies of the system and are referred to as resonance times (modes). In orientational polarization, the characteristic times of the system are called relaxation times [86].

Assuming the alternating electric field, it is given by:

$$\vec{E}(t) = \overrightarrow{E_0}e^{i\omega t} \quad (2\text{-}7)$$

where ω is the angular frequency. The phase difference undergone by the electric displacement is related to it as follows:

$$\vec{D}(t) = \overrightarrow{D_0} e^{i(\omega t - \delta(\omega))} \tag{2-8}$$

where δ is the phase difference between the applied external field and the electric displacement, depending on the applied frequency.

Relating Equation (2-8) to Equation (2-2), the electric permittivity in the frequency domain is given by:

$$\varepsilon(\omega) = \frac{D_0}{E_0}\cos\big(\delta(\omega)\big) - i\frac{D_0}{E_0}\sin\big(\delta(\omega)\big) \tag{2-9}$$

being $\varepsilon(\omega)$ a complex quantity:

$$\varepsilon(\omega) = \varepsilon'^{(\omega)} - i\varepsilon''^{(\omega)} \tag{2-10}$$

where

$$\varepsilon'^{(\omega)} = \frac{D_0}{E_0}\cos\big(\delta(\omega)\big) \tag{2-11}$$

and

$$\varepsilon''^{(\omega)} = \frac{D_0}{E_0}\sin\big(\delta(\omega)\big). \tag{2-12}$$

Then, this results in:

$$\frac{\varepsilon''}{\varepsilon'} = \tan\delta \tag{2-13}$$

The power dissipated by the dielectric is proportional to tan δ. Thus, tan δ is referred to as the system losses. A real capacitor composed of a dielectric has a resistive component related to the DC conductivity of the dielectric. The equivalent circuit for this system is a capacitor in parallel with a resistance, R. The electric current density, J, is given by:

$$J = J_R + \frac{dD}{dt} = J_R + \hat{\varepsilon}\frac{dE}{dt} \tag{2-14}$$

here, $\hat{\varepsilon}$ is the complex dielectric constant of the capacitor, and J_R is the electric current density associated with the resistance, R. By Ohm's law, the following is obtained:

$$J_R = \sigma E \tag{2-15}$$

here, σ is the DC conductivity.

Relating Equation (2-15) to (2-10):

$$J = \sigma E + (\varepsilon' - i\varepsilon'')i\omega E \tag{2-16}$$

Thus, in a non-ideal dielectric, the complex dielectric constant has a contribution from DC conductivity and is defined as:

$$\hat{\varepsilon} = \varepsilon' - i\left(\varepsilon'' + \frac{\sigma}{\varepsilon_0 \omega}\right) \tag{2-17}$$

As the behavior of a real dielectric is not necessarily ohmic, it is common to write Equation (2-17) alternatively with an exponent s:

$$\hat{\varepsilon} = \varepsilon' - i\left(\varepsilon'' + \frac{\sigma}{\varepsilon_0 \omega^s}\right) \tag{2-18}$$

Ignoring the polarization of space charges, P_{ce} , the total polarization in a dielectric (non-ferroelectric) is given by:

$$\vec{P} = \overrightarrow{P_e} + \overrightarrow{P_a} + \overrightarrow{P_o} \tag{2-19}$$

where P_e is the electronic polarization, P_a is the atomic polarization, and P_o is the orientational polarization.

In relative terms, since the electronic and atomic polarizations respond very quickly to an alternating electric field, their contributions can be treated as constants as their ressonances occur at high frequencies. Thus, the polarization can be expressed as:

$$P(t) = P_\infty + P_0(\mathrm{t}) = (\varepsilon_\infty - \varepsilon_0)E + (\varepsilon_s - \varepsilon_\infty)E(t) \tag{2-20}$$

where P_∞ represents the high-frequency term, E is the applied electric field, ε_∞ is the dielectric constant for very high frequencies, ε_0 is the vacuum permittivity, and ε_s is the dielectric constant for zero frequency.

When the electric field is removed, the depolarization rate is proportional to polarization:

$$\frac{dP}{dt} = -\frac{P(t)}{\tau_0} \tag{2-21}$$

where τ_0 is the relaxation time.

This equation indicates that the polarization decays exponentially with time. The solution to this differential equation when the aplied electric field (E) is removed, is given by:

$$P(t) = (\varepsilon_s - \varepsilon_\infty)Ee^{-\frac{t}{\tau_0}} \tag{2-22}$$

where $P_0 = (\varepsilon_s - \varepsilon_\infty)E$ is the initial value of the polarization when the electric field is removed.

The polarization when an electric field is applied at $t = 0$, is given by:

$$P(t) = (\varepsilon_s - \varepsilon_\infty)E\left(1 - e^{-\frac{t}{\tau_0}}\right) \tag{2-23}$$

Equation (2-23) describes how polarization evolves over time as the material responds to the electric field, reaching a maximum value as time progresses.

By convolving depolarization and alternating electric field and using Equation (2-23):

$$P = (\hat{\varepsilon} - 1)\varepsilon_0 E \tag{2-24}$$

The dielectric constant is obtained as [85]:

$$\varepsilon = \varepsilon_\infty + \frac{\varepsilon_s - \varepsilon_\infty}{1 + i\omega\tau_0} \tag{2-25}$$

This equation is known as the Debye equation.

In practice, instead of a single characteristic polarization oscillating with time, there may be a distribution of relaxation times. For this reason, Cole and Cole introduced a factor β to account for this distribution [24]:

$$\varepsilon = \varepsilon_\infty + \frac{\varepsilon_s - \varepsilon_\infty}{1 + (i\omega\tau_{CC})^\beta} \tag{2-26}$$

where β varies between 0 and 1. For $\beta = 1$, the Debye equation is recovered.

The real and imaginary components of Equation (2-26) are, respectively:

$$\varepsilon' = (1 + \omega\tau_{CC})^\beta \cos\left(\frac{\beta\pi}{2}\right) r^{-1}(\omega)\Delta\varepsilon + \varepsilon_\infty \tag{2-27}$$

$$\varepsilon'' = (\omega\tau_{CC})^\beta \sin\left(\frac{\beta\pi}{2}\right) r^{-1}(\omega)\Delta\varepsilon \tag{2-28}$$

where $r(\omega)$ is an auxiliary function defined as:

$$r(\omega) = 1 + 2(\omega\tau_{CC})^\beta \cos\left(\frac{\beta\pi}{2}\right) + (\omega\tau_{CC})^{2\beta} \tag{2-29}$$

and,

$$\Delta\varepsilon = \varepsilon_s - \varepsilon_\infty \tag{2-30}$$

Similar to Equation (2-18), a term of conductivity is added to the imaginary part of the Cole-Cole equation:

$$\varepsilon'' = \frac{\sigma}{\varepsilon_0 2\pi f^s} \tag{2-31}$$

Expressing explicitly the real and imaginary parts of the permittivity from Equation (2-26), a relationship between them is given by:

$$\left[\varepsilon'' + \frac{(\varepsilon_s - \varepsilon_\infty)\tan\left((1-\beta)\frac{\pi}{2}\right)}{2}\right]^2 + \left[\varepsilon' - \frac{\varepsilon_s + \varepsilon_\infty}{2}\right]^2 = \left[\frac{\varepsilon_s - \varepsilon_\infty}{2\cos\left((1-\beta)\frac{\pi}{2}\right)}\right]^2 \tag{2-32}$$

This is a semicircle with the following parameters:

$$Radius = \frac{\varepsilon_s - \varepsilon_\infty}{2\cos\left((1-\beta)\frac{\pi}{2}\right)}; \tag{2-33}$$

$$x_0 = \frac{\varepsilon_s + \varepsilon_\infty}{2}; \tag{2-34}$$

$$y_0 = \frac{(\varepsilon_s - \varepsilon_\infty)\tan\left((1-\beta)\frac{\pi}{2}\right)}{2}. \tag{2-35}$$

Equation (2-18) was generalized by Havriliak and Negami, considering an asymmetric distribution of relaxation times, resulting in a distorted circle-shaped curve ε''vs ε' [85], given by:

$$\varepsilon = \varepsilon_\infty + \frac{\Delta\varepsilon}{(1+(i\omega\tau_{HN})^\beta)^\gamma} \tag{2-36}$$

In Equation (2-26), a new shape parameter, γ, was introduced. Taking $\gamma = \beta = 1$ results in the Debye equation. Thus, the Debye equation and the Cole-Cole equation are particular cases of the general Havriliak-Negami equation.

Separating the real and imaginary components of the dielectric permittivity, the following is obtained:

$$\varepsilon' = r(\omega)\cos[\gamma\psi(\omega)]\Delta\varepsilon + \varepsilon_\infty \tag{2-37}$$

$$\varepsilon'' = r(\omega)\sin[\gamma\psi(\omega)]\Delta\varepsilon \tag{2-38}$$

where $r(\omega)$ and $\psi(\omega)$ are auxiliary functions defined as:

$$r(\omega) = \left[1 + 2(\omega\tau_{HN})^\beta \cos\left(\frac{\beta\pi}{2}\right) + (\omega\tau_{HN})^{2\beta}\right]^{-\frac{\gamma}{2}} \tag{2-39}$$

$$\psi(\omega) = \arctan\left(\frac{sin\left(\frac{\beta\pi}{2}\right)}{(\omega\tau_{HN})^{-\beta} + cos\left(\frac{\beta\pi}{2}\right)}\right) \tag{2-40}$$

In this study, some modifications were necessary to optimize the model beyond the Havriliak-Negami contribution. Thus, a conductivity term was again introduced in the imaginary part of the dielectric permittivity to take into account the finite resistivity of the material. Consequently, the imaginary component of the dielectric permittivity takes the form:

$$\varepsilon'' = r(\omega)\sin[\gamma\psi(\omega)]\Delta\varepsilon + \frac{\sigma}{\varepsilon_0\omega^s} \tag{2-41}$$

where σ is the DC electrical conductivity, and s is a factor that allows altering the curve shape, enabling the study of non-ohmic materials.

In some cases, instead of just one relaxation, it is necessary to consider two relaxations, τ_1 e τ_2. Thus, the real and imaginary components of the dielectric permittivity are given by:

$$\varepsilon' = r_1(\omega)\cos[\gamma_1\psi_1(\omega)]\Delta\varepsilon_1 + r_2(\omega)\cos[\gamma_2\psi_2(\omega)]\Delta\varepsilon_2 + \varepsilon_\infty \quad (2\text{-}42)$$

$$\varepsilon'' = r_1(\omega)\sin[\gamma_1\psi_1(\omega)]\Delta\varepsilon_1 + r_2(\omega)\sin[\gamma_2\psi_2(\omega)]\Delta\varepsilon_2 + \frac{\sigma}{\varepsilon_0\omega^s} \quad (2\text{-}43)$$

The dielectric behavior in the frequency domain is related to that in the time domain by a Fourier transformation. For independent dipoles with relaxation time τ_D, an exponential decay of the dipole correlation function is obtained:

$$\phi(t) = \phi(0)e^{-t/\tau_D} \quad (2\text{-}44)$$

giving the Debye behavior in the frequency domain [85]:

$$\varepsilon(\omega) = \Delta\varepsilon/(1 + i\omega\tau_D) \quad (2\text{-}45)$$

For a non-Debye relaxation, dipole correlations develop, giving a stretched exponential behavior in the time domain described by the Kohlrausch-Williams-Watts (KWW) function:

$$\phi(t) = \phi(0)exp\left(-\left(\frac{t}{\tau_{KWW}}\right)^{\beta_{KWW}}\right) \quad (2\text{-}46)$$

where β_{KWW} is the stretched exponential parameter. β_{KWW} can be connected to the parameters β and γ of the HN function by the relation $\beta_{KWW} = \beta \times \gamma$ [90, 91].

This model allows fitting experimental curves, obtaining the parameters from the equations associated with the characteristic relaxations of each sample.

2.3.3. Variation of τ with temperature

For a specific film, it is useful to determine the variation of the parameter τ with temperature, as this analysis allows obtaining the activation energy of the observed relaxations. Thus, for thermally activated processes, a behavior according to the Arrhenius law is expected [85]:

$$\tau = \tau_0 exp\left(\frac{E_a}{k_B T}\right) \quad (2\text{-}47)$$

where E_a is the activation energy to be calculated, k_B is the Boltzmann constant, and T is the temperature.

Applying the logarithm to Equation (2-47) yealds a linear relation between $ln(\tau)$ and $1/T$:

$$ln(\tau) = \ln(\tau_0) + \frac{E_a}{k_B T} \quad (2\text{-}48)$$

resulting in:

$$E_a = m_a k_B \quad (2\text{-}49)$$

where m_a is the slope of the line for the relaxation.

2.4. Magnetic materials

Magnetic materials are of supreme importance in both fundamental scientific research and application-driven studies. The array of experimental techniques available for characterizing magnetic materials continues to expand [92]. An essential characterization method is magnetic susceptibility, denoted as χ and expressed as [44]:

$$M = \chi H \quad (2\text{-}50)$$

which is the quantity that relates a material's magnetization, M, to the strength of an applied magnetic field, H. Magnetic susceptibility measurements provide insight into a material's reaction to an externally applied magnetic field, thereby aiding in the determination of its magnetic properties. Such measurements can be conducted within a direct current (DC) field to analyze static magnetic characteristics or within an alternating current (AC) field to investigate dynamic properties.

In contemporary research, the precision of magnetic susceptibility measurements has been significantly enhanced with the introduction of the SQUID (Superconducting Quantum Interference Device) magnetometer [92]. This instrument enables the direct measurement of a material's magnetic susceptibility, offering high sensitivity.

Magnetic materials can be categorized into five types based on their magnetic ordering and the characteristics of their magnetic susceptibility: diamagnetic, paramagnetic, ferromagnetic, antiferromagnetic and ferrimagnetic [44]. Diamagnetic and paramagnetic materials exhibit no inherent magnetic order across all temperatures. Conversely, ferromagnetic, antiferromagnetic, and ferrimagnetic materials display magnetic ordering below a transition temperature. Figure 2-14 (page 30) illustrates the spin alignments of the five types of magnetic materials in their solid states. In Figure 2-14 (a), atoms, ions, or molecules within the material exhibit no spin or magnetic moment due to the absence of unpaired electrons. Consequently, in the absence of an external magnetizing field, these materials display no magnetism and are classified as diamagnetic. The susceptibility of diamagnetic substances is

characterized by a small negative value, typically independent of temperature, as the application of a magnetic field induces a magnetization in the opposite sense [44, 93].

The paramagnetic materials are described in Figure 2-14 (b). Here, atoms, ions, or molecules possess unpaired electrons, resulting in inherent magnetic dipole moments. In the absence of a magnetizing field at room temperature ($T > 0$ K), these atomic or molecular dipoles are randomly oriented to minimize the system's magnetic energy, rendering the material non-magnetic [93]. However, upon the application of a magnetizing field, partial alignment of the dipoles occurs in the direction of the field, inducing magnetization in the material. The magnitude of the magnetization increases with increasing field strength until reaching saturation, where all dipoles are aligned with the field. Paramagnetic materials exhibit a positive but small susceptibility [93], as illustrated by the variations with temperature shown in Figure 2-15 (page 31).

Atoms, ions, or molecules in ferromagnetic, antiferromagnetic, and ferrimagnetic materials also possess unpaired electrons, resulting in individual dipole moments similar to those observed in paramagnetic materials [93]. However, unlike paramagnetism, these dipoles interact with each other due to exchange interactions. This interaction leads to the formation of domains within the material, where the spins or magnetic moments of all atoms within a domain are either aligned parallel (in ferromagnetic materials) or anti-parallel (in antiferromagnetic or ferrimagnetic materials).

In ferromagnetic materials (Figure 2-14 (c)), all atoms or ions have their magnetic moments aligned parallel within each domain, resulting in a finite magnetization for each domain. Below the Curie temperature (T_C) and in the absence of an external magnetizing field, the orientations and magnitudes of magnetizations across different domains are random, resulting in a zero magnetization for the material [93]. However, upon the application of an external magnetizing field, domain walls within the sample shift to enlarge the favorable domains, leading to the generation of magnetization aligned with the field direction. The susceptibility of ferromagnetic materials is positive and large, decreasing with temperature, as shown in Figure 2-15 (page 31). Above the T_C, ferromagnetic materials behave similarly to paramagnetic materials.

In antiferromagnetic and ferrimagnetic materials, neighboring atoms or ions exhibit spin alignments in opposite directions, as illustrated in Figure 2-14 (d) and (e). The distinction between the two types of magnetism arises from differences in the relative magnitudes of the magnetic moments of neighboring atoms or ions. In antiferromagnetic materials, the magnetic moments of adjacent atoms are nearly equal, resulting in zero magnetization in the absence of an external magnetizing field and below the Néel temperature (T_N) [93]. Yet, when exposed to a magnetizing field below T_N, domain walls move to enlarge

the favored domain, generating a magnetization along the field direction, although smaller than that of ferromagnetic materials. The susceptibility of antiferromagnetic materials is positive but small and varies with temperature (see Figure 2-15 in page 31). Above the T_N, antiferromagnetic materials exhibit paramagnetic behavior. Many antiferromagnetic materials are transition metal oxides, such as oxides of elements like Cr, Mn, Fe, Co, Ni, and others.

In addition to the magnetic phases previously discussed, superparamagnetism represents a distinct magnetic state observed in ferromagnetic or ferrimagnetic nanoparticles of sufficiently small size. In such nanoparticles, thermal energy overcomes the anisotropy energy barrier, enabling spontaneous reversals of the magnetization direction. As a result, the material exhibits a high magnetic susceptibility similar to ferromagnets but without hysteresis, effectively combining characteristics of both ferromagnetism and paramagnetism [94].

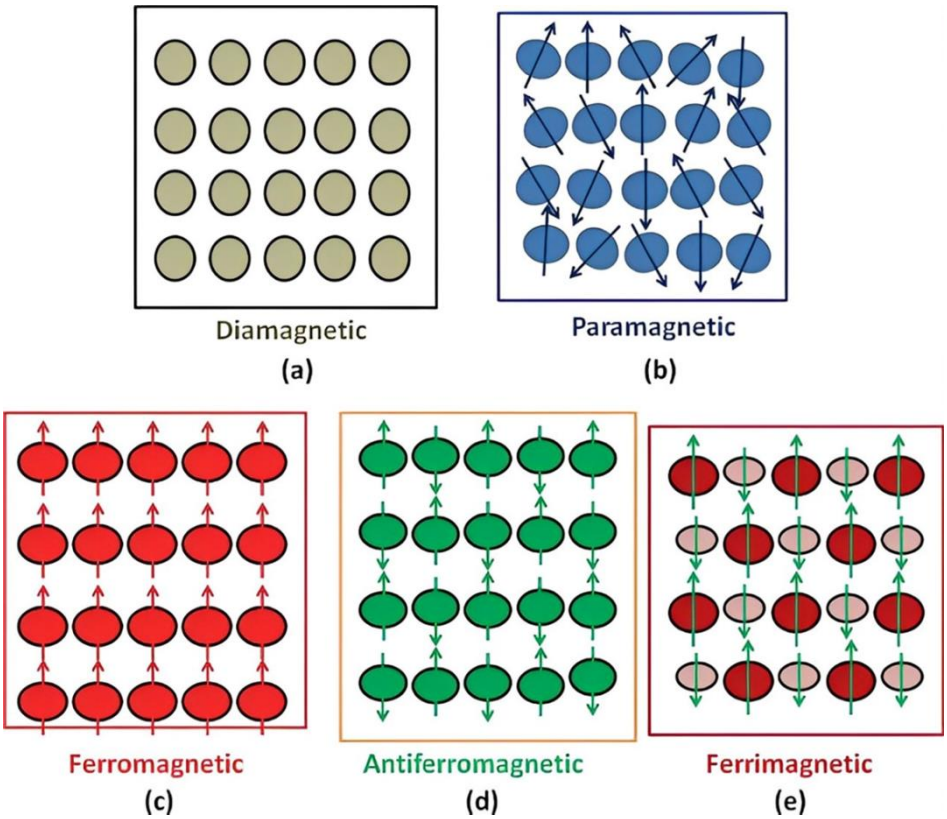


Figure 2-14: Alignment of spin/magnetic moments in different types of magnetic materials: (a) diamagnetic, (b) paramagnetic, (c) ferromagnetic, (d) antiferromagnetic and (e) ferrimagnetic. Taken from reference [93].

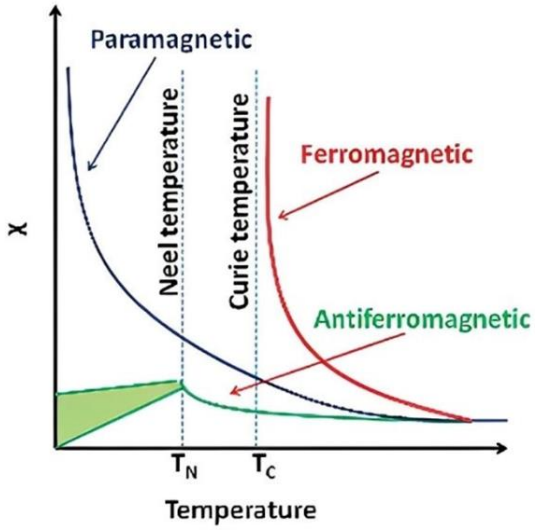


Figure 2-15: Variation of magnetic susceptibility with temperature. Taken from reference [93].

Figure 2-16 (a) illustrates the magnetic unit cell structure of MnO, a typical antiferromagnetic material. When the magnetizing field H aligns parallel to the spins S_1 and S_2 of neighboring atoms, the susceptibility is represented by χ_P. Conversely, when H is perpendicular to S_1 and S_2, the susceptibility is denoted by χ_T. The temperature dependence of χ_P and χ_T is illustrated in Figure 2-16 (c).

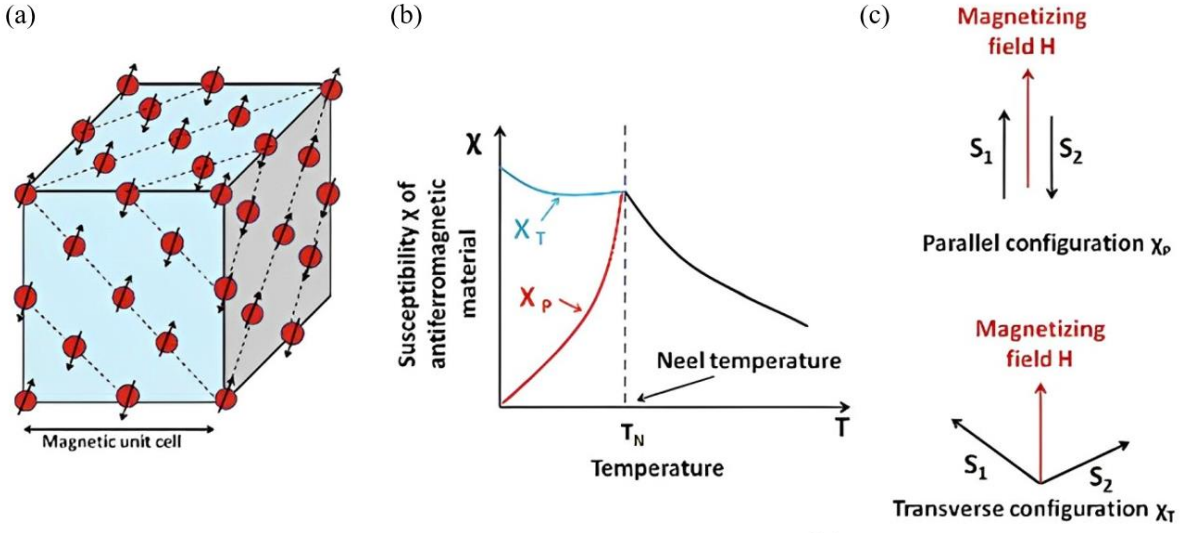


Figure 2-16: (a) Unit magnetic cell of antiferromagnetic MnO compound, (b) dependence of antiferromagnetic material susceptibility with temperature (material below Neel temperature) and (c) the correspondent configurations (parallel and transverse). Taken from reference [93].

The Curie–Weiss law describes the magnetic susceptibility of a ferromagnetic material above its Curie temperature when subjected to low external magnetic fields. This law provides insights into the variation of magnetic susceptibility at temperatures higher than the Curie temperature, where a ferromagnetic material exhibits paramagnetic behavior. The Curie–Weiss law is expressed as [44]:

$$\chi = \frac{C}{T - T_C} \tag{2-51}$$

where χ is the magnetic susceptibility, C is the Curie constant (with units emu K mol^{-1} in cgs or m^3 K mol^{-1} in SI), and T_C (in K units) is the Curie temperature, often referred to as the Curie–Weiss temperature. At this temperature (and below) exists a spontaneous magnetization. This expression captures the trend for the magnetic moments within a paramagnetic material to align with an external magnetic field. Consequently, the susceptibility increases with decreasing temperature, as thermal fluctuations weaken. The Curie constant is directly proportional to the number of unpaired electrons and, once determined, enables the calculation of the effective magnetic moment(μ_{eff}) per ion in terms of Bohr magnetons (μ_β) [92]:

$$\mu_{eff} = \sqrt{8C}\mu_\beta\ [CGS] \cong 800\sqrt{C}\mu_\beta[SI] \tag{2-52}$$

This effective moment can be compared to the calculated value for the specific ion, determined by [92]:

$$\mu_{cal} = g_j\sqrt{J(J+1)}\mu_\beta \tag{2-53}$$

that depends on its total angular momentum, J and its Landé g-factor, g_j. It's important to note that the derivation of the Curie–Weiss law assumes the presence of a clearly defined angular momentum ground state. The constant g_j can be written as [44]:

$$g_j = \frac{3}{2} + \frac{S(S+1) - L(L+1)}{2J(J+1)} \tag{2-54}$$

The Curie–Weiss law holds for low magnetic fields and can be rewritten as [44]:

$$\chi_m \cong \frac{\mu_0 M}{B} \tag{2-55}$$

where μ_0 is the effective paramagnetic moment.

2.5. Multiferroicity

A single-phase multiferroic is a material that concurrently exhibits two or more ferroic order parameters [35]:

- Ferromagnetism: magnetization that can be altered by applying a magnetic field;
- Ferroelectricity: electric polarization that can be switched by applying an electric field;
- Ferroelasticity: deformation that can be changed by applying stress.

Magnetoelectric coupling, often denoting the linear magnetoelectric effect, involves the induction of magnetization by an electric field or polarization by a magnetic field [36]. As a result, their magnetization can be altered by an applied electric field, opening avenues for manipulating magnetic and electronic order parameters through each other. Researchers worldwide are captivated by the potential applications in microelectronics (e.g., multiple-stage memories) or sensors (where, for instance, a magnetic field can be directly detected electrically) arising from this [95]. The strength of the magneto-electric coupling, denoted by α, is quantified as [96]:

$$\alpha = \frac{\partial E}{\partial H} \tag{2-56}$$

Where E is the electric field and H is the applied magnetic field.

Magnetoelectric coupling can be classified into two main types: direct and indirect. Direct magnetoelectric coupling occurs in single-phase multiferroics, where the application of an electric field directly modifies the magnetization, or a magnetic field directly alters the polarization [97]. In some cases, this coupling can include biquadratic interactions, where quadratic terms in the free energy link the electric and magnetic orders, allowing for more complex interactions between the two [98]. Additionally, in some materials, the coupling is mediated by a secondary order parameter, such as strain or lattice distortion, which indirectly influences the electric and magnetic properties [99].

In contrast, indirect magnetoelectric coupling is observed in composite multiferroics, often referred to as elasto-magnetoelectric multiferroics, where the interaction between electric and magnetic fields occurs via mechanical strain. In this case, the application of an electric or magnetic field induces strain in the material, which then affects either the magnetization or polarization, resulting in a strain-mediated magnetoelectric effect [100].

Figure 2-17 (a) demonstrates the required overlap for materials to be classified as multiferroic. While only a subset of materials with magnetic and electric polarizability are ferromagnetic or ferroelectric, even fewer simultaneously exhibit both order parameters. In these specific materials, the unique capability arises for electric fields to not only reorient polarization but also control magnetization, and vice versa — a phenomenon designated magnetoelectricity - Figure 2-17 (b).

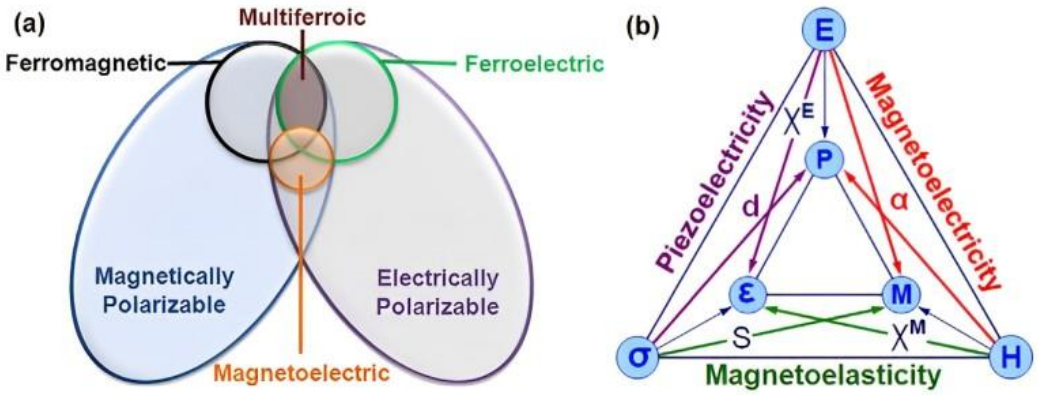


Figure 2-17: (a) Correlation between multiferroic and magnetoelectric materials, outlining the necessary conditions for their coexistence in a material. (b) Diagram illustrating different coupling types found in materials, with a specific focus on those exhibiting coupling between electric and magnetic orders, referred to as magnetoelectric materials. Taken from reference [95].

Considering the properties present above, multiferroic materials are of great interest for two reasons. Firstly, they enable the utilization of both magnetic and electric functionalities, allowing, for instance, the creation of innovative memory elements by combining a magnetic bit with an electric bit [101]. Secondly, the coupling between ferromagnetic and ferroelectric states can introduce novel functionalities that are not present in either state individually. These materials are valuable for technological applications [1, 77, 99, 102, 103] due to their simultaneous tunable mechanical, magnetic, electric/dielectric, thermal, and optical properties. In random-access multi-state memories, the coupling allows for electrically writing and magnetically reading data [99], demonstrating the control of electric properties by magnetic fields and vice versa. One notable advantage of multiferroic materials is the potential to control magnetic properties using electric fields, eliminating the need for magnetic fields. This is exemplified by the ability to use a voltage pulse instead of an electric current to read and write a magnetic bit, avoiding the drawbacks associated with electric currents.

The coexistence of magnetic and electric order in multiferroics is particularly attractive due to its potential applications in information storage, processing, and transmission. However, the simultaneous occurrence of magnetic and electric order is a rarity. This rarity arises from the challenging conditions required for such coexistence. Specifically, the presence of partially filled atomic orbitals, a prerequisite for magnetic dipoles or moments, typically conflicts with the conditions necessary for the existence of local electric dipoles [104]. The interplay of these factors shapes the distinctive behavior of multiferroic materials.

3. Thin film production and characterization techniques

Chapter 3 outlines the methods used for the production and characterization of thin films in this study. The chapter is divided into two main sections: techniques for thin film production and techniques for their characterization.

The production techniques include Pulsed Laser Deposition (PLD), a widely used method for depositing complex oxides, followed by post-deposition processes like thermal annealing, which are critical for tuning the structural properties of the films.

The characterization techniques provide insights into the structural, compositional, and functional properties of thin films. These include X-ray diffraction (XRD) for structural analysis, scanning electron microscopy (SEM) and energy-dispersive X-ray spectroscopy (EDS) for morphological and compositional examination, and Raman spectroscopy for vibrational analysis. Additionally, the films' magnetic properties are studied using a Superconducting Quantum Interference Device (SQUID) magnetometer, while dielectric properties are evaluated through impedance spectroscopy. The optic properties are assessed using second harmonic generation (SHG), and finally, density functional theory (DFT) provides theoretical support for the experimental findings.

3.1. Pulsed laser deposition

Pulsed Laser Deposition (PLD) is a Physical Vapor Deposition (PVD) technique developed to produce thin films. It distinguishes itself from other PVD methods by operating a high-powered pulsed laser to vaporize the target material. Within an ultra-high vacuum chamber, the substrate is positioned on a holder that can potentially be heated, for instance, by electrical resistance, with the temperature measured as closely as possible to the substrate. Through a window in the vacuum chamber, a laser beam strikes the target, removing and transferring material from the target to the substrate. This process enables precise control over the deposition, facilitating the production of thin films with tailored properties. Moreover, the PLD system allows for the inclusion of working gases, further enhancing the versatility and customization of the deposition process to meet specific application requirements. This capability expands the range of materials and structures that can be synthesized using PLD, making it a valuable tool in various fields such as electronics, optics, and materials science. A simplified scheme of a typical PLD equipment is presented in Figure 3-1.

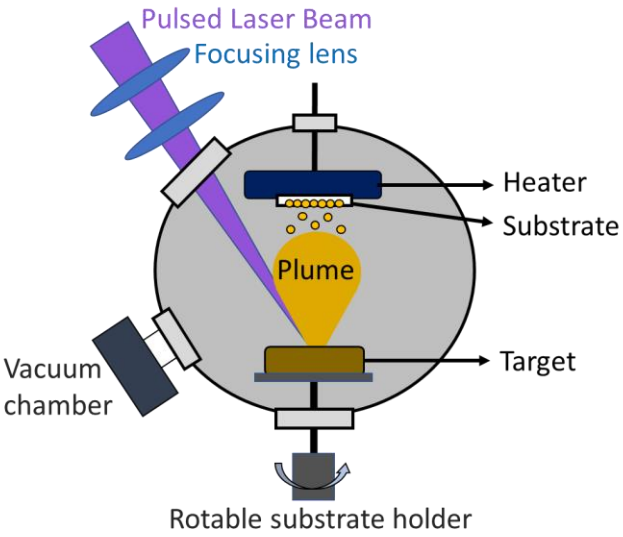


Figure 3-1: Schematic of a PLD system. A pulsed laser impinges on a target, removing material that deposits on a substrate, forming a thin film.

3.1.1. Procedure

The PLD process consists of three distinct stages, which are iterated multiple times throughout the deposition procedure. These stages include the vaporization of the target material, the transport of the resulting vapor plume, and the formation of a thin film on the surface of the substrate. These three processes will be detailed next.

3.1.1.1. Vaporization of the Target Material

The initial step in the deposition process involves extracting material from a target. Various physical vapor deposition techniques employ different methods for this task. In pulsed laser deposition, a high-powered pulsed laser irradiates the target, inducing its melting and vaporization [105].

Throughout the process, a pulsed laser beam irradiates a target composed of the intended deposition material or a material that will subsequently interact with a background gas to form the desired film. This heating process occurs rapidly, resulting in the ejection of material from the target through vaporization, boiling, and explosive boiling, leading to the generation of nano to microparticles [106].

Ablation is initiated by subsurface heating induced by either the pulse itself or the recoil pressure exerted by the material ablated at the pulse's onset [107]. As vaporization progresses, latent heat serves as a cooling mechanism, causing the subsurface of the target to attain a higher temperature than its surface. Ultimately, continuous subsurface heating triggers an explosion of solid material on the surface,

forming a highly forward-directed plasma plume [108]. Upon the pulse's cessation, and thus the end of target heating, the material solidifies, and the melt front recedes. Figure 3-2 provides an overview of the process.

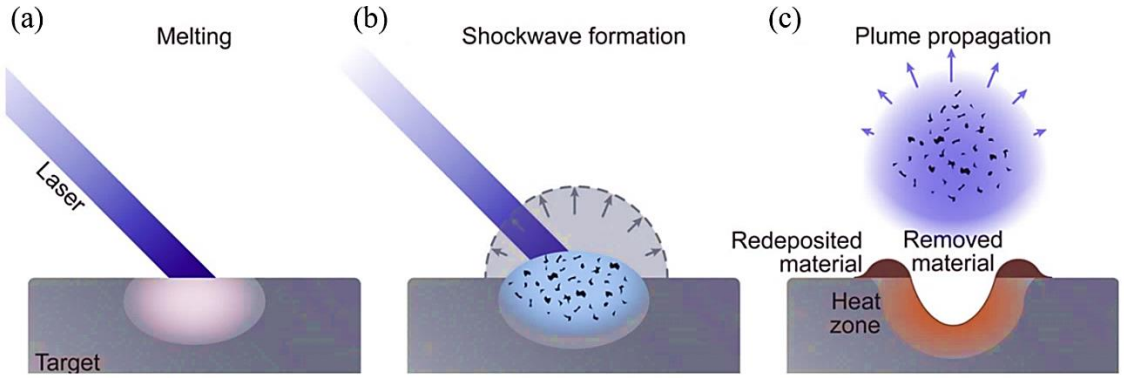


Figure 3-2: Diagram illustrating the sequential processes involved in laser ablation leading to material expulsion from the target: (a) melting and instantaneous vaporization, (b) shockwave formation, and (c) plume expansion following the cessation of the laser pulse. Taken from reference [109].

3.1.1.2. Transport of the Vapor Plume

Heating the target initiates the formation of a plume composed of ejected ions from all target elements, which generally maintains its stoichiometry [110]. The plume is irradiated by the pulsed laser, absorbing energy in regions of higher particle density, particularly within a short distance from the target [111]. This absorption process excites and ionizes species within the plume, leading to the attenuation of laser radiation transmitted through the plume to the target [1, 112].

Initially, the plume propagates in a one-dimensional form [112], then beyond a distance comparable to the dimensions of the laser spot, it transitions to a three-dimensional expansion resulting from ejecta collisions with both the background gas and within the plume itself [1, 108]. The presence of a background gas gradually slows and eventually stops plume propagation after a few microseconds [113, 114], as shown in Figure 3-3 for $LaMnO_3$ laser ablation example [115].

In vacuum conditions, the shape and velocity distribution within the plume asymptotically reaches constant values. However, when ablation occurs in the presence of a background gas, the high pressure within the plume initially drives expansion as if it were in a vacuum [114], as shown in Figure 3-3. After several microseconds, plume expansion dynamics are entirely determined by interactions between plume atoms and background gas atoms [114].

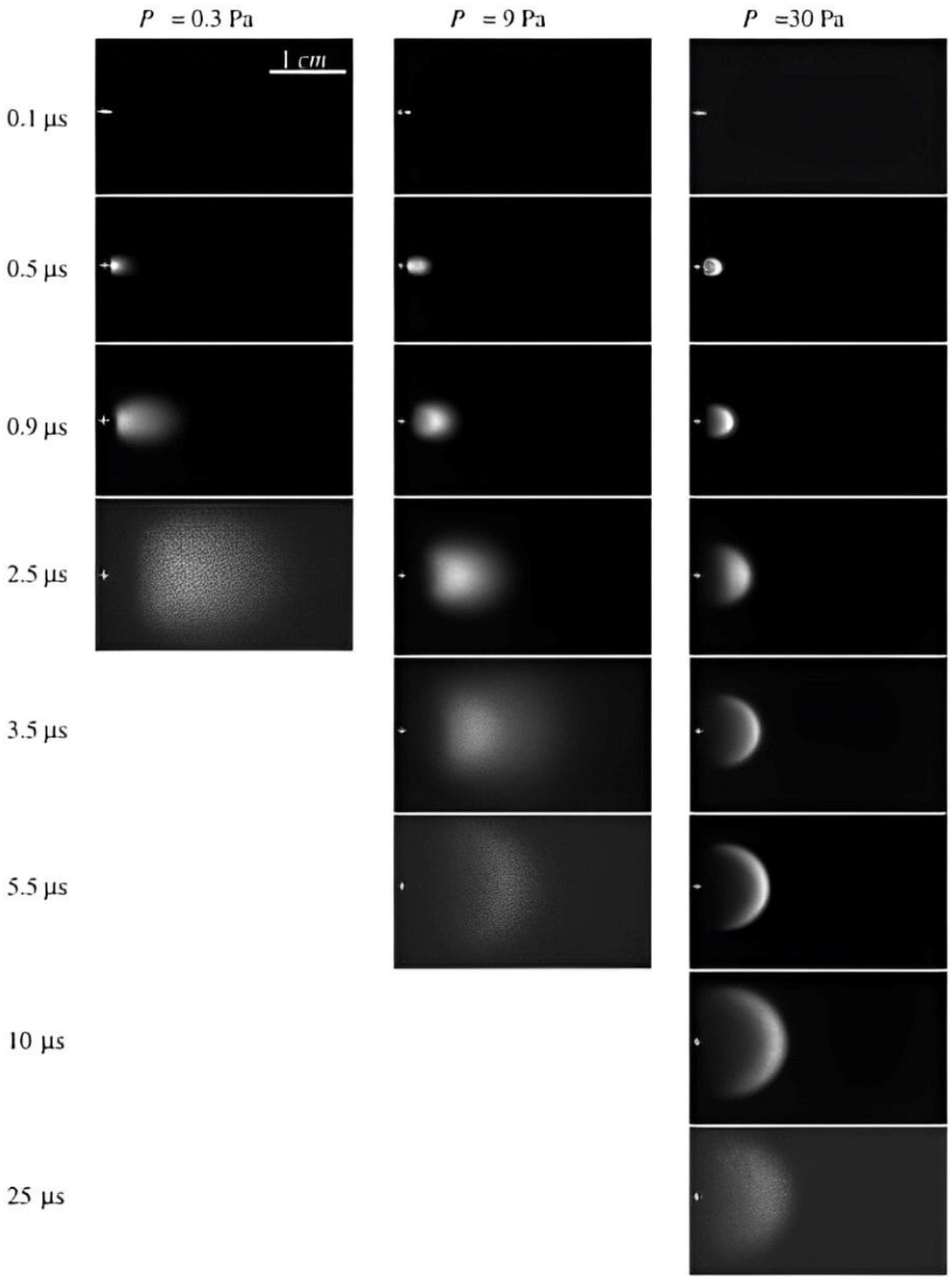


Figure 3-3: Temporal evolution of visible plasma emission from the $LaMnO_3$ laser ablation plume under varying oxygen background pressures. All images are normalized to their maximum intensity. The cross in each image indicates the point of impact of the laser beam on the target surface. Taken from reference [115].

3.1.1.3. Growth of the Thin Film

In the final stage of the process, particles from the plume reach the substrate and diffuse along its surface, leading to the formation of chemical bonds and the growth of a thin film [116]. The resulting

film's morphology is influenced by various factors, including the kinetic energy of the arriving particles, substrate temperature, sticking probability, and deposition rate [117].

Typically, films deposited on room-temperature substrates tend to be amorphous, but their crystallinity can be enhanced by elevating the substrate temperature [114]. Epitaxial growth is facilitated by high substrate temperatures and low deposition rates, allowing adatoms to diffuse on the substrate until they reach equilibrium lattice sites [101]. Conversely, thin films deposited at low temperatures or high deposition rates tend to remain amorphous.

The lattice mismatch between the substrate and thin film also plays a crucial role in determining the quality of the resulting film. Various deposition parameters, such as substrate choice and temperature, laser wavelength, pulse duration and intensity, as well as the presence of a background gas, collectively influence the properties and quality of the thin film produced [114].

3.1.2. Factors that influence deposition

Despite its simple design, the PLD process is extremely complex. The preceding steps often overlap and are interconnected, involving numerous deposition parameters that can be adjusted to directly influence the characteristics of the resulting thin films. These variables encompass the target's composition, laser wavelength, pulse width, spot size, fluence, background gas design, pressure, target-substrate distance, and substrate temperature [118]. The complex interplay among these interdependent deposition parameters empowers the PLD user to achieve the desired structure, thickness and composition of the film [119]. The discussion that follows explores how the main parameters affect thin film deposition and growth in the PLD process.

3.1.2.1. Laser parameters

The wavelength of the laser pulse plays a pivotal role in determining its penetration depth into the target material [109]. Longer wavelengths facilitate deeper penetration, while shorter wavelengths result in shallower penetrating beams, yielding films with more uniform properties and fewer surface particles.

The common laser wavelengths used in PLD include ArF (193 nm, or 6.42 eV), KrF (248 nm, or 4.99 eV), XeCl (308 nm, or 4.03 eV), and Nd:YAG (1064 nm, or 1.16 eV). Ablating metals with ultraviolet (UV) lasers is challenging due to electron shielding and reflection of UV radiation [120]. UV ablation of metals gives lower ablation rates and is primarily a photothermal process, inefficient for most metals [121]. Oxides, however, efficiently absorb UV energy, particularly at 248 nm (KrF excimer). Generally, this

wavelength offers advantages such as a long gas mixture lifetime and little air absorption. For non-metals, laser wavelength selection (photon energy) determines which bonds are preferentially cleaved, affecting the species composition of the ablation plume. Nanosecond ablation at 248 nm and 193 nm primarily yields single atomic plasma species with few binaries, while 308 nm ablation favors binary metal-oxygen species [109, 122]. Consequently, film formation on the substrate depends on the laser wavelength, influencing species diffusion, initial cluster formation, and subsequent film quality.

Pulse frequency also plays a significant role in the deposition process [109]. Lower pulse frequencies allow the laser energy to be thermally dissipated within the target. Otherwise, increasing the rate of emitted laser pulses enhances ablation efficiency and deposition rate. However, higher deposition rates tend to yield films with more amorphous characteristics and smaller grain sizes, whereas lower deposition rates foster epitaxial growth.

Likewise, laser fluence is a critical parameter in the deposition process [123] and fluence is commonly defined as the radiant energy or particle flux. The fluence (F) represents the optical energy delivered per unit area and it can be calculated by [124]:

$$F\ (J/(cm^2\ )) = \frac{Laser\ energy\ (J)}{Beam\ area\ (cm^2)} \tag{3-1}$$

Higher fluence corresponds to increased energy per unit area focused on the target, leading to the generation of a plume containing more energetic particles. This phenomenon influences the growth behavior of the film: energetic particles promote epitaxial growth, whereas less energetic particles favor amorphous films, analogous to the effect of temperature [125]. Moreover, an increase in laser fluence escalates the ablation rate, creating a shielding effect on the target material. Excessive focusing of the laser beam intensifies this effect, further reducing the ablation rate due to the high plasma density near the substrate.

In the context of optimizing laser parameters in PLD, it is crucial to address the influence of laser fluence on droplet formation on the surface, as droplets pose a significant challenge that can potentially impact the final properties of the films [126]. To mitigate droplet formation, one approach involves reducing the laser fluence below the threshold for explosive boiling, reducing the laser energy, or increasing the area of the laser spot [127]. The last option is better since it does not lower the ablation rate.

3.1.2.2. Target

PLD offers a significant advantage in transferring complex stoichiometries from the target to the substrate, forming the basis for thin film stoichiometry. The transfer of material and composition from the

target to the substrate is crucial in deposition processes [128]. However, achieving the desired film composition faces challenges due to factors like mass differentials among target atoms, resulting in compositional deviation [129, 130]. Light elements scatter further and arrive at the substrate surface first, affecting film composition. Volatility differences among target species also influence film stoichiometry, often resulting in deficiencies in light or volatile elements. Modifying deposition parameters can mitigate these effects [129]. Additionally, the absorption properties of the target material, guided by its band gap, impact ablation rates. Furthermore, thermal properties and multi-element deposition further complicate composition control, as target composition can change during ablation and species rebounding from the substrate can alter surface composition [126, 129].

Surface quality in PLD is influenced by various factors, including target density, mechanical stability, and surface degradation during ablation. Maintaining a target density above 90% is crucial to prevent issues with deposition rate and reduce the ejection of macroparticles onto the substrate [109]. Moreover, the degradation of the target surface during ablation can significantly impact the quality and composition of the deposited thin film. Consequently, ensuring a clean target surface through mechanical polishing and in situ pre-ablation is critical. Additionally, directional particulate formation, caused by the angle of laser incidence, can be mitigated through bidirectional ablation to distribute particulates more evenly and reduce surface defects [131]. Proper storage of targets is also essential to prevent reactions that could alter the target's composition and optical properties. Also, pre-ablation of the target surface before deposition further minimizes undesirable effects, ensuring the desired film quality and composition [109].

The distance between the target and substrate plays a crucial role in PLD process [132]. Most ablated material is contained within a narrow angular range of the plume, making the target-to-substrate distance pivotal in determining the plume's expansion angle and consequently affecting film thickness and composition. A greater target-to-substrate distance leads to thinner films, while a shorter distance can cause species rebound due to higher kinetic energies. Additionally, for the elemental composition of thin films, maintaining a distance below the mean free path is essential for proper element distribution [133]. This is particularly significant in reactive gas environments like O_2, O_3, N_2O, N_2, or NH_3, where interactions between plume species and background gas are crucial for deposition success [109].

Regarding the characteristics of the target and potential enhancements in the PLD process, it is necessary to revisit the formation of droplets. Droplets are also formed due to surface roughening and the development of structural features on the target surface. As surface structures, such as columnar features, form and align with the laser beam, the ablation rate decreases while the number of particulates increases with successive laser pulses [134]. Moreover, an uneven surface leads to continuous changes

in the direction of plume expansion, resulting in non-uniform material deposition. Experimental studies have shown that these issues can be mitigated or even avoided by simultaneously rotating and translating the target during ablation [134, 135], as depicted in Figure 3-4. Furthermore, implementing procedural modifications such as rotation and translation of the target and scanning the laser across the target surface are commonly employed techniques [136]. These methods facilitate the solidification of the target material between consecutive laser pulses, thereby minimizing the occurrence of droplets on the substrate.

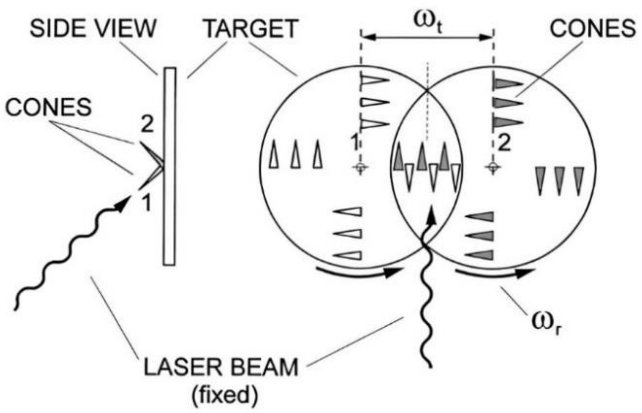


Figure 3-4: Description of simultaneous rotation and translation of the target with frequencies ω_r and ω_t, respectively [136].

3.1.2.3. Laser spot size

The spot size of the laser beam, typically a few square millimeters in area, is crucial for achieving the necessary energy density at the target surface to induce plasma formation [118]. The focusing of the beam allows energy density values exceeding a few Joules per square centimeter, significantly above the ablation threshold for many materials. The spot size correlates with the number of species removed per pulse and is influenced by target properties such as density and laser wavelength absorption [109]. Two approaches for projecting the laser beam onto the target are commonly used: direct focusing and defining the beam profile with an aperture before focusing. While the latter approach offers better control over energy distribution and fluence homogeneity, it requires a longer imaging beam path. A smaller spot results in a larger opening angle for ejected species, leading to a visually larger plasma plume, while a larger spot produces a tighter plume due to the emission of more species and intra-plume collisions [130].

When examining the impact of beam size on the ablation plume (Figure 3-5), it's observed that a rectangular-shaped spot will result in a broader plume profile along its shorter dimension (Figure 3-5 (a)), and conversely along its longer dimension (Figure 3-5 (b)) [109]. This phenomenon is known as the flip-

over effect [130]. This effect can even occur with a square-shaped spot, where the plume preferentially expands perpendicular to the edges. The size and aspect ratio of the laser beam profile significantly influence the composition and propagation of species in the plume, with increasing fluence leading to more scattering events and a deficiency of certain species in the plume [137].

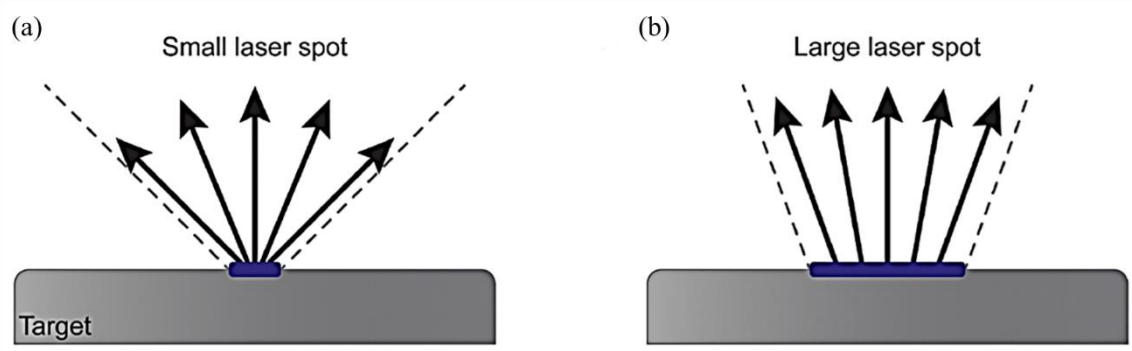


Figure 3-5: Diagram depicting variations in the opening angle of the plasma plume concerning the dimensions of the spot size for (a) a small laser spot and (b) a large laser spot. Taken from reference [109].

3.1.2.4. Atmosphere

The vacuum within the chamber is established through a combination of turbo-molecular and rough pumps. Typically, the base pressure in vacuum chambers employed for PLD ranges between 10^{-6} mbar and 10^{-9} mbar. This vacuum level directly influences the rate at which a monolayer of contaminants and impurities can accumulate on the substrate surface, disregarding other potential sources of contamination within the chamber.

The mean free path, which defines how far a molecule travels before colliding with another, is influenced by the level of vacuum in the chamber [138]. This vacuum level significantly impacts the mean free path of species within the chamber and consequently affects the entire plasma dynamics [139]. Environmental pressure notably alters the mean free path, spanning from micrometers to kilometers as the pressure decreases from atmospheric values to 10^{-6} mbar.

The addition of background gas during deposition has several effects. It slows down the ablated species, reducing the number of ions ejected from the target. Moreover, the background gas alters the kinetic energies of the species arriving at the substrate, enabling the incorporation of elements such as O, C, or N to form oxide, carbide, or nitride thin films, respectively [109]. Thus, the type and pressure of the background gas influence the crystallinity, thickness and composition of the thin film, with the gas composition often tailored to the specific application [109]. In fundamental studies, inert gases like Ar are commonly used to examine the kinetic interaction between the plasma plume and the background gas, affecting material transport, laser light attenuation, and surface instability development [134].

Reactive background gases, such as O_2 or N_2O, facilitate the incorporation of deficient elements into the composition of the film [140]. When selecting a background gas, factors such as gas type, mass, constituent element size, reactivity, and chosen pressure must be carefully considered [109].

3.1.2.5. Pressure

The pressure within the chamber is a critical parameter that significantly influences the quality of the films deposited. Firstly, the base pressure is indicative of the number of impurities present in the deposition atmosphere. Maintaining a low base pressure is essential for ensuring high-quality film production, as the presence of impurities can adversely affect film properties [59]. When using an inert gas like Ar, these collisions regulate the kinetic energy of the species, thereby modulating the growth process. Instead, in the presence of a reactive gas, the partial pressure affects both the chemical composition and the kinetic energy of the plasma, owing to interactions with the substrate, as explained in section 3.1.2.4.

3.1.2.6. Substrate

The substrate's role is pivotal as it must exhibit compatibility with the chemical species and lattice parameters since upon reaching the substrate, the species undergo diffusion and reactions, both amongst themselves and with the substrate [140]. The formation of ordered monolayers hinges on high surface diffusion, dictating the structure and morphology of the resulting thin film based on particle nucleation [141]. The substrate's role is crucial, determined by the compatibility of chemical species and lattice parameters [142]. Typically, crystalline thin films are grown at high temperatures, facilitating epitaxial growth by aiding impurity removal, enhancing adatom surface diffusion, and promoting island coalescence [109]. Maintaining the correct substrate temperature is vital and is achieved through thermal contact between the substrate and the holder, typically using clamps or metallic adhesive pastes like Pt or Ag. This contact may change during heating, emphasizing the importance of finding suitable methods for maintaining proper thermal contact [143]. Substrate selection depends on the film to be deposited, considering the material, crystallographic orientation, and resulting lattice parameters that induce strain or enable film relaxation through defects. Surface stability and chemical compatibility with film material are also vital considerations in substrate choice.

The possibility of epitaxial growth is determined by the lattice mismatch (ε_m), which can be calculated using the lattice parameters of the substrate surface and the film [143]:

$$\varepsilon_m(\%) = \left(1 - \frac{a_s}{a_f}\right) \times 100 \quad (3\text{-}2)$$

where a_f and a_s are the lattice plane spacing in the in-plane direction for the film and substrate, respectively.

For small mismatches, coherent epitaxy can occur, where the film growth proceeds with a one-to-one match of lattice planes until it becomes energetically favorable for the film to accommodate dislocations (Figure 3-6 (a)) [109]. The film can grow with a direct alignment of lattice planes until it reaches a critical thickness, at which point it becomes energetically favorable for the film to accommodate dislocations [144]. These dislocations originate at the film surface and migrate towards the interface.

In cases of relatively large lattice mismatch between the film and substrate, epitaxial growth typically does not occur, and the film commonly grows relaxed. This relaxed state can manifest as a textured structure or a largely polycrystalline morphology, where the crystalline grains are not aligned with each other or with the substrate lattice (Figure 3-6 (b)) [109, 145]. However, even in systems with a large lattice mismatch, there is still a possibility for epitaxial growth through a phenomenon known as domain-matching epitaxy [146]. This occurs when the film and substrate have similar crystal structures, despite their mismatched lattice parameters. In such cases, certain domains or regions of the film may align with corresponding regions of the substrate, allowing for partial epitaxial growth within these matched domains [146]. This phenomenon enables some degree of structural alignment between the film and substrate, even in systems with significant lattice mismatch, although the overall film may still exhibit a relaxed or polycrystalline structure.

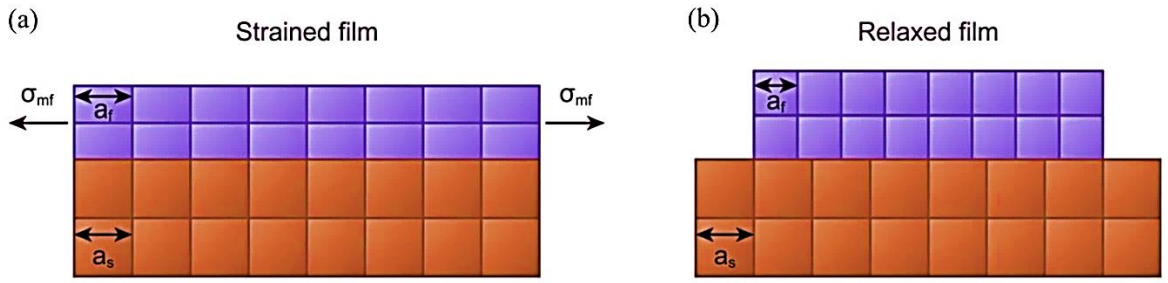


Figure 3-6: Schematic illustrating two potential growth scenarios for films with lattice parameters distinct from the substrate. (a) Coherent growth under strain, where the in-plane lattice parameter aligns with the substrate, and (b) incoherent growth in a relaxed state, maintaining the film's original lattice parameter. Taken from reference [109].

The film's unit cell structure tends to adopt the intrinsic lattice parameter of its relaxed form, which is energetically favorable in bulk [147]. During the initial monolayer formation, the film attempts to match the lattice parameter of the substrate. If the incoming species have sufficient energy, suitable substrate temperature, minimal lattice mismatch, and compatible chemical species, the film will conform to the

substrate's lattice parameter [109, 147]. This results in significant misfit stress on both the film and substrate, causing the film's lattice parameter to adjust in all crystallographic directions to maintain unit cell volume. When the film experiences tensile in-plane strain, the in-plane lattice parameter increases while the out-of-plane lattice parameter decreases, and vice versa [147].

Strain engineering enables precise control over material properties by utilizing various single crystalline substrates (Figure 3-7). By selecting a substrate with a specific lattice parameter and applying a predetermined strain to the film, new functionalities can be unlocked. For example, strain-induced tuning of the metal-insulator transition in $NdNiO_3$ can be achieved by using a lattice-mismatch epitaxial strain with a (100) Si substrate [148]. This method allows for precise control of the metal-insulator transition temperature of $NdNiO_3$ films, thereby enhancing the potential of these films for applications.

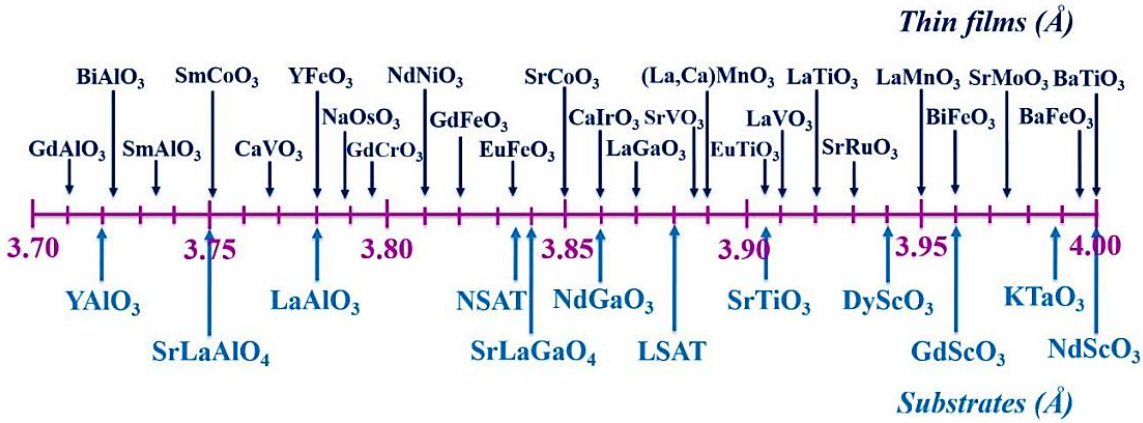


Figure 3-7: List of cubic (pseudo-cubic) substrates and thin films within the lattice constant range from 3.70 to 4.00 Å. Taken from reference [149].

A formation of interfaces occurs between the film and substrate, as well as with other films and the surrounding environment, ultimately influencing the properties of the film. Coherent interfaces occur when interfaced crystals have matching atomic configurations and continuous lattices across the interface [150]. It can be achieved in material pairs with mismatched lattice spacing by applying in-plane strain to one or both lattices. Moderate strain favors semi-coherent interfaces, with periodic misfit dislocations reducing the mismatch [151]. With increasing strain, dislocations become more closely spaced until they merge, leading to incoherent interfaces. These incoherent interfaces act as the boundaries between misaligned grains, independent of their orientation [151].

3.1.2.7. Substrate temperature

The substrate temperature plays a crucial role in the deposition and growth of the film. Elevated substrate temperatures combined with lower deposition rates provide particles with ample time and energy to diffuse across the substrate surface, favoring epitaxial growth and larger grain sizes [117].

Conversely, lower temperatures and higher deposition rates tend to promote amorphous film growth. Increased substrate temperature enhances particle creep, leading to greater particle ejection and higher kinetic energies conducive to epitaxial growth. However, excessively high fluences can result in nearly complete radiation absorption by the plume, shielding the target material and reducing ablation. The resulting film structure is heavily influenced by the substrate temperature T_S relative to the target melting temperature T_M, see [152]. When $T_S < 0.3T_M$, the films exhibit granular structures. Between $0.3 < T_S/T_M < 0.5$, the film has a columnar structure and an epitaxial growth. For $T_S > 0.5T_M$, the film may develop grains larger than its thickness [152]. However, the presence of large grains with few boundaries can induce tensile stress, leading to cracks in the films.

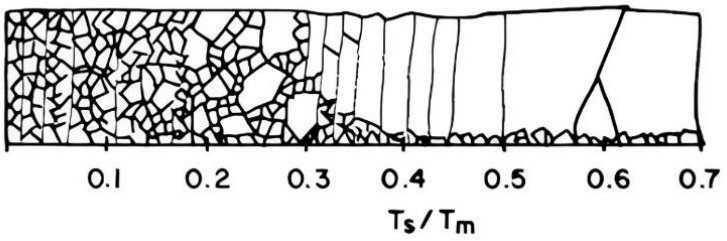


Figure 3-8: Model with the different types of grain structure that occur on vapor-deposited metal films [153].

3.1.3. Advantages and disadvantages

Laser ablation, like other deposition techniques, offers both advantages and disadvantages. Some of its main advantages include:

It is effective for developing epitaxial films and fabricating multilayers, heterostructures, and superlattices on lattice-matched substrates.

- Flexibility in wavelength and fluency: allows for the adjustment of deposition parameters based on the material to be deposited. This flexibility enables precise control over the process.
- Precise control of film growth rate: enables accurate control over the rate at which thin films grow, offering reproducibility and uniformity in the deposition process.
- Effective transfer of material: ensures the transfer of material from the target to the film while preserving its stoichiometry. This is particularly beneficial for materials with complex stoichiometry, as it maintains the desired composition in the deposited thin films.
- Adjustment of kinetic energy: allows for the adjustment of the kinetic energy of ejected particles, providing control over the growth of the thin film.

- Enables rapid deposition of complex oxide compositions with high melting points, provided that target materials absorb laser energy.
- Facilitates quick optimization of growth conditions, which is advantageous when experimenting with different target compositions.

However, laser ablation deposition also presents some disadvantages:

- Excessive kinetic energy: High kinetic energy can lead to re-pulverization of the material, resulting in flaws in film growth and reduced quality of the deposited thin films.
- Heterogeneous energy distribution: The uneven distribution of laser pulse energy can cause angular energy distribution within the plume, leading to variations in film thickness along the substrate. Typically, films deposited using laser ablation have sizes around 1×1 cm^2.
- Angular distribution of chemical composition: Lighter elements may exhibit different expansion speeds during the deposition process, resulting in angular distributions of the chemical composition within the plume. However, this issue can be mitigated by adjusting the pressure and composition of the background gas during deposition.

3.1.4. Setup used in this work

The equipment used for the measurements is in a laboratory at Centro de Física of Universidade do Minho - Campus de Gualtar. The setup includes a substrate holder furnace capable of reaching temperatures up to 730°C, heated by a resistance connected to a temperature controller (Eurotherm 2116). Temperature measurement is facilitated by a thermocouple inserted into the furnace, positioned near the substrate. The substrate is attached to the holder using silver paint near the tip of the thermocouple. The furnace is movable, allowing for up to 14 cm from the target. Additionally, the system features a KrF excimer laser (Lambda Physik LPXpro 210) with a wavelength of 248 nm, pulse duration of 25 ns, energies up to 800 mJ, and a repetition rate of up to 100 Hz. The laser beam is directed and focused onto the target using a set of mirrors and a lens with a focal length of 50 cm, as shown in Figure 3-9. It enters the chamber through a silica window at a 45-degree angle concerning the target's normal. Then, the laser beam reaches the target, removing its material and forming the plume, as shown in Figure 3-10 and Figure 3-11.

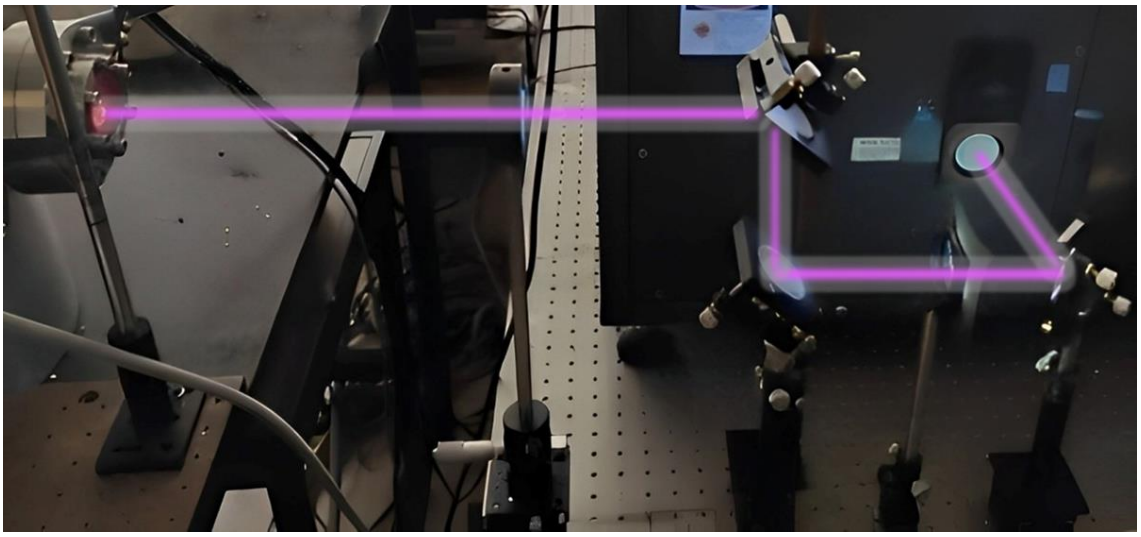


Figure 3-9: The laser beam is directed and focused on the camera window using a set of mirrors and a lens.

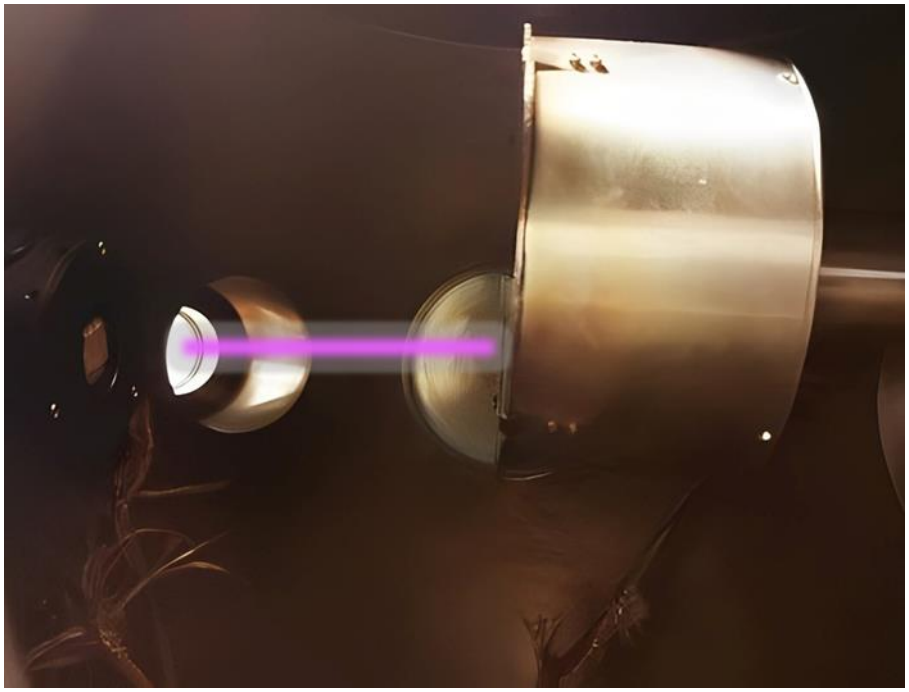


Figure 3-10: View of the interior of the camera showing the path taken by the laser beam from the window to the target.

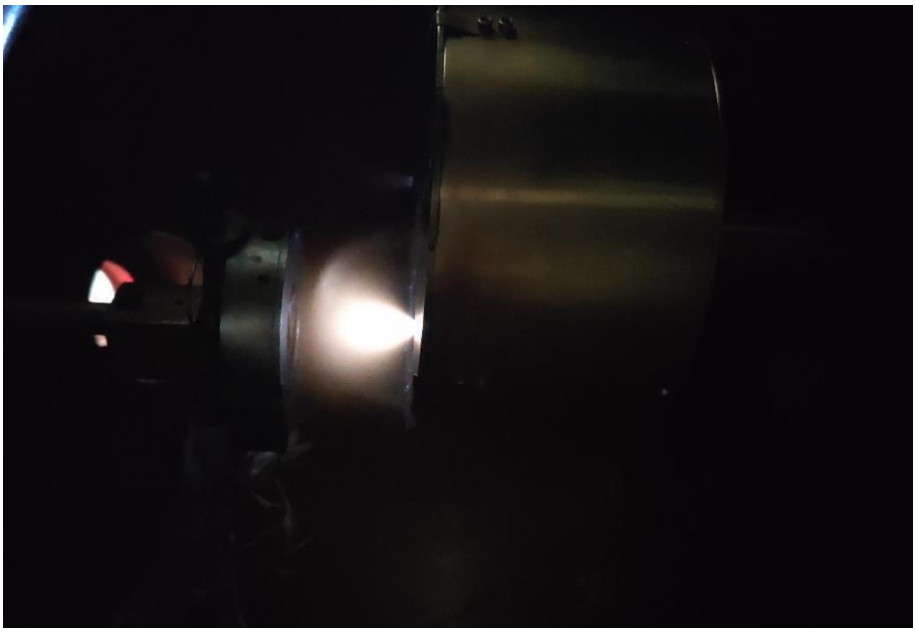


Figure 3-11: Photograph of the interior of the chamber during deposition where it is possible to see the plume formed after the laser beam reaches the target.

3.2. Post-thermal annealing treatment

Among the array of techniques utilized for thin film preparation, PLD holds attraction due to its relative simplicity and the adjustability of parameters (see section 3.1.2.), notably substrate temperature. During film deposition, various physical processes occur on the substrate surface, significantly influenced by the activation energy of plume particles. This energy, inherently tied to the substrate temperature, dictates the movement and interaction of particles such as ions, atoms, and clusters. Consequently, substrate temperature directly impacts atom mobility on the surface, intricately shaping film crystallinity, optical properties, particle size, and stoichiometry [154]. Notably, annealing temperature variations exert profound effects on crystallite sizes, optical band gaps, and surface porosities. These differences yield varied phases, each exhibiting unique physical or electrical features, thus post-annealing thermal treatment stands out as a highly effective process for modifying both the structure and compositional properties of thin films [155]. During the annealing treatment, surface atoms may either adsorb onto or decompose within the film, leading to the emergence of new structures, change of the existing film structure, or change the stoichiometry [50, 156].

Moreover, the versatility of post-annealing treatment extends beyond mere substrate adjustments during PLD. It can also be conducted with dedicated equipment capable of reaching temperatures surpassing those attainable within PLD chambers. Such specialized equipment not only allows for higher

temperatures but also enables the inclusion of working gases, further enhancing the annealing process. These annealing systems offer a broader spectrum of control over annealing conditions, facilitating precise manipulation of thin film properties.

The post-annealing thermal treatment was conducted using a Carbolite Digital Tube Furnace (see Figure 3-12), with a maximum operating temperature of 1200 °C, located at the Centro de Física of Universidade do Minho - Campus de Gualtar. Following the pulsed laser deposition (PLD) process, the films underwent annealing at temperatures up to 1100 °C, in an ambient air environment. The heating rate utilized to attain these temperatures was set at 10 °C/min.



Figure 3-12: Carbolite Digital Tube Furnace utilized for thin films post-annealing thermal treatment.

3.3. X-Ray Diffraction

X-ray Diffraction (XRD) is a non-destructive characterization technique involving the diffraction of radiation with wavelengths on the order of angstroms (10^{-10} m) in a crystalline structure under analysis. The wavelengths of the incident radiation are within the X-ray region of the electromagnetic spectrum, precisely chosen because the distance between atoms in a crystal lattice is also of the order of angstroms. This technique enables the identification of crystalline phases, analysis of preferential crystallographic orientation, determination of lattice parameters, assessment of mechanical stress states, and grain size determination. Moreover, XRD is non-destructive, allowing for the analysis of valuable or sensitive samples without altering their structure or composition.

According to Bragg's law [157], when radiation is incident upon a crystal lattice, interference occurs between the diffracted waves from different planes, resulting in a pattern where the maximum intensity corresponds to constructive interference. Bragg's law is expressed as [157]:

$$2d_{hkl}\sin\theta = n\lambda \tag{3-3}$$

where λ is the wavelength of the radiation, d_{hkl} is the interplanar spacing, θ is the angle of incidence of the radiation, and n is a positive integer.

When constructive interference occurs (resulting in a peak in X-ray diffraction), θ_{hkl} is the angle at which this interference is observed for a given interplanar atomic spacing d_{hkl} [158]. A schematic representation of the Bragg's law is depicted in Figure 3-14.

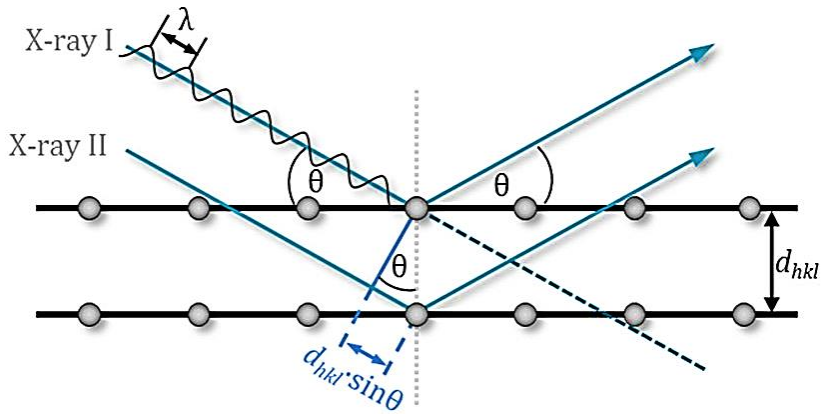


Figure 3-13: Schematic representation of Bragg diffraction in a crystalline lattice, which describes the condition for constructive interference. This interference depends on the X-ray wavelength (λ), the diffraction angle (θ), and the perpendicular interplanar spacing between the lattice planes (d_{hkl}). The integer n represents the order of the interference. Taken from reference [159].

Diffractometers consist of a detector, a monochromator, a collimator, an X-ray source, and a sample holder. In Bragg-Brentano geometry, the source, sample and detector are in the focusing plane [160]. The diffractometers used in this study adhere to the Bragg-Brentano geometry, as illustrated in Figure 3-14. This setup allows for accurate measurement of diffraction angles and intensities, facilitating precise analysis of the sample's crystal structure and properties.

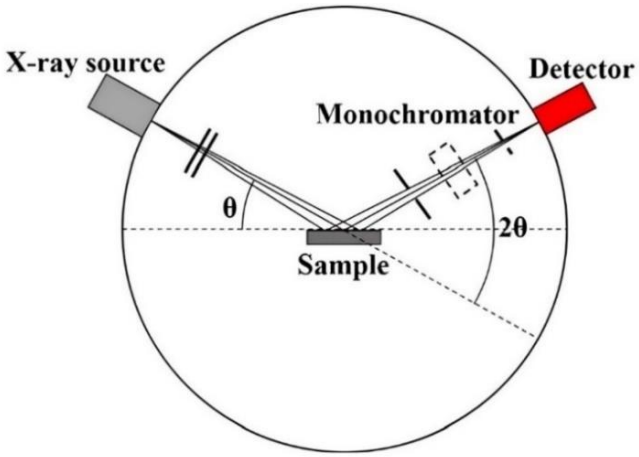


Figure 3-14: Schematic diagram of XRD. Taken from reference [160].

The X-ray diffraction measurement was conducted in the $\theta = 2\theta$ geometry (as shown in Figure 3-14), wherein the X-ray source remains fixed, while the sample rotates at angle θ and the detector rotates at angle 2θ for measurement purposes [160]. In this configuration, the incident radiation has a wavevector $\vec{K}_0$, where $\left|\vec{K}_0\right| = 2\pi/\lambda$ and λ is the X-ray wavelength, and the diffracted beam has wavevector $\vec{K}$, since XRD is an elastic process $\left|\vec{K}\right| = \left|\vec{K}_0\right|$. On the other hand, the diffraction vector $\vec{Q}$ is defined as the vector difference between the diffracted and incident wavevectors, so that $\vec{Q} = \vec{K} - \vec{K}_0$ and $\left|\vec{Q}\right| = \left(\frac{4\pi}{\lambda}\right)\sin(\theta)$. In a XRD measurement, the Bragg condition is fulfilled when the diffraction vector equals a reciprocal lattice vector. When this occurs, $\left(\frac{4\pi}{\lambda}\right)\sin(\theta) = 2\pi/d_{hkl}$, where d_{hkl} is the interplanar distance and hkl are the Miller indices of the planes, leading to the Bragg equation [161]. This measurement allows seeing if there is a preferential growth direction in the films (among other information). In the $\theta = 2\theta$ configuration, the calculated diffraction vector $\vec{Q} = \vec{K} - \vec{K}_0$ is always perpendicular to the sample surface, as shown in Figure 3-15. Changing the angle θ only changes the length of the vector $\vec{Q}$, but not its orientation, since the incident and diffracting angles keep being the same. As such, the measurements always observe planes parallel to the sample surface, along a direction that is perpendicular to it. This approach is versatile and applicable to single-crystal, polycrystalline, and oriented specimens, allowing for comprehensive characterization of crystalline materials.

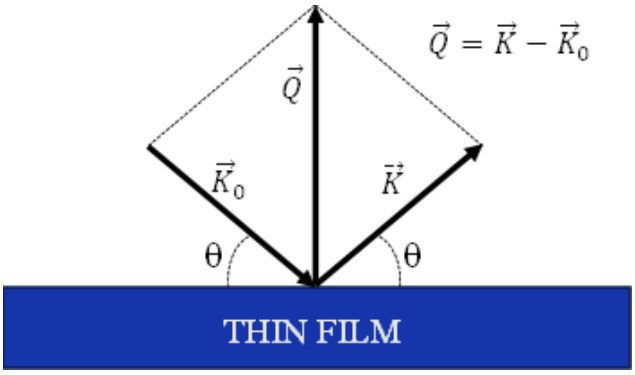


Figure 3-15: Schematics of the incidence vector $\vec{K}_0$, the reflected vector $\vec{K}$and the scattering vector $\vec{Q}$ in $\theta = 2\theta$ XRD measurements.

The peaks observed in the diffraction patterns of the samples were fitted, and the distances d_{hkl} between lattice planes in the films were determined employing Bragg's law. Subsequently, upon the determination of interplanar distances, the crystallographic phases present in the samples were identified by comparison with data from the Powder Diffraction Files.

The broadening of diffraction peaks can arise from various factors, including instrumental effects, stress, and crystallite grain size [158]. The grain size, L can thus be estimated from the width of the diffraction peaks using Scherrer's equation [162]:

$$L = \frac{f\lambda}{\omega \cos\theta} \tag{3-4}$$

where ω represents the full width at half maximum (FWHM) of the diffraction peak in radians, and f is a numerical factor dependent on the shape of the crystallites [158] ($f = 0.9$ for spherical grains).

In this study, the samples were analyzed using the Bruker D8 Discover diffractometer housed at the SEMAT - Serviços de Caracterização de Materiais da Universidade do Minho, located at the Universidade do Minho – Campus de Azurém. The film's structure was studied using Cu-Kα radiation (λ=1.5406 Å) at 40 kV and 40 mA and Bragg-Brentano geometry. Each sample was scanned in the 2θ range: 10°-80° at a speed of 0.04° s^{-1}.

3.4. Scanning Electron Microscopy

Scanning Electron Microscopy (SEM) has become widely utilized across various disciplines globally, serving as an effective method for analyzing organic and inorganic materials on a nanometer to micrometer (μm) scale. Operating at high magnifications, SEM can reach up to 300,000x and even 1,000,000x in some modern models, facilitating precise imaging of a broad range of materials [163]. It is an experimental characterization technique that relies on the analysis and quantification of electrons

scattered from a sample when an electron beam is directed onto it, ultimately allowing for the acquisition of high-definition images. Energy Dispersive X-ray Spectroscopy (EDS) is often employed in conjunction with SEM, providing qualitative and semi-quantitative chemical results. Together, these techniques have the potential to offer fundamental insights into the material morphology and composition of scanned specimens, surpassing the capabilities of common optical laboratory tests [163].

The analysis in SEM involves directing an electron beam onto a sample and studying the interaction between the incident electrons and the atoms. The different shades of gray in SEM images are formed by detecting two primary types of electrons: secondary electrons (SE) and backscattered electrons (BSE) [164]. Backscattered electrons are reflected after elastic interactions between the electron beam and the sample, originating from deeper regions of the sample [164]. They are highly sensitive to differences in atomic numbers, with heavier elements appearing brighter in the image due to their higher backscattering coefficient. On the other hand, secondary electrons result from inelastic interactions between the electron beam and the sample's surface atoms [164]. They originate from the surface regions and provide high-resolution images with detailed surface topography [165]. Thus, BSE images offer compositional contrast based on atomic number, while SE images provide detailed surface information [165]. This combination allows SEM to simultaneously deliver detailed topographical and compositional information, resulting in the varying shades of gray observed in SEM images [165].

Figure 3-16 illustrates the typical setup of a SEM equipment, comprising the electron gun (consisting of the electron source and accelerating anode), electromagnetic lenses for electron focusing, a vacuum chamber housing the specimen stage, and various detectors to capture signals emitted from the specimen [166].

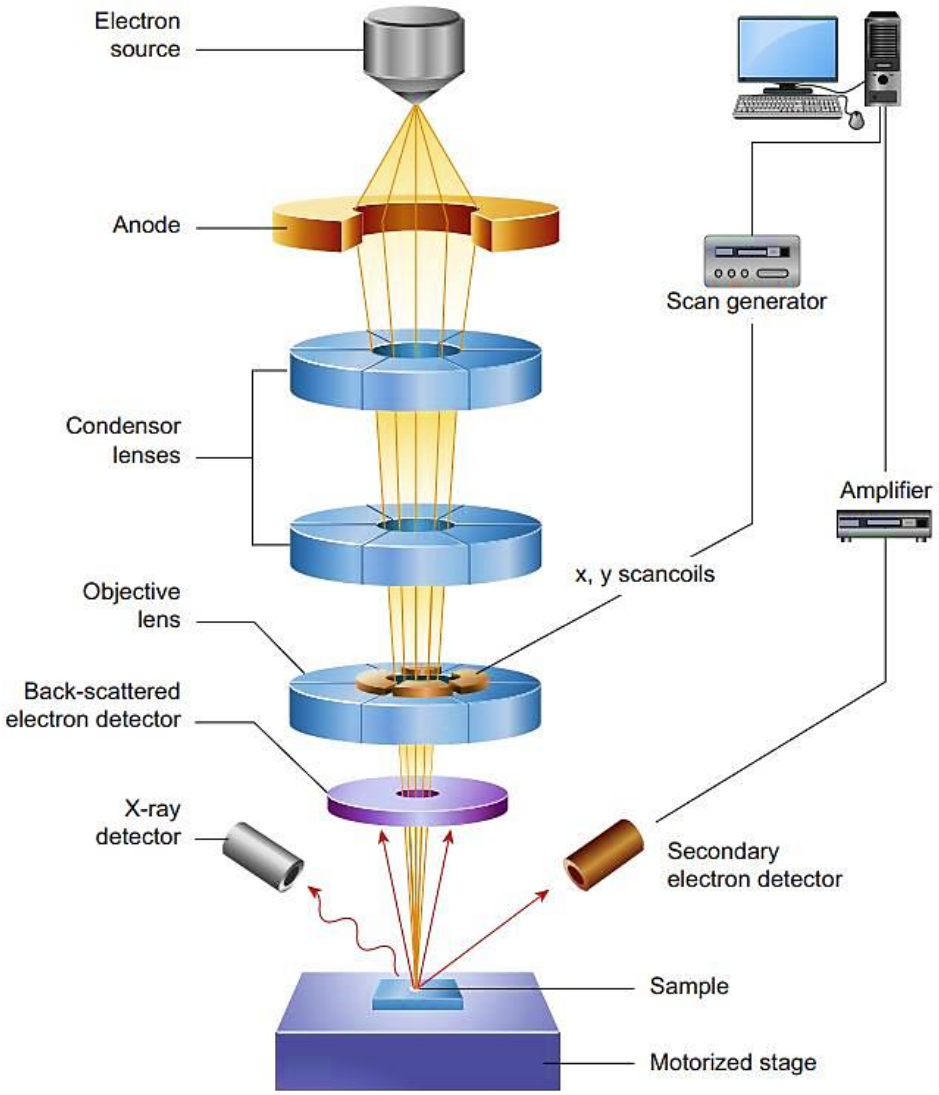


Figure 3-16: Schematic diagram outlining the core components of an SEM microscope. Taken from reference [166].

The process of SEM analysis, as described by references [163, 167], involves several key steps:

- Electron Beam Generation and Focusing:
  - A high-energy electron beam ranging between 100-30,000 electron volts is applied to the sample, typically emitted from a thermal source.
  - The initial spot size produced by the electron gun is large, necessitating the use of magnetic lenses within the SEM to compress the spot and focus the electrons onto the specimen. Most SEMs achieve a spot size of less than 10 nm.
- Image Formation:
  - The specimen's image is generated point by point as the scan coils move the electron beam in discrete locations, forming a rectangular raster on the specimen's surface.

- The magnification depends on the movement of the scan coils, with higher magnification achieved by deflecting the beam across a smaller area.
- The working distance, or distance from the last lens to the specimen surface, affects magnification, which is automatically adjusted in modern SEMs.

- Electron Detection:
  - Electron detectors are utilized to capture emitted electrons (signals) from the scanned sample.
  - Both secondary electrons (SE) and backscattered electrons (BSE) contribute to SEM image production. SE and BSE are collected differently based on the voltage applied to the collector screen.
- Image Optimization:
  - The captured signals are displayed on the viewing screen, allowing the operator to adjust brightness and intensity for clear image visualization.
  - Higher magnifications exceeding 10,000x are employed to observe small details within the specimen, with the electron voltage mode influencing the level of detail provided.
- Surface Information and Penetration Depth:
  - Low accelerating voltages (<5 kV) provide surface-rich information, while high accelerating voltages (15-30 kV) penetrate deeper into the sample, revealing interior details. Figure 3-17 illustrates the varying penetration levels of electrons through the sample and the resulting reflected signals.
- Topographic Imaging:
  - SEM images provide partly three-dimensional representations of the sample's topography, including shape, size, and surface texture.
  - The number of BSE and SE signals, crucial for topographic contrast, increases with the angle of inclination (tilt angle) of the sample surface, particularly at angles exceeding 50° up to 70°.
  - Through meticulous control and understanding of these processes, SEM enables comprehensive visualization and analysis of materials at the micro and nanoscale levels, offering invaluable insights across various scientific disciplines.

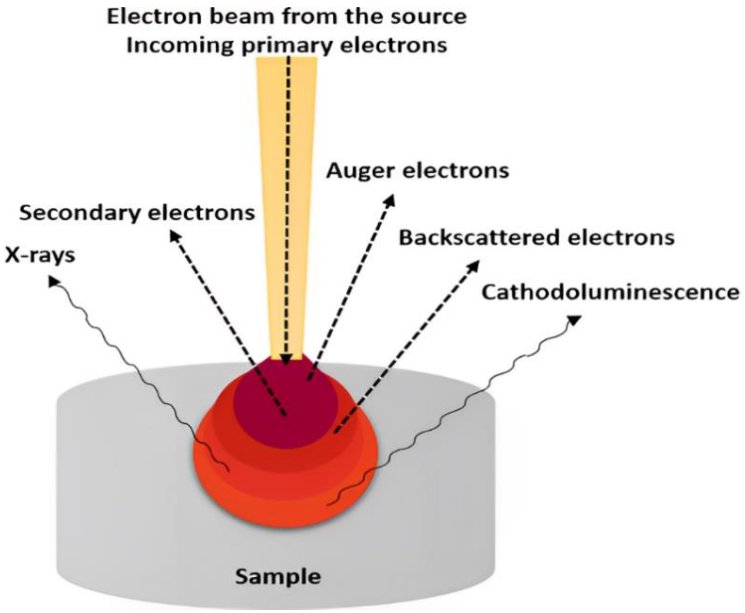


Figure 3-17: The electron beam interaction with the specimen, leading to the emission of signals from the sample [168].

To characterize the grain structure of thin films and measure their thickness the NanoSEM - FEI Nova 200 at SEMAT - Serviços de Caracterização de Materiais da Universidade do Minho was utilized. This instrument is an Ultra High-Resolution Scanning Electron Microscope (SEM) with field emission, equipped with an integrated system for microanalysis via X-ray energy dispersive spectrometer (EDS) and analysis of patterns of backscattered electrons diffraction (EBSD - Electron Backscatter Diffraction).

3.5. Energy-dispersive X-ray Spectroscopy

Energy-dispersive X-ray spectroscopy (EDS), also known as EDX, EDXS or XEDS, is a versatile analytical technique used for both qualitative and quantitative analysis of a sample's elemental composition. It relies on the interaction between a source of X-ray excitation and the sample and can determine which chemical elements are present and estimate their relative abundance. This capability allows EDS to provide compositional information on various types of samples, including individual points, lateral distributions across an imaged area, quasi-bulk specimens, specific particles, morphologies, or isolated areas within deposits.

In the EDS spectrum, most peaks are obtained from X-rays produced by characteristic fluorescence radiation. Each element in the periodic table has a unique atomic configuration, resulting in a specific array of peaks in an X-ray radiation spectrum. When a high-energy beam of particles, such as electrons or X-rays, is incident on the sample, it emits characteristic X-ray radiation due to energy transitions. The

energy of these X-rays radiated from a specimen can be estimated via an energy-dispersive spectrometer. Consequently, different X-ray peaks with specified positions in a spectrum are identified during qualitative analysis [169].

When an atom is ionized through electron bombardment, creating a vacancy in its electron configuration, subsequent transitions within its electron shells can lead to the emission of characteristic X-rays [170]. For instance, when a K-shell electron transitions into a higher energy state or vacuum, it leaves behind a "hole" that can be filled by an electron from a lower energy shell, like the L shell. This process has a certain probability of resulting in the excitation of characteristic X-rays, specifically Kα radiation for the described transition [170]. Similarly, if an electron from the M shell fills the vacancy, it can lead to the emission of Kβ X-rays. However, Auger electrons may also be emitted, with the combined fluorescence yield of X-rays and Auger electron emission totaling 100% [171]. The fluorescence yield of X-rays generally increases with the atomic number (Z) of the element, while the proportion of emitted Auger electrons behaves inversely. Additionally, ionization of the L shell and subsequent filling by electrons from the M or N shells can result in the emission of Lα or Lβ radiation, respectively. This process is illustrated in the Figure 3-18.

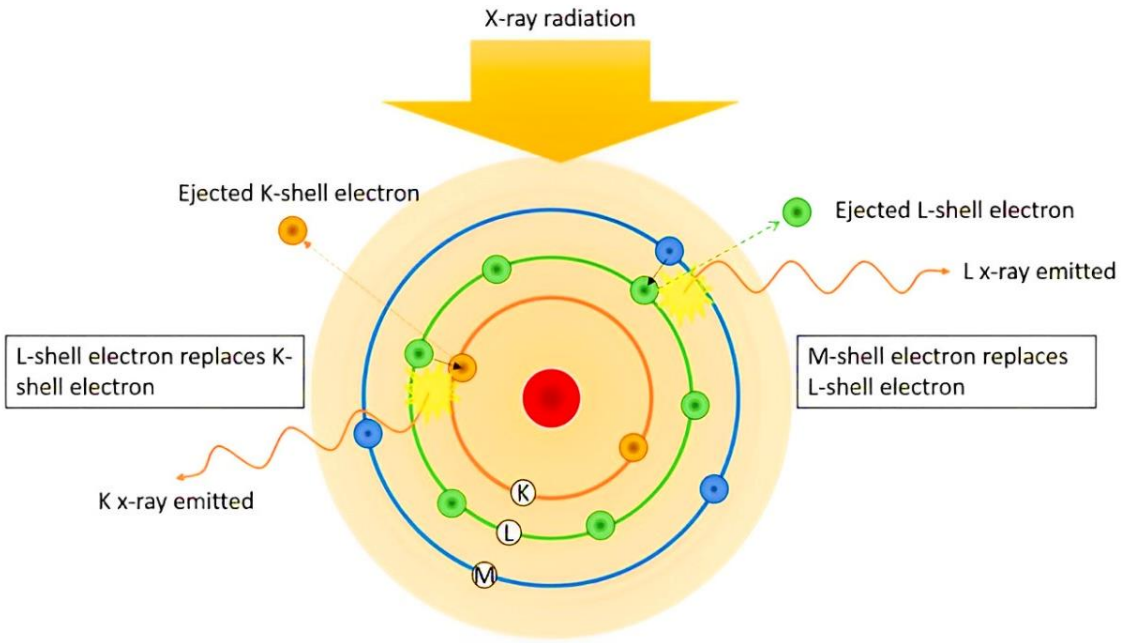


Figure 3-18: Working principle of EDS where a sample of interest is bombarded with a focused beam of electrons, which can excite and eject an inner shell electron, leaving behind a vacancy that is filled by an electron from an outer shell. Taken from reference [172].

These processes contribute to the emission and analysis of characteristic X-rays in X-ray spectroscopy techniques. The emitted X-rays are captured by a detector, producing fluorescent photons. The energy of these characteristic fluorescent photons can be calculated by [173]:

$$E = \frac{hc}{\lambda} \tag{3-5}$$

where E is energy, h is Planck's constant, c is the speed of light, and λ is the wavelength.

Accurately measuring the emitted X-rays from each element within a sample enables the calculation of the concentration of that specific element in terms of mass or atomic fraction [174].

Electron beam excitation is employed in various microscopy techniques, including electron microscopy, SEM, and scanning transmission electron microscopy (STEM), enabling the detection and measurement of trace elements. EDS integration with these microscopy methods enhances the analytical capabilities, allowing for comprehensive elemental analysis and characterization of samples at the micro and nano scales.

Microanalysis of the samples was performed with the EDS equipment at SEMAT - Serviços de Caracterização de Materiais da Universidade do Minho. It used an INCA XZ-act detector, which typically operates at an acceleration voltage of 20 kV. Samples surfaces were covered with a conductive thin film (15 nm) of Au–Pd (80–20 wt%), using a high-resolution sputter coater, model 208HR, from Cressington Company, coupled to an MTM-20 Cressington High-resolution Thickness Controller.

3.6. Raman Spectroscopy

Raman spectroscopy is a powerful spectroscopic technique used to analyze the vibrational modes of molecules, rotational dynamics, and other low-frequency modes within a system [175–177]. In addition, Raman spectroscopy is also widely used for the investigation of phase transitions [178–181] and subtle structural distortions in perovskites [182–186]. The technique is sensitive to changes in molecular environments, making it a valuable tool for studying the dynamic behavior of materials under different conditions [172].

Raman spectroscopy relies on the principle of inelastic scattering of monochromatic light focused onto a sample [187], as described in Figure 3-19.

When incident light photons strike a molecule, they can produce scattered photons with different frequencies. This scattered light may have a lower frequency than the original incident photon [172], known as Stokes Raman scattering, or a higher frequency, known as anti-Stokes Raman scattering. In the case of anti-Stokes Raman scattering, the photon acquires energy from the molecular bond when the bond is initially in an excited vibrational state. The energy shift observed in the scattered light spectrum is influenced by the chemical composition of the molecules responsible for scattering. This shift depends

on the displacement of constituent atoms from their equilibrium positions due to molecular vibrations [187]. The energy shift occurs due to the transfer of vibrational energy quanta between the interacting radiation and the medium, resulting in spectrally shifted lines. The vibrational frequencies of functional groups within molecular systems can be characterized by the spacing of Raman lines since each bond is associated with a specific energy [188].

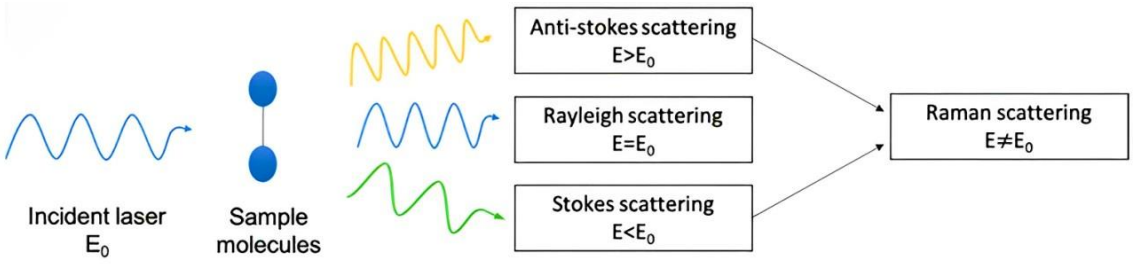


Figure 3-19: Working principle of Raman spectroscopy. Taken from reference [172].

The setup for Raman spectroscopy typically involves a narrowband laser beam expanded through a telescope and focused on the sample by an objective lens [189]. The scattered light is collected by the same lens, filtered to remove the excitation laser light, and guided to a spectrometer for analysis using liquid nitrogen or a thermally cooled Charged-couple device camera (technology used in digital imaging) [189]. In Raman imaging, similar equipment is used, with the addition of a motorized stage that moves the sample in the x and y directions, allowing for the acquisition of hundreds to thousands of Raman spectra across the specimen. This enables the creation of chemical maps that reveal the distribution of different components within the sample [190].

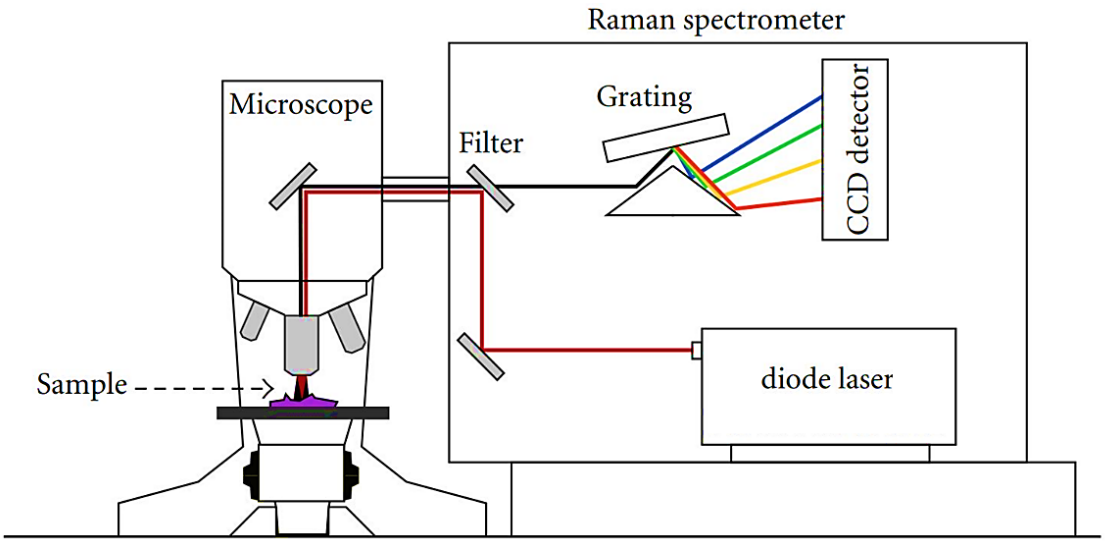


Figure 3-20: Standard configuration of a Raman spectrometer featuring a microscope coupled with a near-infrared laser. Taken from reference [191].

One of the main advantages of Raman spectroscopy and imaging is the minimal sample preparation required and its non-destructive nature. This makes it a valuable tool in various fields, including materials

science, chemistry, and biology [172]. There are several variations of Raman spectroscopy, each tailored to specific applications. These variations aim to enhance sensitivity, improve spatial resolution, or provide very specific information and offer a powerful analytical tool for studying molecular structures, crystals and identifying functional groups within complex molecular systems [192].

Raman spectroscopy measurements were carried out on an ALPHA300 R Confocal Raman Microscope (WITec) using 532 nm laser light for excitation in the backscattering geometry at room temperature at INL - International Iberian Nanotechnology Laboratory. The laser beam was focused on the sample using a 50x Zeiss lens.

3.7. Magnetic characterization by a Superconducting Quantum Interference Device magnetometer

In the area of magnetic field and magnetization measurement, various techniques have been developed, each with different sensitivities. Among these methods stands out the Superconducting Quantum Interference Device (SQUID) magnetometers renowned for their unmatched sensitivity. Operating on the principles of superconductivity and quantum interference, and inductively coupled to an appropriate input circuit, SQUIDs serve as versatile instruments capable of measuring magnetic field, magnetic field gradient, voltage, and magnetic susceptibility [193]. By utilizing superconducting loops containing Josephson junctions and operating at cryogenic temperatures, the SQUID achieves sensitivity and field resolutions down to an impressive level of 10^{-17} T.

The SQUID operates on the principle of the Josephson effect, enabling the measurement of extremely small variations in magnetic flux. A SQUID consists of a superconducting ring interrupted by one or more Josephson junctions [194], as shown in Figure 3-21. To achieve optimal performance, a bias current (I_b) is applied, positioning the operational point on the I-V curve (Figure 3-22 (a)) midway between superconducting and resistive behaviors. Shunt resistors are employed to prevent hysteretic behavior in the I-V curve. Inductively coupling magnetic flux into the SQUID loop generates screening currents ($I_{loop} = \Phi_{loop}/L_{loop}$), effectively modulating the critical current (I_c) depending on the direction of the induced flux. By maintaining I_b slightly higher than I_c, any external magnetic flux ($\Phi_{loop} = B_{ext}A$) coupled into the Josephson loop induces a change in voltage across the junction. This change occurs periodically with the period corresponding to the flux quantum (Φ_0), Figure 3-22 (b). Monitoring the voltage variation enables the determination of the magnetic flux within the SQUID loop. Through external feedback, it's possible to put the SQUID at a specific point on the V-Φ curve, with the feedback current

serving as a measure of the applied flux (Figure 3-21). SQUIDs are typically operated at the steepest part of the $\mathrm{V}-\Phi_0$ curve, where the $\partial V/\partial\Phi$ is at its maximum.

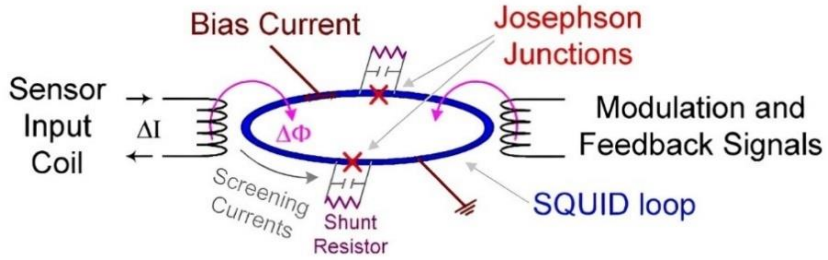


Figure 3-21: The dual-junction DC (direct current) SQUID loop incorporates a capacitor, which symbolizes the self-capacitance of the junction. Taken from reference [194].

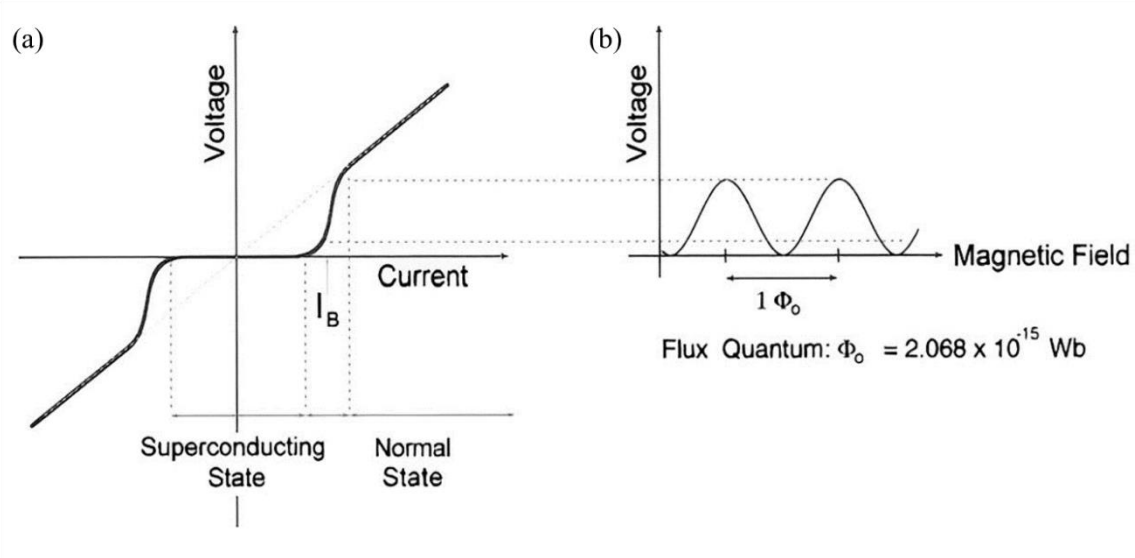


Figure 3-22: (a) Bias point (I_b) for the Josephson junction. (b) Voltage in the function of externally applied flux at constant bias current. Taken from reference [194].

To track large changes in applied fields, the feedback electronics must respond swiftly [194]. For signal changes exceeding $\Phi_0/4$, the electronics need to apply negative feedback promptly to maintain the voltage at the lock point. Failure to adjust the feedback current quickly enough may lead to flux jumping, necessitating faster electronics or limitations on the dynamic range or bandwidth of the input signal [194].

SQUIDs can be categorized as RF or DC SQUIDs based on whether the Josephson junction is biased with an alternating current (RF) or a direct current (DC) [193]. Due to their lower noise characteristics, most commercial SQUIDs are DC SQUIDs. Typically, flux is inductively coupled into the SQUID loop via an input coil, which connects the SQUID to the experiment. In the case of high-temperature superconducting SQUIDs, the input coil may be integrated into the Josephson loop or connected via a flip chip [194].

All measurements in this study were conducted at the Institute of Physics for Advanced Materials, Nanotechnology and Photonics (IFIMUP) (physics Research Unit of the University of Porto), using the Magnetic Property Measurement Superconducting Quantum Interference Device magnetometer manufactured by Quantum Design. This magnetometer allows for the measurement of the magnetic moment as a function of applied magnetic field (up to 7T) and temperature (from 350 to 2K). The measurement sensitivity with the SQUID MPMS-3 model is ≤ 10^{-8} emu. Figure 3-23 shows the diagram of the MPMS3 SQUID system illustrating components and the location of the sample, gradiometer and magnet [195].

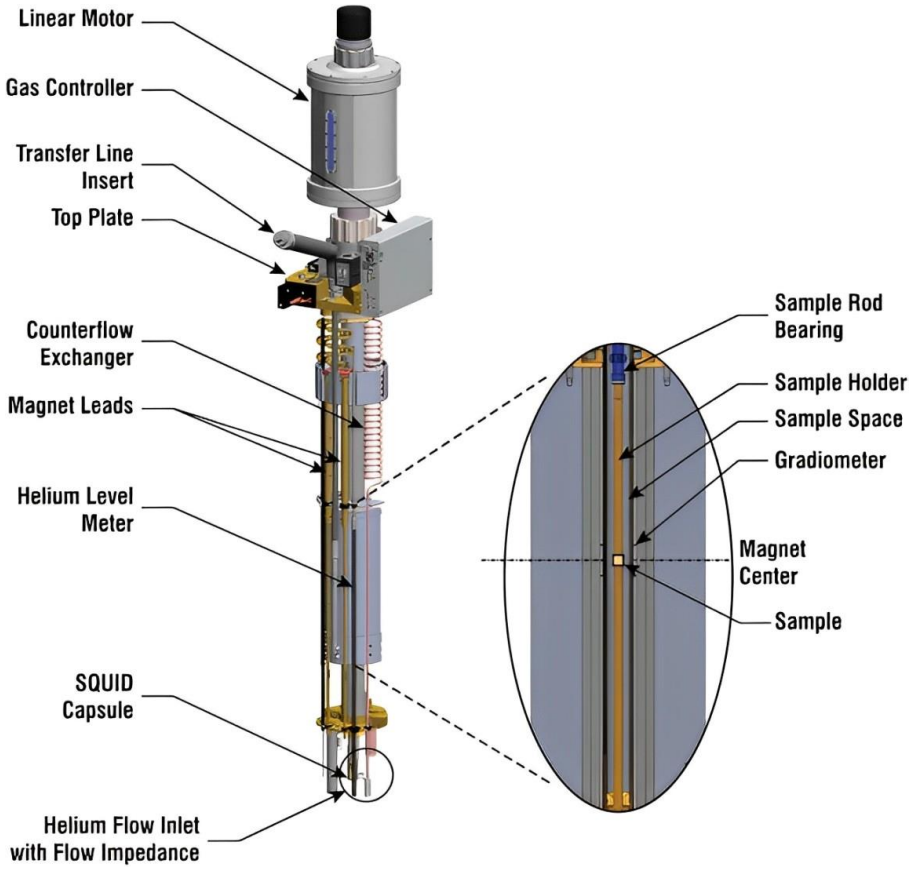


Figure 3-23: Diagram of the MPMS3 SQUID system illustrating key components. Taken from reference [195].

3.8. Dielectric characterization by Impedance Spectroscopy

Dielectric spectroscopy (DS) comprises a versatile array of techniques that exploit the interactions between materials and electromagnetic fields spanning radio and microwave frequency regions of the spectrum. These interactions provide a comprehensive understanding of molecular behavior and the reorientation mobility of dipoles within materials. DS emerges as a universal and powerful tool, especially

adept at investigating soft matter, offering insights into the frequency-dependent complex permittivity of materials [196].

At its core, dielectric spectroscopy capitalizes on the frequency dependence of electrical impedance, admittance, or related parameters, serving as a robust tool for discerning and characterizing material properties [196]. Within the domain of solid-state physics, dielectric spectroscopy finds application in elucidating the behavior of a wide range of materials, including electroceramics, polymers, and glasses [197]. Particularly, it is instrumental in unraveling the intricate complexities of polycrystalline solids, where phenomena such as grain boundaries give rise to distinctive electrical behaviors.

DS provides crucial information regarding material parameters such as static dielectric permittivity (ε) and DC electrical conductivity (σ) [196]. It examines both current and voltage (amplitude and phase of an AC system), allowing the evaluation of dielectric properties in polymers, fibers, nanomaterials and others [197]. DS operates across a broad frequency range, from very low frequencies (millihertz) useful for assessing interfaces between insulation components, to ultra-high frequencies (terahertz) [196].

The analyzed films can be measured by depositing a silver ink contact on them, forming a capacitor with parallel flat plates. The bottom contact can also be constructed using silver ink or it can be the substrate itself if it is conductive (as is often the case with thin films deposited on substrates of $SrTiO_3$:Nb, Si:As, or SiPt). Therefore, the capacitance (C) of the formed capacitor (Figure 3-24) and the loss factor ($\tan\delta$) under an alternating (AC) sinusoidal supply voltage, can be obtained as a function of frequency. The real component of permittivity, also known as the dielectric constant (ε'), and the imaginary component of permittivity (ε''), can be calculated using the following equations [85]:

$$\varepsilon' = \frac{CL}{\varepsilon_0 A} \tag{3-6}$$

$$\varepsilon'' = \varepsilon' \tan\delta \tag{3-7}$$

where L is the thickness of the film capacitor, A is the area of the contact and ε_0 is the permittivity of free space, ~8.854 x 10^{-12} F/m..

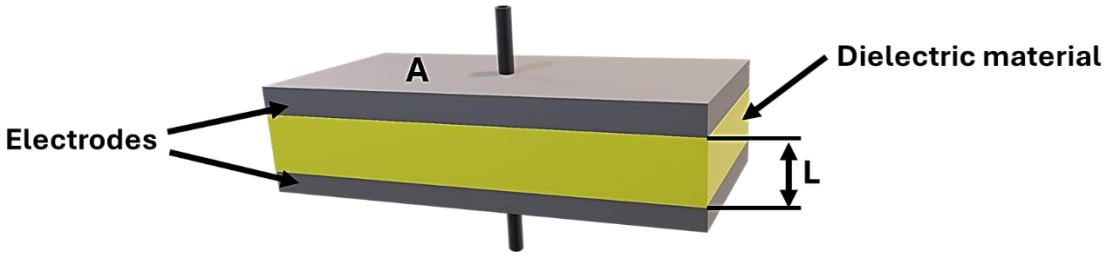


Figure 3-24: Parallel plate capacitor illustrating its components: dielectric material, electrodes, area (A), and thickness of the film capacitor (L).

Figure 3-25 depicts the permittivity as a vector in the complex plane, relating it to the real and imaginary components of permittivity and dielectric loss.

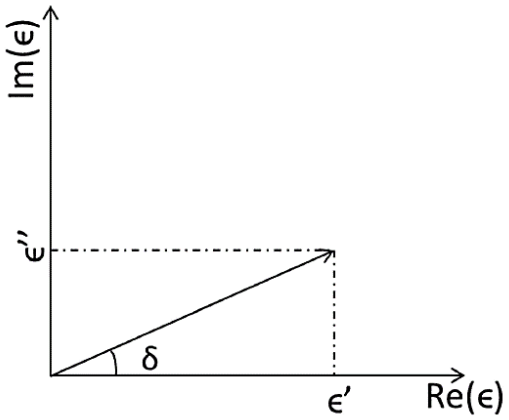


Figure 3-25: Representation of the dielectric constant as a vector in the complex plane.

Dielectric data analysis typically involves presenting the data as a function of frequency at a constant temperature or as a function of temperature at a constant frequency. By conducting experiments across multiple frequencies, the same dataset can be utilized to generate multi-frequency curves plotted against temperature, or multi-temperature curves plotted against frequency. Temperature scans, whether conducted at a single frequency or across multiple frequencies, yield direct information about critical temperatures or frequencies, relaxation characteristics, and transition temperatures, providing a comprehensive understanding of the material's behavior across different environmental conditions or preparation conditions/deposition. Furthermore, the ability to probe the material's response across a range of frequencies enhances our understanding of its dynamic behavior and enables the identification of frequency-dependent phenomena.

By analyzing the dielectric function, particularly when the frequency of the applied electric field matches the reorientation times of molecular dipoles, characteristic patterns emerge in the complex dielectric function [85]. This pattern is characterized by a step-like decrease in the real part (ε') and a maximum in the imaginary part (ε'') with increasing frequency (Figure 3-26). From this behavior,

essential parameters characterizing the dielectric relaxation process can be extracted [85]. The frequency of maximal loss (ν_p) is associated with a characteristic relaxation rate (ω_p) or relaxation time (τ_p) of the fluctuating dipoles. Furthermore, the shape of the loss peak provides insights into the distribution of relaxation times.

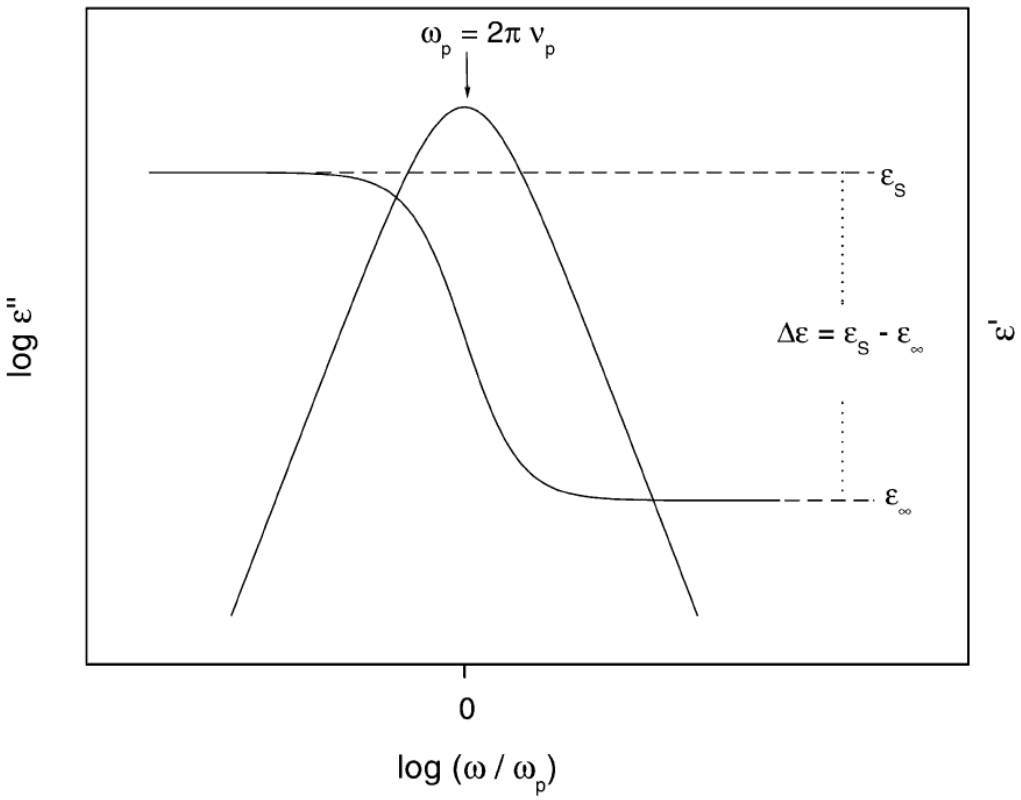


Figure 3-26: Real ε' and imaginary part ε'' of the complex dielectric function vs normalized frequency for a Debye relaxation process. Taken from reference [85].

The results of dielectric spectroscopy are commonly analyzed based on Cole-Cole diagrams, which represent the imaginary dielectric constant, ε'', as a function of the real dielectric constant, ε'. In this representation, for a Debye function [85], the data points align along a semicircle intersecting the ε' axis at ε_∞ and $\varepsilon_\infty + \Delta\varepsilon$, even if the data cannot be described by a single relaxation time. This circular arc provides insights into the symmetric relaxation function, with the shape parameter β (symmetrical broadening) also estimable. The Cole-Cole plot enables an easy determination of whether the data should be described by a symmetric or asymmetric distribution of relaxation times. This distinction is evident in Figure 3-27, showcasing a Cole-Cole representation for the Havriliak-Negami-functions, where the angle of intersection with the ε' axis varies at different frequency ranges.

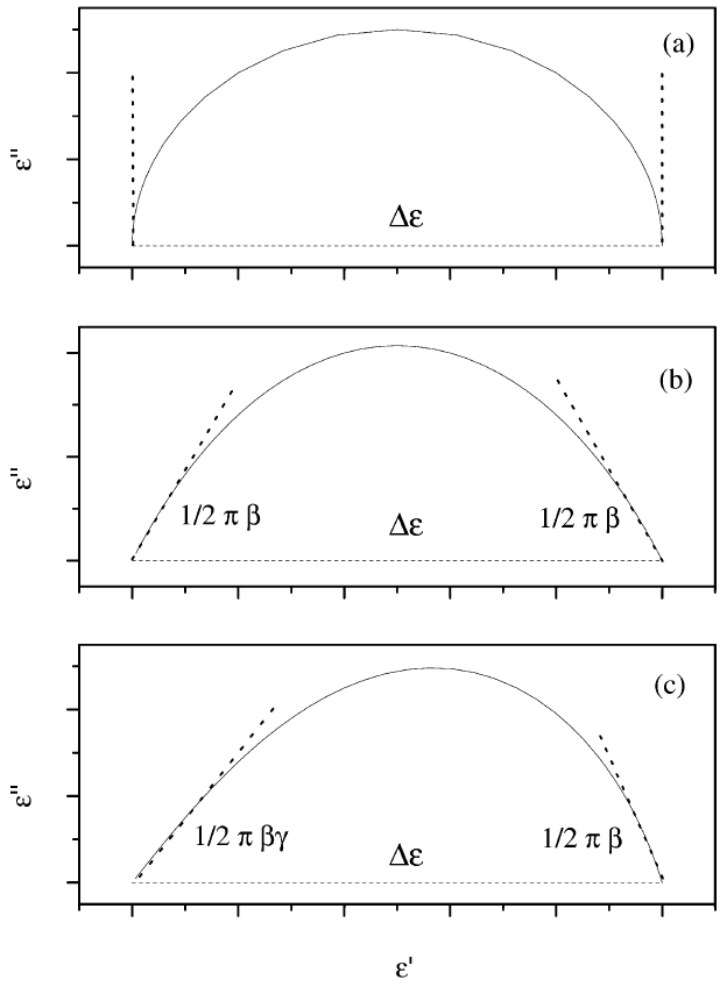


Figure 3-27: Cole-Cole plots for different model functions with $\Delta\varepsilon$ = 1, ε_∞ = 1 and τ = 1 s: (a) Debye-function; (b) Cole-Cole-function with β = 0.5; (c) HN-function with β = 0.7 and γ = 0.6. Taken from reference [85].

Moreover, the Cole-Cole plot serves as a useful tool for characterizing isolated relaxation processes and separating overlapping relaxation regions. These diagrams can reveal a semicircle, a distribution of semicircles, or two main semicircles. The presence of multiple semicircles indicates the existence of different polarization mechanisms within the material [85]. Illustrated in Figure 3-28, the Cole-Cole plot for an example sample, exhibits a double arc, indicating the presence of two relaxation processes. Typically, when two main semicircles are visible, one is expected to correspond to the grain boundary and the other to the grain interior. For each process, the dielectric strength and shape parameters can be extracted, facilitating a detailed understanding of the material's behavior. For further details on data analysis techniques, models utilized, and a critical analysis thereof, additional information can be found in the reference [85] and section 2.3.2.

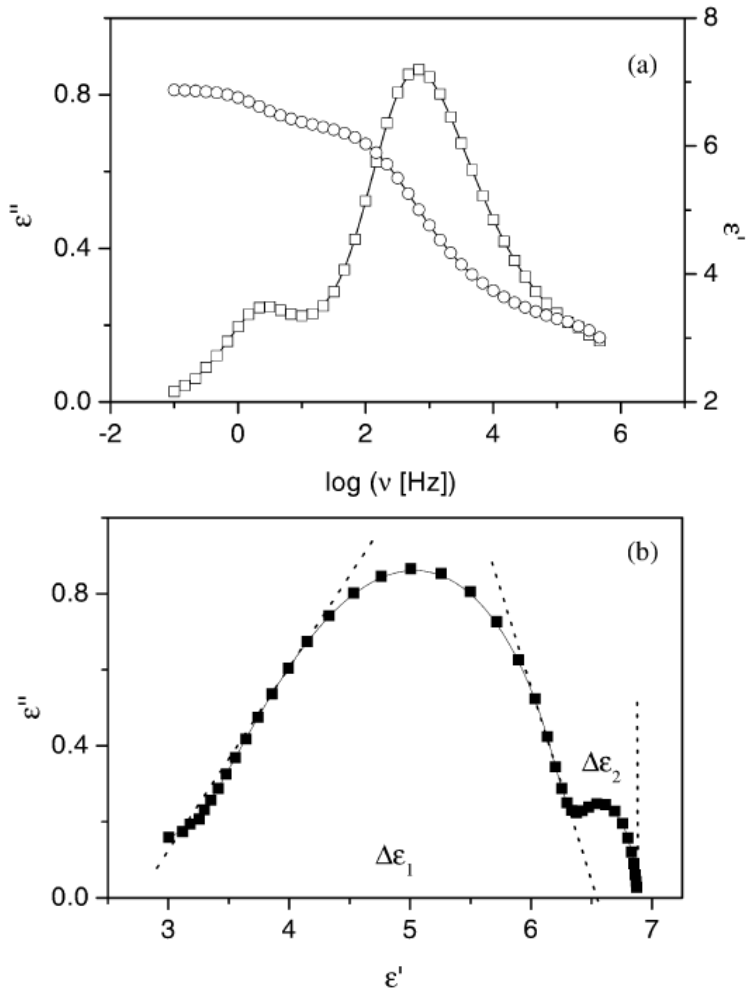


Figure 3-28: (a) Real part ε' (circles) and imaginary part ε''(squares) of poly(propylene glycol) at T = 213.7 K. (b) Cole-Cole representation of the data in a. Taken from reference [85].

Dielectric spectroscopy offers several advantages, but it also has some disadvantages. One key advantage is its straightforward sample preparation process, requiring minimal effort [196]. Additionally, DS enables low-frequency measurements using two electrodes, either attached to or immersed in the samples, allowing for the examination of a wide range of sample types, including solid compacts, powders and gels. Moreover, DS offers flexibility in method and measurement conditions, facilitating examinations under various temperatures, pressures, humidities, and other conditions that might be challenging with other techniques [196]. Importantly, DS is generally noninvasive, employing only small voltages, which minimizes disruption to the sample. However, DS also presents drawbacks [196]. Some samples may not yield comprehensive analysis, as they may exhibit very low responses that escape detection by the instrument. Additionally, the response of a sample of interest may be overshadowed by that of a less relevant constituent, limiting the effectiveness of the technique in certain cases.

The dielectric measurements were conducted at the Centro de Física da Universiade do Minho - Campus de Gualtar. The dielectric properties were characterized by impedance spectroscopy, at

temperatures of 30–295 K and in the frequency range of 20 Hz – 3 MHz. A Wayne Kerr 6440A precision component analyzer, together with a dedicated computer and software, was used to acquire the data. Shielded test leads were employed to avoid parasitic impedances due to the connecting cables. The temperature was controlled using a Scientific Instruments INC Series 5500–5 temperature gauge, and temperature-dependent measurements were performed at a rate of 2 K/min. The schematic representation of the setup is depicted in Figure 3-29.

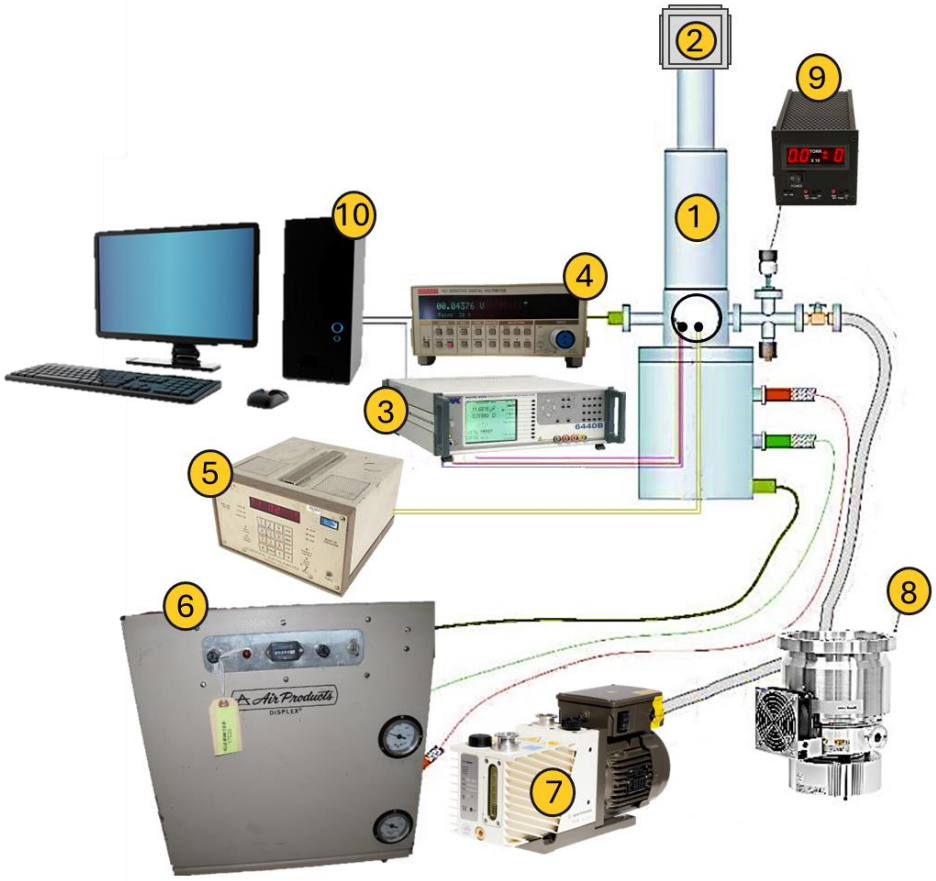


Figure 3-29: Low-temperatures dielectric spectroscopy test stand: 1 – helium cryostat head, 2 – vacuum chamber with sample holder - cryostat, 3 - precision component analyzer, 4 - digital voltmeter, 5 - temperature controller, 6 - compressor of helium cryostat, 7 – rotary vacuum pump, 8 — turbomolecular vacuum pump, 9 – pressure vacuum gauge, 10 – computer with software controller. Adapted from reference [198].

3.9. Optic characterization by Second Harmonic Generation

Second Harmonic Generation (SHG) has emerged as a potent tool for studying the symmetry properties of non-centrosymmetric structures [199]. While bulk crystals have been extensively studied for ferroic states, the exploration of thin films presents unique challenges and opportunities. Reviews in the

literature provide comprehensive insights into SHG and its potential for probing ferroic states in bulk crystals [200, 201].

Optical SHG becomes particularly powerful at surfaces and interfaces, where the inversion symmetry is broken by a polar distortion [202]. This technique has been instrumental in probing various aspects of surface and interface physics, including molecular absorption, surface electric states, and magnetic domain structures [203, 204]. Additionally, it has found applications in studying epitaxially grown thin films, such as strain-induced ferroelectricity and electro-optic responses [205–207]. Complementing scanning probe microscopy techniques, optical SHG offers a non-invasive, contact-free method to probe the entire volume of thin film structures, including buried layers in heterostructures.

The phenomenon of SHG involves the frequency doubling of a light wave, with emission dependent on the crystal's point group symmetry. SHG is present on non-centrosymmetric structures, making it well-suited for probing ferroic order [200, 208, 209]. Furthermore, it can detect coexisting ferroic states, as seen in multiferroics [202, 210].

The second harmonic measurements were conducted utilizing the layout presented in reference [211] at the Centro de Física da Universidade do Minho - Campus de Gualtar. Here, a mode-locked Ti:sapphire laser (model: Mira, Coherent Inc., Santa Clara, CA, USA) was used with a central wavelength of 800 nm. Despite the Fourier limit of the pulse duration being approximately 85 fs, the duration extended to approximately 120 fs upon incidence on the sample, with a pulse repetition rate of 76 MHz and a FWHM of 12 nm, due to the combined effects of the calcite polarizer and the microscope objective. Typically, the incident energy per pulse was around 0.66 nJ. The generated second harmonic light was measured in reflection, as illustrated in Figure 3-30. To control the incident polarization, a calcite Glan–Taylor polarizer followed by a zero-order half-wave plate was employed. Focusing the beam onto the samples was achieved through a Nikon CFI Plan Fluor ×10 objective, while a *xyz* translation stage ensured precise positioning of the samples in the focal plane with micrometer accuracy. After passing through a dichroic mirror (Thorlabs DMLP650) and a narrow band-pass filter (Thorlabs FBH400-40 nm), the signal was focused by a short focal length lens to an optical fiber bundle (30 cm length) coupled to a spectrograph (model: Shamrock 300i, Andor Technology Belfast, UK) and integrated over a 60 s time window on a cooled CCD array (model: Andor Technology Belfast, Newton, UK).

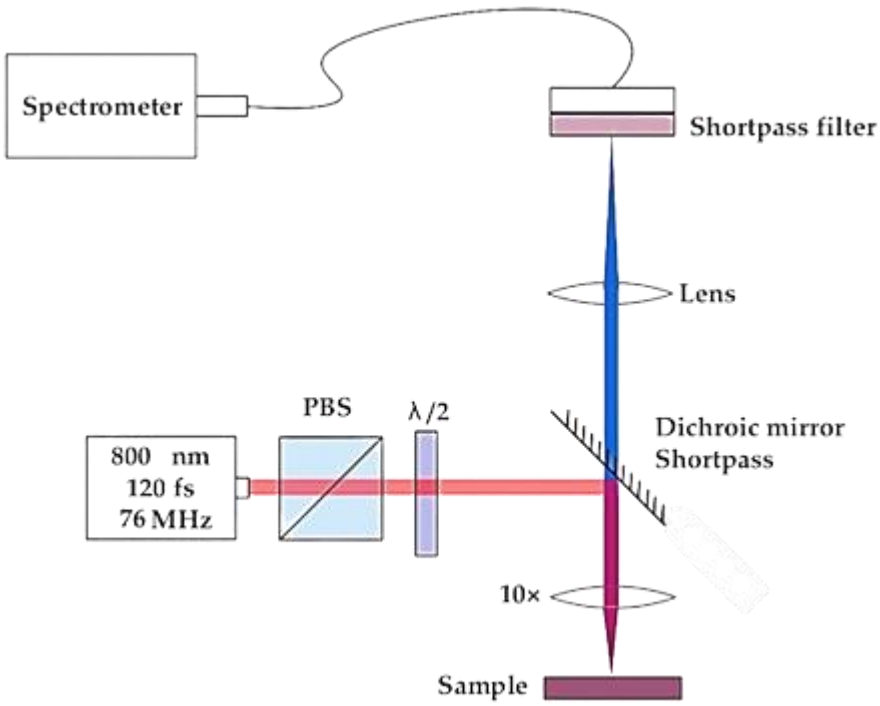


Figure 3-30: Layout of the second harmonic microscope. PBS represents the polarized beam splitter, and λ/2 denotes the half-wave plate.

For signal acquisition, the sample was positioned perpendicular to the laser beam, and the surface was scanned to locate the most intense SHG signal. Since the sample may present some crystalline organization, resulting in SHG polarization-dependent magnitude, the signal was maximized by rotating the direction of the incident polarization, using the half-waveplate. Once a position with a significant signal was found, the time accumulated spectra was taken.

3.10. Density Functional Theory

Density Functional Theory (DFT) is a prominent quantum mechanical method in physics and chemistry that allows for in-depth analysis of the electronic structure in complex systems, from atoms and molecules to condensed phases. Developed on the idea that all essential properties of an electronic system in its ground state can be represented solely by its electron density, DFT streamlines the many-body problem and has become essential in materials science [212]. Today, it is widely applied to predict atomic behaviors, often without relying on experimental parameters [43].

Through DFT, the system's ground state energy is calculated as a function of electron density, which enables valuable insights into electronic interactions, energy levels, and the magnetic and dielectric characteristics of materials [213]. This method finds a range of applications, from exploring electronic properties in organic and inorganic chemistry to modeling semiconductors and other electronic materials

[214]. By incorporating spin degrees of freedom, DFT can also describe magnetic systems, while relativistic adjustments extend their use to studying unique phenomena like superconductivity. A major advantage of DFT is its predictive strength, as it allows for the theoretical exploration of new materials and molecules ahead of physical synthesis. This capability often narrows down experimental options, saving time and resources, especially with intricate or potentially hazardous materials.

For the calculations performed in this work, the computational package VASP (Vienna Ab-initio Simulation Package) was used [215, 216], employing the PBEsol functional (Perdew-Burke-Ernzerhof for solids), which is adjusted to enhance the accuracy of lattice interactions in solids. The energy cutoff was set at $E_{cut} = 600$ eV, with Hubbard U corrections applied to correctly address the localization of d-electron states. To accommodate the structural peculiarities and anisotropy of $Ca_3Mn_2O_7$, different sampling points in reciprocal space were used: a Γ-centered grid of 5×5×4 for unit cell calculations and 2×2×3 for supercell calculations. The force convergence was configured to achieve a limit of 10 meV/Å, ensuring that the optimized structures accurately represented the equilibrium conditions of the system. Furthermore, the structural models for property simulations in $A_{1-x}B_x$ alloys were based on the concept of Special Quasirandom Structures (SQS) [217], which mimic the radial correlations of a perfectly random structure. This method allows for more accurate modeling of the optical and thermodynamic properties of semiconductor alloys, benefiting from local density formalism for a refined description of electronic interactions in random systems.

To study the presence of the magneto-elastic coupling effect in $Ca_3Mn_2O_7$ three distinct magnetic orderings of the *A2₁am* phase were considered: ferromagnetic (FM), antiferromagnetic type-G (AFM-G), antiferromagnetic type-C (AFM-C), represented in Figure 3-31 respectively.

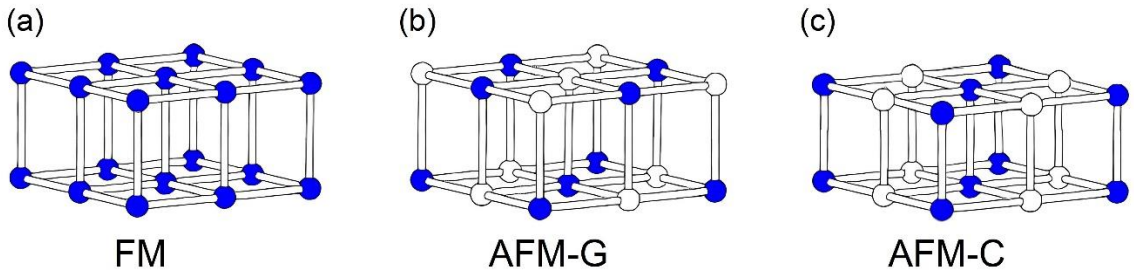


Figure 3-31: Schematic representations of the Mn spin arrangements in the (a) FM, (b) the AFM-G, and (c) AFM-C states of $Ca_3Mn_2O_7$. Dark blue and white open spheres refer to up- and down-spin alignments, respectively. Adapted from reference [218].

Consider a generalized Ising model Hamiltonian with the following matrix elements:

$$H_i = \sum_{k=1,2} (z_k^{\uparrow\uparrow} - z_k^{\uparrow\downarrow}) J_k S_i S_k \tag{3-8}$$

where H_i is the Hamiltonian for the i-th atom, the index k accounts for all 1st and 2nd neighbors with corresponding magnetic coupling constant J_k, $z_k^{\uparrow\uparrow}$ and $z_k^{\uparrow\downarrow}$ denote the number of neighbors whose spins are aligned in a parallel and anti-parallel way compared to the i-th atom. The coupling constants J_1 and J_2, are associated with the nearest neighbor (NN) and next-nearest neighbor (NNN), respectively, and can be calculated by comparing the relative energies between magnetic orderings. By comparing the relative energies for the different magnetic orderings, the following expressions for J_1 and J_2 is obtained [218]:

$$J_1 = \frac{E_{AFM-G} - E_{FM}}{5S^2 k_B}, \tag{3-9}$$

$$J_2 = \frac{E_{AFM-C} - E_{FM}}{4S^2 k_B} - J_1. \tag{3-10}$$

S can be fully derived from DFT using the relationship $\mu = 2S$, μ being the magnetic moment, however, for simplicity, a value of $S = 5/2$ was adopted [218]. In the mean-field approximation (MFA) [161, 219, 220] the transition temperature between the AFM and PM phases for the calculated J_1 and J_2 can be approximated as:

$$T_N = \frac{S(S+1)}{3} \sum_{k=1,2} \left(z_k^{\uparrow\uparrow} - z_k^{\uparrow\downarrow}\right) J_k = \frac{S(S+1)}{3S^2 k_B} (E_{AFM-G} - E_{FM}) \tag{3-11}$$

This work employs DFT to explore the interplay between the magnetic and dielectric properties of $Ca_3Mn_2O_7$ under varying strain conditions, both positive and negative. The analysis tries to clarify how structural changes and crystal orientation influence the antiferromagnetic transition temperature.

4. Calcium Manganese Oxides Thin Films: Influence of Deposition Parameters on Magnetic and Dielectric Properties

Chapter 4 focuses on the synthesis and characterization of $Ca_3Mn_2O_7$ (CMO) thin films, highlighting the influence of deposition parameters on their magnetic and dielectric properties. The ability to form film-on-substrate structures provides precise control over the magnetization and polarization [26, 27], essential for device applications. These structures are characterized by well-defined strain states and interfaces, which are crucial for tuning the functional properties of the films.

The chapter begins with an overview of thin film synthesis, detailing the methods employed to produce $Ca_3Mn_2O_7$ thin films. Following this, the structural and morphological characterization section explores the physical attributes of the films, employing techniques such as Raman spectroscopy and Second Harmonic Generation to assess their crystallinity and phase behavior. The chapter then progresses to examine the magnetic characterization of the films, providing insights into their magnetization behavior, before concluding with an assessment of their dielectric properties. Finally, the chapter concludes with a section on Density Functional Theory, which complements the experimental findings by providing theoretical insights into the electronic structure and properties of the $Ca_3Mn_2O_7$ thin films.

4.1. Thin film synthesis

To obtain high-quality $Ca_3Mn_2O_7$ thin films and study the influence of the deposition conditions on the structure, a set of thin films was deposited on (100) $SrTiO_3$ and Nb-doped (100) $SrTiO_3$ ($SrTiO_3$:Nb) substrates by pulsed laser deposition, changing the deposition parameters, such as deposition temperature, oxygen pressure, laser fluence, target-substrate distance and influence of post-deposition annealing.

The $SrTiO_3$ (STO) substrates were used since they tend to promote oriented film growth of perovskite materials akin to $Ca_3Mn_2O_7$ thanks to the similar crystal structures. However, despite this structural compatibility, there is a significant lattice mismatch between the $Ca_3Mn_2O_7$ films and the $SrTiO_3$ substrates. The $SrTiO_3$ substrate has a cubic structure with a lattice parameter of 3.905 Å [221]. In contrast, the $Ca_3Mn_2O_7$ films exhibit an orthorhombic structure with lattice constants of 5.23954 Å (a-axis), 5.23840 Å (b-axis) for the $A2_1am$ phase and 5.21189 Å (a and b axes) for the *Acaa* phase at 300 K [18]. As the

diagonal of the STO cube is 5.521 Å the rotated growth of the CMO film, relative to the substrate, gives a lattice mismatch of ~ 5%.

The films stoichiometry, in particular the Ca/Mn relative concentration, depends on the oxygen pressure, where the different mean free paths of the elements in the plume, due to the different masses of the elements, can lead to different relative concentrations of the materials arriving at the substrate during deposition [222, 223]. Their stoichiometry also depends on laser fluence, since, along with the forward-directed stoichiometric plume, there is an evaporative component of the ablated material. This latter component contributes more at lower fluences and can induce different Ca/Mn relative concentrations, compared to the target, due to different Ca and Mn vaporization temperatures [223, 224]. Additionally, the crystallinity of the films and stabilized phases depend on the deposition temperatures and post-deposition annealing procedures.

The calcium manganese oxide thin films were prepared on (100) $SrTiO_3$ and Nb-doped (100) $SrTiO_3$ substrates, simultaneously. The 1.4 at% niobium doping of the (100) $SrTiO_3$:Nb substrates makes them more conductive, allowing their use in dielectric measurements, while their crystalline properties remain the same as in (100) $SrTiO_3$. The films were produced by laser ablation with a KrF excimer laser (wavelength $\lambda = 248$ nm) in the ablation system described in the reference [225]. In each run, the (100) $SrTiO_3$ and (100) $SrTiO_3$:Nb substrates were placed side-by-side on the substrate holder. The repetition rate was 6 Hz, the target-substrate distance was 3-6 cm and the laser energy was 250, 400 and 600 mJ/pulse, corresponding to fluences of 1.4, 2.3 and 3.4 J/cm^2, respectively. The oxygen pressure during film preparation ranged from 10^{-2} to 10^{-1} mbar, while the substrate temperature ranged from room temperature to 730 °C. To avoid under-oxidation of the samples, they were cooled to room temperature after deposition, at a rate of 10 °C/min, in an oxygen atmosphere and at room pressure [225, 226]. After deposition, the films were annealed at temperatures between 700 °C and 900 °C for 2 hours, in air. The heating rate to achieve these temperatures was 10 °C/min.

For the laser ablation targets, polycrystalline samples of $Ca_3Mn_2O_7$ were prepared by the solid-state reaction method. Stoichiometric amounts of $CaCO_3$ (99.0%; Sigma-Aldrich) and MnO_2 (99.99%; Sigma-Aldrich) were used as starting materials. The mixture was calcinated for 3 h at 1123 K in air. Three more steps of grinding and subsequent annealing during 12 h at 1648 K were performed. Single phase purity was confirmed by Le Bail refinement on powder X-ray diffraction data collected with a Rigaku smartlLab diffractometer, as described in the reference [18]. Table 4-1 presents the deposition conditions used to produce the samples.

Table 4-1: Deposition laser conditions of the thin films on (100) $SrTiO_3$ substrates and the respective post-deposition annealing conditions at atmospheric pressure.

Sample	Pulsed laser deposition				Post-annealing	
	T (°C)	O_2 Pressure (mbar)	Laser fluence (J/cm²)	$d_{target-sub}$ (cm)	T (°C)	t (h)
CMO2	700	0.05	2.3	4.5	N/A	N/A
CMO4	700	0.1	1.1	4.5	N/A	N/A
CMO5	725	0.1	1.1	4.5	N/A	N/A
CMO6	700	0.05	2.3	4.5	N/A	N/A
CMO7	732	0.01	2.3	4.5	N/A	N/A
CMO8	731	0.01	2.3	6	N/A	N/A
CMO9	728	0.01	3.4	6	N/A	N/A
CMO10	RT	0.01	3.4	6	730	2
CMO11	RT	0.01	3.4	6	730	10
CMO12	RT	0.01	3.4	3	730	2
CMO14	700	0.01	3.4	6	900	2
CMO15	700	0.01	3.4	6	800	2

4.2. Structural and morphological characterization

Figure 4-1 shows the X-ray diffraction measurements performed on the CMO films prepared with different deposition temperatures, laser fluences, oxygen pressures and target-substrate distances. No annealing was done on these samples. In Figure 4-1, the vertical black and green lines indicate the X-ray diffraction peak positions of the $SrTiO_3$ substrate, with the cubic $Pm\bar{3}m$ structure (ICDD card number 35-734), and $CaMnO_3$ with the *Pnma* orthorhombic structure [227]. Similarly, Figure 4-2 shows the X-ray diffraction measurements performed on the CMO films prepared with different deposition temperatures, oxygen pressures and target substrate distances, but with high pulse energies (high fluences) and with an annealing step after deposition. The vertical red and blue lines indicate the peak positions of $Ca_3Mn_2O_7$ with the *Acaa* orthorhombic structure [228] and of the ferroelectric $A2_1am$ orthorhombic structure [229], respectively.

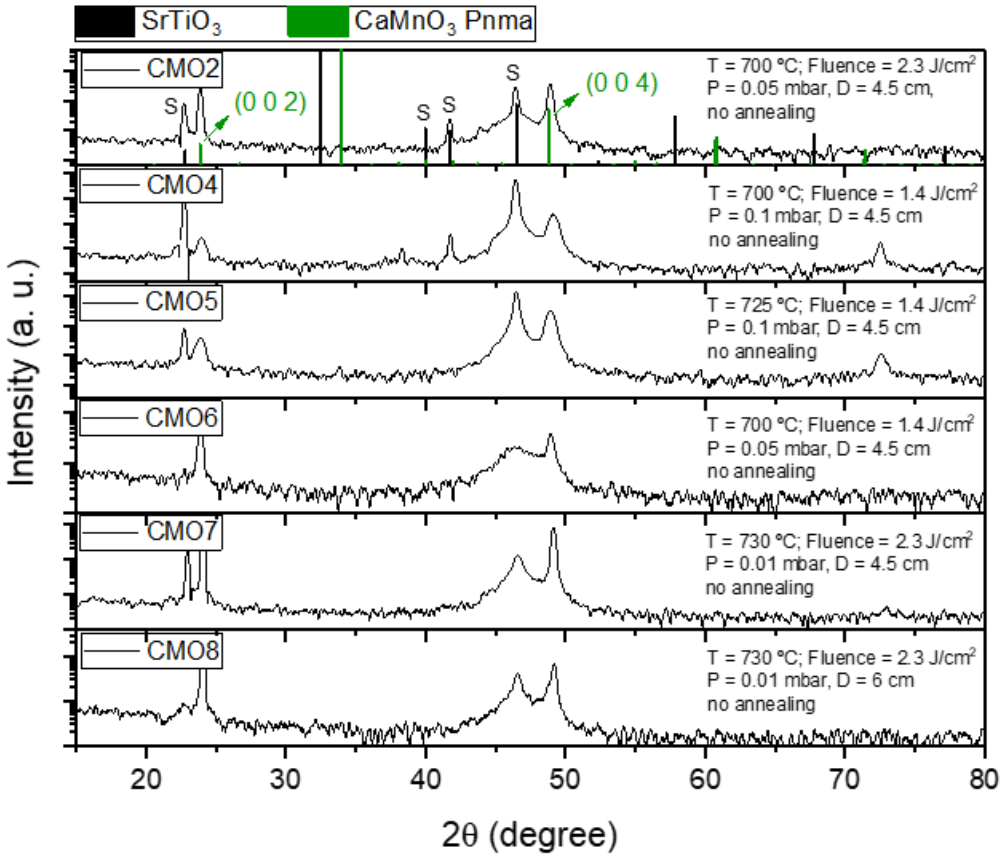


Figure 4-1: X-ray diffraction spectra measured on the samples prepared with different oxygen pressures and deposition temperatures. The peaks marked with "S" are from the substrate. The green lines mark the reference diffraction peaks of the $CaMnO_3$ *Pnma* phase.

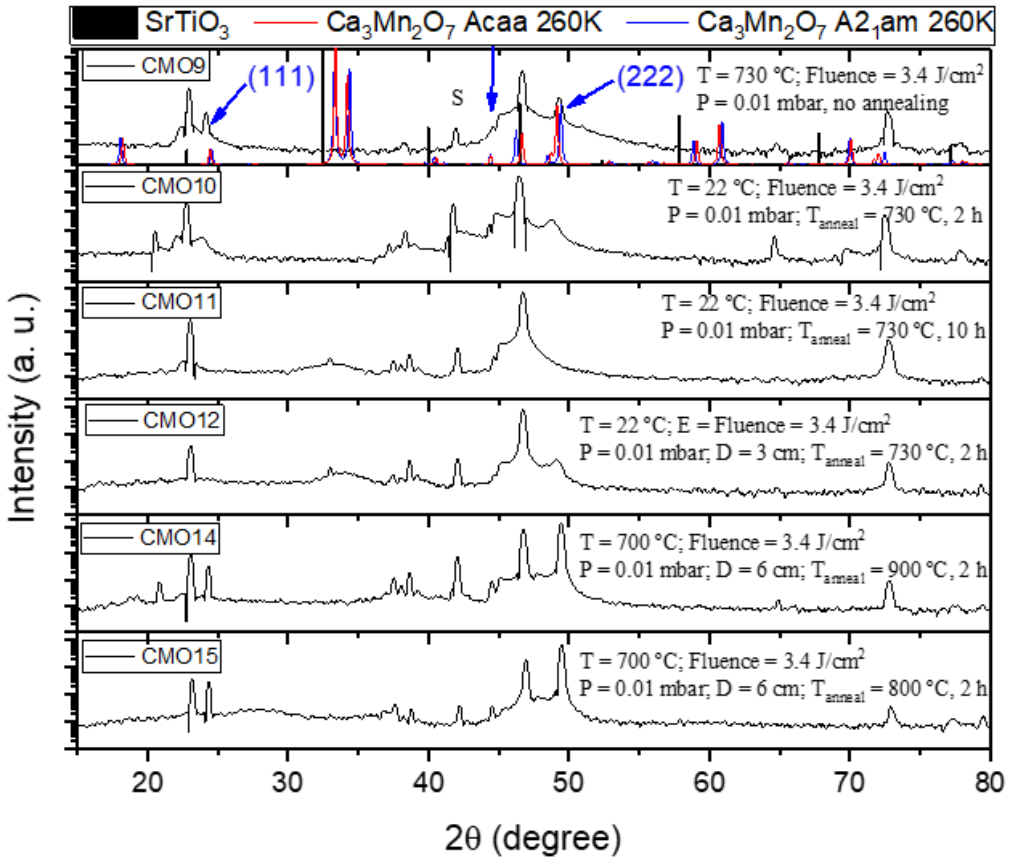


Figure 4-2: X-ray diffraction spectra measured in the samples prepared with different oxygen pressures and deposition temperatures, but with higher laser pulse energies (high fluences) and with an annealing step after deposition. The peaks marked with "S" are from the substrate. The red and blue patterns were obtained on bulk $Ca_3Mn_2O_7$ powder samples with *Acaa* or *A2₁am* phases, respectively. The blue arrows mark the corresponding peaks observed in the films.

Figure 4-3 (a) and Figure 4-3 (b) show SEM micrographs obtained from samples CMO10 and CMO14**,** respectively. They were chosen, since their preparation conditions already indicated the presence of the desired $Ca_3Mn_2O_7$ phase, as obtained from the X-ray diffraction (XRD) and X-ray energy dispersive spectrometer (EDS) results. Both samples were produced under the same conditions, except for the deposition and post-annealing temperatures. The sample CMO10 (Figure 4-3 (a)) was deposited with the substrate at room temperature and subsequently annealed at 730 °C. On the other hand, the sample CMO14 (Figure 4-3 (b)) was deposited with the substrate at 730 °C and annealed at 900 °C for 2 h. As depicted in Figure 4-3 (a), the film deposited and annealed at lower temperatures presents a granular surface with an average grain size of 81 nm, determined from the SEM micrographs. However, for higher deposition and annealing temperatures, the surface becomes progressively smoother, as seen in Figure 4-3 (b). Figure 4-3 (c) shows the FIB-SEM cross-section for the CMO14 sample prepared with 50 minutes of deposition time (sample shown in Figure 4-3 (b)). The thickness of the film is uniform along the

sample's area, showing some slight local variation attributable to roughness, giving an average thickness of approximately 298 nm. This gives a ~ 6.1 nm/min deposition rate. The sample presents a columnar growth morphology with column width between 65 and 120 nm as shown in Figure 4-3 (d).

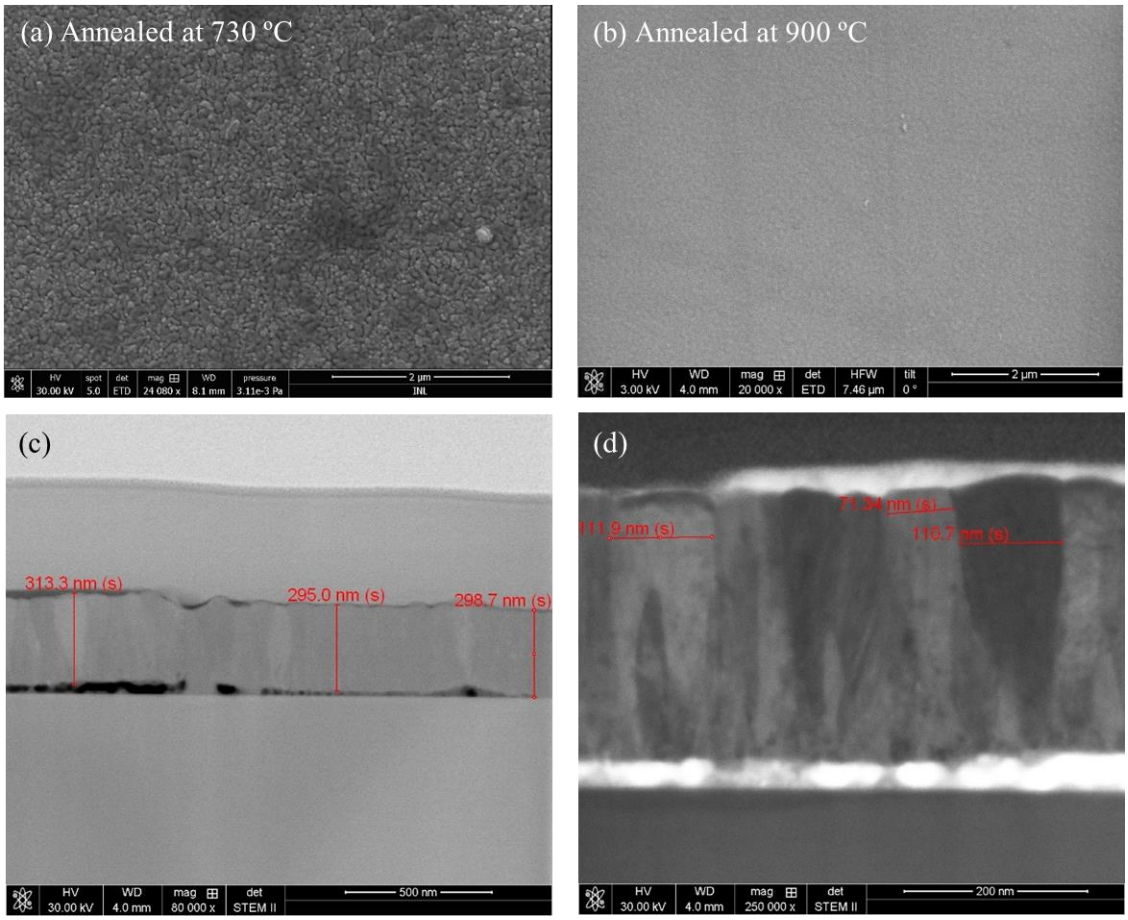


Figure 4-3: Scanning electron microscopy (SEM) micrographs of the surface of the samples: (a) CMO10 deposited at room temperature and annealed at 730 °C and (b) CMO14 deposited at 700 °C and annealed at 900 °C. (c)-(d) Corresponding FIB-SEM cross-section micrographs of sample CMO14, which was presented in (b).

To further explore the chemical and stoichiometric properties of the films and to understand the conditions for the stabilization of the phases, EDS was performed on the prepared films. The EDX spectra of the CMO10 and CMO14 samples are depicted in Figure 4-4**.** In the EDX of Figure 4-4, besides oxygen, the spectra present Sr and Ti due to the $SrTiO_3$ substrate, as expected. Additionally, peaks corresponding to Ca and Mn are also observed as a result of the deposited thin films. No other elements were found indicating a high purity level of the samples.

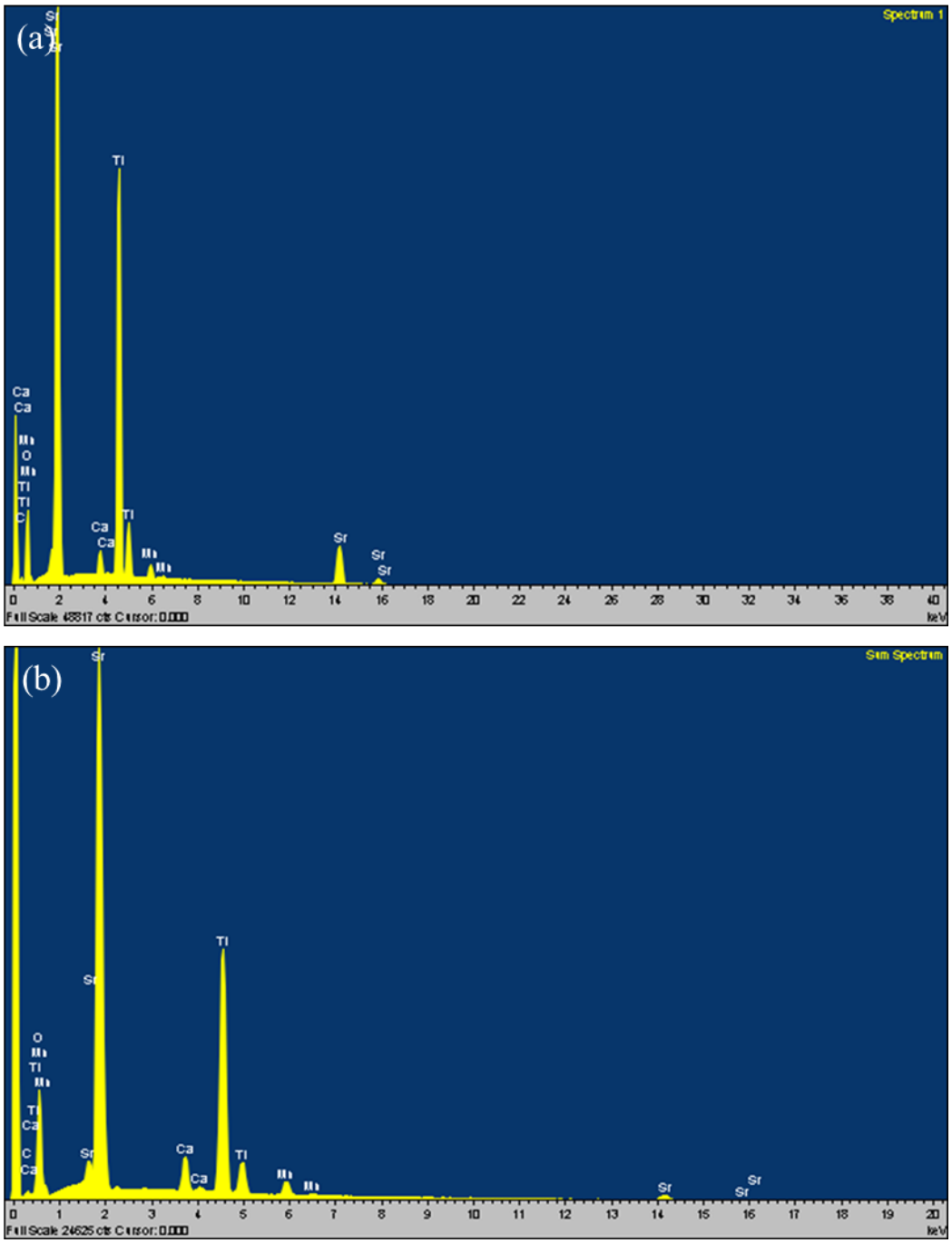


Figure 4-4: Energy-dispersive X-ray spectroscopy (EDX) spectrum measured in samples (a) CMO10 and (b) CMO14.

Combining the XRD results obtained from the samples with different deposition conditions (Figure 4-1 and Figure 4-2) and the chemical information obtained from the EDX characterization (Figure 4-4), the values of the preparation parameters that led to stabilized phases were determined. The Ca/Mn atomic percentages, determined from the EDX results for the samples with higher laser fluences (2.3 and 3.4 J/cm^2) are shown in Figure 4-5 (a). For $CaMnO_3$, the Ca/Mn ratio is expected to be 1 (1:1 Ca:Mn) and for $Ca_3Mn_2O_7$ the ratio is 1.5 (3:2 Ca:Mn). The evolution of the Ca/Mn relative concentration was

observed to be strongly dependent on the laser fluence and the post-annealing temperatures, as shown in Figure 4-5 (a). For low oxygen pressures and without annealing, as the laser fluence increases, the Ca/Mn relative percentage starts to increase from approximately 1:1, in $CaMnO_3$, towards the 3:2 proportion as expected from the stabilization of phases with $Ca_3Mn_2O_7$. Nevertheless, the obtained XRD and EDX results indicate the coexistence of the $CaMnO_3$ and $Ca_3Mn_2O_3$ phases in these non-annealed samples at high fluence.

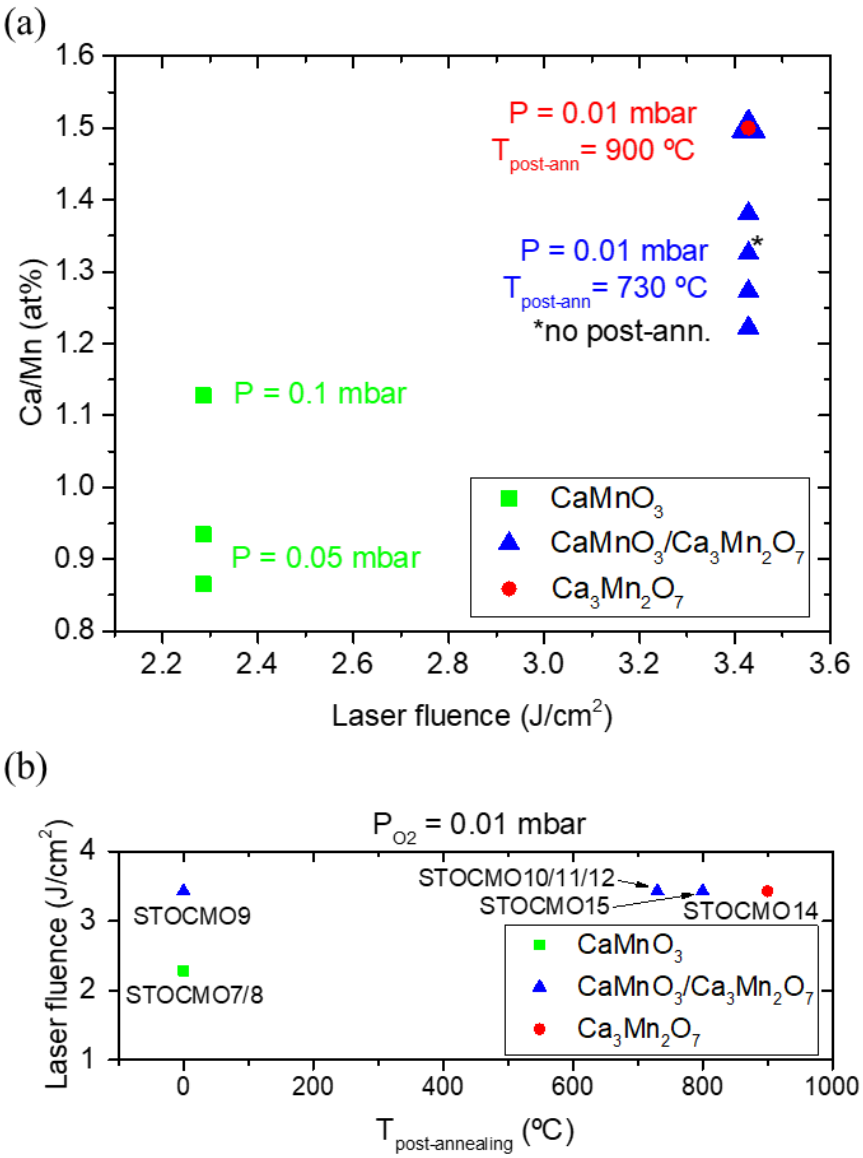


Figure 4-5: (a) Ca/Mn atomic ratio represented as a function of the laser fluence applied during the film deposition. (b) The corresponding stabilized phases as a function of the laser fluence and annealing temperature, as obtained from the XRD and EDX results.

The further evolution towards 3:2 is due to the post-deposition annealing step. Figure 4-5 (b) shows the obtained phases, identified from the XRD observed structures and EDX relative Ca/Mn percentage

compositions, indicating that, as the annealing temperature increases, the $Ca_3Mn_2O_7$ becomes progressively the majority phase, so that for T_{anneal} = 900 °C only the $Ca_3Mn_2O_7$ phases are present in the films (CMO14 sample).

Considering the results presented above, using a 700 °C deposition temperature, a 0.01 mbar oxygen pressure, and a laser fluence of 3.4 J/cm^2 and performing post-deposition annealing in air, at 900 °C, for 2 hours, led to laser-ablated CMO thin films on $SrTiO_3$ substrates, with the $Ca_3Mn_2O_7$ stoichiometry.

In the X-ray diffraction results of Figure 4-2, two main $Ca_3Mn_2O_7$ XRD peaks are observed corresponding to the (111) and (222) atomic planes. This indicates that the $Ca_3Mn_2O_7$ films have grown oriented, presenting the [111] direction perpendicular to the substrate plane. However, the presence of the small (206) peak in the XRD patterns of Figure 4-2, at $2\theta \sim 44.5^{\circ}$, indicates a slight degree of polycrystallinity. Since the *Acaa* phase of $Ca_3Mn_2O_7$ is pseudo-tetragonal [17, 18] the observed peaks were used to calculate the lattice parameters using this phase as a reference (for the *A2$_1$am* an extra peak with a different orientation would be needed). The lattice parameters obtained from the X-ray diffraction peaks observed in the CMO14 film are presented in Table 4-2 along with the reference *Acaa* room temperature phase, for comparison. A distortion is observed to occur along the *c* axis where a contraction strain was observed, compared to the reference. On the other hand, the *a* and *b* axes tend to be larger than those of the bulk. As the polarization of the ferroelectric phase of $Ca_3Mn_2O_7$ is along the *a* axis [17], the observed distortions indicate that the interfacial substrate/film strain induced on the $Ca_3Mn_2O_7$ films deposited on the $SrTiO_3$ substrates promotes the formation of the polar distortion, enhancing the stabilization of the ferroelectric phase of $Ca_3Mn_2O_7$.

Table 4-2: Lattice parameters of the CMO14 thin film with the $Ca_3Mn_2O_7$ phase. Reference values taken from reference [18].

Phase	**Lattice parameters**				
	Parameter	Obtained (Å)	*Acaa* reference (Å)	Deformation strain along growth direction (*Acaa*)	*A2$_1$am* reference (Å)
$Ca_3Mn_2O_7$	a	5.31	5.21189	2.0 %	5.23954
	b	5.31	5.21189	2.0 %	5.23840
	c	19.0	19.59600	-3.0%	19.42711

4.3. Raman Spectroscopy

To further understand the structure and phases of the deposited films, Raman spectroscopy was performed on the prepared $Ca_3Mn_2O_7$ samples at room temperature (T_{RT} = 290 K). Raman spectroscopy yields phonon parameters that reflect the local crystal symmetry, which can indicate structural distortions of the unit cell. Figure 4-6 shows the Raman spectra of sample CMO14. The observed Raman modes are identified by B and P symbols according to the notation in reference [182]. The B modes are attributed to the *Acaa* structure, normally stabilized in $Ca_3Mn_2O_7$ at intermediate temperatures, while the P modes are due to the polar *A2₁am* low-temperature $Ca_3Mn_2O_7$ phase. There is some degree of overlap between the modes of *Acaa* and *A2₁am* structures, as the phonon energies anticipated for the *A2₁am* and *Acaa* symmetries are nearly degenerate [182]. However, the modes due to the *Acaa* and *A2₁am* (ferroelectric) structures are visible in Figure 4-6**.** This indicates the coexistence of the ferroelectric *A2₁am* and orthorhombic *Acaa* phases at room temperature, which has also been observed in bulk $Ca_3Mn_2O_7$ crystals/ceramics [1, 3, 18].

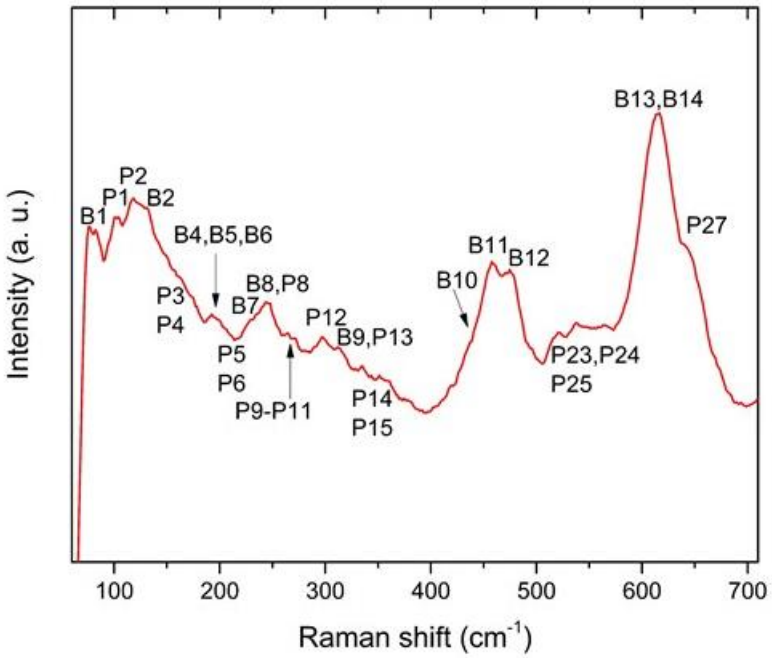


Figure 4-6: Raman spectrum of the CMO14 sample showing the *A2₁am* (marked with P) and *Acaa* (marked with B) modes.

4.4. Second Harmonic Generation

The Second Harmonic Generation (SHG) analysis was performed to confirm the non-centrosymmetric properties of the $Ca_3Mn_2O_7$ thin film. Thus, a thin film of approximately 300 nm of $Ca_3Mn_2O_7$ (SiCMO-300) was deposited on a silicon substrate under the same conditions as the previously mentioned sample CMO14. The choice of a Si substrate ensures that there is no contribution to the SHG signal from the substrate itself, as silicon is centrosymmetric and does not generate SHG [230].

Figure 4-7 shows the SHG spectrum obtained from sample SiCMO-300. As expected, light was detected over a small wavelength centered at half the incident beam's wavelength of 800 nm. The result is consistent with the presence of a non-centrosymmetric phase. For $Ca_3Mn_2O_7$, there are two distinct phases near room temperature, with space groups *Acaa* and *A2₁am* [18]. The *A2₁am* phase is non-centrosymmetric and polar, while crystals with *Acaa* symmetry are centrosymmetric, SHG is forbidden by symmetry in the *Acaa* phase [231]. Therefore, the SHG signal observed at 400 nm indicates that the non-centrosymmetric *A2₁am* phase is present in the film. The observed uniformity of the SHG signal across the sample suggests a consistent, homogeneous *A2₁am* phase distribution in the thin film.

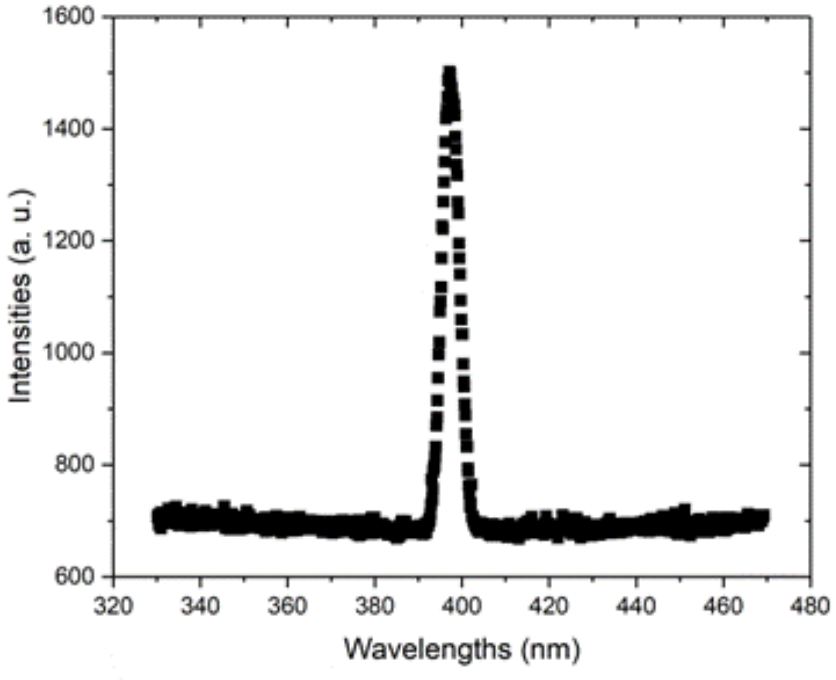


Figure 4-7: Second Harmonic Generation response of $Ca_3Mn_2O_7$ 300 nm-thick thin film over Si substrate.

4.5. Magnetic Characterization

The magnetic properties of the CMO11, CMO12 and CMO14 samples were measured using a superconducting quantum interference device, SQUID, to investigate the magnetic properties of the samples, specifically to identify the presence of magnetic transitions, such as canted antiferromagnetic (AFM) ordering characteristic of the $Ca_3Mn_2O_7$ phase. This measurement is crucial as it provides insight into the material's magnetic behavior as a function of temperature, which is essential for understanding its potential as a multiferroic nanostructured thin film. Identifying these transitions helps determine the optimal preparation conditions for producing materials with desirable magnetic properties.

Figure 4-8 presents the temperature dependence of the magnetization (M(T)) under a 2500 Oe field. The M(T) curves show that CMO11 and CMO12 samples have a large paramagnetic component (seen by the Curie type curve, C/T, at low temperatures), added to a diamagnetic background attributed to the $SrTiO_3$ substrate. To determine the transition temperature, the minimum of the 1st derivative of M(T) was used. In the CMO14 sample, a transition with $T_N \approx 112$ K was found (see Figure 4-9), close to the canted antiferromagnetic transition temperature reported in bulk $Ca_3Mn_2O_3$, $T_N \sim 112.5$ K [70].

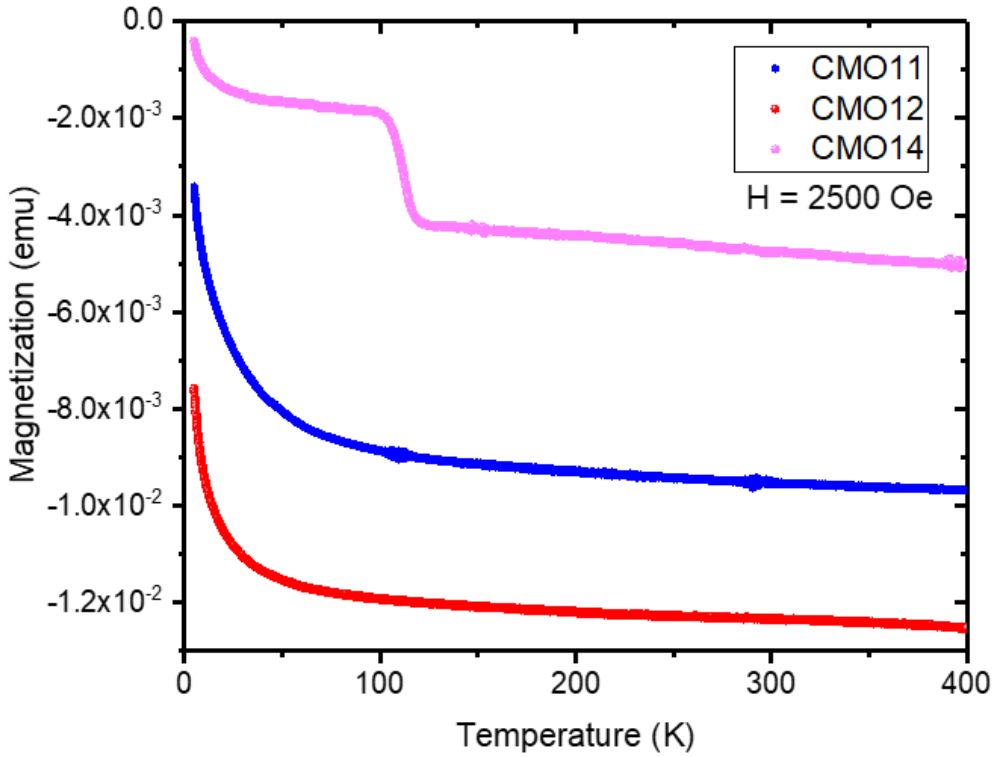


Figure 4-8: Temperature-dependent magnetization of CMO11, CMO12 and CMO14 samples, under an applied magnetic field of 2500 Oe.

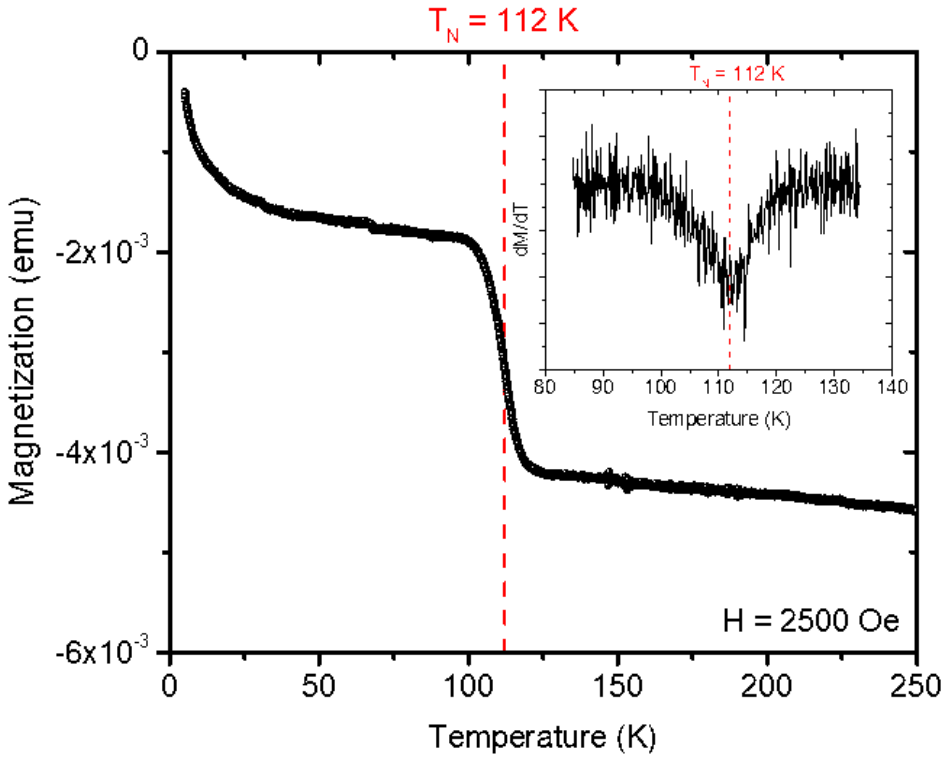


Figure 4-9: Temperature-dependent magnetization of sample CMO14, under 2500 Oe, showing an AFM transition with T_N = 112 K in CMO14 sample, obtained through the derivative of magnetization as a function of temperature (dM/dT graph) (inset).

Among these three samples, sample CMO14 stood out by exhibiting the typical canted antiferromagnetic transition of the $Ca_3Mn_2O_7$ material. This transition is of particular interest due to its potential applications in technological devices, such as magnetic storage and sensors. The antiferromagnetic transition observed in sample CMO14 is crucial for the development of advanced materials with tunable magnetic properties, making CMO14 a key sample for further investigation and potential application. The successful identification of this transition in CMO14 validates the synthesis and characterization methods used. Thus, as previously indicated by structural spectroscopic characterizations, it is established that the preparation conditions used for CMO14 are a guide for producing thin films of $Ca_3Mn_2O_7$ with the characteristic antiferromagnetic transition.

4.6. Dielectric Characterization

The dielectric properties are sensitive to polar order/disorder and cooperative polar behavior present in a material, thus, to understand the influence of substrate strain on electric polarization and coupled magnetic-electric behavior, the electrical properties of $Ca_3Mn_2O_7$ thin films need to be studied. Since the sample CMO14 was prepared on $SrTiO_3$ substrate, it does not directly allow dielectric measurements due

to the non-conductive nature of the thin film base. For that, a new thin film was deposited on conductive niobium-doped strontium titanate substrates ((100) $SrTiO_3$:Nb) under the same conditions used to produce sample CMO14. Figure 4-10 shows the SEM cross-section of the newly produced sample, named cCMO-305. The film maintains a consistent thickness across the sample area, with minor local variations caused by surface roughness, leading to an average thickness of approximately 305 nm.

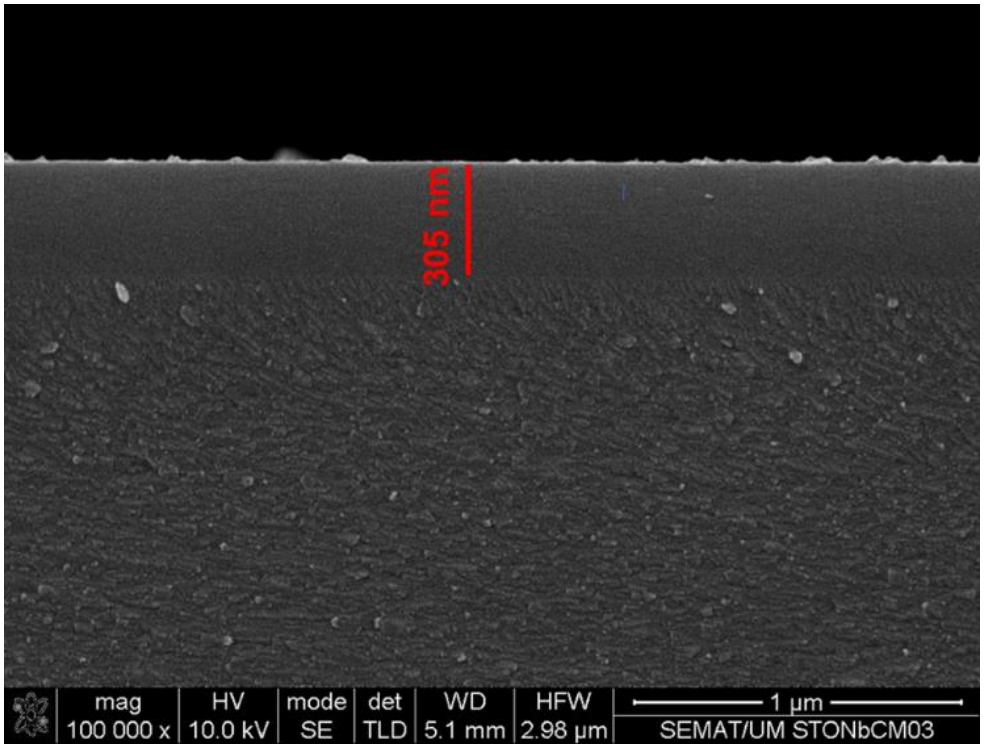


Figure 4-10: SEM cross-section micrographs of sample CMO-305.

The dielectric properties of sample CMO-305 were characterized by impedance spectroscopy, in the temperature interval 30-295 K (the region of expected stabilization of the ferroelectric phase [18]) and in the frequency range of 20 Hz – 3 MHz. To perform the measurements, the samples were connected, forming a parallel plate capacitor included in an LCR network. To form the capacitor, the $SrTiO_3$:Nb substrate was used as the bottom electrode while the top electrode was a small circular air-cured silver paint contact with approximately 1 mm in diameter. A Wayne Kerr 6440A precision component analyzer, together with a dedicated computer and software, was used to acquire the data. Shielded test leads were employed to avoid parasitic impedances due to the connecting cables. The temperature was controlled using a Scientific Instruments INC Series 5500-5 temperature gauge**,** and temperature-dependent measurements were performed at a rate of 2 K/min.

Figure 4-11 (a) shows the temperature-dependent real part of the electrical permittivity at different frequencies. A sharp frequency-dependent step-like change is noted, with decreasing temperature, due to increased polar interactions in the ferroelectric phase at low temperatures. Figure 4-11(b) shows the

temperature-dependent imaginary part of the permittivity at the same frequencies for the CMO-305 sample. Here, a peak that shifts to a higher frequency with increasing temperature is visible, suggesting a thermally activated behavior. The peak maximum coincides with the inflection point in the corresponding $\varepsilon'(T)$ curves indicating an intrinsic polar relaxation behavior [17]. In addition, the low values of the loss tangent, with $\tan\delta < 1$, indicates a small contribution of conductivity, due to free charge carriers [232] to the permittivity of the films.

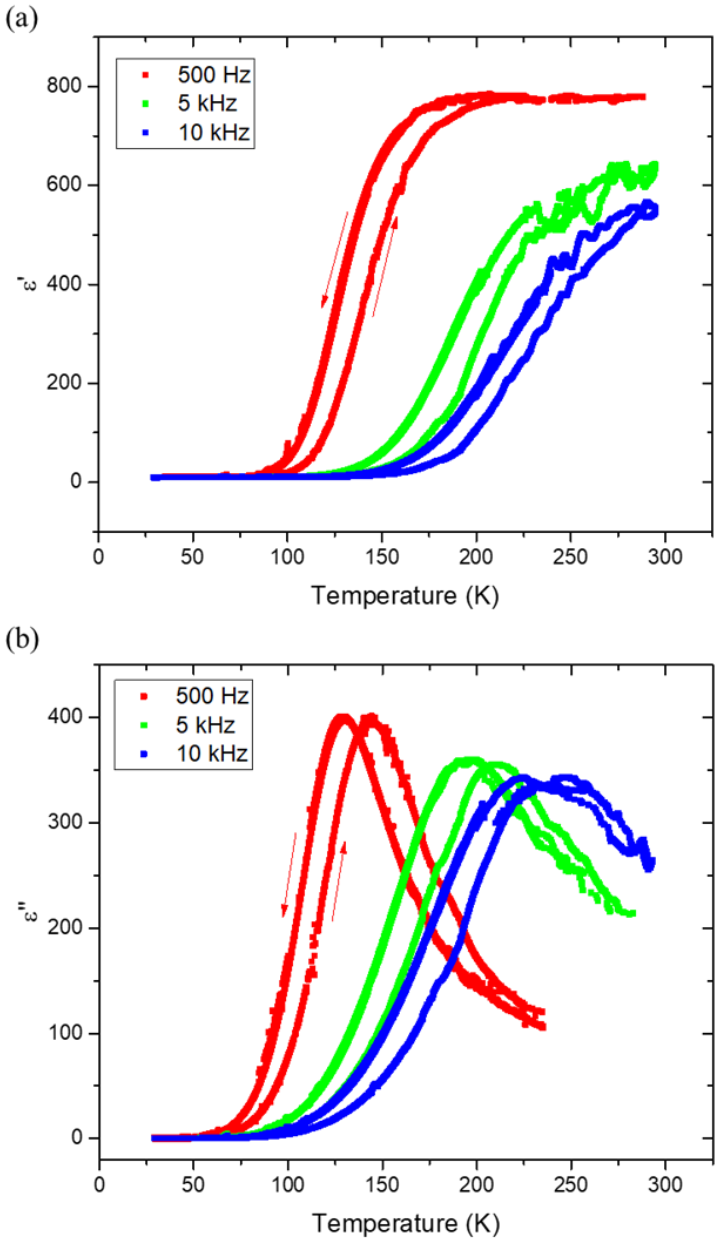


Figure 4-11: (a) Temperature-dependent real part of the permittivity at 500 Hz (red curve), 5 kHz (green curve) and 10 kHz (blue curve). (b) The temperature-dependent imaginary part of the permittivity at the same frequencies for the CMO-305 sample.

Figure 4-12 presents the real (Figure 4-12 (a)) and imaginary (Figure 4-12 (b)) parts of the permittivity as a function of frequency at temperatures between 68 K and 242 K, for the CMO-305 film. Two distinct regimes, corresponding to two relaxations, are visible at low and high frequencies marked by a change of slope at low frequencies in the real and imaginary parts of the permittivity. The observed relaxations are broad, indicating a distribution of relaxation times and the presence of correlated dipole behavior. Thus, as previously introduced in Equations (2-37) and (2-38) to fit the electrical permittivity curves, the Havriliak-Negami (HN) model function [85, 233], with two relaxation times was considered:

$$\varepsilon(\omega) = \varepsilon_{\infty} + \sum_{j=1}^{2} \frac{\Delta\varepsilon_j}{\left[1+(i\omega\tau_j)^{\beta_j}\right]^{\gamma_j}} \quad (4\text{-}1)$$

where $\Delta\varepsilon_j$ is the intensity associated with each component, ε_{∞} is the high-frequency dielectric constant, ω is the angular frequency, τ_j are the relaxation times and β_j and γ_j are coefficients of each HN function, with the constraints $0 < \beta_j \leq 1$ and $0 < \beta_j\gamma_j \leq 1$. For $\beta = \gamma = 1$ the HN model reduces to the Debye function, with only one relaxation time. The real and imaginary parts of the permittivity were fitted with Equation (4-1) as shown in Figure 4-12 (a) and Figure 4-12 (b), respectively, to determine the function parameters. To ensure transparency and reproducibility, the parameters extracted from the fitting of the dielectric measurements are presented in Appendix. Although the Havriliak–Negami function can account for multiple relaxation processes, in this work only the main relaxation was thoroughly analyzed. A secondary relaxation contribution was consistently identified and included in the fitting procedure; however, due to its very low intensity and the large associated uncertainties, it was not the focus of the discussion. This contribution likely represents the effect of the electrodes. The corresponding Nyquist plot data with the HN equation fit are presented in Figure 4-13. Here, the two distinct regimes corresponding to two relaxations can be seen more clearly.

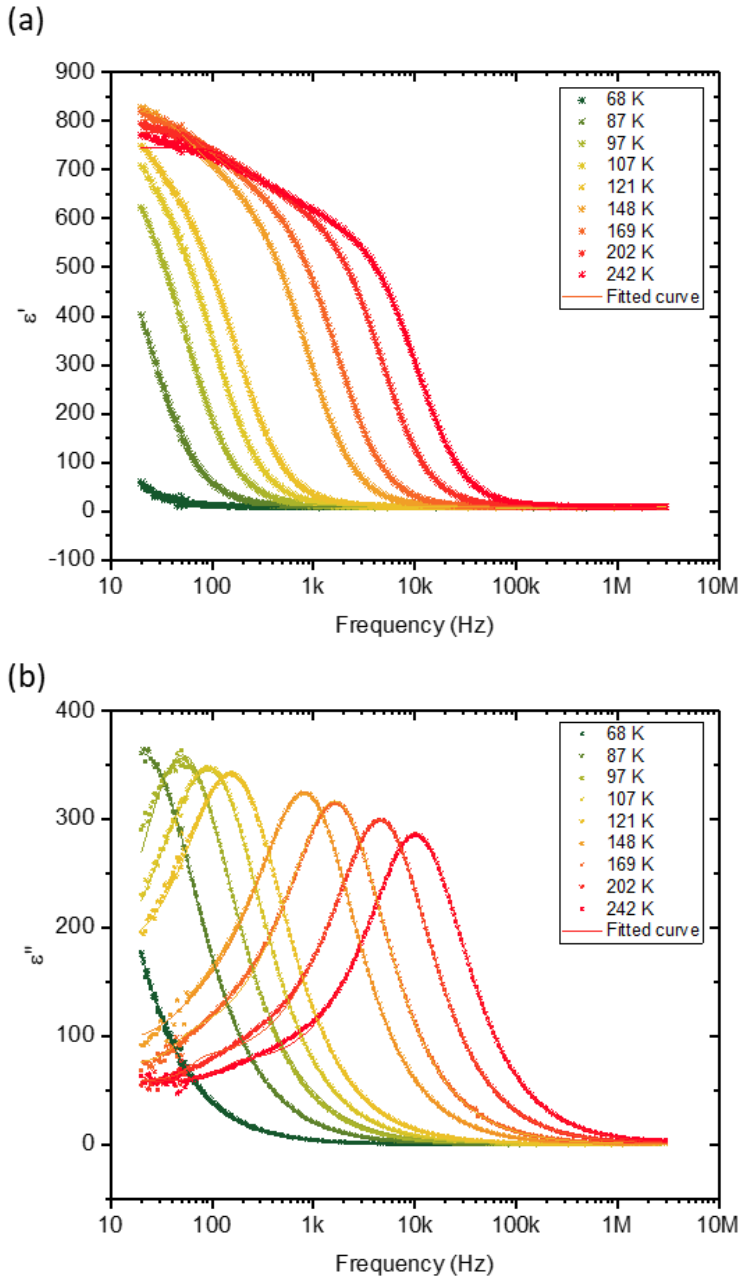


Figure 4-12: (a) Real and (b) imaginary parts of the permittivity as a function of frequency at temperatures between 68 and 242 K with the HN equation fit for the CMO-305 sample.

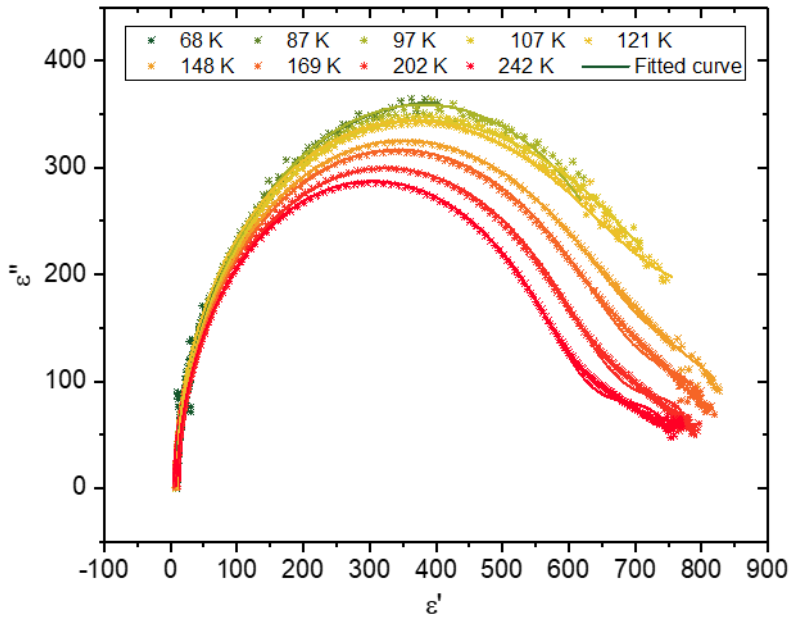


Figure 4-13: Nyquist plot of the imaginary part as a function of the real part of the complex permittivity at temperatures between 68 K and 242 K with the HN equation fit for the CMO-305 sample.

The relaxation times obtained from the HN fit for the main relaxation process, occurring at higher frequencies, show a thermally activated temperature-dependent behavior. As such, to determine the activation energies (E_a), the Arrhenius equation (Equation (2-47)) was applied). Figure 4-14 shows the logarithm of relaxation times as a function of the inverse of temperature. The graph shows two different regimes, one for temperatures below 107 K in the region where the films become antiferromagnetic and the other for temperatures above 121 K. The activation energies were calculated for each temperature-dependent regime, obtaining $E_{a\ T\leq 107\ K} = 0.054\ eV$ and $E_{a\ T\geq 121\ K} = 0.084\ eV$.

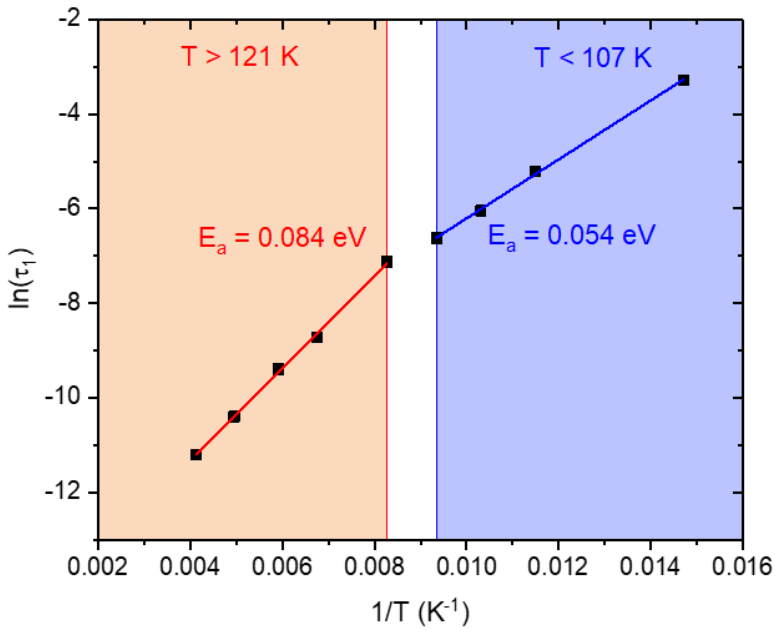


Figure 4-14: Logarithm of the relaxation times as a function of the inverse of temperature with linear fits to the two different regimes, for temperatures below 107 K (blue fit) and temperatures above 121 K (red fit).

Figure 4-15 shows the temperature dependence of the β and γ parameters, obtained from the fits with the HN function, for the main relaxation in Equation (4-1). The β and γ parameters describe the symmetric and asymmetric broadening of the complex dielectric HN function, respectively. The parameter β increases with increasing temperature, while γ shows the opposite behavior.

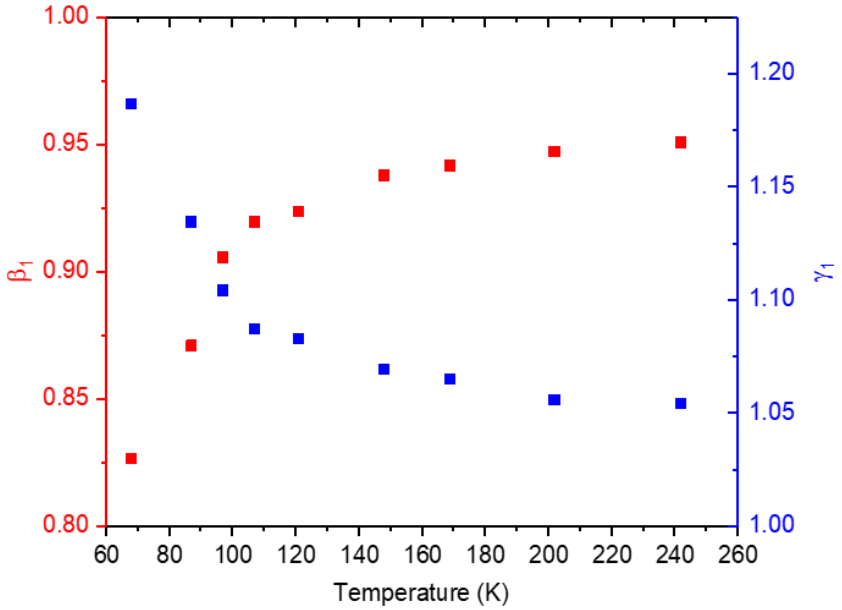


Figure 4-15: Parameter β and γ values obtained for the main relaxation.

Figure 4-16 shows the temperature dependence of the stretched exponential parameter obtained from Equation (2-46). An abrupt decrease of β_{KWW} is observed around $\sim$ 110 K, close to the

antiferromagnetic transition temperature (T_N) of $Ca_3Mn_2O_3$ ($T_N \sim 112.5$ K) [70]. In the $Ca_3Mn_2O_3$ films, the T_N value obtained from temperature-dependent magnetic measurements was $T_N \sim 112$ K, as shown in section 4.5. The abrupt drop in β_{KWW} across the AFM transition thus indicates the presence of magnetoelectric interactions and magnetically induced enhancement of dipolar correlations with decreasing temperature.

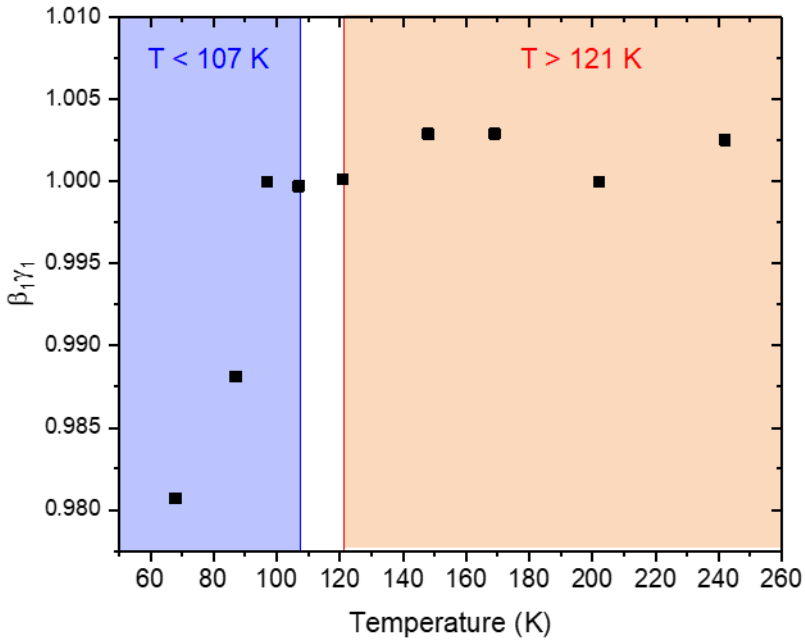


Figure 4-16: Temperature dependence of the stretched exponential parameter, β_{KWW} marked by an abrupt decrease around $\sim$ 100 K, close to the antiferromagnetic transition temperature $T_N \sim 112$ K, found from temperature-dependent magnetic measurements (section 4.5).

Compared to $Ca_3Mn_2O_7$ in bulk [234], the thin films analyzed here have higher permittivity. This is due to the influence of the Maxwell–Wagner–Sillars polarization that occurs at the nanoscale, where the charge carriers can be blocked at the inner dielectric boundary layers or the interfaces of films-on-substrate samples [85].

4.7. Density-functional theory calculations

Density functional theory (DFT) calculations were performed to study different magnetic orderings of the *Acaa* and *A2₁am* phases of $Ca_3Mn_2O_7$. DFT calculations were employed using the Vienna Ab initio Simulation Package (VASP) 6.4.1 [215, 216, 235, 236]. The structure relaxations were performed using the GGA (Generalized Gradient Approximation) and the PBEsol functional [237] and carried on until forces converged to a threshold of 1 meV/Å. In-plane equibiaxially strained structures were allowed to relax in the out-of-plane direction until the out-of-plane stress component converged to a threshold of 0.1 GPa.

The plane-wave cutoff energy was set to 600 eV and the size of Γ-centered k-point mesh was fixed to $5 \times 5 \times 4$. The special quasi-random structures (SQS) [238] were generated using the MCSQS utility in the ATAT toolkit [239]. The magnetic couplings were calculated according to previous work [240] where the hybrid functional PBE0 [241–243] was used for single-point energy calculations on relaxed structures to obtain the magnetic coupling constants. The FINDSYM webserver [244] was used to confirm the presence of the *I4/mmm*, *Acaa* and *A2₁am* phases while the atomistic representations were generated using VESTA [245].

The *Acaa* and *A2₁am* phases were fully relaxed in the antiferromagnetic G-type (AFM-G) state and paramagnetic (PM) state, which was properly described by means of a special quasi-random structure (SQS). The ferroelectric transition from +P to -P states of the *A2₁am* phase involves the X_2^- mode (see Figure 4-17), where the intermediate state of the transition is the *Acaa* phase. The energy difference between these two phases represents the activation energy for the polarization switching, E_a for a given magnetic ordering. As shown in Figure 4-18, for the AFM state $E_a = 68\ meV$ was obtained and for the PM state, $E_a = 85\ meV$ was found. These values are in good agreement with the ones obtained experimentally (Figure 4-14). The dependence of E_a on magnetic ordering clearly indicates the presence of magneto-electric interactions in the films.

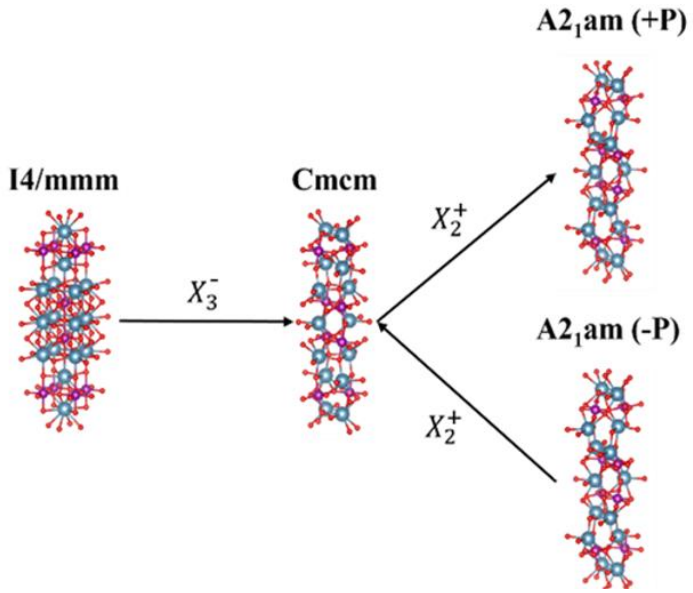


Figure 4-17: Sequence of phase transitions in $Ca_3Mn_2O_7$ from the paraelectric *I4/mmm* phase to the ferroelectric *A2₁am* phase. (c) Antiferromagnetic to paramagnetic transition temperatures as a function of biaxial strain. The line is a guide to the eye.

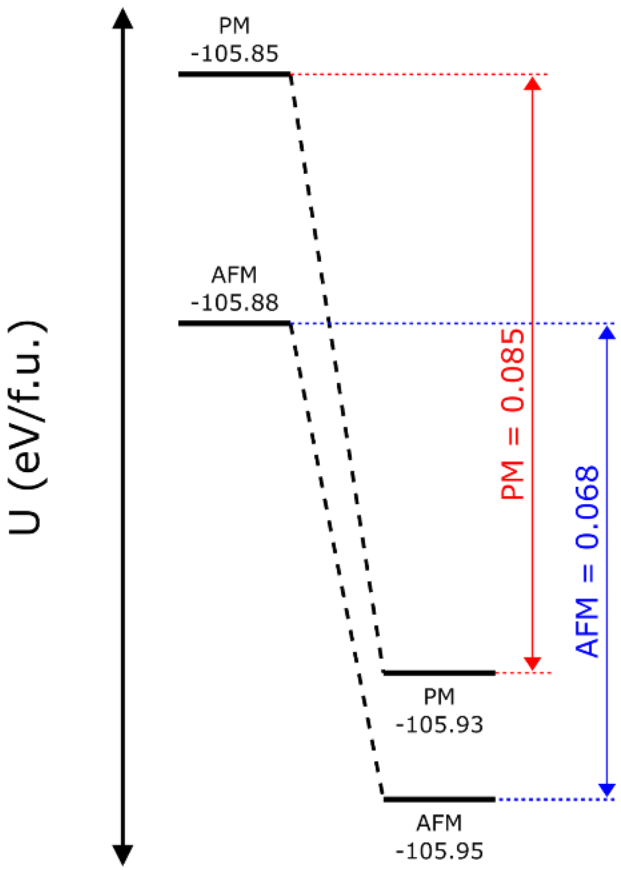


Figure 4-18: Ferroelectric polarization switching barrier as a function of magnetic ordering for $Ca_3Mn_2O_7$.

5. Calcium Manganese Oxides: Strain-Dependent Magnetic and Dielectric Properties

In the previous chapter, it was demonstrated that the ferroelectric *A2₁am* phase in $Ca_3Mn_2O_7$ 205 nm thin film, prepared by pulsed laser deposition on (100) $SrTiO_3$ substrate, has been successfully stabilized. The results also indicated the presence of magnetoelectric interactions and a magnetically induced enhancement of dipolar correlations in the samples. These findings suggest that substrate-induced strain plays a crucial role in enhancing multiferroicity in these films. Therefore, the focus of this chapter is to further investigate the multiferroic properties of $Ca_3Mn_2O_7$ by exploring the influence of strain on these properties, through thickness variation. Thin films of calcium manganese oxide with varying thicknesses, prepared by pulsed laser deposition on (100) $SrTiO_3$ substrates, will be studied to understand how the interfacial strain on the $Ca_3Mn_2O_7$ layer affects its magnetic and dielectric properties.

5.1. Structural and Morphological Characterization

To understand the influence of substrate strain on electric and magnetic polarization and coupled magnetic-electric behavior, five thin films of $Ca_3Mn_2O_7$ (CMO), were deposited on (100) $SrTiO_3$ substrates, with thicknesses of 34 nm, 42 nm, 96 nm, 165 nm, and 293 nm. Additionally, five thin films were deposited on (100) $SrTiO_3$:Nb (1.4 at%Nb) conductive substrates, with thicknesses of 53 nm, 57 nm, 107 nm, 183 nm, and 346 nm, and are here called cCMO. The sample cCMO-305, presented in the previous chapter, will also be included in the current study of dielectric properties.

The 1.4at% niobium doping of the (100) $SrTiO_3$:Nb substrates enhances their conductivity, enabling their use in dielectric measurements while maintaining their crystalline properties identical to those of (100) $SrTiO_3$. The films were produced using the same pulsed laser deposition system and under the optimal deposition conditions determined in the previous chapter, utilizing the same target. The deposition process involved a repetition rate of 6 Hz, a target-substrate distance of 6 cm, and a fluence of 3.4 J/cm^2. The oxygen pressure during film preparation was maintained at 10^{-2} mbar, with a deposition temperature of 730 °C. Subsequently, the films were cooled to room temperature at a rate of 10 °C/min in an oxygen atmosphere at ambient pressure. Following deposition, the films underwent annealing at 900 °C for 2 hours in air, with a heating rate of 10 °C/min.

Table 5-1 provides details of the substrates used, the produced samples and the corresponding thicknesses of the $Ca_3Mn_2O_7$ thin films, as determined from SEM cross-section images.

Table 5-1: Details of the substrates used, the samples produced and the corresponding thicknesses of the $Ca_3Mn_2O_7$ thin films. *Sample cCMO-305 was studied in the previous chapter.

Substrate	**Sample**	**$Ca_3Mn_2O_7$ thin film thickness (nm)**
(100) $SrTiO_3$	CMO-34	34
	CMO-42	42
	CMO-96	96
	CMO-165	165
	CMO-293	293
(100) $SrTiO_3$:Nb	cCMO-53	53
	cCMO-57	57
	cCMO-107	107
	cCMO-183	183
	cCMO-305*	305
	cCMO-346	346

The microstructure, morphology and cross-section of the deposited films were examined by scanning electron microscopy (SEM) with a Thermofischer Quanta 650 FEG Environmental SEM. Figure 5-1 and Figure 5-2 show the SEM cross-section images obtained for the samples produced.

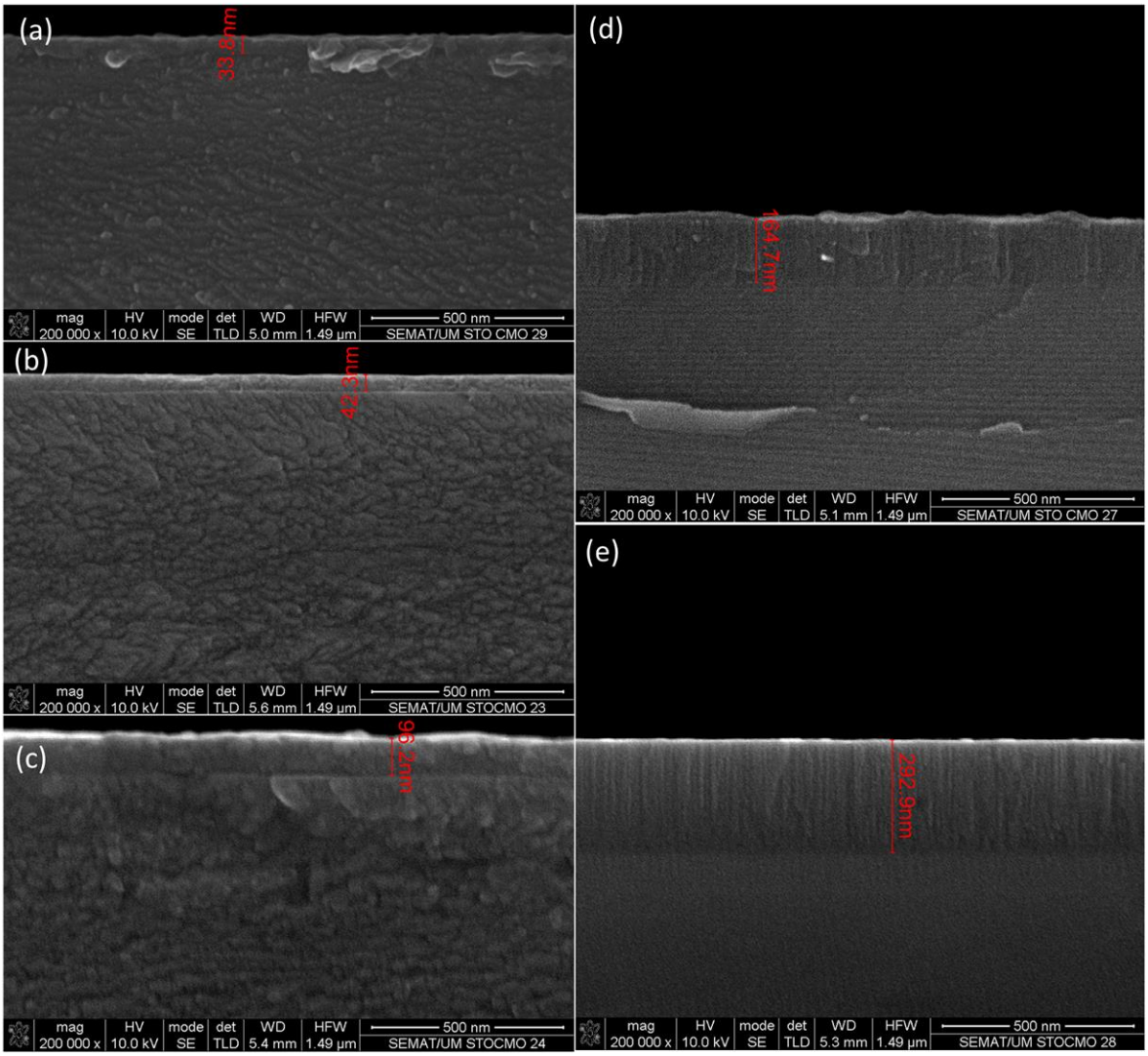


Figure 5-1: SEM micrographs of the cross-section of the samples over $SrTiO_3$ substrate: (a) CMO-34, (b) CMO-42, (c) CMO-96, (d) CMO-165 and (e) CMO-293.

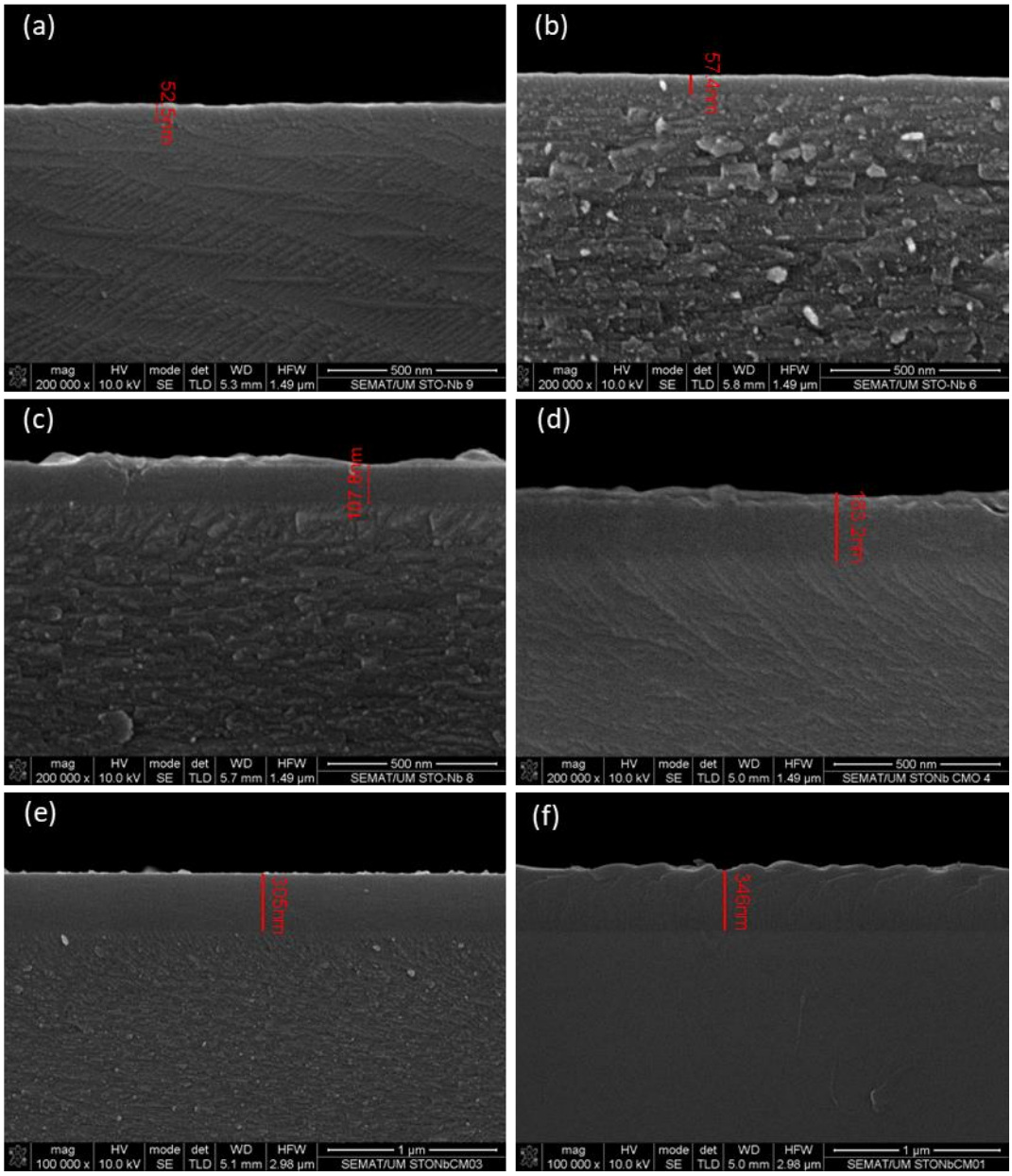


Figure 5-2: SEM micrographs of the cross-section of the samples over $SrTiO_3$:Nb substrate: (a) cCMO-53, (b) cCMO-57, (c) cCMO-107, (d) cCMO-183, (e) cCMO-305 and (f) cCMO-346.

The samples prepared $SrTiO_3$ and (100) Nb-doped $SrTiO_3$ (1.4 at%) substrates were examined by XRD and no significant structural differences were observed between them, due to the low dopant concentration [246, 247]. Under identical deposition conditions, the resulting films exhibited similar characteristics, irrespective of whether the substrate contained Nb at 1.4 at% or not.

Figure 5-3 shows the X-ray diffraction spectra of the five thin films of $Ca_3Mn_2O_7$ (CMO), deposited on (100) $SrTiO_3$ substrates. Vertical green lines indicate the peak positions of the $SrTiO_3$ substrate with the cubic $Pm\bar{3}m$ structure. The red and blue patterns indicate the peak positions of $Ca_3Mn_2O_7$ with the *Acaa* orthorhombic structure [228] and with the ferroelectric $A2_1am$ orthorhombic structure [229], respectively. The XRD results depicted in Figure 5-3 show the presence of two main $Ca_3Mn_2O_7$ XRD peaks (assigned

with red vertical lines) that correspond to the bulk *A2₁am* atomic planes (111) and (222). The XRD analysis thus indicates that $Ca_3Mn_2O_7$ may have coexistence of the *A2₁am* ferroelectric orthorhombic phase and the Acaa phase. Due to the small angular separation between the *Acaa* and *A2₁am* peaks, both phases could be present as also reported in the literature [248]. Additionally, other small peaks were identified in samples CMO-96 and CMO-293 (such as the (206) peak), suggesting a slight degree of polycrystallinity. Nevertheless, these peaks are very small and are not visible in all samples, indicating that the $Ca_3Mn_2O_7$ films have grown oriented, with a preferential growth direction along the [111] direction perpendicular to the substrate plane.

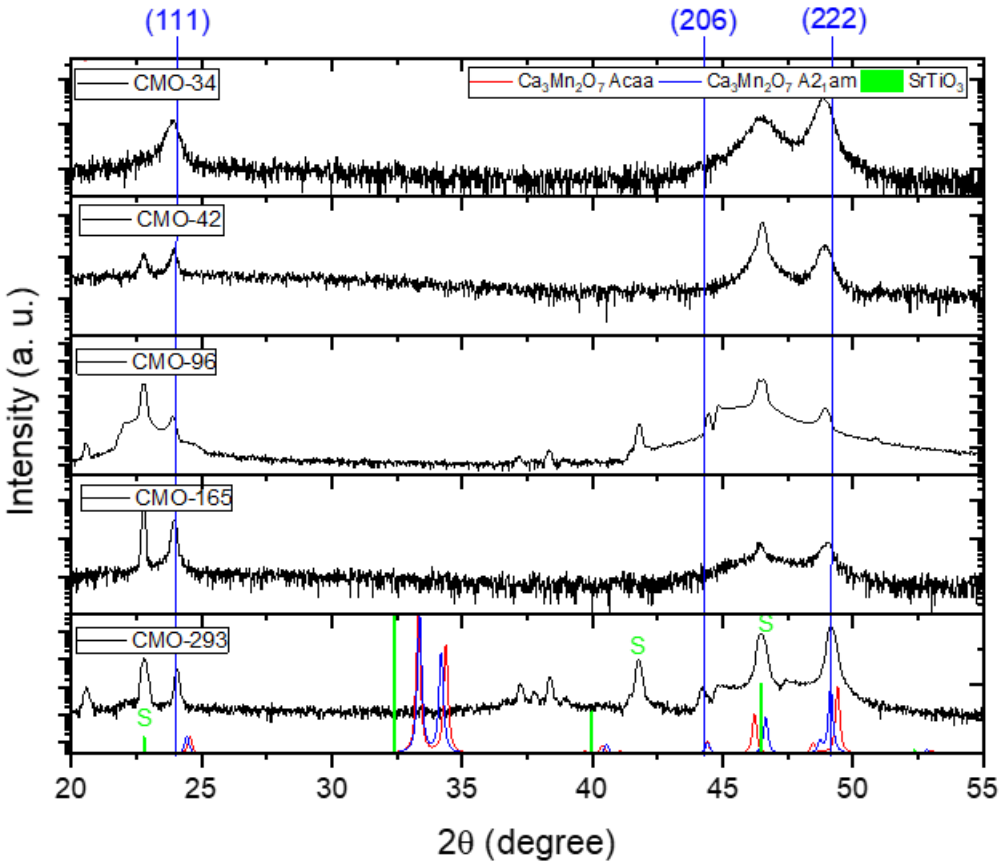


Figure 5-3: X-ray diffraction spectra measured on the samples with different thicknesses deposited over $SrTiO_3$ substrates. The peaks marked with "S" are from the substrate. The blue vertical lines mark the reference diffraction peaks (111), (206) and (222) of the $Ca_3Mn_2O_7$ *A2₁am* phase. The blue and red curve lines (shown in the bottom line of the graph) mark the reference diffraction diffractograms of the $Ca_3Mn_2O_7$ *A2₁am* and *Acaa* phases.

Considering the results of XRD measurements and applying Bragg's law, the interplanar spacing of the samples on the $SrTiO_3$ substrate was determined based on the peak position corresponding to the atomic plane (222). Figure 5-4 shows the zoomed region around the measured (222) XRD peak positions of the films. It is observed that the position of the peaks shifts to lower angles with the increase in film thickness. The interplanar spacing obtained for each sample was then compared with that of the bulk

A2₁am phase (most preponderant phase at room temperature) and the strain, $\varepsilon = (d_{film} - d_{bulk})/d_{bulk}$, obtained as a function of the thin film thickness is shown in Figure 5-5. The interplanar distance percentage increases with decreasing thickness showing an expansion strain along the growth direction indicative of an in-plane compression of the films. The strain is higher for the thinner CMO-34 sample. This occurs due to the dominant influence of the substrate-induced strain in thinner samples, causing a deformation in the crystalline structure. However, with increasing thickness, the crystal lattice structure tends to relax towards that of the bulk material.

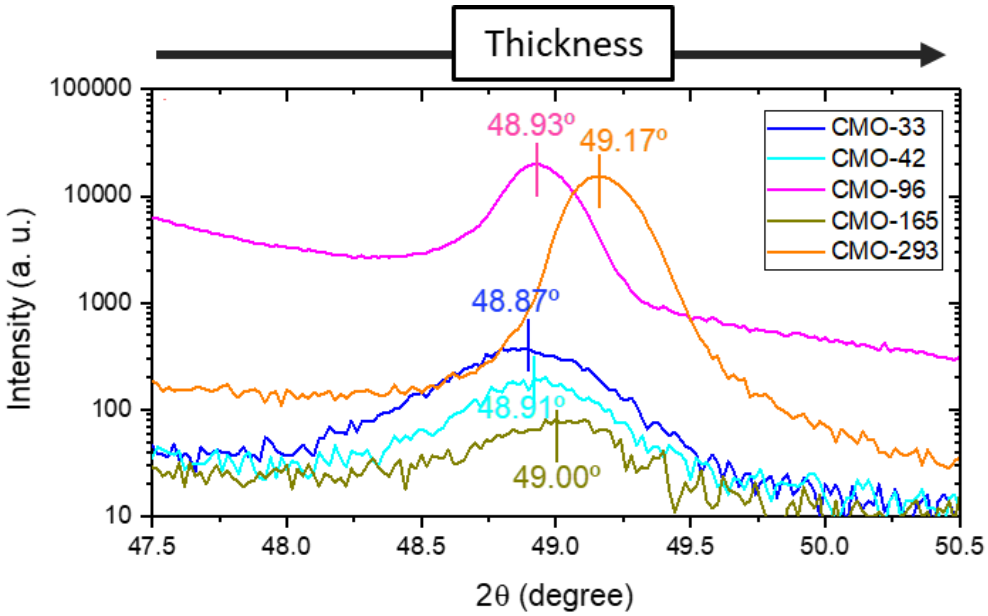


Figure 5-4: Zoom-in of the X-ray diffraction spectra measured on the samples with different thicknesses around the (222) peak.

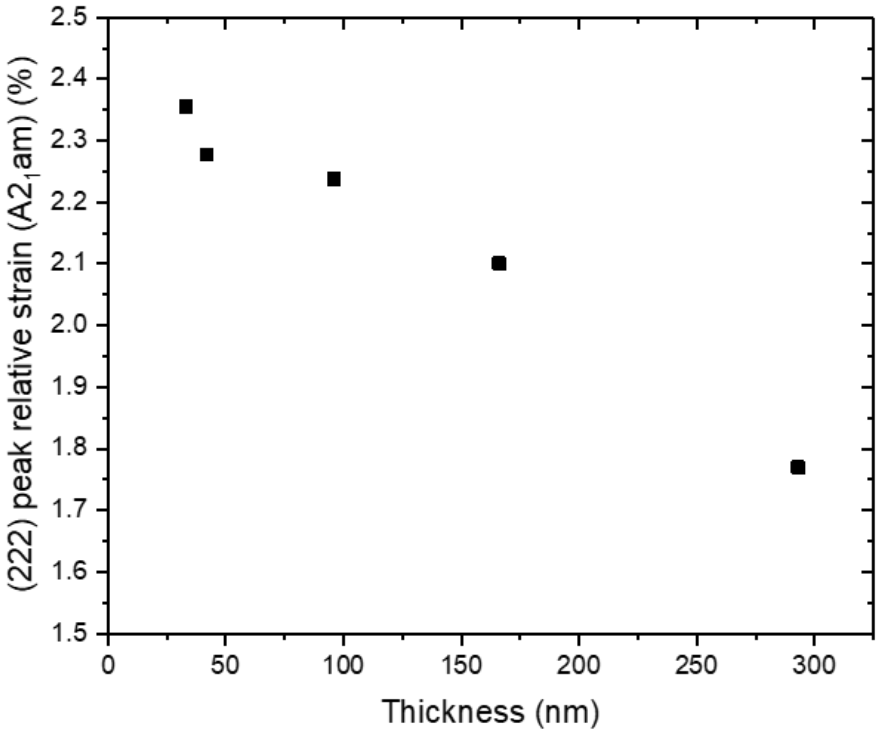


Figure 5-5: Percentage of strain calculated from the (222) *A2$_1$am* peak position.

5.2. Magnetic Characterization

To study the influence of the strain, through thickness variation, the set of $Ca_3Mn_2O_7$ thin films deposited on strontium titanate substrates ($SrTiO_3$) by pulsed laser deposition were analyzed using a SQUID magnetometer. The samples studied in dielectric measurements are identified in Table 5-1 (substrate $SrTiO_3$), together with information regarding their average thickness. The magnetic measurement was performed with a Quantum Design's Magnetic Property Measurement 3 (MPMS3) magnetometer, under field cooling with a 100 Oe applied magnetic field.

Figure 5-6 shows the temperature dependence of the magnetic moment measured on the $Ca_3Mn_2O_7$ thin films after field cooling (FC). The sharp increase below 50 K is attributed to the paramagnetic contribution from the $SrTiO_3$ substrate. A clear change of slope is observed in the thin films in the temperature interval 90-110 K depending on the sample thickness, marking the canted antiferromagnetic phase transition temperature (Nèel temperature, T_N) characteristic of $Ca_3Mn_2O_7$ [70].

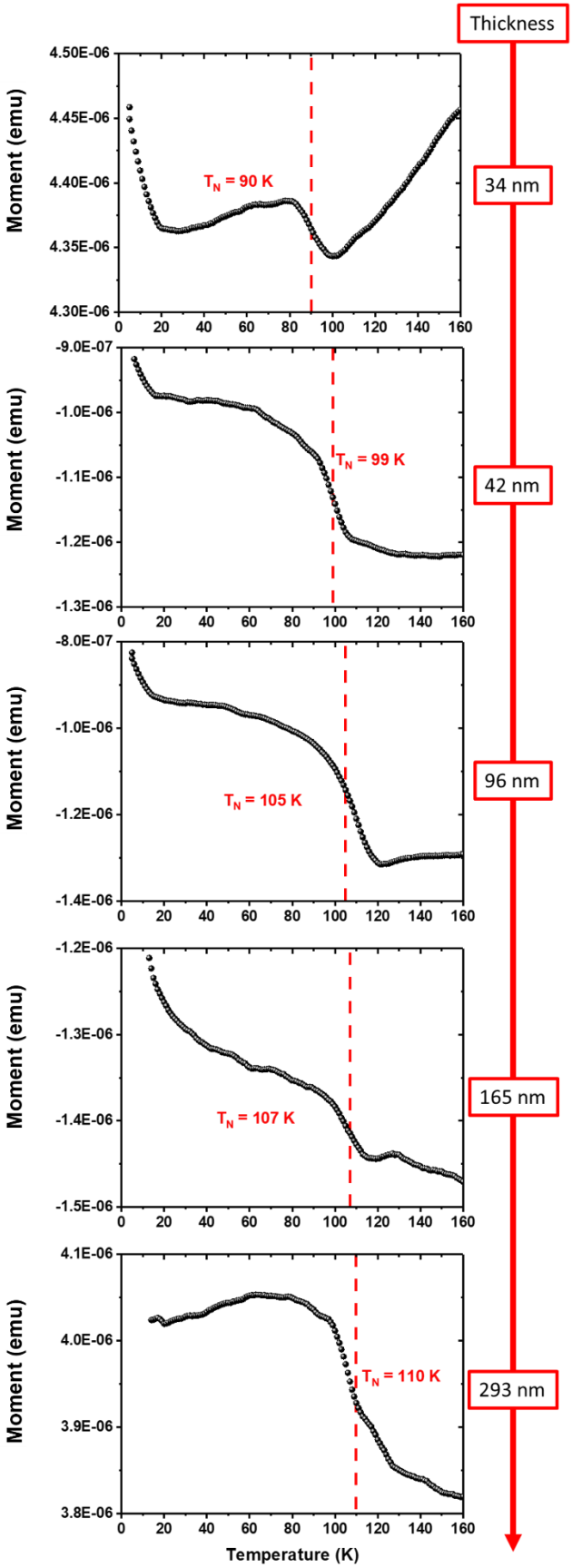


Figure 5-6: Temperature dependence of the moment measured in $Ca_3Mn_2O_7$ thin films with 100 Oe applied. In the figure, the samples are presented in increasing order of CMO layer thickness, from top to bottom. In the same direction, the AFM transition temperature also increases.

Figure 5-7 shows the T_N values obtained as a function of the thickness of each measured $Ca_3Mn_2O_7$ thin film. For thinner films, the T_N is reduced due to the influence of the strain imposed by the substrate. However, as the film thickness increases, strain progressively decreases, so that for the thicker film, the T_N approaches the bulk value (T_N ~112.5 K [70]). This result is consistent with the XRD results presented in Figure 5-3 (page 102) and Figure 5-4 (page 103) where more significant changes in the crystal lattice are observed for thinner samples.

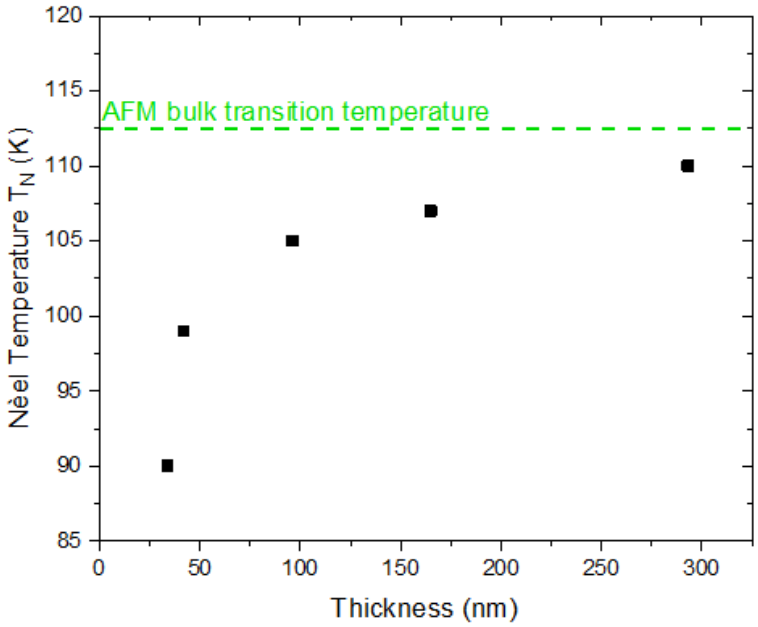


Figure 5-7: Transition temperature as a function of deposition time. The dashed green line marks the AFM transition temperature of bulk $Ca_3Mn_2O_7$ [70].

To further analyze the dependence of transition temperature on film thickness, the scaling theory of phase transitions can be applied [249]. This method allows for determining whether the system follows a power-law relationship between thickness and the transition temperature, a hallmark of systems belonging to a specific universality class. Universality classes group together systems that exhibit the same critical behavior near a phase transition, regardless of their microscopic details. Critical exponents, such as the one governing the dependence of T_N on thickness, describe how key physical quantities scale near the transition point. These exponents depend on fundamental properties such as dimensionality, symmetry, and interaction range.

In the case of thin films, the scaling behavior of the transition temperature (T_N) with thickness can be described by the equation [250]:

$$t = \frac{T_{N\infty} - T_N}{T_{N\infty}} = \left(\frac{\xi_0}{d_{CMO}}\right)^{\lambda} \tag{5-1}$$

where $T_{N\infty}$ is the transition temperature of the bulk crystal and d_{CMO} is the CMO thin film thickness. The parameter ξ_0 represents the correlation length in the limit of $T = 0\ K$, while λ is a critical exponent that defines the material's universality class [251]. The exponent λ is related to the critical exponent υ, which describes the correlation length behavior ($\xi \propto (T_{N\infty} - T_N)^{-\nu}$ [252]), through the relationship $\lambda = 1/\upsilon$ [250, 253, 254]. According to the following equation:

$$ln(t) = \frac{\ln(\xi_0) - ln(d_{CMO})}{\upsilon} \tag{5-2}$$

the correlation length (υ) can be determined from a linear fitting to the plot of $\ln(\xi_0)$ versus $ln(d_{CMO})$ as presented in Figure 5-8**.** The obtained values are $\lambda = 0.90588$, so $\upsilon = 1/\lambda \approx 1.10$.

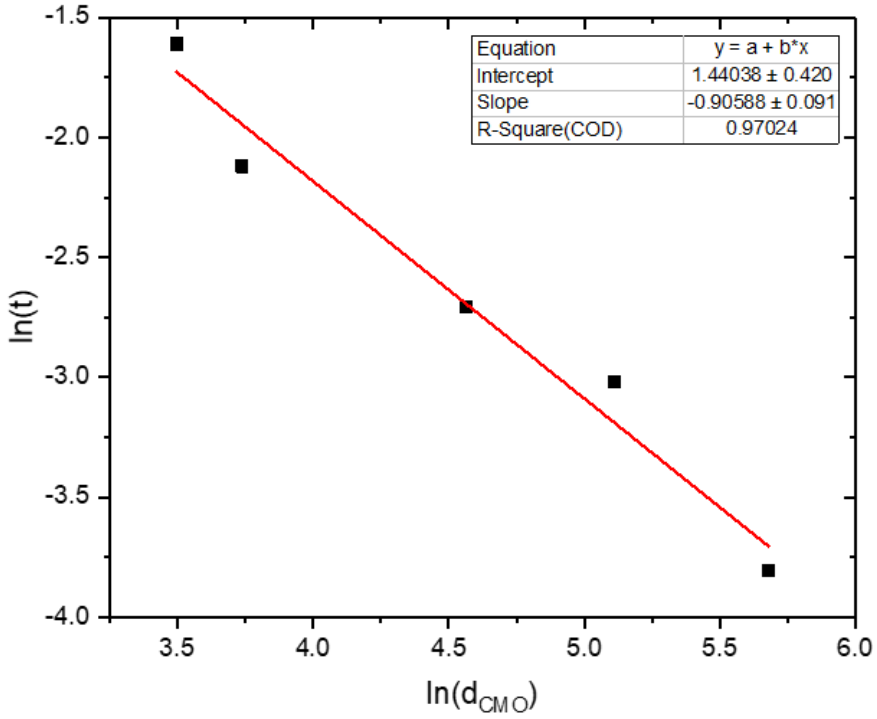


Figure 5-8: Plot of the logarithm of T_N versus the logarithm of thickness for $Ca_3Mn_2O_7$ thin films. The linear fit is shown, with the slope corresponding to $\lambda = 0.90588$.

The obtained critical exponent of $\upsilon \approx 1.10$ is remarkably close to the theoretical value for the 2D Ising universality class (ν = 1.00) [255, 256]. This indicates that the system behaves effectively as two-dimensional and suggests the presence of local disorder or strain-induced inhomogeneities, which can further support a comparison with the 2D random Ising model [256]. Such behavior aligns with the thin film geometry, where reduced dimensionality and interface effects play a dominant role near the magnetic transition. In $Ca_3Mn_2O_7$ thin films, the strained interfacial layer is particularly influential in thinner samples, where substrate-induced strain is more pronounced and leads to deviations from the bulk Néel

temperature. This strain-driven inhomogeneity likely underpins the observed critical exponent, highlighting a complex interplay between strain relaxation, lattice distortions, and local magnetic interactions in the films.

Isothermal magnetization curves (M(H)) of samples CMO-42 and CMO-96 were measured at 5 K, as shown in Figure 5-9. The curves exhibit a tendency toward not fully magnetic saturation at high fields, which is likely associated with the saturation of the paramagnetic component superimposed on the antiferromagnetic contribution of the samples. A hysteresis between the field-increasing and field-decreasing branches is observed, but it is attributed to the sensitivity of the measurement, given the very small net magnetic moment involved.

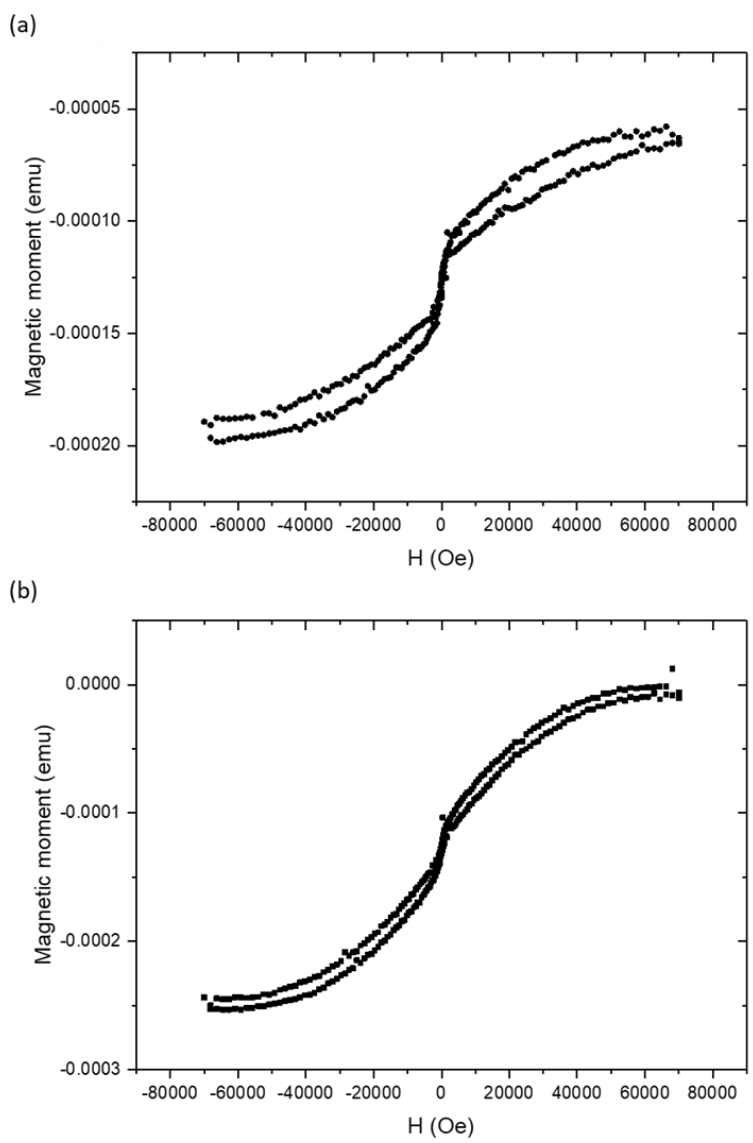


Figure 5-9: Antiferromagnetic hysteresis curves measured in samples (a) CMO-42 and (b) CMO-96.

5.3. Dielectric characterization

5.3.1. Antiferromagnetic transition temperature analysis

To further understand the influence of substrate strain on the electric polarization and coupled magnetic-electric behavior, the $Ca_3Mn_2O_7$ thin films were analyzed by impedance spectroscopy. The dielectric properties were systematically investigated through impedance spectroscopy at temperatures below 305 K and within a frequency spectrum covering 20 Hz to 3 MHz. The thin films deposited onto niobium-doped strontium titanate substrates ((100) $SrTiO_3$:Nb) were used for measurements. A parallel plate capacitor was formed by connecting the samples, with the $SrTiO_3$:Nb substrate serving as the bottom electrode and a small circular air-cured silver paint contact, approximately 1 mm in diameter, acting as the top electrode. Data acquisition was carried out using a Wayne Kerr 6440A precision component analyzer interfaced with a dedicated computer and software. To minimize parasitic impedances arising from connecting cables, shielded test leads were employed. The temperature control was achieved using a Scientific Instruments INC Series 5500-5 temperature gauge, with temperature-dependent measurements conducted at a rate of 2 K/min.

The samples studied in dielectric measurements are identified in Table 5-1 (substrate $SrTiO_3$:Nb), providing insight into their average thickness.

Figure 5-10**,** Figure 5-11 and Figure 5-12 present the dielectric analysis of the samples cCMO53, cCMO107 and cCMO183, respectively. In these analyses, the HN model function with two relaxation times was considered (Equation (4-1)). The real and imaginary parts of the permittivity as a function of frequency, at fixed temperatures, were fitted with using this model, as illustrated in the (a) and (b) panels of Figure 5-10, Figure 5-11 and Figure 5-12. Additionally, the corresponding Nyquist plots with the HN equation fits are presented in the (c) panels of these figures. A detailed list of the fitting parameters can be found in Appendix.

The parameters β and γ characterize the symmetric and asymmetric broadening of the complex dielectric response, and are shown as a function of temperature in Figure 5-10 (d), Figure 5-11 (d) and Figure 5-12 (d) for each sample. The temperature dependence of the stretched exponential parameter, β_{KWW}, which reflects the distribution of relaxation times and captures non-exponential relaxation processes, is presented in Figure 5-10 (e), Figure 5-11 (e) and Figure 5-12 (e). This parameter, which reflects the distribution of relaxation times in the system, is often used to describe complex, non-exponential relaxation processes where the response is slower than predicted by a simple exponential

decay (see section 2.3.2). This behavior is commonly associated with systems exhibiting disorder or heterogeneity.

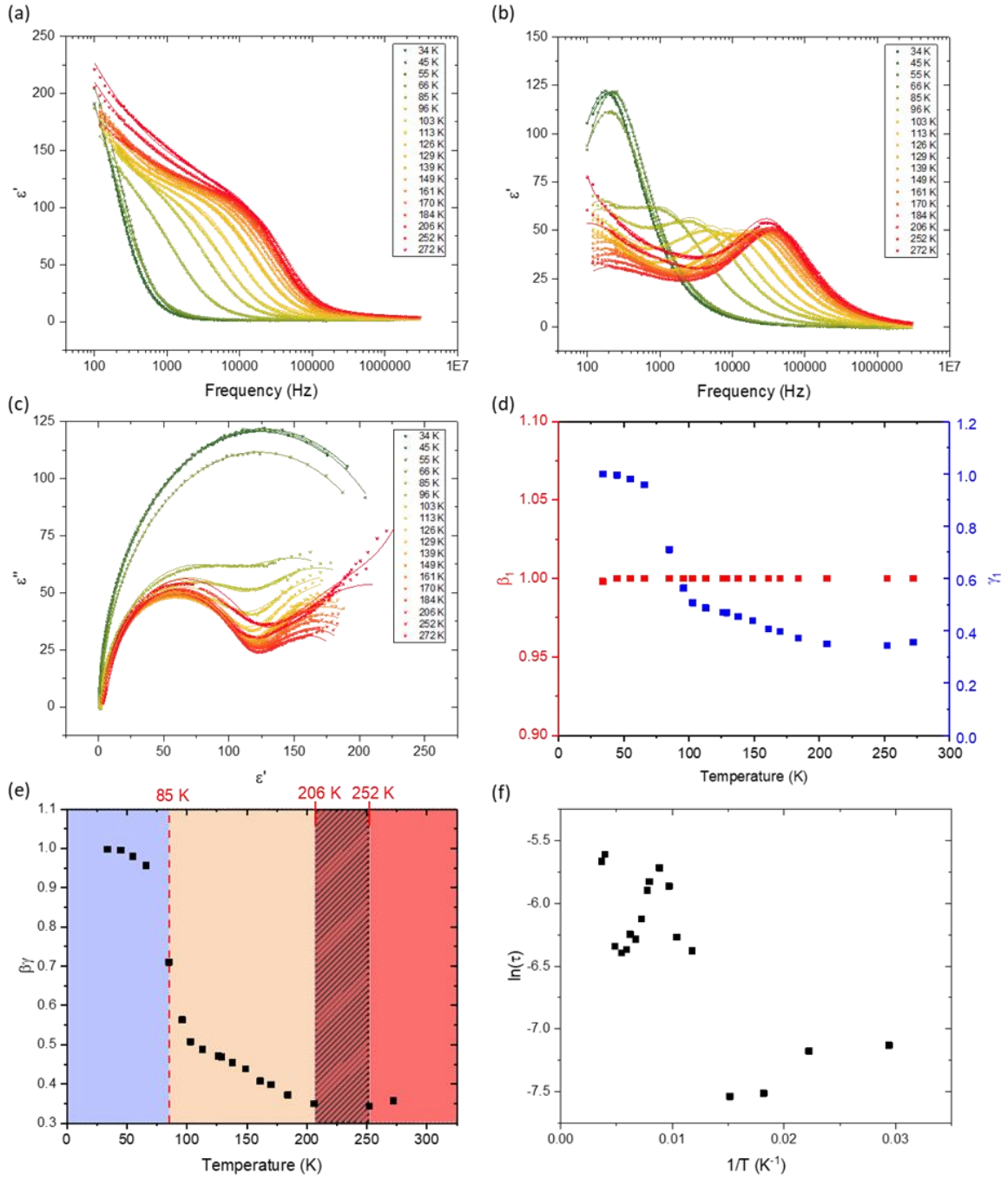


Figure 5-10: Sample cCMO-53. (a) Real and (b) imaginary parts of the permittivity as a function of the HN equation fit. (c) Nyquist plot of the imaginary part as a function of the real part of the complex permittivity at temperatures with the HN equation fit. (d) Parameter β and γ values obtained for the main relaxation. (e) Temperature dependence of the stretched exponential parameter, βKWW, marked by an abrupt decrease near 85 K and by another regime shift between 206 K and 252 K (marked by the filled area). (f) Logarithm of relaxation times as a function of the inverse of temperature.

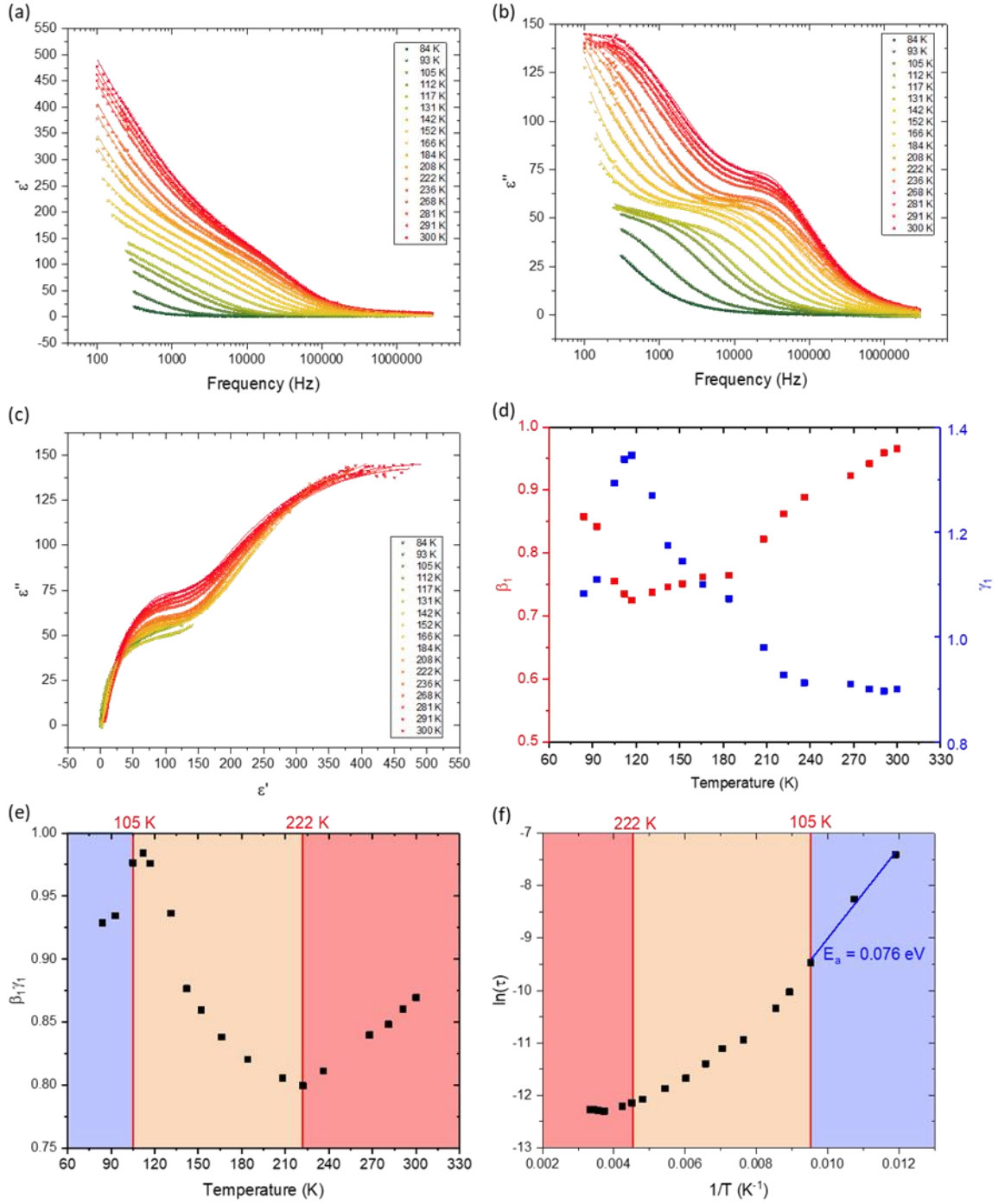


Figure 5-11: Sample cCMO-107. (a) Real and (b) imaginary parts of the permittivity as a function of the HN equation fit. (c) Nyquist plot of the imaginary part as a function of the real part of the complex permittivity at temperatures with the HN equation fit. (d) Parameter β and γ values obtained for the main relaxation. (e) Temperature dependence of the stretched exponential parameter, β_{KWW}, marking an abrupt decrease near 105 K and a new increase at 222 K. (f) Logarithm of the relaxation times as a function of the inverse of temperature with linear fit corresponding to the AFM region.

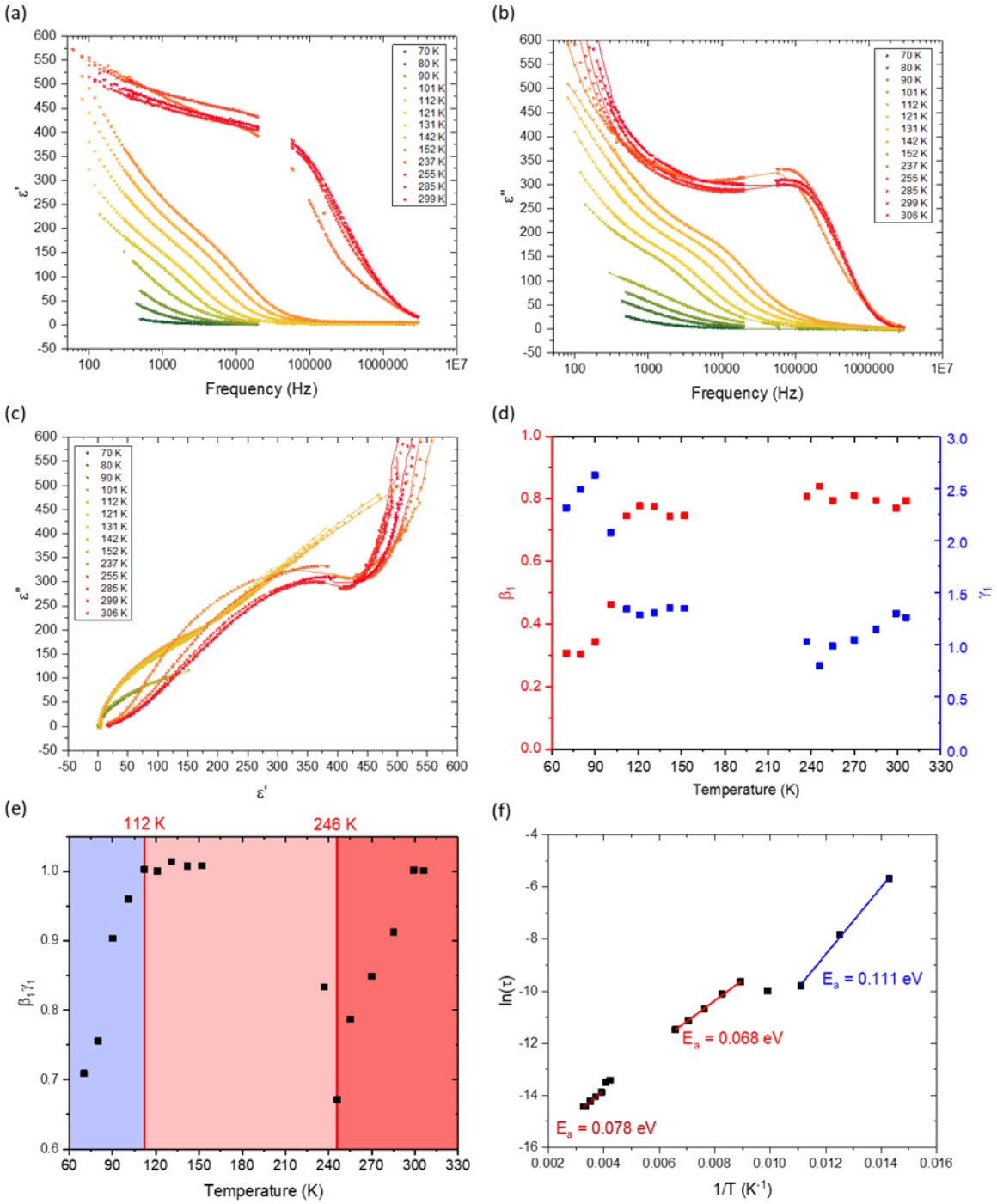


Figure 5-12: Sample cCMO-183. (a) Real and (b) imaginary parts of the permittivity as a function of the HN equation fit. (c) Nyquist plot of the imaginary part as a function of the real part of the complex permittivity at temperatures with the HN equation fit. (d) Parameter β and γ values obtained for the main relaxation. (e) Temperature dependence of the stretched exponential parameter, β_{KWW}, marking an abrupt drop across de AFM near 112 K and a second drop near 246 K. (f) Logarithm of the relaxation times as a function of the inverse of temperature with linear fits for the three different identified regions.

In sample cCMO-53 (Figure 5-10 (e)) with 53 nm thickness, two distinct relaxation processes are observed. The first relaxation occurs at low temperatures, near 85 K, which corresponds to the onset of antiferromagnetic (AFM) ordering in the material. This transition temperature aligns well with the Néel

temperature of 99 K obtained from temperature-dependent magnetic measurements for similar thicknesses, such as the 42 nm-thick sample. The second relaxation is observed at higher temperatures, indicating a different dynamic regime. To further analyze these relaxations, the experimental data were fitted using the Havriliak-Negami (HN) equation, as shown in Figure 5-11 (a-c). This model is applied to account for the broad and asymmetric features of the dielectric relaxation processes. Figure 5-11 (d) shows the temperature dependence of the β and γ parameters, which describe the symmetric and asymmetric broadening of the relaxation. Additionally, Figure 5-11 (e) presents the temperature dependence of the stretched exponential parameter β_{KWW}. A noticeable decrease in β_{KWW} is observed around 85 K, marking the AFM transition. Another regime shift is identified between 206 K and 252 K, as indicated by the filled area in Figure 5-11 (e), suggesting a second transition or change in the dynamic behavior of the material. This behavior is consistent with the transition temperature observed in magnetic measurements for films of this thick range.

In sample, cCMO-107 (Figure 5-11 (a-c)), two clear relaxations are observed in the experimental curves. These relaxations likely correspond to different dynamic processes within the material. The first relaxation, observed at lower temperatures, is associated with the AFM transition near 105 K, as indicated by magnetic measurements for this thickness and strain regime. The second relaxation becomes prominent at higher temperatures, near 222 K, indicating another transition in the material. To better understand these processes, the experimental data were fitted using the Havriliak-Negami equation, as shown in Figure 5-11 (a-c) The HN model is particularly useful for capturing the broad and asymmetric nature of dielectric relaxations in complex systems like this one. Figure 5-11 (d) presents the temperature dependence of the β and γ parameters which describe the symmetric and asymmetric broadening of the relaxation, respectively. Furthermore, Figure 5-11 (e) shows the temperature dependence of the stretched exponential parameter, β_{KWW}. Here, three distinct regimes were identified. One at low temperatures (T < 105 K), another at intermediate temperatures (222 K < T < 105 K), and the last one at high temperatures (T > 222 K). The low-temperature change of behavior at $\sim$ 105 K marks the AFM transition temperature observed from the magnetic measurements to occur for this thickness/strain range. At T* = 222 K another transition was identified, and it will be discussed later.

In sample cCMO-183 (Figure 5-12), with 183 nm thickness, two clear relaxation processes are observed, corresponding to distinct dynamic regimes. The first transition occurs at low temperatures, near 112 K, marking the antiferromagnetic (AFM) ordering temperature, as confirmed by magnetic measurements for a thin film of similar thickness. This transition approaches the bulk Néel temperature of $Ca_3Mn_2O_7$, which is approximately 112.5 K. A second transition is observed at higher temperatures,

around 246 K, which suggests another change in the dielectric relaxation behavior. To analyze these relaxations in more detail, the experimental data were fitted using the HN equation, as shown in Figure 5-12 (a-c). This model was used to characterize the broadening and asymmetry of the relaxation processes. Figure 5-12 (d) shows the temperature dependence of the parameters β and γ, which describe the symmetric and asymmetric broadening of the dielectric response. In addition, Figure 5-12 (e) shows the temperature dependence of the stretched exponential parameter, β_{KWW}. Here, two significant drops in β_{KWW} are observed: one at 112 K, corresponding to the AFM transition, and another at 246 K, indicating a secondary transition. These temperature regions are consistent with the behavior observed in similar samples.

The dielectric results presented here allow the creation of a summary graph of the AFM transition temperature obtained from the dielectric measurements, as a function of the thickness of the CMO thin film (Figure 5-13).

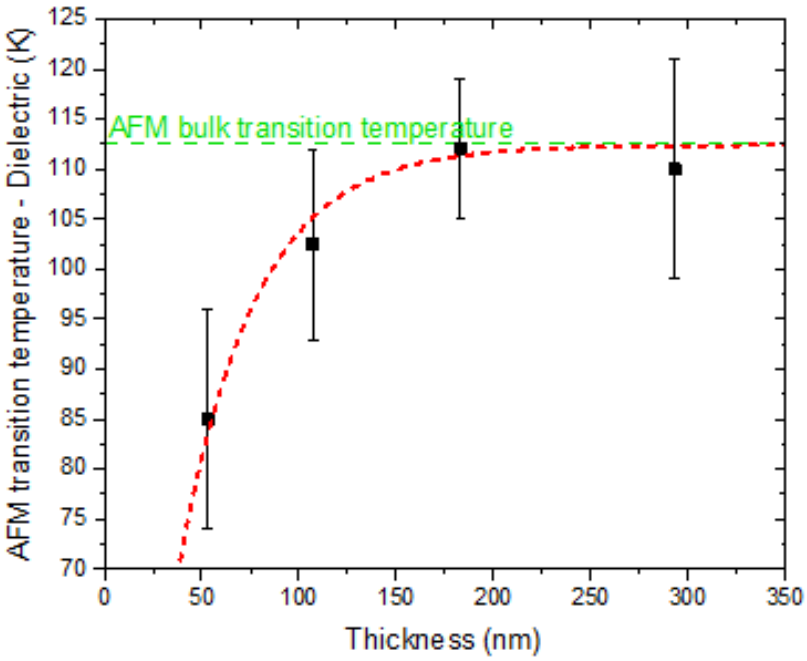


Figure 5-13: AFM transition temperature as a function of the thickness obtained through the dielectric measurements. The thickest sample (305 nm) presented here comes from a study carried out in reference [50]. The dashed red line is a guide to the eye. The dashed green line marks the AFM transition temperature of bulk $Ca_3Mn_2O_7$ [70].

Figure 5-14 compares the AFM transition temperatures obtained through magnetic measurements with the dielectric ones. For thin samples, the AFM temperature transition is significantly lower than the bulk reference value (~112.5 K) [14,18], reaching values below 100 K. With increasing thickness, the transition temperature exhibits a gradual rise until it stabilizes around 112 K, nearing the characteristic

temperature of bulk $Ca_3Mn_2O_7$. This observation applies to all $Ca_3Mn_2O_7$ thin films studied, encompassing both magnetic and dielectric measurements (see Figure 5-14). The consistent trend and similar results across both sets of results suggest the presence of magnetoelectric interactions and magnetically induced enhancement of dipolar correlations. The variations noted in the transition temperature and magnetic-electric correlations suggest that the deformation induced by the $SrTiO_3$ and $SrTiO_3$:Nb substrates in the $Ca_3Mn_2O_7$ thin films enables the manipulation of both the $Ca_3Mn_2O_7$ film's magnetization and polarization.

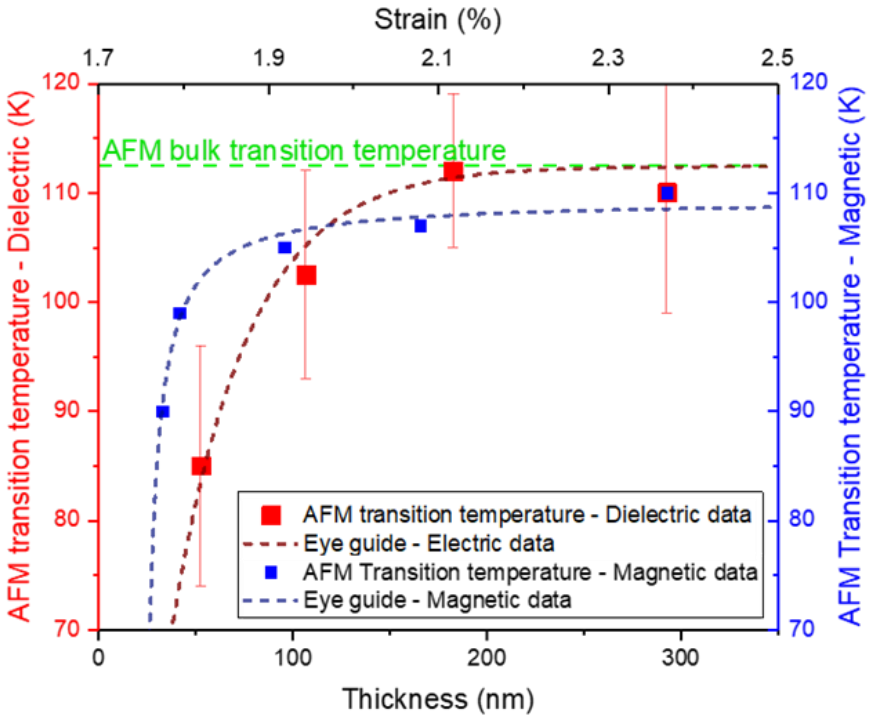


Figure 5-14: Comparison of AFM transition temperatures obtained through magnetic measurements (blue) with dielectric measurements (red). The thickest sample (305 nm) presented here comes from a study carried out in reference [50]. The dashed red and blue lines shall guide the eye. The dashed green line marks the AFM transition temperature of bulk $Ca_3Mn_2O_7$ [70]. The upper axis displays the strain scale, which allows for a direct association with the thickness.

5.3.2. Anomalous temperature region analysis

As previously presented, in samples cCMO-107 (Figure 5-11) and cCMO-183 (Figure 5-12) a temperature-dependent permittivity behavior change was identified for temperatures in the 210-250 K region, depending on the sample strain. In order to deepen the study of this anomalous temperature behavior and complete the results presented previously, other samples were studied in this temperature region. Figure 5-15 and Figure 5-16 present the impedance spectroscopy study carried out on samples cCMO-57 and cCMO-346, respectively. Figure 5-15 and Figure 5-16 present the real (a) and imaginary (b) parts of the permittivity as a function of frequency, and in (c) is the corresponding Nyquist plot. Figure 5-15 (d) and Figure 5-16 (d) show the β and γ parameters values in function of the temperature, and Figure 5-15 (e) and Figure 5-16(e) the corresponding temperature dependence of the stretched exponential parameter. Figure 5-15 (f) and Figure 5-16 (f) present the logarithm of the relaxation times as a function of the inverse of temperature with linear fits of the identified regions. A detailed list of the fitting parameters can be found in Appendix.

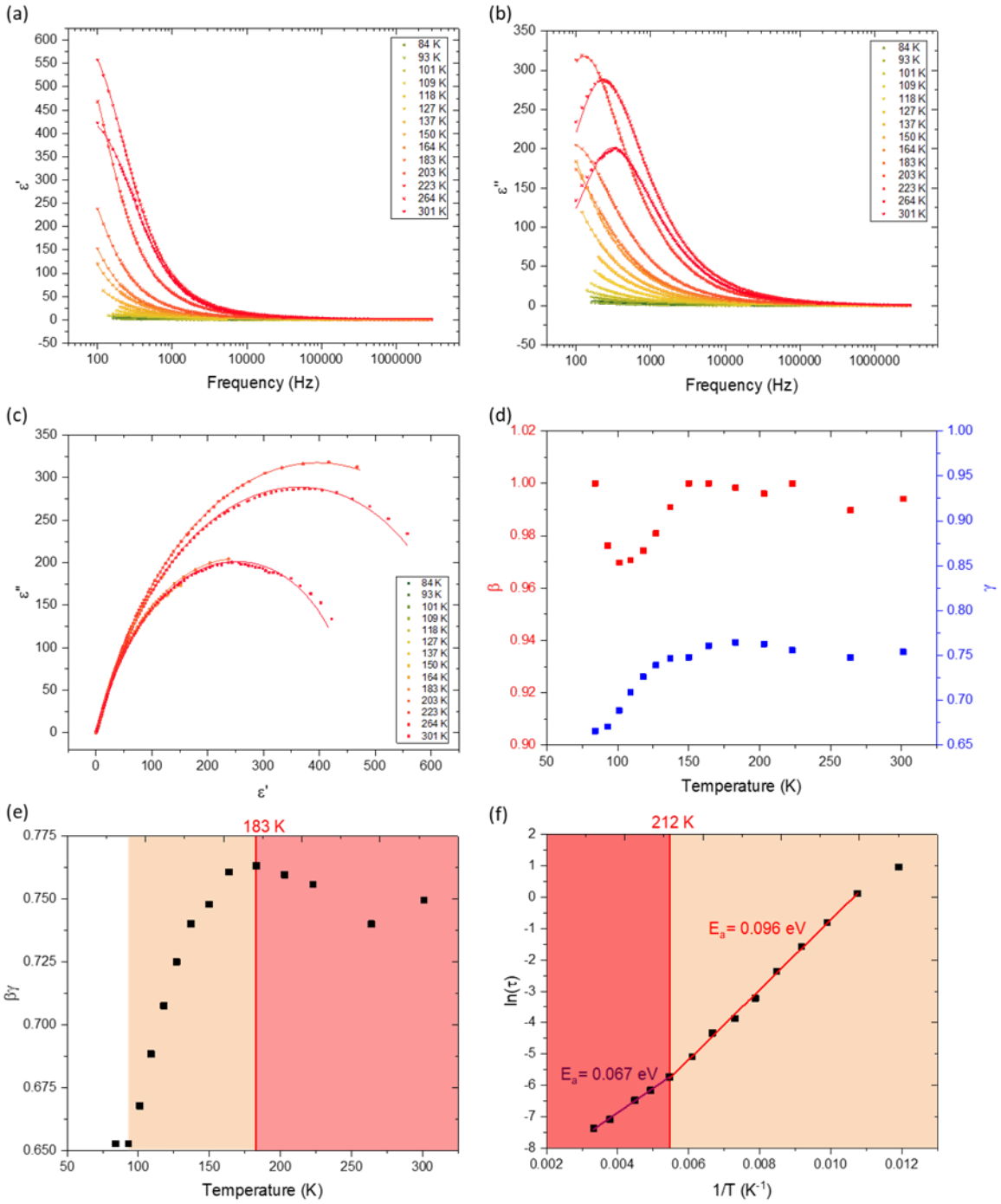


Figure 5-15: Sample cCMO-57. (a) Real and (b) imaginary parts of the permittivity as a function of the HN equation fit. (c) Nyquist plot of the imaginary part as a function of the real part of the complex permittivity at temperatures with the HN equation fit. (d) Parameter β and γ values obtained for the main relaxation. (e) Temperature dependence of the stretched exponential parameter, β_{KWW} with a peak at 183 K. (f) Logarithm of the relaxation times as a function of the inverse of temperature with linear fits for two distinct regions, for temperatures above and below 212 K.

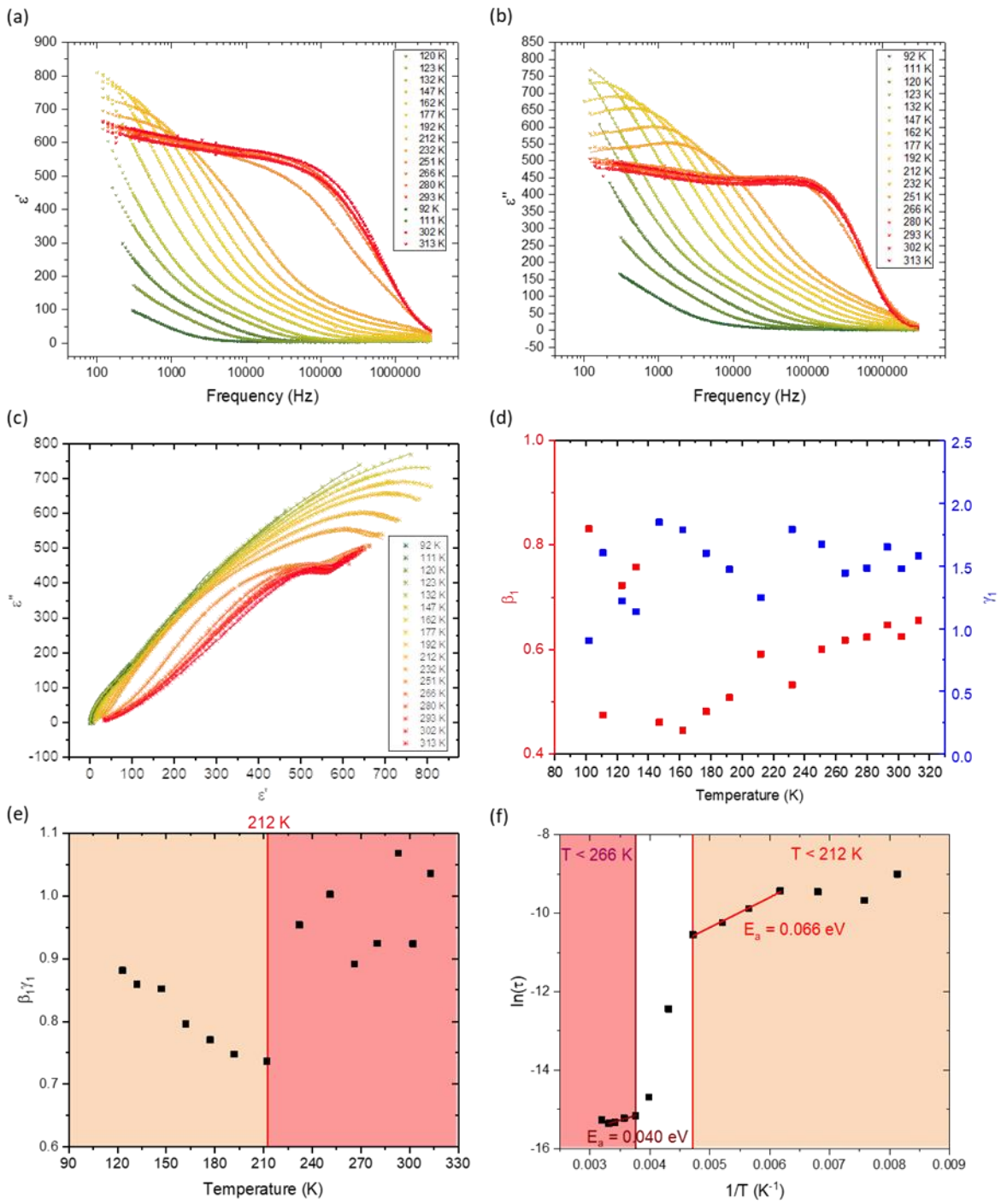


Figure 5-16: Sample cCMO-346. (a) Real and (b) imaginary parts of the permittivity as a function of the HN equation fit. (c) Nyquist plot of the imaginary part as a function of the real part of the complex permittivity at temperatures with the HN equation fit. (d) Parameter β and γ values obtained for the main relaxation. (e) Temperature dependence of the stretched exponential parameter, β_{KWW}, marking an abrupt increase near 212 K. (f) Logarithm of the relaxation times as a function of the inverse of temperature with a linear fit, marking an abrupt increase between 266 and 212 K.

In sample cCMO-57, two distinct regimes were identified, for temperatures below and above T* = 183 K. On the other hand, the cCMO-346 sample analysis also shows two distinct regimes, but for temperatures below and above T* = 212 K. These regime changes appear in the range of temperatures

previously presented in samples cCMO-107 and cCMO-183, describing a similar behavior change in this temperature range. The AFM transition temperature is not shown in these results as it is below the lowest measured temperature. A graph that summarizes the temperature obtained for the thickness dependence of the temperature T* is shown in Figure 5-17.

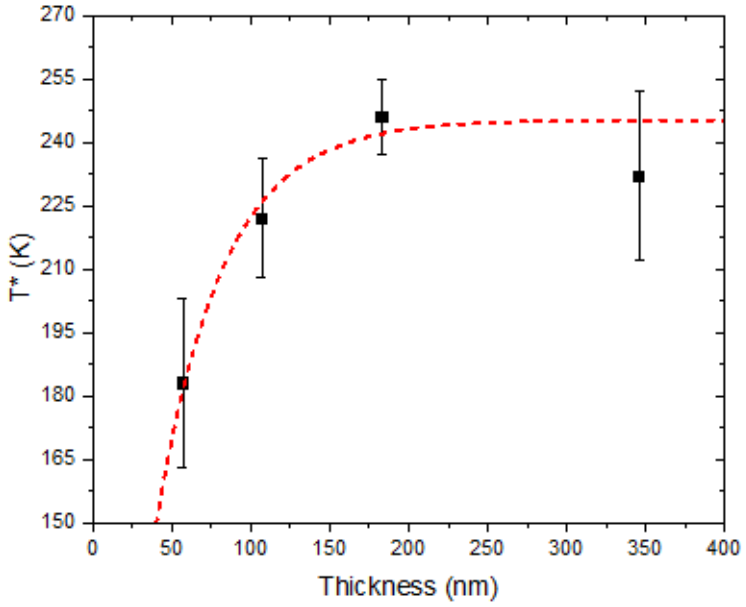


Figure 5-17: Anomalous temperature as a function of the thickness. The dashed red line is a guide to the eye.

Previous studies on the microscopic nature of the ferroelectricity mechanisms in $Ca_3Mn_2O_7$ studied the crystallographic phases of $Ca_3Mn_2O_7$ (refined at 300 K) [55, 69]. These studies indicate that the *A2₁am* phase occurs in the temperature range of 0 K to 350 K and the *Acaa* phase between 200 K and 500 K. This indicates that in this temperature window, ~ 200–350 K, a mixture of the *A2₁am* and *Acaa* structures is possible. More recently, another study investigated the structural phase transition path from the low-temperature polar structure up to the highest symmetric phase in the hybrid improper ferroelectric $Ca_3Mn_2O_7$ compound at the atomic scale using the perturbed angular correlation local probe technique and ab initio electronic structure calculations [18]. Here, the presence of a hybrid improper ferroelectric *A2₁am* phase up to 500 K at local scale was reported in contrast with previous macroscopic results that showed a near full conversion to the *Acaa* phase already at around 350 K.

Considering the above, the anomalous temperature described in Figure 5-17 may be related to the onset of the appearance of the nonpolar *Acaa* phase, which is expected in this temperature range. Regardless of the nature of this process, the anomalous temperature is lower when the CMO is thinner. As the thickness increases, the anomalous temperature exhibits a more gradual rise until it stabilizes around 240 K.

5.3.3. Relaxation times analysis

The relaxation times obtained from the HN fit for the main relaxation process, occurring at higher frequencies, show a thermally activated temperature-dependent behavior. As such, to determine the activation energies (E_a), the Arrhenius equation (Equation (2-47) [85] was considered).

Figure 5-10 (e), Figure 5-11 (e), Figure 5-12 (e), Figure 5-15 (e) and Figure 5-16 (e) show the logarithm of the relaxation times as a function of the inverse of temperature.

In the previous chapter, sample cCMO-305 (305 nm) was studied, and the activation energies were also calculated for each temperature-dependent regime, obtaining $E_{a\,\leq 121K} = 0.084\ eV$ and $E_{a\,\geq 148\,K} = 0.054\ eV$.

Considering the three identified regions, Table 5-2 summarizes the activation energies obtained in the regions and samples where their values could be determined.

Table 5-2: Activation energies (eV) obtained through dielectric characterization of the different samples and considering the distinct temperature regions determined.

Sample	**Activation energies, E_a (meV)**		
	Low T region	Intermediate T region	High T region
cCMO-53	-	-	-
cCMO-57		67	96
cCMO-107	76	-	-
cCMO-183	78	68	111
cCMO-305	54	84	
cCMO-346	-	66	40

The variation in activation energies across the different samples suggests a strong thickness dependence of the dielectric behavior. Thinner films, such as cCMO-53, exhibit distinct characteristics compared to thicker samples like cCMO-183 and cCMO-305. This behavior is expected in thin films due to dimensional confinement and strain effects, which can alter the structural and electronic properties.

The activation energies were determined in three temperature regions: low, intermediate, and high. The absence of E_a values in certain regions (e.g., cCMO-53 and cCMO-107) suggests that relaxation processes in some samples, and the dominant phenomena in those regions are not significant enough to be described by an Arrhenius model. In contrast, samples like cCMO-183 and cCMO-305 exhibit activation energies in multiple regions, indicating complex, multi-step relaxation processes.

The range of activation energies, from 40 meV (cCMO-346 at high temperatures) to 111 meV (cCMO-183 at high temperatures), reflects transitions between different dynamic regimes. These could

correspond to dipolar polarization relaxations at lower temperatures and more complex mechanisms, such as magnetoelectric coupling or magnetic phase transitions, at higher temperatures. The overall range of activation energies, spanning 40 to 111 meV, indicates moderately energetic relaxation processes dominated by thermally activated dynamics. Activation energies below 100 meV are often associated with dielectric and magnetic relaxation phenomena, suggesting relatively low energy barriers in these materials. In several samples, like cCMO-57 and cCMO-183, the activation energy increases at higher temperatures, consistent with the activation of more energetic thermal processes.

In conclusion, these results highlight the complexity of $Ca_3Mn_2O_7$ thin films, where both thickness and temperature play crucial roles in the observed relaxation dynamics. The dependence of activation energies on both parameters may be linked to strain imposed by the substrates and temperature-dependent magnetoelectric interactions.

To obtain a more comprehensive understanding of the observed activation energy values, density functional theory (DFT) calculations were performed, and the corresponding results are presented in the following section.

5.4. Density-functional theory calculations

To better understand the observed variations in activation energies, density functional theory calculations were performed to explore different magnetic orderings in the *Cmcm* and *A2₁am* phases of $Ca_3Mn_2O_7$. In this analysis, the influence of substrate-induced strain was considered using an Ising model [240] with collinear spins, incorporating different magnetic coupling constants for the first (J_1) and second (J_2) neighbors. The transition temperature (T_N) from the antiferromagnetic (AFM) to paramagnetic (PM) states can be estimated by comparing the energies for different magnetic orderings obtained from DFT calculations.

Figure 5-18 shows the variation of T_N (ΔT_N, where $\Delta T_N = 0$ K represents the zero-strain transition temperature) as a function of the calculated substrate imposed in-plane strain. The DFT calculations are performed at 0 K, meaning the resulting magnetic couplings are approximations of their finite-temperature ($T \neq 0$ K) counterparts.

The effect of both comprehensive and tensile strain on ΔT_N is demonstrated. The linear strain-dependent trend reveals that the calculated T_N decreases with increasing out-of-plane expansion strain (corresponding to in-plane compression), and increases as the strain shifts toward compressive, a trend also observed experimentally from XRD results. There, an expansion strain along the growth direction of

the films was observed, due to the presence of compressive in-plane stresses, which lead to a decrease in T_N. The observed ΔT_N dependence on strain reveals a clear magneto-elastic effect in this material. Thus, the dependence on strain not only highlights a distinct magneto-elastic effect but also confirms the potential to precisely control T_N through strain engineering.

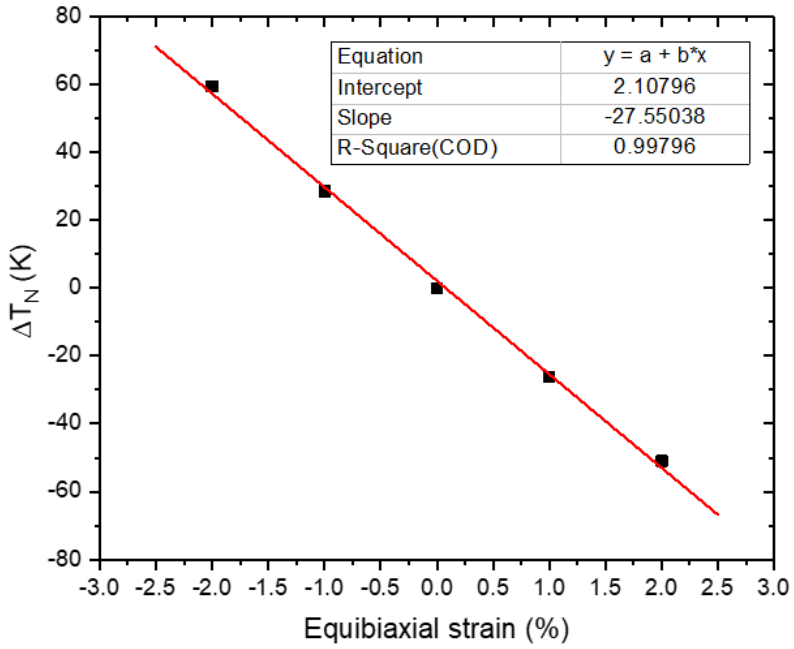


Figure 5-18: Variation of the antiferromagnetic to paramagnetic transition temperature ΔT_N as a function of the calculated substrate-imposed in-plane strain for $Ca_3Mn_2O_7$ thin films. Here, $\Delta T_N = 0$ K represents the zero-strain transition temperature, introduced to emphasize the relative changes in T_N due to strain rather than absolute values.

The $SrTiO_3$ substrates with a (100) orientation used in this study primarily induce in-plane compressions stresses, leading to a decrease in the transition temperature. For practical applications, however, increasing the transition temperature would be desirable. One potential approach to achieve this is by changing the substrate orientation, as this can significantly influence the type and magnitude of the strain imposed on thin films. Orientations such as (110) or (111) may introduce alternative stress configurations, potentially generating in-plane tensile stress and out-of-plane compressive strain, which may enhance transition temperature.

To explore this possibility, the next chapter investigates $Ca_3Mn_2O_7$ thin films deposited on $SrTiO_3$ substrates with (111) and (110) orientations, studying their impact on the structural and dielectric properties.

6. Calcium Manganese Oxides: Influence of Substrate Orientation

The previous chapter highlighted the impact of strain induced by $SrTiO_3$ substrates with a (100) orientation on the magnetic and dielectric properties of $Ca_3Mn_2O_7$ thin films. These substrates were found to induce compressive strains within the plane of the films, leading to an out-of-plane expansion. This specific strain configuration was shown to lower the Néel transition temperature underscoring the strong dependence of the material's multiferroic behavior on substrate-induced strain. However, this outcome also reveals a limitation: the (100) orientation of $SrTiO_3$ substrates. While effective in stabilizing the $Ca_3Mn_2O_7$ phase in the films, it inadvertently reduces the Néel transition temperature, which is less favorable for practical applications.

To overcome this limitation, it is worth exploring alternative substrate orientations, such as (111) and (110). These orientations have the potential to modify the strain profile by introducing different stress configurations. For instance, they might induce tensile stress within the plane of the film, paired with compressive strain out of the plane, which could lead to an increase in transition temperature. Such changes in the strain environment present an opportunity to fine-tune the multiferroic properties of $Ca_3Mn_2O_7$, making the material more suitable for technological applications.

6.1. Structural Characterization

Two thin films of $Ca_3Mn_2O_7$ (CMO), were deposited on $SrTiO_3$ substrates with orientations (110) and (111). The films were produced using the same pulsed laser deposition system and under the optimal deposition conditions determined in section 4.1 “Thin film synthesis”, using the same target. The deposition process involved a repetition rate of 6 Hz, a target-substrate distance of 6 cm, and a fluence of 3.4 J/cm^2. The oxygen pressure during film preparation was held at 10^{-2} mbar, with a deposition temperature of 730 °C. Each deposition lasted 20 minutes, with the estimated film thickness ranging between 80 and 110 nm. Then, the films were cooled to room temperature at a rate of 10 °C/min in an oxygen atmosphere at ambient pressure. The samples underwent annealing at 900 °C for 2 hours in air, with a heating rate of 10 °C/min. These samples were designated as STO(111)CMO1 and STO(110)CMO2.

Figure 6-1 shows the X-ray diffraction measurements performed on the samples STO(110)CMO1 and STO(111)CMO2. The vertical red and blue lines indicate the peak positions of $Ca_3Mn_2O_7$ with the *Acaa* orthorhombic structure [228] and of the ferroelectric *A2$_1$am* orthorhombic structure [229], respectively.

In Figure 6-1 (a) and (b), the vertical green lines indicate the peak positions of the $SrTiO_3$ substrates with orientations (110) and (111), respectively.

For the film deposited on $SrTiO_3$ substrates with (110) orientation, the observed diffraction peaks, which may correspond to either *A2₁am* (020) or (200) and (002) or (020) atomic planes, as well as additional peaks from *A2₁am* (040) or (400) and (004) or (040) atomic planes, suggest that the film exhibits a preferred orientation during growth. The proximity of the reference peaks makes it difficult to quantify the degree of the structural mix.

In contrast, for the film deposited on the (111)-oriented substrate, no distinct diffraction peaks from $Ca_3Mn_2O_7$ were observed, suggesting that the film did not form a well-defined crystalline structure. This absence of crystallinity can be attributed to the strain configuration at the interface between the film and the (111) substrate, which may have interfered with the film's ability to form a dense, ordered crystal structure. Despite having an adequate amount of material, the film seems to exhibit structural disorder, preventing the detection of significant diffraction peaks typically associated with a crystalline phase.

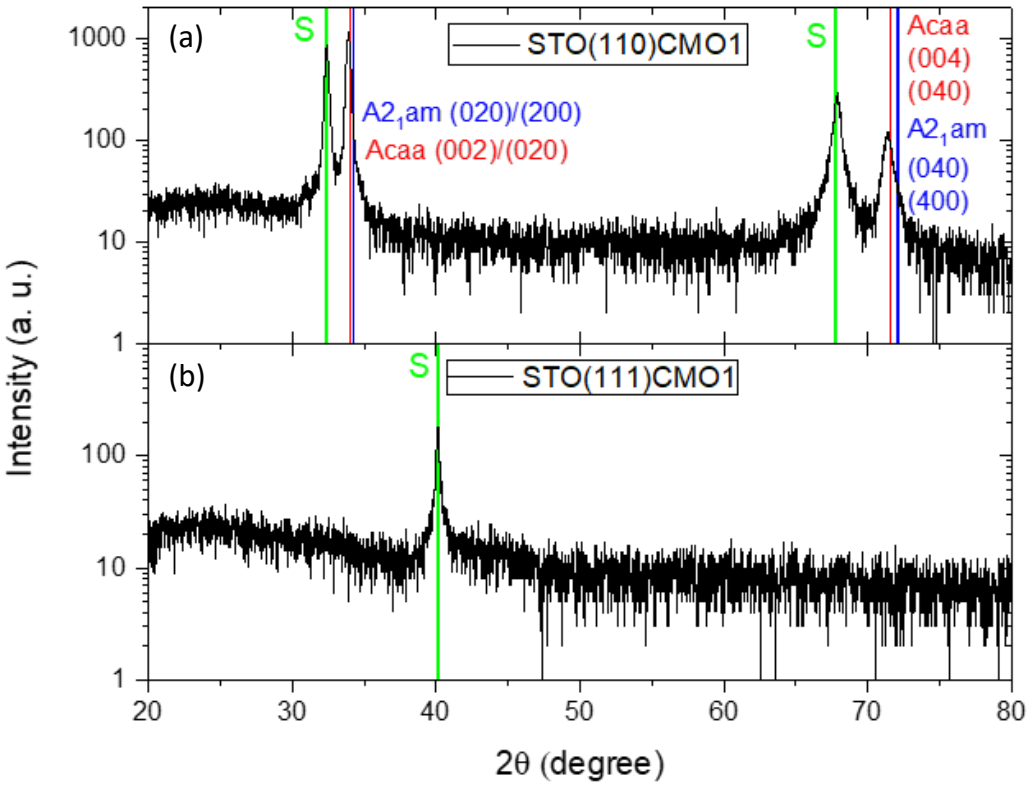


Figure 6-1: X-ray diffraction spectra measured on the samples prepared on $SrTiO_3$ substrates with orientations (a) (110) and (b) (111). The vertical green lines mark the reference diffraction peaks of the respective substrates

(marked with "S"). The vertical red and blue lines indicate the peak positions of $Ca_3Mn_2O_7$ with the orthorhombic structure [228] and of the ferroelectric *A2₁am* orthorhombic structure [229], respectively

Based on these results, from this point forward, the focus will be on studying the dielectric properties of films deposited on (110) oriented substrates. The study of films grown on (111) substrates will be suspended, as the film did not show an oriented growth up to now.

6.2. Dielectric characterization

To understand the influence of substrate orientation on the electric polarization and coupled magnetic-electric behavior of the $Ca_3Mn_2O_7$ thin films and to compare with previously presented results, two new thin films of $Ca_3Mn_2O_7$ were deposited on Nb-doped (110) $SrTiO_3$ substrates. The 1.4 at% niobium doping of the (110) $SrTiO_3$:Nb substrates gives them conductivity, enabling their use in dielectric measurements while preserving the same crystalline properties as (110) $SrTiO_3$. The samples studied in the dielectric measurements are identified in Table 6-1 (substrate (110) $SrTiO_3$:Nb), providing insights into their average thickness.

Table 6-1: Details of the substrate used, produced samples and the corresponding thicknesses of the $Ca_3Mn_2O_7$ thin films.

Substrate	**Sample**	**$Ca_3Mn_2O_7$ thin film thickness (nm)**
(110) $SrTiO_3$:Nb	(110)STOcCMO-100	100.5
	(110)STOcCMO-112	112.2

Figure 6-2 and Figure 6-3 shows the SEM cross-section of the samples (110)STOcCMO-100 and (110)STOcCMO-112, respectively. The film exhibits a uniform thickness across the sample area, with only slight local variations attributed to surface roughness.

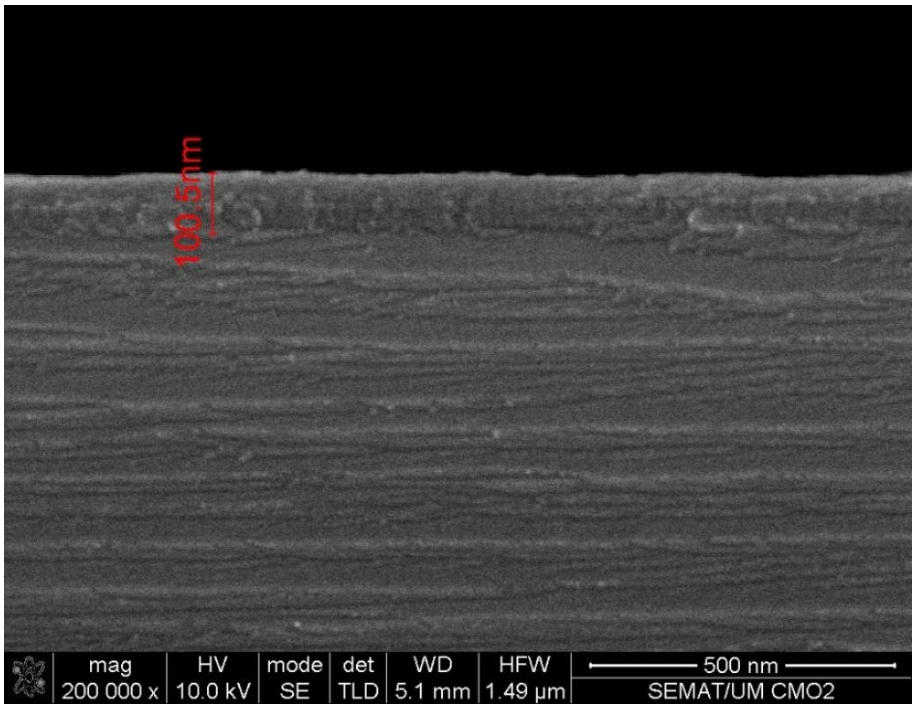


Figure 6-2: SEM micrograph of the cross-section of the sample (110)STOcCMO-100 prepared over (110) $SrTiO_3$:Nb substrate.

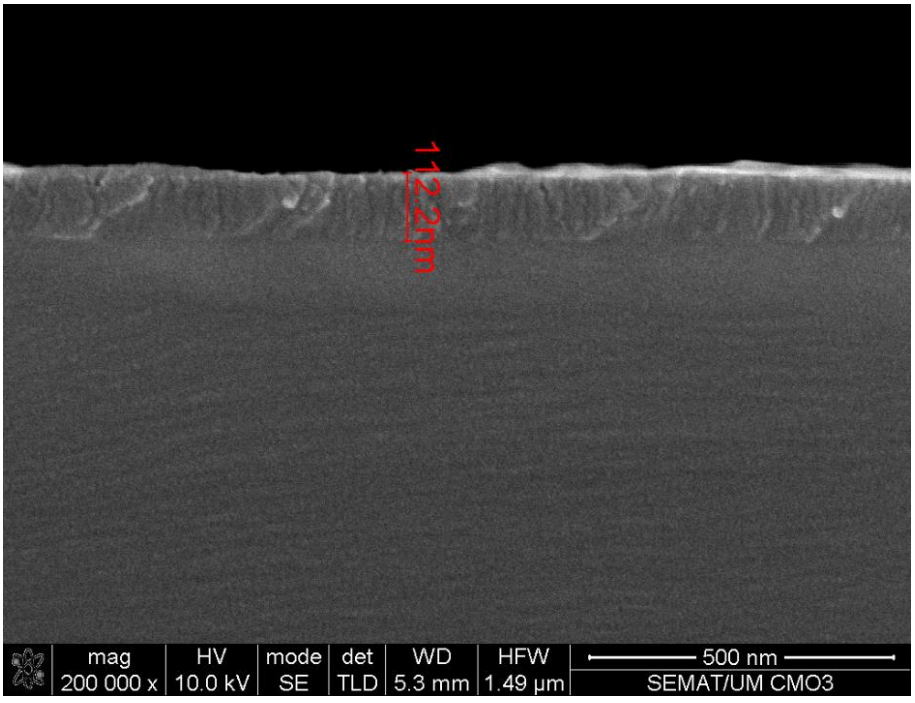


Figure 6-3: SEM micrograph of the cross-section of the sample (110)STOcCMO-112 prepared over (110) $SrTiO_3$:Nb substrate.

These films were analyzed through impedance spectroscopy to systematically investigate their dielectric properties. The measurements were performed at temperatures ranging from approximately 50 K to 300 K and across a frequency range from 20 Hz to 3 MHz. Figure 6-4 and Figure 6-5 present the

dielectric analysis of the samples (110)STOcCMO-100 and (110)STOcCMO-112, respectively. The observed relaxations exhibit broad characteristics, implying a distribution of relaxation times and the presence of correlated dipole interactions. Therefore, the HN model function with two relaxation times was considered (Equation (4-1)). The real and imaginary parts of the permittivity as a function of frequency, at fixed temperatures, were fitted using this model, as illustrated in the (a) and (b) panels of Figure 6-4 and Figure 6-5. Additionally, the corresponding Nyquist plots with the HN equation fits are presented in the (c) panels of these figures. The parameters β and γ are shown as a function of temperature in Figure 6-4 (d) and Figure 6-5 (d). The temperature dependence of the stretched exponential parameter, β_{KWW}, is presented in Figure 6-4 (e) and Figure 6-5 (e). A detailed list of the fitting parameters can be found in Appendix.

The (110)STOcCMO-100 and (110)STOcCMO-112 samples exhibit two distinct dielectric relaxation processes, as presented in Figure 6-4 and Figure 6-5. These findings are in line with previous analyses of films deposited on (100) $SrTiO_3$:Nb substrates.

In the case of (110)STOcCMO-100 (Figure 6-4), the first relaxation process presents a change of behavior at approximately 124 K, indicating the onset of the transition to the antiferromagnetic phase, similar to what was observed in the other CMO films at low temperature. However, here, this temperature is significantly higher than the bulk Néel temperature ($T_N \sim 112.5$ K) [70]), highlighting the role of the (110)-oriented substrate in raising the transition temperature. The second relaxation, occurring around 242 K, marks the appearance of the *Acaa* phase and the onset of the coexistence with *A2₁am* phase. The relaxation times derived from the HN fit for the primary relaxation process, observed at higher frequencies, exhibit a temperature-dependent behavior consistent with thermal activation. Here, the activation energy calculated is 61 meV, reflecting the energy barrier associated with ferroelectric switching in the antiferromagnetic phase. This value falls within the range reported for the same temperature regime for substrates with (100) orientation, as presented in Table 5-2 (58–78 meV). At intermediate temperature regime, an activation energy of 25 meV was obtained.

For (110)STOcCMO-112 (Figure 6-5), a similar behavior is observed. The first relaxation process takes place at approximately 145 K, and the second occurs near 198 K. As with (110)STOcCMO-100, these transitions mark the appearance of the antiferromagnetic phase and the onset of the coexistence of the *A2₁am* and *Acaa* phases, as the temperature increases. The activation energy for (110)STOcCMO-112,

calculated as 43 meV, is within the same order of magnitude as the ferroelectric switching barriers reported for the same temperature regime for substrates with (100) orientation (see Table 5-2).

The dielectric data reveals a clear phase evolution, consistent with the behavior observed in the samples discussed in previous chapters. At low temperatures, the material predominantly exhibits the $A2_1am$ phase. As the temperature increases, the relaxation behavior reflects the transition from the antiferromagnetic to a paraelectric phase, showing clear magnetoelectric interactions in the films. At even higher temperatures, the *Acaa* phase appears and the coexistence between the $A2_1am$ and $A2_1am$ phases occurs, which remains up to room temperature as observed from the X-ray diffraction and Raman data in the films.

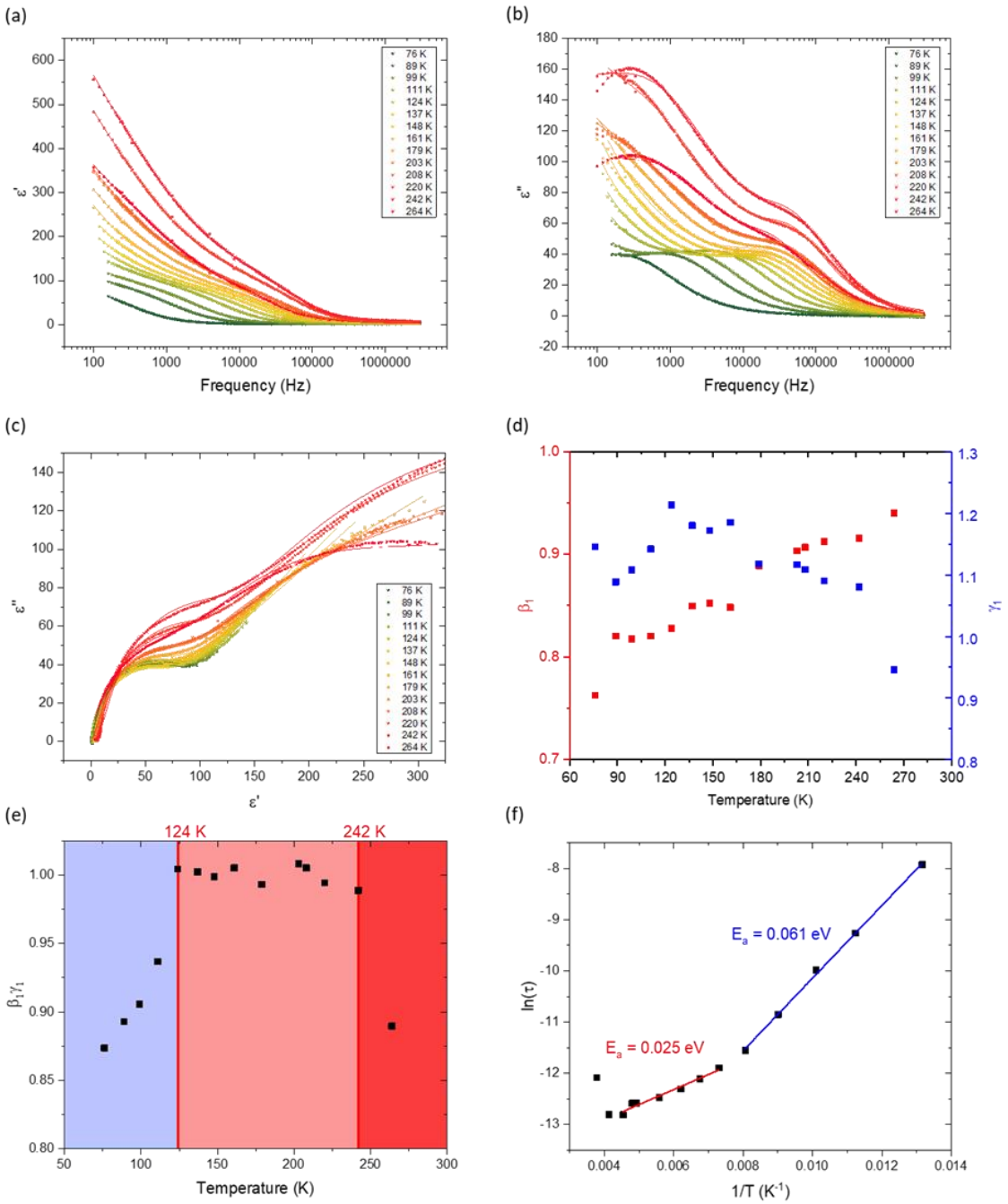


Figure 6-4: Sample (110)STOcCMO-100. (a) Real and (b) imaginary parts of the permittivity as a function of the HN equation fit. (c) Nyquist plot of the imaginary part as a function of the real part of the complex permittivity at temperatures with the HN equation fit. (d) Parameter β and γ values obtained for the main relaxation. (e) Temperature dependence of the stretched exponential parameter, β_{KWW}, marking an abrupt decrease near 124 K and a new increase at 242 K. f) Logarithm of the relaxation times as a function of the inverse of temperature with linear fit corresponding to the AFM region.

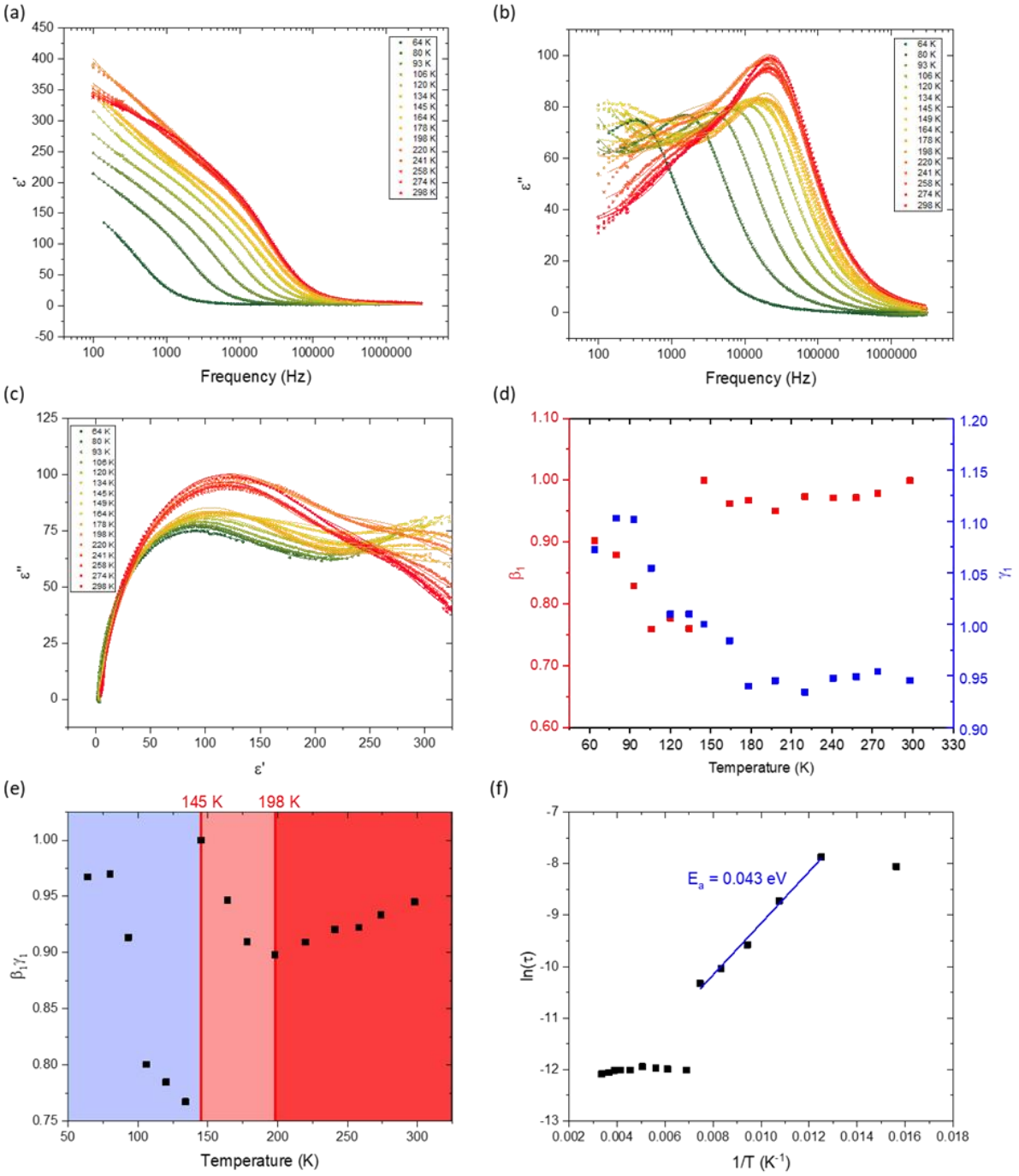


Figure 6-5: Sample (110)STOcCMO-112. (a) Real and (b) imaginary parts of the permittivity as a function of the HN equation fit. (c) Nyquist plot of the imaginary part as a function of the real part of the complex permittivity at temperatures with the HN equation fit. (d) Parameter β and γ values obtained for the main relaxation. (e) Temperature dependence of the stretched exponential parameter, β_{KWW}, marking an abrupt decrease near 124 K and a new increase near 198 K. f) Logarithm of the relaxation times as a function of the inverse of temperature with linear fit corresponding to the AFM region.

The diagram present in Figure 6-6 serves as a visual synthesis of the key observations and results for the (110)STOcCMO-112 sample, providing a concise representation of the phase transitions and associated regimes as a function of temperature. This figure not only highlights the observed ferroelectric

(FE) and antiferromagnetic (AFM) phases but also maps their evolution through the temperature range investigated. At low temperatures (T < 145 K), the material exhibits a coexistence of FE and AFM orders within the *A2₁am* phase, consistent with the magnetoelectric interactions observed in these films. As the temperature rises, at approximately 145 K, a transition occurs where the AFM order disappears, leaving the system in a purely FE state while still within the *A2₁am* phase. A second transition, observed around 198 K, marks the appearance of the phase, leading to a coexistence between the *A2₁am* and *Acaa* phases at higher temperatures. This behavior persists up to room temperature, as corroborated by complementary structural analyses (XRD and Raman spectroscopy).

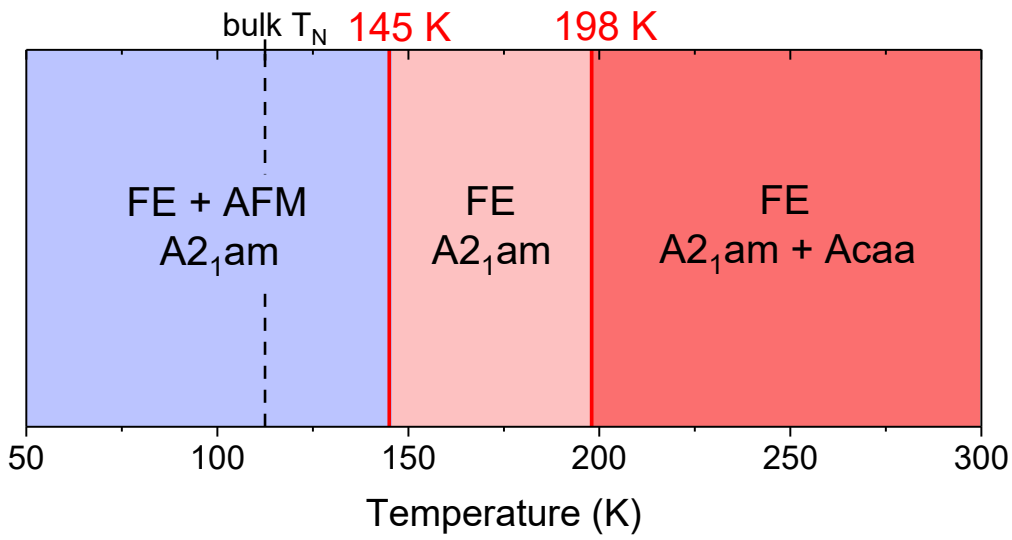


Figure 6-6: Phases diagram and space groups of the regimes observed for the (110)STOcCMO-112 sample. At low temperatures, the material exhibits a coexistence of ferroelectric (FE) and antiferromagnetic (AFM) orders within the *A2₁am* phase. A transition occurs at 145 K, leading to a purely FE state, followed by the appearance of the *Acaa* phase at 198 K, which coexists with the *A2₁am* phase at higher temperatures.

The increase in transition temperatures observed in these samples underscores the substantial influence of substrate orientation on the dielectric properties of $Ca_3Mn_2O_7$ thin films. Compared to (100)-oriented substrates, the (110)-orientation leads to a pronounced improvement in the dielectric transition temperatures. The ability to significantly increase the magnetic transition temperatures by using (110)-oriented substrates, to strain tune the films properties and to electrically detect their magnetic behavior through impedance spectroscopy represents a promising path to optimize these materials for practical applications, as they allow to aim towards room temperature magneto-electric devices and magnetoelectricity.

7. Conclusions

Thin films of calcium manganese oxide ($Ca_3Mn_2O_7$) were synthesized on $SrTiO_3$ (STO) substrates using pulsed laser deposition under various preparation conditions. SEM analysis revealed that the films exhibited a dense and homogeneous morphology. At low laser fluences, high oxygen pressures, and without post-deposition heat treatment, the films stabilized in the $CaMnO_3$ *Pnma* orthorhombic structure. As the laser fluence increased and oxygen pressure decreased, the Ca ratio adjusted towards the improper 3:2 $Ca_3Mn_2O_7$ ferroelectric Ruddlesden-Popper n = 2 phase, achieved through post-deposition annealing at 900°C. X-ray diffraction and Raman spectroscopy confirmed the presence of the intermediate-temperature $Ca_3Mn_2O_7$ phase alongside the low-temperature ferroelectric *A2₁am* $Ca_3Mn_2O_7$ structure, exhibiting a preferential [111] growth orientation.

Dielectric properties of the films showed a pronounced frequency-dependent step-like change due to increased polar interactions in the ferroelectric phase at low temperatures. A Havriliak-Negami function with two relaxation times was fitted to the frequency-dependent permittivity at different temperatures, indicating two distinct regimes: one below 107 K, corresponding to the films' antiferromagnetic (AFM) transition, and another above 121 K. From the Kohlrausch-Williams-Watts function, an abrupt decrease of the stretched exponential parameter below ~ 110 K was observed in the AFM phase, suggesting magnetoelectric interactions and magnetically induced enhancement of dipolar correlations with decreasing temperature.

Furthermore, structural, magnetic, and dielectric properties of $Ca_3Mn_2O_7$ thin films with varying thicknesses deposited on STO substrates were investigated. XRD analysis confirmed that the $Ca_3Mn_2O_7$ films stabilized in the ferroelectric *A2₁am* orthorhombic phase, which coexist with the *Acaa* phase. Thinner films exhibited higher substrate-induced strain, resulting in significant interplanar spacing variations, whereas thicker films showed relaxation towards bulk material characteristics. This strain-related effect was further supported by SEM and FIB-SEM observations, showing that the surface morphology and film relaxation varied notably with thickness, influencing overall material properties.

Magnetic measurements indicated that the AFM Néel temperature (T_N) increased from 90 K in the thinnest films to 110 K in the thicker films, approaching the bulk value. Density Functional Theory (DFT) calculations aligned well with experimental findings, indicating that strain affects the energy landscape between AFM and paramagnetic states, thus effectively tuning T_N. The magnetic coupling constants derived from DFT highlights that even small strain variations can impact magnetic ordering, reinforcing the potential of strain engineering as a tool for modulating magnetic properties in multiferroic materials.

Dielectric permittivity analyses revealed non-Debye relaxation behaviors, indicating the presence of dipole correlations and stretched exponential behaviors. Additionally, the Kohlrausch-Williams-Watts stretched exponential parameter displayed abrupt changes near the AFM transition temperatures, indicative of strong magnetoelectric interactions. The AFM transition temperatures and dielectric permittivity behaviors exhibited a clear thickness dependence: thinner films showed lower transition temperatures and enhanced substrate-induced strain effects. Anomalous dielectric behaviors observed between 180 K and 240 K, linked to the onset of the nonpolar *Acaa* phase, were also thickness dependent.

DFT calculations provided further insight, supporting the experimental findings by confirming the presence of both magnetoelectric and magnetoelastic effects in $Ca_3Mn_2O_7$ thin films. Calculated transition temperatures and activation energies were consistent with experimental observations, elucidating strain effects on magnetic and ferroelectric properties. Furthermore, these calculations suggest that strain-mediated control of the magnetic and ferroelectric orders could be a promising approach for enhancing room-temperature multiferroicity in this system.

The dielectric analysis of $Ca_3Mn_2O_7$ thin films over (110) $SrTiO_3$:Nb substrates exhibits a broad profile, suggesting a range of relaxation times and evidence of correlated dipole interactions. The results reveal a clear phase evolution, with antiferromagnetic transitions observed at higher temperatures ($T_N = 124$ K and $T_N = 145$ K) when compared to $Ca_3Mn_2O_7$ thin films on (100) $SrTiO_3$:Nb substrates. The samples exhibited distinct dynamic behavior with temperature, with the *A2₁am* phase predominating at low temperatures, followed by the coexistence of the *A2₁am* and *Acaa* phases up to room temperature. The observed Néel transition temperature, which exceeds the bulk material transition ($T_{N,Bulk} \sim 112.5$ K) [70]), suggests that the (110) substrate orientation favors greater stability of both ferroelectric and antiferromagnetic phases, a key feature for future applications in multiferroic devices. The activation energy calculations fall within the range observed for (100) oriented substrates.

In conclusion, the present research reveals that the strain induced by substrate in $Ca_3Mn_2O_7$ films has a great impact on the multiferroic properties of the films. The strain can be controlled by the film thickness, therefore affecting the magnetic and dielectric properties which in turn enhance the multiferroic properties. The results from this study also highlight the promising increase in transition temperature when using the (110) $SrTiO_3$:Nb substrates, with the transition temperature observed in the films approaching values significantly higher than the bulk material. This suggests that it may be possible to improve the multiferroic properties of $Ca_3Mn_2O_7$ films towards room temperature magnetoelectricity, for their use in emerging electronic and spintronic devices in which magnetic and electric properties are

desired to be manipulated with low energetic costs. Due to their adjustable magnetic and dielectric aspects, these films are expected to find future applications in memory devices, sensors, and actuators that require precise tuning of electric and magnetic responses. The ability to control strain and thickness also provides additional scope for the enhancement of these materials for use in applications that require multiple functionalities within a single material.

8. Critical Analysis and Future Perspectives

Having presented the conclusions of this study, it is now important to critically analyze the main results obtained and contextualize them within the current state of development in the field. This chapter will explore the implications of the findings and address how these results could help overcome some of the current challenges in the field and contribute to advancing research in multiferroic materials. In addition, it will discuss possible directions for future work.

In multiferroic systems, the interplay between magnetic and electric properties is essential for the development of advanced memory devices. For $Ca_3Mn_2O_7$, magnetic and electric behaviors are closely linked to the alignment of electron spins, which can be manipulated by magnetic and electric fields. The transition temperature, at which the material shifts from an ordered to a disordered state, plays a critical role, as it directly impacts the stability of information storage. For spin-based memory devices, precise adjustment of the transition temperature is essential to ensure that the alignment of the spins remains stable and reliable.

A major achievement of this study was the successful synthesis of $Ca_3Mn_2O_7$ thin films, a material that had not been previously reported in thin film form. This accomplishment is significant because thin film fabrication allows for better control over the material's properties, enabling its application in microelectronics, information storage and spintronic devices. Furthermore, it was demonstrated that the antiferromagnetic transition temperature of $Ca_3Mn_2O_7$ can be effectively tuned by using $SrTiO_3$ substrates.

Additionally, the choice of substrates with different crystallographic orientations, such as $SrTiO_3$ with a (110) orientation, proved crucial. This change in substrate orientation caused a significant modification in the transition temperature, ultimately leading to an increase in the transition temperature of $Ca_3Mn_2O_7$. These results demonstrate that controlling the strain induced by the substrate has a direct impact on the material's properties. Precisely tuning the transition temperature, achieved through strain control, is vital for creating multiferroic devices with adaptable characteristics, essential for applications in spintronics and data storage.

These advancements mark a step toward the development of high-performance memory devices, as the transition temperature plays a central role in the stability and efficiency of information storage. The ability to control the transition temperature through strain control and appropriate substrate selection opens new possibilities for the creation of faster memory devices with higher storage capacity. In a multiferroic device, simultaneous reading and writing are possible due to the separation of magnetic and electric properties. Information can be read using a magnetic field, which manipulates the alignment of

spins, while an electric field can be employed to write or modify information by altering the material's polarization state. This ability to perform both operations in parallel is crucial for the efficiency and speed of memory devices, enabling simultaneous reading and writing, which is a desired feature for the next generation of data storage systems. Thus, the precise tuning of the transition temperature, combined with the manipulation of magnetic and electric properties, represents a significant step forward in the development of efficient, stable, and high-capacity memory and sensor technologies.

Looking ahead, there are several promising directions for future research in the field of multiferroic materials and their potential applications in devices. One area to explore is the development of alternative substrates, such as those with different crystal symmetries or more advanced epitaxial techniques, which could further enhance the control over strain and improve the stability of the transition temperature. This could be complemented by strain engineering strategies, using buffer layers or multilayer structures to more precisely tune the strain in $Ca_3Mn_2O_7$ films. Additionally, doping strategies could be employed to modulate the electronic and magnetic interactions, potentially leading to the stabilization of multiferroicity near room temperature. This would open the door for applications in various fields, such as memory devices, magnetic sensors and energy-efficient microelectronic systems.

9. Appendix: Fitting Parameters from Dielectric Measurements

This appendix presents the parameters obtained from the fitting of the dielectric permittivity data using the Havriliak–Negami function. For each sample and temperature, the parameters were extracted by fitting both the real and imaginary parts of the permittivity.

Although the fitting procedure suggested the presence of a secondary relaxation process, only the parameters corresponding to the main relaxation are reported here. The secondary contributions were not included due to their very low intensity and high associated uncertainty. The samples are presented in the order in which they appear throughout work.

cCMO-305

Table 9-1: Fitting parameters obtained from the Havriliak–Negami model for the dielectric response of sample cCMO-305 at various temperatures.

Temperature (K)	β	γ	τ	ε_∞	$\Delta\varepsilon$
242	0.95085	1.05433	1.37E-05	6.66097	554.0568
202	0.9471	1.0558	3.05E-05	2.30647	575.4909
169	0.94164	1.06504	8.31E-05	5.20996	604.9925
148	0.93772	1.06949	1.63E-04	6.59863	617.1651
121	0.9235	1.08296	8.01E-04	10.54396	647.6051
107	0.91955	1.08716	0.00133	7.66523	648.0939
97	0.90566	1.1041	0.00237	7.98634	650.5755
87	0.87098	1.13448	0.00545	7.27837	669.3779
68	0.82655	1.18651	0.03722	8.31835	855.1047

cCMO-53

Table 9-2: Fitting parameters obtained from the Havriliak–Negami model for the dielectric response of sample cCMO-53 at various temperatures.

Temperature (K)	β	γ	τ	ε_∞	$\Delta\varepsilon$
272	1	0.35637	0.00346	1	198.5653
252	1	0.34358	0.00366	1	181.3361
206	1	0.34955	0.00176	1	101.6044
184	1	0.37174	0.00167	1	107.9472
170	1	0.39772	0.00172	1	114.9805
161	1	0.40709	0.00194	1	121.9394
149	1	0.43816	0.00187	1	128.1201
138	1	0.45378	0.00219	1	131.1882

129	1	0.4693	0.00275	1	134.2337
126	1	0.47092	0.00295	1	136.6588
113	1	0.48724	0.00329	1	146.4331
103	1	0.50729	0.00285	1	145.1784
96	1	0.56325	0.0019	0.5214	146.3858
85	1	0.70978	0.0017	1.00087	126.1471
66	1	0.95757	5.15E-04	1.17792	92.72103
55	1	0.97993	5.46E-04	1.1703	94.44061
45	1	0.99535	7.64E-04	1.1044	196.6291
34	0.99803	0.9994	8.01E-04	1.09097	235.9566

cCMO-107

Table 9-3: Fitting parameters obtained from the Havriliak–Negami model for the dielectric response of sample cCMO-107 at various temperatures.

Temperature (K)	β	γ	τ	ε_∞	$\Delta\varepsilon$
300	0.9655	0.90047	4.68487E-6	0	94.32196
291	0.95928	0.89651	4.68912E-6	0	92.79747
281	0.94188	0.90052	4.60232E-6	0	93.31304
268	0.92283	0.9097	4.54606E-6	0	92.6582
236	0.88864	0.91252	4.99985E-6	0	92.91572
222	0.86196	0.92734	5.31945E-6	0	95.36432
208	0.82198	0.97972	5.69135E-6	0	94.45605
184	0.76457	1.07276	6.99969E-6	0	106.49631
166	0.76183	1.09993	8.5117E-6	0	94.02685
152	0.75109	1.14423	1.124E-5	0	92.46708
142	0.7462	1.1747	1.49827E-5	0	90.16067
131	0.73771	1.26922	1.76099E-5	0	75.9722
117	0.72503	1.34621	3.21899E-5	0.24839	75.62421
112	0.73526	1.33877	4.42478E-5	0.63266	72.64317
105	0.7551	1.29315	7.74308E-5	0.94609	68.55626
93	0.84205	1.10965	2.59191E-4	1.11045	56.63067
84	0.8579	1.08251	6.05045E-4	1.09623	38.60008

cCMO-183

Table 9-4: Fitting parameters obtained from the Havriliak–Negami model for the dielectric response of sample cCMO-183 at various temperatures.

Temperature (K)	β	γ	τ	ε_∞	$\Delta\varepsilon$
306	0.79412	1.26	5.36E-07	0	857.7246
299	0.77048	1.3	5.41E-07	0	928.0625
285	0.79598	1.14653	6.62E-07	0	806.9597
270	0.8108	1.04673	7.91E-07	0	777.8479
255	0.7952	0.98946	9.39E-07	0	888.934
246	0.84088	0.79826	1.38E-06	0	764.3253
237	0.80777	1.03149	1.48E-06	0	695.7858
152	0.74649	1.35	1.04E-05	0	456.4636
142	0.74359	1.355	1.46E-05	0	417.8854
131	0.77526	1.30765	2.3E-05	0	345.2454
121	0.7778	1.286	4.07E-05	0	298.1491
112	0.74533	1.34527	6.49E-05	0	338.3162
101	0.46241	2.07546	4.55E-05	0	185.1365
90	0.34366	2.62833	5.58E-05	0	281.6079
80	0.30341	2.49021	0.000396	0	436.8993
70	0.30648	2.31299	0.00339	0	518.968

cCMO-57

Table 9-5: Fitting parameters obtained from the Havriliak–Negami model for the dielectric response of sample cCMO-57 at various temperatures.

Temperature (K)	β	γ	τ	ε_∞	$\Delta\varepsilon$
301	0.99407	0.75404	6.27E-04	0.45796	459.1486
264	0.98975	0.74775	8.46E-04	0.45208	661.5847
223	1	0.75577	0.00154	0.51162	723.3327
203	0.99609	0.76263	0.00212	0.40693	464.5386
183	0.99836	0.76448	0.00327	0.34842	434.3675
164	1	0.76074	0.00618	0.34682	628.3217
150	1	0.74789	0.01319	0.2333	746.2977
137	0.99094	0.74695	0.02083	0.19635	746.2677
127	0.98089	0.73917	0.03995	0.11327	746.2677
118	0.97435	0.72616	0.09337	0.04113	746.2677

cCMO-346

Table 9-6: Fitting parameters obtained from the Havriliak–Negami model for the dielectric response of sample cCMO-346 at various temperatures.

Temperature (K)	β	γ	τ	ε_∞	$\Delta\varepsilon$
313	0.65555	1.58	2.35E-07	0	3433.224
302	0.62518	1.47769	2.27E-07	68529.16	4458.242
293	0.64728	1.64988	2.19E-07	471.0473	3363.585
280	0.6238	1.48197	2.44E-07	821.1035	4314.066
266	0.61794	1.44286	2.60E-07	5847.748	4231.004
251	0.60014	1.67046	2.80E-07	450515.1	2626.06
232	0.53256	1.7911	3.96E-06	78525.88	2265.98
212	0.59135	1.2461	2.62E-05	89897.91	1301.241
192	0.50827	1.47155	3.56E-05	149934.6	2661.548
177	0.48176	1.5997	5.15E-05	13725.1	3537.398
162	0.4453	1.78671	7.98E-05	15624.26	5395.41
147	0.4612	1.84747	7.83E-05	32874.83	5014.199
132	0.75783	1.13411	6.30E-05	43301.86	853.1318
123	0.72248	1.2196	1.23E-04	45065.18	1117.923
111	0.4747	1.60365	6.87E-04	91785.22	1671.047
102	0.83074	0.90443	0.00199	92729.26	1234.709

(110)STOcCMO-100

Table 9-7: Fitting parameters obtained from the Havriliak–Negami model for the dielectric response of sample (110)STOcCMO-100 at various temperatures.

Temperature (K)	β	γ	τ	ε_∞	$\Delta\varepsilon$
264	0.94007	0.94637	5.66E-06	0	26.12984
242	0.91563	1.08	2.75E-06	0	36.07565
220	0.91239	1.09	2.74E-06	0	31.96764
208	0.90675	1.10865	3.42E-06	0	26.47356
203	0.90321	1.11635	3.42E-06	0	26.94938
179	0.88886	1.11756	3.84E-06	0	26.32858
161	0.84837	1.185	4.51E-06	0	22.81464
148	0.85245	1.1716	5.54E-06	0	23.51214
137	0.84955	1.18	6.84E-06	0	23.70854
124	0.82785	1.21346	9.61E-06	0	25.55451
111	0.82053	1.14179	1.93E-05	0	30.40014
99	0.81741	1.10782	4.60E-05	0	31.22508
89	0.82042	1.08842	9.46E-05	0.12616	30.36852
76	0.76269	1.14545	3.60E-04	0.21996	30.9432

(110)STOcCMO-112

Table 9-8: Fitting parameters obtained from the Havriliak–Negami model for the dielectric response of sample (110)STOcCMO-112 at various temperatures

Temperature (K)	β	γ	τ	ε_∞	$\Delta\varepsilon$
298	0.99947	0.94557	5.65E-06	0	224.4656
274	0.97823	0.95431	5.79E-06	0	230.788
258	0.97177	0.94913	6.05E-06	0	235.2408
241	0.97165	0.94758	6.06E-06	0	227.7564
220	9.73E-01	0.93426	6.07E-06	0	235.5953
198	9.50E-01	0.94514	6.50E-06	0	252.0609
178	9.68E-01	0.94	6.31E-06	0	204.4417
164	9.62E-01	0.98403	6.19E-06	0	192.7791
145	1.00	1.00	6.06E-06	0	136.8908
134	7.60E-01	1.01	3.28E-05	0	134.4199
120	7.77E-01	1.01	4.36E-05	0.64559	91.91134
106	7.59E-01	1.05442	6.93E-05	0	118.3693
93	8.29E-01	1.102	1.62E-04	3.06194	103.211
80	8.79E-01	1.10304	3.81E-04	3.43716	83.42064
64	9.02E-01	1.0725	3.16E-04	3.51561	192.9564

10. References

[1] N.A. Spaldin, R. Ramesh, Advances in magnetoelectric multiferroics, Nat. Mater. 18 (2019) 203–212. https://doi.org/10.1038/s41563-018-0275-2.

[2] M. Fiebig, T. Lottermoser, D. Meier, M. Trassin, The evolution of multiferroics, Nat. Rev. Mater. 1 (2016) 1–14. https://doi.org/10.1038/natrevmats.2016.46.

[3] M. Trassin, Low energy consumption spintronics using multiferroic heterostructures, J. Phys. Condens. Matter 28 (2016) 033001. https://doi.org/10.1088/0953-8984/28/3/033001.

[4] H. Lin, Y. Gao, X. Wang, T. Nan, M. Liu, J. Lou, G. Yang, Z. Zhou, X. Yang, J. Wu, M. Li, Z. Hu, N.X. Sun, Integrated Magnetics and Multiferroics for Compact and Power-Efficient Sensing, Memory, Power, RF, and Microwave Electronics, IEEE Trans. Magn. 52 (2016). https://doi.org/10.1109/TMAG.2016.2514982.

[5] S. Manipatruni, D.E. Nikonov, I.A. Young, Beyond CMOS computing with spin and polarization, Nat. Phys. 14 (2018) 338–343. https://doi.org/10.1038/s41567-018-0101-4.

[6] J.-M. Hu, C.-W. Nan, L.-Q. Chen, Perspective: voltage control of magnetization in multiferroic heterostructures, Natl. Sci. Rev. 6 (2019) 621–624. https://doi.org/10.1093/nsr/nwz047.

[7] C.M. Leung, J. Li, D. Viehland, X. Zhuang, A review on applications of magnetoelectric composites: From heterostructural uncooled magnetic sensors, energy harvesters to highly efficient power converters, J. Phys. D. Appl. Phys. 51 (2018) 263002. https://doi.org/10.1088/1361-6463/aac60b.

[8] D.K. Pradhan, S. Kumari, P.D. Rack, Magnetoelectric Composites: Applications, Coupling Mechanisms, and Future Directions, Nanomaterials 10 (2020) 2072. https://doi.org/10.3390/nano10102072.

[9] K. Yamauchi, P. Barone, Electronic ferroelectricity induced by charge and orbital orderings, J. Phys. Condens. Matter 26 (2014) 103201. https://doi.org/10.1088/0953-8984/26/10/103201.

[10] X. Xi, L. Zhao, Z. Wang, H. Berger, L. Forró, J. Shan, K.F. Mak, Strongly enhanced charge-density-wave order in monolayer NbSe 2, Nat. Nanotechnol. 10 (2015) 765–769. https://doi.org/10.1038/nnano.2015.143.

[11] T. Nagata, P.E. Janolin, M. Fukunaga, B. Roman, K. Fujiwara, H. Kimura, J.M. Kiat, N. Ikeda, Electric spontaneous polarization in YbFe2O4, Appl. Phys. Lett. 110 (2017) 052901. https://doi.org/10.1063/1.4974994.

[12] V. Garcia, M. Bibes, A. Barthélémy, Artificial multiferroic heterostructures for an electric control of magnetic properties, Comptes Rendus Phys. 16 (2015) 168–181. https://doi.org/10.1016/j.crhy.2015.01.007.

[13] M. Lorenz, V. Lazenka, P. Schwinkendorf, M.J. Van Bael, A. Vantomme, K. Temst, M. Grundmann, T. Höche, Epitaxial Coherence at Interfaces as Origin of High Magnetoelectric Coupling in Multiferroic $BaTiO_3$-$BiFeO_3$ Superlattices, Adv. Mater. Interfaces 3 (2016) 1500822. https://doi.org/10.1002/admi.201500822.

[14] Z. Chu, M. Pourhosseiniasl, S. Dong, Review of multi-layered magnetoelectric composite materials and devices applications, J. Phys. D. Appl. Phys. 51 (2018) 243001. https://doi.org/10.1088/1361-6463/aac29b.

[15] A. Baghizadeh, P.M. Vaghefi, X. Huang, J. Borme, B. Almeida, A.N. Salak, M. Willinger, V.B. Amaral, J.M. Vieira, Interplay of Magnetic Properties and Doping in Epitaxial Films of h-REFeO3 Multiferroic Oxides, Small 17 (2021) 2005700. https://doi.org/10.1002/smll.202005700.

[16] M.J. Pitcher, P. Mandal, M.S. Dyer, J. Alaria, P. Borisov, H. Niu, J.B. Claridge, M.J. Rosseinsky, Tilt engineering of spontaneous polarization and magnetization above 300 K in a bulk layered perovskite, Science. 347 (2015) 420–424. https://doi.org/10.1126/science.1262118.

[17] M. Liu, Y. Zhang, L.F. Lin, L. Lin, S. Yang, X. Li, Y. Wang, S. Li, Z. Yan, X. Wang, X.G. Li, S. Dong, J.M. Liu, Direct observation of ferroelectricity in Ca3Mn2O7 and its prominent light absorption, Appl. Phys. Lett. 113 (2018) 022902. https://doi.org/10.1063/1.5037525.

[18] P. Rocha-Rodrigues, S.S.M. Santos, I.P. Miranda, G.N.P. Oliveira, J.G. Correia, L.V.C. Assali, H.M. Petrilli, J.P. Araújo, A.M.L. Lopes, Ca3Mn2O7 structural path unraveled by atomic-scale properties: A combined experimental and ab initio study, Phys. Rev. B 101 (2020) 64103. https://doi.org/10.1103/PhysRevB.101.064103.

[19] J. Nordlander, M. Campanini, M.D. Rossell, R. Erni, Q.N. Meier, A. Cano, N.A. Spaldin, M. Fiebig, M. Trassin, The ultrathin limit of improper ferroelectricity, Nat. Commun. 10 (2019) 1–7. https://doi.org/10.1038/s41467-019-13474-x.

[20] P. Adler, S.A. Medvedev, P.G. Naumov, S. Mohitkar, R. Rüffer, M. Jansen, C. Felser, High-pressure magnetism of the double perovskite Sr2FeOsO6 studied by synchrotron Fe 57 Mössbauer spectroscopy, Phys. Rev. B 99 (2019) 134443. https://doi.org/10.1103/PhysRevB.99.134443.

[21] Y.S. Oh, X. Luo, F.T. Huang, Y. Wang, S.W. Cheong, Experimental demonstration of hybrid improper ferroelectricity and the presence of abundant charged walls in (Ca,Sr)3Ti2O7 crystals, Nat. Mater. 14 (2015) 407–413. https://doi.org/10.1038/nmat4168.

[22] Y. Wang, F.-T. Huang, X. Luo, B. Gao, S.-W. Cheong, The First Room-Temperature Ferroelectric Sn Insulator and Its Polarization Switching Kinetics, Adv. Mater. 29 (2017) 1601288. https://doi.org/10.1002/adma.201601288.

[23] B. Yuan, J. Yang, D.P. Song, X.Z. Zuo, X.W. Tang, X.B. Zhu, J.M. Dai, W.H. Song, Y.P. Sun, Structural, magnetic, and dielectric studies of the Aurivillius compounds SrBi5Ti4MnO18 and SrBi5Ti4Mn0.5Co0.5O18, J. Appl. Phys. 117 (2015) 023907. https://doi.org/10.1063/1.4905848.

[24] Z. Li, V. Koval, A. Mahajan, Z. Gao, C. Vecchini, M. Stewart, M.G. Cain, K. Tao, C. Jia, G. Viola, H. Yan, Room-temperature multiferroic behavior in layer-structured Aurivillius phase ceramics, Appl. Phys. Lett. 117 (2020) 052903. https://doi.org/10.1063/5.0017781.

[25] J. Varignon, L. Vila, A. Barthélémy, M. Bibes, A new spin for oxide interfaces, Nat. Phys. 14 (2018) 322–325. https://doi.org/10.1038/s41567-018-0112-1.

[26] X.Z. Lu, J.M. Rondinelli, Epitaxial-strain-induced polar-to-nonpolar transitions in layered oxides, Nat. Mater. 15 (2016) 951–955. https://doi.org/10.1038/nmat4664.

[27] M. Ghidini, R. Mansell, F. Maccherozzi, X. Moya, L.C. Phillips, W. Yan, D. Pesquera, C.H.W. Barnes, R.P. Cowburn, J.M. Hu, S.S. Dhesi, N.D. Mathur, Shear-strain-mediated magnetoelectric effects revealed by imaging, Nat. Mater. 18 (2019) 840–845. https://doi.org/10.1038/s41563-019-0374-8.

[28] B.M. Silva, J. Oliveira, T. Rebelo, V.B. Isfahani, P. Rocha-Rodrigues, N. Lekshmi, J.H. Belo, F.L. Deepak, A.M.L. Lopes, J.P. Araújo, B.G. Almeida, Synthesis, structural and dielectric properties of Ca3Mn2O7 thin films prepared by pulsed laser deposition, Mater. Res. Bull. 158 (2023). https://doi.org/10.1016/j.materresbull.2022.112066.

[29] A. Navrotsky, D.J. Weidner, Perovskite: A Structure of Great Interest to Geophysics and Materials Science, American Geophysical Union, Washington, D. C., 1989. https://doi.org/10.1029/GM045.

[30] R.J.H. Voorhoeve, Advanced Materials in Catalysis, Elsevier, 1977. https://doi.org/10.1016/C2013-0-04943-2.

[31] A.K. Bera, S.M. Yusuf, Functional Perovskites: Structure-Properties Correlations, OAJ Mater. Devices 5 (2021). https://doi.org/10.23647/ca.md20202105.

[32] H. Wenk, A. Bulakh, Minerals: Their Constitution and Origin, Cambridge University Press, New York, 2004. https://doi.org/10.5860/CHOICE.42-2243.

[33] M. Johnsson, P. Lemmens, Crystallography and Chemistry of Perovskites, in: Handb. Magn. Adv.

Magn. Mater., 2007. https://doi.org/10.1002/9780470022184.hmm411.

[34] Q. Wang, H.Z. Yan, X. Zhao, C.M. Wang, Polymorphic phase transition and piezoelectric performance of BaTiO3-casno3 solid solutions, Actuators 10 (2021). https://doi.org/10.3390/act10060129.

[35] H. Schmid, Multi-ferroic magnetoelectrics, Ferroelectrics 162 (1994) 317–338. https://doi.org/10.1080/00150199408245120.

[36] M. Fiebig, Revival of the magnetoelectric effect, J. Phys. D. Appl. Phys. 38 (2005) R123–R152. https://doi.org/10.1088/0022-3727/38/8/R01.

[37] A. Kojima, K. Teshima, Y. Shirai, T. Miyasaka, Organometal Halide Perovskites as Visible-Light Sensitizers for Photovoltaic Cells, J. Am. Chem. Soc. 131 (2009) 6050–6051. https://doi.org/10.1021/ja809598r.

[38] J. Huang, Y. Yuan, Y. Shao, Y. Yan, Understanding the physical properties of hybrid perovskites for photovoltaic applications, Nat. Rev. Mater. 2 (2017) 17042. https://doi.org/10.1038/natrevmats.2017.42.

[39] N. Nuraje, K. Su, Perovskite ferroelectric nanomaterials, Nanoscale 5 (2013) 8752. https://doi.org/10.1039/c3nr02543h.

[40] H.-Y. Ye, Y.-Y. Tang, P.-F. Li, W.-Q. Liao, J.-X. Gao, X.-N. Hua, H. Cai, P.-P. Shi, Y.-M. You, R.-G. Xiong, Metal-free three-dimensional perovskite ferroelectrics, Science. 361 (2018) 151–155. https://doi.org/10.1126/science.aas9330.

[41] B. V. Beznosikov, K.S. Aleksandrov, Perovskite-like crystals of the Ruddlesden-Popper series, Crystallogr. Reports 45 (2000) 792–798. https://doi.org/10.1134/1.1312923.

[42] B. Frit, J.P. Mercurio, The crystal chemistry and dielectric properties of the Aurivillius family of complex bismuth oxides with perovskite-like layered structures, J. Alloys Compd. 188 (1992) 27–35. https://doi.org/10.1016/0925-8388(92)90639-Q.

[43] K.M. Rabe, M. Dawber, C. Lichtensteiger, C.H. Ahn, J.M. Triscone, Modern physics of ferroelectrics: Essential background, Top. Appl. Phys. 105 (2007). https://doi.org/10.1007/978-3-540-34591-6_1.

[44] Kittel C, Introduction to Solid State Physics, 8th edition, Berkeley, 1996.

[45] R.E. Schaak, T.E. Mallouk, Prying apart Ruddlesden-Popper phases: Exfoliation into sheets and nanotubes for assembly of perovskite thin films, Chem. Mater. 12 (2000). https://doi.org/10.1021/cm000495r.

[46] P. V. Balachandran, A. Cammarata, B.B. Nelson-Cheeseman, A. Bhattacharya, J.M. Rondinelli,

Inductive crystal field control in layered metal oxides with correlated electrons, APL Mater. 2 (2014). https://doi.org/10.1063/1.4890544.

[47] P.R. Slater, J.P. Hodges, M.G. Francesconi, C. Greaves, M. Slaski, Fluorination of the Ruddlesden-Popper type cuprates, Ln2-xA1+xCu2O6-y (Ln = La, Nd; a = Ca, Sr), J. Mater. Chem. 7 (1997). https://doi.org/10.1039/a703735j.

[48] F.D. Romero, P.A. Bingham, S.D. Forder, M.A. Hayward, Topochemical fluorination of Sr3(M0.5Ru 0.5)2O7 (M = Ti, Mn, Fe), n = 2, Ruddlesden-popper phases, Inorg. Chem. 52 (2013). https://doi.org/10.1021/ic400125x.

[49] C.C. Stoumpos, D.H. Cao, D.J. Clark, J. Young, J.M. Rondinelli, J.I. Jang, J.T. Hupp, M.G. Kanatzidis, Ruddlesden-Popper Hybrid Lead Iodide Perovskite 2D Homologous Semiconductors, Chem. Mater. 28 (2016). https://doi.org/10.1021/acs.chemmater.6b00847.

[50] B.M. Silva, J. Oliveira, T. Rebelo, V.B. Isfahani, P. Rocha-Rodrigues, N. Lekshmi, J.H. Belo, F.L. Deepak, A.M.L. Lopes, J.P. Araújo, B.G. Almeida, Synthesis, structural and dielectric properties of Ca3Mn2O7 thin films prepared by pulsed laser deposition, Mater. Res. Bull. 158 (2023) 112066. https://doi.org/https://doi.org/10.1016/j.materresbull.2022.112066.

[51] J. Qing, C. Kuang, H. Wang, Y. Wang, X. Liu, S. Bai, M. Li, T.C. Sum, Z. Hu, W. Zhang, F. Gao, High-Quality Ruddlesden–Popper Perovskite Films Based on In Situ Formed Organic Spacer Cations, Adv. Mater. 31 (2019). https://doi.org/10.1002/adma.201904243.

[52] X. Xiao, J. Zhou, K. Song, J. Zhao, Y. Zhou, P.N. Rudd, Y. Han, J. Li, J. Huang, Layer number dependent ferroelasticity in 2D Ruddlesden–Popper organic-inorganic hybrid perovskites, Nat. Commun. 12 (2021) 1332. https://doi.org/10.1038/s41467-021-21493-w.

[53] G. Cao, S. McCall, J. Crow, Observation of itinerant ferromagnetism in layer single crystals, Phys. Rev. B - Condens. Matter Mater. Phys. 55 (1997). https://doi.org/10.1103/PhysRevB.55.R672.

[54] K. Lee, B.H. Goodge, D. Li, M. Osada, B.Y. Wang, Y. Cui, L.F. Kourkoutis, H.Y. Hwang, Aspects of the synthesis of thin film superconducting infinite-layer nickelates, APL Mater. 8 (2020). https://doi.org/10.1063/5.0005103.

[55] M.S. Senn, A. Bombardi, C.A. Murray, C. Vecchini, A. Scherillo, X. Luo, S.W. Cheong, Negative thermal expansion in hybrid improper ferroelectric Ruddlesden-popper Perovskites by symmetry trapping, Phys. Rev. Lett. 114 (2015) 1–5. https://doi.org/10.1103/PhysRevLett.114.035701.

[56] A.T. Mulder, N.A. Benedek, J.M. Rondinelli, C.J. Fennie, Turning ABO3 Antiferroelectrics into Ferroelectrics: Design Rules for Practical Rotation-Driven Ferroelectricity in Double Perovskites and A 3 B 2 O 7 Ruddlesden-Popper Compounds, Adv. Funct. Mater. 23 (2013).

https://doi.org/10.1002/adfm.201300210.

[57] H. Tsai, W. Nie, J.C. Blancon, C.C. Stoumpos, R. Asadpour, B. Harutyunyan, A.J. Neukirch, R. Verduzco, J.J. Crochet, S. Tretiak, L. Pedesseau, J. Even, M.A. Alam, G. Gupta, J. Lou, P.M. Ajayan, M.J. Bedzyk, M.G. Kanatzidis, A.D. Mohite, High-efficiency two-dimensional ruddlesden-popper perovskite solar cells, Nature 536 (2016). https://doi.org/10.1038/nature18306.

[58] X. Yang, X. Zhang, J. Deng, Z. Chu, Q. Jiang, J. Meng, P. Wang, L. Zhang, Z. Yin, J. You, Efficient green light-emitting diodes based on quasi-two-dimensional composition and phase engineered perovskite with surface passivation, Nat. Commun. 9 (2018). https://doi.org/10.1038/s41467-018-02978-7.

[59] J.M. Rondinelli, C.J. Fennie, Octahedral rotation-induced ferroelectricity in cation ordered perovskites, Adv. Mater. 24 (2012). https://doi.org/10.1002/adma.201104674.

[60] A.T. Mulder, N.A. Benedek, J.M. Rondinelli, C.J. Fennie, Turning ABO3 antiferroelectrics into ferroelectrics: Design rules for practical rotation-driven ferroelectricity in double perovskites and A3B2O7 Ruddlesden-popper compounds, Adv. Funct. Mater. 23 (2013). https://doi.org/10.1002/adfm.201300210.

[61] A. Tarancón, M. Burriel, J. Santiso, S.J. Skinner, J.A. Kilner, Advances in layered oxide cathodes for intermediate temperature solid oxide fuel cells, J. Mater. Chem. 20 (2010) 3799. https://doi.org/10.1039/b922430k.

[62] A. Chroneos, B. Yildiz, A. Tarancón, D. Parfitt, J.A. Kilner, Oxygen diffusion in solid oxide fuel cell cathode and electrolyte materials: mechanistic insights from atomistic simulations, Energy Environ. Sci. 4 (2011) 2774. https://doi.org/10.1039/c0ee00717j.

[63] J.G. Bednorz, K.A. Miiller, Condensed Possible High T c Superconductivity in the Ba-La-Cu-0 System, Z. Phys. B-Condensed Matter 64 (1986) 189–193.

[64] Y. Maeno, H. Hashimoto, K. Yoshida, S. Nishizaki, T. Fujita, J.G. Bednorz, F. Lichtenberg, Superconductivity in a layered perovskite without copper, Nature 372 (1994). https://doi.org/10.1038/372532a0.

[65] Y.F. Nie, Y. Zhu, C.H. Lee, L.F. Kourkoutis, J.A. Mundy, J. Junquera, P. Ghosez, D.J. Baek, S. Sung, X.X. Xi, K.M. Shen, D.A. Muller, D.G. Schlom, Atomically precise interfaces from non-stoichiometric deposition, Nat. Commun. 5 (2014). https://doi.org/10.1038/ncomms5530.

[66] J.H. Lee, G. Luo, I.C. Tung, S.H. Chang, Z. Luo, M. Malshe, M. Gadre, A. Bhattacharya, S.M. Nakhmanson, J.A. Eastman, H. Hong, J. Jellinek, D. Morgan, D.D. Fong, J.W. Freeland, Dynamic layer rearrangement during growth of layered oxide films by molecular beam epitaxy, Nat. Mater.

13 (2014). https://doi.org/10.1038/nmat4039.

[67] N.A. Benedek, C.J. Fennie, Hybrid improper ferroelectricity: A mechanism for controllable polarization-magnetization coupling, Phys. Rev. Lett. 106 (2011) 3–6. https://doi.org/10.1103/PhysRevLett.106.107204.

[68] G. Lawes, N.A. Benedek, C.J. Fennie, Viewpoint Twisting and turning towards new multiferroics Subject Areas: Materials Science A Viewpoint on: Hybrid Improper Ferroelectricity: A Mechanism for Controllable Polarization-Magnetization Coupling, Phys. Rev. Lett 4 (2011) 107204. https://doi.org/10.1103/Physics.4.18.

[69] C. Ablitt, A.A. Mostofi, N.C. Bristowe, M.S. Senn, Control of Uniaxial Negative Thermal Expansion in Layered Perovskites by Tuning Layer Thickness, Front. Chem. 0 (2018) 455. https://doi.org/10.3389/FCHEM.2018.00455.

[70] M. V. Lobanov, M. Greenblatt, E.N. Caspi, J.D. Jorgensen, D. V. Sheptyakov, B.H. Toby, C.E. Botez, P.W. Stephens, Crystal and magnetic structure of the Ca3Mn2O7 Ruddlesden-Popper phase: Neutron and synchrotron x-ray diffraction study, J. Phys. Condens. Matter 16 (2004) 5339–5348. https://doi.org/10.1088/0953-8984/16/29/023.

[71] The 32 Crystallographic Point Groups, in: Sp. Groups Solid State Sci., Elsevier, 2013: pp. 325–326. https://doi.org/10.1016/B978-0-12-394400-9.15004-X.

[72] T. Hahn, H. Klapper, Crystallographic and noncrystallographic point groups, in: Int. Tables Crystallogr., International Union of Crystallography, Chester, England, 2006: pp. 762–803. https://doi.org/10.1107/97809553602060000520.

[73] M.E. Lines, A.M. Glass, Basic Concepts, in: Princ. Appl. Ferroelectr. Relat. Mater., Oxford University Press, 2001: pp. 1–23. https://doi.org/10.1093/acprof:oso/9780198507789.003.0001.

[74] S. Trolier-McKinstry, Crystal Chemistry of Piezoelectric Materials, in: Piezoelectric Acoust. Mater. Transducer Appl., Springer US, Boston, MA, 2008: pp. 39–56. https://doi.org/10.1007/978-0-387-76540-2_3.

[75] T. Vijayakanth, D.J. Liptrot, E. Gazit, R. Boomishankar, C.R. Bowen, Recent Advances in Organic and Organic–Inorganic Hybrid Materials for Piezoelectric Mechanical Energy Harvesting, Adv. Funct. Mater. 32 (2022). https://doi.org/10.1002/adfm.202109492.

[76] C.W. Nan, M.I. Bichurin, S. Dong, D. Viehland, G. Srinivasan, Multiferroic magnetoelectric composites: Historical perspective, status, and future directions, J. Appl. Phys. 103 (2008). https://doi.org/10.1063/1.2836410.

[77] R. Ramesh, N.A. Spaldin, Multiferroics: Progress and prospects in thin films, Nat. Mater. 6 (2007). https://doi.org/10.1038/nmat1805.

[78] J.F. Scott, Applications of modern ferroelectrics, Science. 315 (2007). https://doi.org/10.1126/science.1129564.

[79] D. Isarakorn, Epitaxial Piezoelectric MEMS on Silicon, EPFL, 2011. https://doi.org/10.5075/epfl-thesis-4939.

[80] M. Riede, B. Lüssem, K. Leo, Organic Semiconductors, in: Compr. Semicond. Sci. Technol., Elsevier, 2011: pp. 448–507. https://doi.org/10.1016/B978-0-44-453153-7.00123-1.

[81] R.C.G. Naber, K. Asadi, P.W.M. Blom, D.M. De Leeuw, B. De Boer, Organic nonvolatile memory devices based on ferroelectricity, Adv. Mater. 22 (2010). https://doi.org/10.1002/adma.200900759.

[82] E. Bousquet, M. Dawber, N. Stucki, C. Lichtensteiger, P. Hermet, S. Gariglio, J.-M. Triscone, P. Ghosez, Improper ferroelectricity in perovskite oxide artificial superlattices, Nat. 2008 4527188 452 (2008) 732–736. https://doi.org/10.1038/nature06817.

[83] I. Etxebarria, J.M. Perez-Mato, P. Boullay, The role of trilinear couplings in the phase transitions of aurivillius compounds, in: Ferroelectrics, 2010. https://doi.org/10.1080/00150191003670325.

[84] N.A. Benedek, M.A. Hayward, Hybrid Improper Ferroelectricity: A Theoretical, Computational, and Synthetic Perspective, Annu. Rev. Mater. Res. 52 (2022) 331–355. https://doi.org/10.1146/annurev-matsci-080819-010313.

[85] F. Kremer, A. Schönhals, Broadband dielectric spectroscopy, Springer, Berlin, 2003.

[86] K.C. Kao, Dielectric Phenomena in Solids, 2004. https://doi.org/10.1016/B978-0-12-396561-5.X5010-5.

[87] A.R. von Hippel, S.O. Morgan, Dielectrics and Waves, 1955. https://doi.org/10.1149/1.2430013.

[88] T.W. Dakin, Conduction and polarization mechanisms and trends in dielectric, IEEE Electr. Insul. Mag. 22 (2006). https://doi.org/10.1109/MEI.2006.1705854.

[89] X.-J. Liu, M.-S. Zheng, G. Chen, Z.-M. Dang, J.-W. Zha, High-temperature polyimide dielectric materials for energy storage: theory, design, preparation and properties, Energy Environ. Sci. 15 (2022) 56–81. https://doi.org/10.1039/D1EE03186D.

[90] F. Alvarez, A. Alegra, J. Colmenero, Relationship between the time-domain Kohlrausch-Williams-Watts and frequency-domain Havriliak-Negami relaxation functions, Phys. Rev. B 44 (1991) 7306.

https://doi.org/10.1103/PhysRevB.44.7306.

[91] K. Górska, A. Horzela, L. Bratek, G. Dattoli, K.A. Penson, The Havriliak–Negami relaxation and its relatives: the response, relaxation and probability density functions, J. Phys. A Math. Theor. 51 (2018) 135202. https://doi.org/10.1088/1751-8121/AAAFC0.

[92] S. Mugiraneza, A.M. Hallas, Tutorial: a beginner's guide to interpreting magnetic susceptibility data with the Curie-Weiss law, Commun. Phys. 5 (2022) 95. https://doi.org/10.1038/s42005-022-00853-y.

[93] R. Prasad, Physics and Technology for Engineers, 2023. https://doi.org/10.1007/978-3-031-32084-2.

[94] S. Bedanta, W. Kleemann, Supermagnetism, J. Phys. D. Appl. Phys. 42 (2009) 013001. https://doi.org/10.1088/0022-3727/42/1/013001.

[95] L.W. Martin, S.P. Crane, Y.H. Chu, M.B. Holcomb, M. Gajek, M. Huijben, C.H. Yang, N. Balke, R. Ramesh, Multiferroics and magnetoelectrics: Thin films and nanostructures, J. Phys. Condens. Matter 20 (2008) 434220. https://doi.org/10.1088/0953-8984/20/43/434220.

[96] M.M. Vopson, Y.K. Fetisov, G. Caruntu, G. Srinivasan, Measurement techniques of the magneto-electric coupling in multiferroics, Materials (Basel). 10 (2017). https://doi.org/10.3390/ma10080963.

[97] A. Anatolievich Zakharenko, Investigation of SH-Wave Fundamental Modes in Piezoelectromagnetic Plate: Electrically Closed and Magnetically Closed Boundary Conditions, Open J. Acoust. 04 (2014). https://doi.org/10.4236/oja.2014.42009.

[98] G. Catalan, J.F. Scott, Magnetoelectric coupling and multiferroic materials, in: Multifunct. Oxide Heterostruct., Oxford University Press, 2012: pp. 38–70. https://doi.org/10.1093/acprof:oso/9780199584123.003.0002.

[99] W. Eerenstein, N.D. Mathur, J.F. Scott, Multiferroic and magnetoelectric materials, Nature 442 (2006) 759–765. https://doi.org/10.1038/nature05023.

[100] R. Zhang, Y. Duan, S.W. Or, Y. Zhao, Smart elasto-magneto-electric (EME) sensors for stress monitoring of steel cables: Design theory and experimental validation, Sensors (Switzerland) 14 (2014). https://doi.org/10.3390/s140813644.

[101] M. Fiebig, T. Lottermoser, D. Meier, M. Trassin, The evolution of multiferroics, Nat. Rev. Mater. 1 (2016) 1–14. https://doi.org/10.1038/natrevmats.2016.46.

[102] N.A. Hill, Why are there so few magnetic ferroelectrics?, J. Phys. Chem. B 104 (2000). https://doi.org/10.1021/jp000114x.

[103] S.-W. Cheong, M. Mostovoy, Multiferroics: a magnetic twist for ferroelectricity, Nat. Mater. 6 (2007) 13–20. https://doi.org/10.1038/nmat1804.

[104] A.J.C. Buurma, G.R. Blake, T.T.M. Palstra, U. Adem, Multiferroic Materials: Physics and Properties, in: Ref. Modul. Mater. Sci. Mater. Eng., Elsevier, 2016. https://doi.org/10.1016/B978-0-12-803581-8.09245-6.

[105] M.N.R. Ashfold, F. Claeyssens, G.M. Fuge, S.J. Henley, Pulsed laser ablation and deposition of thin films, Chem. Soc. Rev. 33 (2004). https://doi.org/10.1039/b207644f.

[106] E.W.T. Rhodes, E.B. a Adibi, T. Asakura, T.W. Hansch, T. Kamiya, F. Krausz, B. Monemar, H. Venghaus, H. Weber, H. Weinfurter, W.T. Rhodes, Laser Ablation and its applications, 2007.

[107] T.J. Jackson, S.B. Palmer, Oxide superconductor and magnetic metal thin film deposition by pulsed laser ablation: A review, J. Phys. D. Appl. Phys. 27 (1994). https://doi.org/10.1088/0022-3727/27/8/001.

[108] D. Pantel, S. Goetze, D. Hesse, M. Alexe, Reversible electrical switching of spin polarization in multiferroic tunnel junctions, Nat. Mater. 11 (2012). https://doi.org/10.1038/nmat3254.

[109] N.A. Shepelin, Z.P. Tehrani, N. Ohannessian, C.W. Schneider, D. Pergolesi, T. Lippert, A practical guide to pulsed laser deposition, Chem. Soc. Rev. 52 (2023) 2294–2321. https://doi.org/10.1039/D2CS00938B.

[110] L.W. Martin, Y.H. Chu, R. Ramesh, Advances in the growth and characterization of magnetic, ferroelectric, and multiferroic oxide thin films, Mater. Sci. Eng. R Reports 68 (2010). https://doi.org/10.1016/j.mser.2010.03.001.

[111] R.K. Singh, O.W. Holland, J. Narayan, Theoretical model for deposition of superconducting thin films using pulsed laser evaporation technique, J. Appl. Phys. 68 (1990). https://doi.org/10.1063/1.347123.

[112] V. Gomes, Micro e Nanofibras multiferróicas preparadas por electrospinning, Universidade do Minho, 2016.

[113] J. Schou, Physical aspects of the pulsed laser deposition technique: The stoichiometric transfer of material from target to film, Appl. Surf. Sci. 255 (2009). https://doi.org/10.1016/j.apsusc.2008.10.101.

[114] J. Schou, S. Amoruso, J.G. Lunney, Plume Dynamics, in: Laser Ablation Its Appl., 2007: pp. 67–95. https://doi.org/10.1007/978-0-387-30453-3_4.

[115] S. Amoruso, A. Sambri, M. Vitiello, X. Wang, Propagation of LaMnO3 laser ablation plume in oxygen gas, Appl. Surf. Sci. 252 (2006) 4712–4716.

https://doi.org/10.1016/j.apsusc.2005.07.107.

[116] J.A. Venables, G.D.T. Spiller, M. Hanbucken, Nucleation and growth of thin films, Reports Prog. Phys. 47 (1984). https://doi.org/10.1088/0034-4885/47/4/002.

[117] M. Ohring, The Materials Science of Thin Films, 2013. https://doi.org/10.1016/C2009-0-22199-4.

[118] A.J. Haider, T. Alawsi, M.J. Haider, B.A. Taha, H.A. Marhoon, A comprehensive review on pulsed laser deposition technique to effective nanostructure production: trends and challenges, Opt. Quantum Electron. 54 (2022) 488. https://doi.org/10.1007/s11082-022-03786-6.

[119] A. Ojeda-G-P, M. Döbeli, T. Lippert, Influence of Plume Properties on Thin Film Composition in Pulsed Laser Deposition, Adv. Mater. Interfaces 5 (2018). https://doi.org/10.1002/admi.201701062.

[120] J. Brandenburg, V. Neu, H. Wendrock, B. Holzapfel, H.-U. Krebs, S. Fähler, Pulsed laser deposition of metals: consequences of the energy distribution within the laser spot on film growth, Appl. Phys. A 79 (2004) 1005–1007. https://doi.org/10.1007/s00339-004-2615-0.

[121] H.U. Krebs, M. Weisheit, J. Faupel, E. Süske, T. Scharf, C. Fuhse, M. Störmer, K. Sturm, M. Seibt, H. Kijewski, others, Advances in Solid State Physics, Springer 40 (2003) 505–518.

[122] J. Chen, Analysis of Laser-Induced Plasmas Utilizing $18O_2$as Oxygen Tracer, ETH Zurich, 2014.

[123] M.A. Fakhri, H.D. Jabbar, M.J. AbdulRazzaq, E.T. Salim, A.S. Azzahrani, R.K. Ibrahim, R.A. Ismail, Effect of laser fluence on the optoelectronic properties of nanostructured GaN/porous silicon prepared by pulsed laser deposition, Sci. Rep. 13 (2023) 21007. https://doi.org/10.1038/s41598-023-47955-3.

[124] F.M. Dickey, T.E. Lizotte, Laser beam shaping applications, CRC press, 2018. https://doi.org/10.1201/9781420028065.

[125] T. Ohnishi, K. Shibuya, T. Yamamoto, M. Lippmaa, Defects and transport in complex oxide thin films, J. Appl. Phys. 103 (2008). https://doi.org/10.1063/1.2921972.

[126] S. Fähler, M. Störmer, H.. Krebs, Origin and avoidance of droplets during laser ablation of metals, Appl. Surf. Sci. 109–110 (1997) 433–436. https://doi.org/10.1016/S0169-4332(96)00782-9.

[127] S. Mustofa, S. Tsuyuguchi, T. Araki, M. Nishida, T. Hino, Formation of droplets on thin film surface in pulsed laser deposition using metal targets, Yosetsu Gakkai Ronbunshu/Quarterly J. Japan Weld. Soc. 21 (2003). https://doi.org/10.2207/qjjws.21.338.

[128] H.M. Christen, G. Eres, Recent advances in pulsed-laser deposition of complex oxides, J. Phys. Condens. Matter 20 (2008). https://doi.org/10.1088/0953-8984/20/26/264005.

[129] A. Ojeda-G-P, C.W. Schneider, M. Döbeli, T. Lippert, A. Wokaun, Plasma plume dynamics, rebound, and recoating of the ablation target in pulsed laser deposition, J. Appl. Phys. 121 (2017). https://doi.org/10.1063/1.4979780.

[130] A. Ojeda-G-P, C.W. Schneider, M. Döbeli, T. Lippert, A. Wokaun, The flip-over effect in pulsed laser deposition: Is it relevant at high background gas pressures?, Appl. Surf. Sci. 357 (2015) 2055–2062. https://doi.org/10.1016/j.apsusc.2015.09.184.

[131] J.J. Prentice, J.A. Grant-Jacob, S. V. Kurilchik, J.I. Mackenzie, R.W. Eason, Particulate reduction in PLD-grown crystalline films via bi-directional target irradiation, Appl. Phys. A 125 (2019) 152. https://doi.org/10.1007/s00339-019-2456-5.

[132] Z. Vakulov, E. Zamburg, D.A. Golosov, S.M. Zavadskiy, A.P. Dostanko, A. V Miakonkikh, I.E. Klemente, K. V Rudenko, O.A. Ageev, Influence of target-substrate distance during pulsed laser deposition on properties of LiNbO 3 thin films, J. Phys. Conf. Ser. 917 (2017) 032024. https://doi.org/10.1088/1742-6596/917/3/032024.

[133] A. Ojeda-G-P, C.W. Schneider, M. Döbeli, T. Lippert, A. Wokaun, The importance of pressure and mass ratios when depositing multi-element oxide thin films by pulsed laser deposition, Appl. Surf. Sci. 389 (2016). https://doi.org/10.1016/j.apsusc.2016.07.003.

[134] D. Bäuerle, Laser Processing and Chemistry, Springer Berlin Heidelberg, Berlin, Heidelberg, 2011. https://doi.org/10.1007/978-3-642-17613-5.

[135] C. Doughty, A.T. Findikoglu, T. Venkatesan, Steady state pulsed laser deposition target scanning for improved plume stability and reduced particle density, Appl. Phys. Lett. (1995). https://doi.org/10.1063/1.113261.

[136] N. Arnold, D. Bäuerle, Uniform target ablation in pulsed-laser deposition, Appl. Phys. A Mater. Sci. Process. 68 (1999) 363–367. https://doi.org/10.1007/s003390050905.

[137] J. Chen, M. Döbeli, D. Stender, K. Conder, A. Wokaun, C.W. Schneider, T. Lippert, Plasma interactions determine the composition in pulsed laser deposited thin films, Appl. Phys. Lett. 105 (2014). https://doi.org/10.1063/1.4895788.

[138] G. Reich, On the significance of mean free path to vacuum physics and technology, Vacuum 41 (1990). https://doi.org/10.1016/0042-207X(90)94170-U.

[139] M. Escalona, H. Bhuyan, J.C. Valenzuela, S. Ibacache, E. Wyndham, M. Favre, F. Veloso, H.M. Ruiz, E. Wagenaars, Comparative study on the dynamics and the composition between a pulsed laser deposition (PLD) and a plasma enhanced PLD (PE-PLD), Results Phys. 24 (2021). https://doi.org/10.1016/j.rinp.2021.104066.

[140] A. Gupta, Gas-phase oxidation chemistry during pulsed laser deposition of YBa2Cu3O7−δ films, J. Appl. Phys. 73 (1993) 7877–7886. https://doi.org/10.1063/1.353939.

[141] C. Ratsch, J.A. Venables, Nucleation theory and the early stages of thin film growth, J. Vac. Sci. Technol. A Vacuum, Surfaces, Film. 21 (2003) S96–S109. https://doi.org/10.1116/1.1600454.

[142] D.G. Schlom, L.-Q. Chen, C.-B. Eom, K.M. Rabe, S.K. Streiffer, J.-M. Triscone, Strain Tuning of Ferroelectric Thin Films, Annu. Rev. Mater. Res. 37 (2007) 589–626. https://doi.org/10.1146/annurev.matsci.37.061206.113016.

[143] S. Amoruso, C. Aruta, R. Bruzzese, X. Wang, U. Scotti di Uccio, Substrate heating influence on the deposition rate of oxides during pulsed laser deposition in ambient gas, Appl. Phys. Lett. 98 (2011). https://doi.org/10.1063/1.3565157.

[144] J. Narayan, S. Sharan, Mechanism of formation of 60° and 90° misfit dislocations in semiconductor heterostructures, Mater. Sci. Eng. B 10 (1991) 261–267. https://doi.org/10.1016/0921-5107(91)90100-A.

[145] J.W. Matthews, A.E. Blakeslee, Defects in epitaxial multilayers: I. Misfit dislocations, J. Cryst. Growth 27 (1974). https://doi.org/10.1016/S0022-0248(74)80055-2.

[146] J. Narayan, B.C. Larson, Domain epitaxy: A unified paradigm for thin film growth, J. Appl. Phys. 93 (2003) 278–285. https://doi.org/10.1063/1.1528301.

[147] R.P. Vinci, J.J. Vlassak, Mechanical Behavior of Thin Films, Annu. Rev. Mater. Sci. 26 (1996) 431–462. https://doi.org/10.1146/annurev.ms.26.080196.002243.

[148] A. Tiwari, C. Jin, J. Narayan, Strain-induced tuning of metal–insulator transition in NdNiO3, Appl. Phys. Lett. 80 (2002) 4039–4041. https://doi.org/10.1063/1.1480475.

[149] A. Biswas, Y.H. Jeong, Strain Effect in Epitaxial Oxide Heterostructures, in: Epitaxy, InTech, 2018. https://doi.org/10.5772/intechopen.70125.

[150] R.E. Smallman, A.H.W. Ngan, Surfaces, Grain Boundaries and Interfaces, in: R.E. Smallman, A.H.W. Ngan (Eds.), Mod. Phys. Metall. (Eighth Ed., Eighth Edi, Butterworth-Heinemann, Oxford, 2014: pp. 415–442. https://doi.org/10.1016/B978-0-08-098204-5.00010-9.

[151] R.E. Smallman, A.H.W. Ngan, Modern Physical Metallurgy, Elsevier, 2014. https://doi.org/10.1016/C2011-0-05565-5.

[152] H.T.G. Hentzell, C.R.M. Grovenor, D.A. Smith, Grain structure variation with temperature for evaporated metal films, J. Vac. Sci. Technol. A Vacuum, Surfaces, Film. 2 (1984). https://doi.org/10.1116/1.572727.

[153] C.R.M. Grovenor, H.T.G. Hentzell, D.A. Smith, The development of grain structure during growth

of metallic films, Acta Metall. 32 (1984) 773–781. https://doi.org/10.1016/0001-6160(84)90150-0.

[154] E. Hasabeldaim, O.M. Ntwaeaborwa, R.E. Kroon, E. Coetsee, H.C. Swart, Effect of substrate temperature and post annealing temperature on ZnO:Zn PLD thin film properties, Opt. Mater. (Amst). 74 (2017) 139–149. https://doi.org/10.1016/j.optmat.2017.03.027.

[155] S.A.J. Beden, H.A. Dumboos, M.K. Ismael, M. Kadhim Mejbel, The Role of Annealing Treatment on Crystallographic, Optical, and Electrical Features of Bi2O3 Thin Films Prepared Using Reactive Plasma Sputtering Technology, J. Nanotechnol. 2023 (2023) 1–8. https://doi.org/10.1155/2023/8638512.

[156] B. Tiss, D. Martínez-Martínez, B. Silva, N. Bouguila, L. El Mir, B. Almeida, C. Moura, L. Cunha, Growth of Al:ZnO nano-flowers by pulsed laser ablation deposition, Opt. Laser Technol. 174 (2024) 110673. https://doi.org/10.1016/j.optlastec.2024.110673.

[157] W.H. Bragg, W.L. Bragg, The reflection of X-rays by crystals, Proc. R. Soc. London. Ser. A. 88 (1913) 428–438. https://doi.org/10.1098/rspa.1913.0040.

[158] B.D. Cullity, S.R. Stock, Elements of X-ray diffraction, 3rd ed., Prentice-Hall, New York, 2001.

[159] C. Paula, In situ solid-state NMR and XRD investigations of structural transformations in crystalline porous solids, 2021. https://doi.org/10.25593/978-3-96147-450-9.

[160] H. Jung, S. Jeong, Y. Park, Y. Shin, H. Jeong, X-ray Diffraction Analysis of Damaged Layer During Polishing of Silicon Carbide, Int. J. Precis. Eng. Manuf. 24 (2023) 25–32. https://doi.org/10.1007/s12541-022-00711-5.

[161] Von N. W. Ashcroft; N. D. Mermin, Solid State Physics, Saunders College Publishing, Fort Worth, 1976.

[162] A.L. Patterson, The scherrer formula for X-ray particle size determination, Phys. Rev. 56 (1939). https://doi.org/10.1103/PhysRev.56.978.

[163] A. Mohammed, A. Abdullah, Scanning Electron Microscopy (SEM): A review, Pro808 Ceedings Int. Conf. Hydraul. Pneum. (2018).

[164] W. Zhou, R. Apkarian, Z.L. Wang, D. Joy, Fundamentals of Scanning Electron Microscopy (SEM), in: Scanning Microsc. Nanotechnol., Springer New York, New York, NY, 2006: pp. 1–40. https://doi.org/10.1007/978-0-387-39620-0_1.

[165] J. Huang, T. Cavanaugh, B. Nur, An Introduction to SEM Operational Principles and Geologic Applications for Shale Hydrocarbon Reservoirs, in: Electron Microsc. Shale Hydrocarb. Reserv., American Association of Petroleum Geologists, 2013.

https://doi.org/10.1306/13391699M1023580.

[166] B.J. Inkson, Scanning electron microscopy (SEM) and transmission electron microscopy (TEM) for materials characterization, in: Mater. Charact. Using Nondestruct. Eval. Methods, Elsevier, 2016: pp. 17–43. https://doi.org/10.1016/B978-0-08-100040-3.00002-X.

[167] J.I. Goldstein, D.E. Newbury, J.R. Michael, N.W.M. Ritchie, J.H.J. Scott, D.C. Joy, Scanning Electron Microscopy and X-Ray Microanalysis, 4th ed., Springer New York, New York, NY, 2018. https://doi.org/10.1007/978-1-4939-6676-9.

[168] K. Akhtar, S.A. Khan, S.B. Khan, A.M. Asiri, Scanning Electron Microscopy: Principle and Applications in Nanomaterials Characterization, in: Handb. Mater. Charact., Springer International Publishing, Cham, 2018: pp. 113–145. https://doi.org/10.1007/978-3-319-92955-2_4.

[169] J. Wollman, D. , Irwin, K. , Hilton, G. , Dulcie, L. , Newbury, D. and Martinis, High-resolution, energy-dispersive microcalorimeter spectrometer for X-ray microanalysis, J. Microsc. 188 (1997) 196–223. https://doi.org/10.1046/j.1365-2818.1997.2670824.x.

[170] R. Schneider, Energy-Dispersive X-Ray Spectroscopy (EDXS), in: G. Friedbacher, H. Bubert (Eds.), Surf. Thin Film Anal., Wiley, 2011: pp. 293–310. https://doi.org/10.1002/9783527636921.ch18.

[171] R.W. Kelsall, I.W. Hamley, M. Geoghegan, Nanoscale Science and Technology, Wiley, 2005. https://doi.org/10.1002/0470020873.

[172] J. Long, A. Nand, S. Ray, Application of Spectroscopy in Additive Manufacturing, Materials (Basel). 14 (2021) 203. https://doi.org/10.3390/ma14010203.

[173] D.J. Griffiths, D.F. Schroeter, Introduction to Quantum Mechanics, Cambridge University Press, 2018. https://doi.org/10.1017/9781316995433.

[174] R.K. Mishra, A.K. Zachariah, S. Thomas, Energy-Dispersive X-ray Spectroscopy Techniques for Nanomaterial, in: Microsc. Methods Nanomater. Charact., Elsevier, 2017: pp. 383–405. https://doi.org/10.1016/B978-0-323-46141-2.00012-2.

[175] J.R. Ferraro, K. Nakamoto, C.W. Brown, Introductory Raman Spectroscopy: Second Edition, 2003. https://doi.org/10.1016/B978-0-12-254105-6.X5000-8.

[176] C. V. Raman, K.S. Krishnam, Polarisation of Scattered Light-quanta, Nature 122 (1928) 169–169. https://doi.org/10.1038/122169a0.

[177] R.S. Das, Y.K. Agrawal, Raman spectroscopy: Recent advancements, techniques and applications, Vib. Spectrosc. 57 (2011) 163–176. https://doi.org/10.1016/j.vibspec.2011.08.003.

[178] P.A. Fleury, J.F. Scott, J.M. Worlock, Soft Phonon Modes and the 110°K Phase Transition in

SrTiO3, Phys. Rev. Lett. 21 (1968) 16–19. https://doi.org/10.1103/PhysRevLett.21.16.

[179] P. Bouvier, J. Kreisel, Pressure-induced phase transition in LaAlO3, J. Phys. Condens. Matter 14 (2002) 3981–3991. https://doi.org/10.1088/0953-8984/14/15/312.

[180] J. Kreisel, P. Jadhav, O. Chaix-Pluchery, M. Varela, N. Dix, F. Sánchez, J. Fontcuberta, A phase transition close to room temperature in BiFeO3 thin films, J. Phys. Condens. Matter 23 (2011) 342202. https://doi.org/10.1088/0953-8984/23/34/342202.

[181] M. Guennou, P. Bouvier, J. Kreisel, D. MacHon, Pressure-temperature phase diagram of SrTiO3 up to 53 GPa, Phys. Rev. B - Condens. Matter Mater. Phys. 81 (2010). https://doi.org/10.1103/PhysRevB.81.054115.

[182] A. Glamazda, D. Wulferding, P. Lemmens, B. Gao, S.W. Cheong, K.Y. Choi, Soft tilt and rotational modes in the hybrid improper ferroelectric Ca3Mn2O7, Phys. Rev. B 97 (2018) 094104. https://doi.org/10.1103/PhysRevB.97.094104.

[183] N.D. Todorov, M. V. Abrashev, V.G. Ivanov, G.G. Tsutsumanova, V. Marinova, Y.-Q. Wang, M.N. Iliev, Comparative Raman study of isostructural YCrO3 and YMnO3: Effects of structural distortions and twinning, Phys. Rev. B 83 (2011) 224303. https://doi.org/10.1103/PhysRevB.83.224303.

[184] M.N. Iliev, M. V. Abrashev, J. Laverdière, S. Jandl, M.M. Gospodinov, Y.-Q. Wang, Y.-Y. Sun, Distortion-dependent Raman spectra and mode mixing in RMnO3 perovskites (R=La,Pr,Nd,Sm,Eu,Gd,Tb,Dy,Ho,Y), Phys. Rev. B 73 (2006) 064302. https://doi.org/10.1103/PhysRevB.73.064302.

[185] J. Laverdière, S. Jandl, A.A. Mukhin, V.Y. Ivanov, V.G. Ivanov, M.N. Iliev, Spin-phonon coupling in orthorhombic RMnO3(R=Pr,Nd,Sm,Eu,Gd,Tb,Dy,Ho,Y): A Raman study, Phys. Rev. B 73 (2006) 214301. https://doi.org/10.1103/PhysRevB.73.214301.

[186] C. Girardot, J. Kreisel, S. Pignard, N. Caillault, F. Weiss, Raman scattering investigation across the magnetic and metal-insulator transition in rare earth nickelate RNiO3 (R=Sm, Nd) thin films, Phys. Rev. B 78 (2008) 104101. https://doi.org/10.1103/PhysRevB.78.104101.

[187] P. Vandenabeele, Practical Raman Spectroscopy – An Introduction, John Wiley & Sons, Ltd, Chichester, UK, 2013. https://doi.org/10.1002/9781119961284.

[188] B. Martin, J. Puentes, L. Wruck, T.A. Osswald, Degree of cure of epoxy/acrylic photopolymers: Characterization with raman spectroscopy and a modified phenomenological model, Polym. Eng. Sci. 58 (2018). https://doi.org/10.1002/pen.24550.

[189] A.K. Adya, E. Canetta, Nanotechnology and Its Applications to Animal Biotechnology, in: A.S. Verma, A. Singh (Eds.), Anim. Biotechnol., Academic Press, San Diego, 2014: pp. 247–263.

https://doi.org/https://doi.org/10.1016/B978-0-12-416002-6.00014-6.

[190] R. Zhang, Y. Zhang, Z.C. Dong, S. Jiang, C. Zhang, L.G. Chen, L. Zhang, Y. Liao, J. Aizpurua, Y. Luo, J.L. Yang, J.G. Hou, Chemical mapping of a single molecule by plasmon-enhanced Raman scattering, Nature 498 (2013). https://doi.org/10.1038/nature12151.

[191] M.B. Fenn, P. Xanthopoulos, G. Pyrgiotakis, S.R. Grobmyer, P.M. Pardalos, L.L. Hench, Raman Spectroscopy for Clinical Oncology, Adv. Opt. Technol. 2011 (2011) 1–20. https://doi.org/10.1155/2011/213783.

[192] D.A. Long, The Raman Effect, John Wiley & Sons, Ltd, 2002. https://doi.org/10.1002/0470845767.

[193] R. Kleiner, D. Koelle, F. Ludwig, J. Clarke, Superconducting quantum interference devices: State of the art and applications, Proc. IEEE 92 (2004) 1534–1548. https://doi.org/10.1109/JPROC.2004.833655.

[194] R.L. Fagaly, Superconducting quantum interference device instruments and applications, Rev. Sci. Instrum. 77 (2006). https://doi.org/10.1063/1.2354545.

[195] D. Hurt, S. Li, A. Amann, Versatile SQUID Susceptometer With Multiple Measurement Modes, IEEE Trans. Magn. 49 (2013) 3541–3544. https://doi.org/10.1109/TMAG.2013.2241029.

[196] K. Deshmukh, S. Sankaran, B. Ahamed, K.K. Sadasivuni, K.S.K. Pasha, D. Ponnamma, P.S. Rama Sreekanth, K. Chidambaram, Dielectric Spectroscopy, in: S. Thomas, R. Thomas, A.K. Zachariah, R.K. Mishra (Eds.), Spectrosc. Methods Nanomater. Charact., Elsevier, 2017: pp. 237–299. https://doi.org/https://doi.org/10.1016/B978-0-323-46140-5.00010-8.

[197] J.T.S. Irvine, D.C. Sinclair, A.R. West, Electroceramics: Characterization by Impedance Spectroscopy, Adv. Mater. 2 (1990) 132–138. https://doi.org/10.1002/adma.19900020304.

[198] T.N. Kołtunowicz, P. Gałaszkiewicz, K. Kierczyński, P. Rogalski, P. Okal, A.D. Pogrebnjak, V. Buranich, M. Pogorielov, K. Diedkova, V. Zahorodna, V. Balitskyi, V. Serhiienko, I. Baginskyi, O. Gogotsi, Investigation of AC Electrical Properties of MXene-PCL Nanocomposites for Application in Small and Medium Power Generation, Energies 14 (2021) 7123. https://doi.org/10.3390/en14217123.

[199] R.W. Boyd, Nonlinear Optics, Academic Press, San Diego, 2008.

[200] S.A. Denev, T.T.A. Lummen, E. Barnes, A. Kumar, V. Gopalan, Probing ferroelectrics using optical second harmonic generation, J. Am. Ceram. Soc. 94 (2011). https://doi.org/10.1111/j.1551-2916.2011.04740.x.

[201] M. Fiebig, V. V. Pavlov, R. V. Pisarev, Second-harmonic generation as a tool for studying electronic

and magnetic structures of crystals: review, J. Opt. Soc. Am. B 22 (2005). https://doi.org/10.1364/josab.22.000096.

[202] J. Nordlander, G. De Luca, N. Strkalj, M. Fiebig, M. Trassin, Probing Ferroic States in Oxide Thin Films Using Optical Second Harmonic Generation, Appl. Sci. 8 (2018) 570. https://doi.org/10.3390/app8040570.

[203] M. Dawber, P. Chandra, P.B. Littlewood, J.F. Scott, Depolarization corrections to the coercive field in thin-film ferroelectrics, J. Phys. Condens. Matter 15 (2003). https://doi.org/10.1088/0953-8984/15/24/106.

[204] S.K. Streiffer, J.A. Eastman, D.D. Fong, C. Thompson, A. Munkholm, M. V. Ramana Murty, O. Auciello, G.R. Bai, G.B. Stephenson, Observation of Nanoscale 180° Stripe Domains in Ferroelectric PbTiO3 Thin Films, Phys. Rev. Lett. 89 (2002) 067601. https://doi.org/10.1103/PhysRevLett.89.067601.

[205] J.T. Heron, D.G. Schlom, R. Ramesh, Electric field control of magnetism using BiFeO3 -based heterostructures, Appl. Phys. Rev. 1 (2014) 021303. https://doi.org/10.1063/1.4870957.

[206] M. Dawber, N. Stucki, C. Lichtensteiger, S. Ganglio, P. Ghosez, J.M. Triscone, Tailoring the properties of artificially layered ferroelectric superlattices, Adv. Mater. 19 (2007). https://doi.org/10.1002/adma.200700965.

[207] R.M.F. Baptista, C.S.B. Gomes, B. Silva, J. Oliveira, B. Almeida, C. Castro, P. V. Rodrigues, A. Machado, R.B. Freitas, M.J.L.F. Rodrigues, E. de Matos Gomes, M. Belsley, A Polymorph of Dipeptide Halide Glycyl-L-Alanine Hydroiodide Monohydrate: Crystal Structure, Optical Second Harmonic Generation, Piezoelectricity and Pyroelectricity, Materials (Basel). 16 (2023). https://doi.org/10.3390/ma16103690.

[208] H. Yokota, J. Kaneshiro, Y. Uesu, Optical Second Harmonic Generation Microscopy as a Tool of Material Diagnosis, Phys. Res. Int. 2012 (2012) 1–12. https://doi.org/10.1155/2012/704634.

[209] J. Kaneshiro, Y. Uesu, T. Fukui, Visibility of inverted domain structures using the second harmonic generation microscope: Comparison of interference and non-interference cases, J. Opt. Soc. Am. B 27 (2010). https://doi.org/10.1364/josab.27.000888.

[210] N. Strkalj, A. Bortis, M. Campanini, M.D. Rossell, M. Fiebig, M. Trassin, Optical second harmonic signature of phase coexistence in ferroelectric|dieclectric heterostructures, Phys. Rev. B 105 (2022) 174101. https://doi.org/10.1103/PhysRevB.105.174101.

[211] D. Santos, R.M.F. Baptista, A. Handa, B. Almeida, P. V. Rodrigues, C. Castro, A. Machado, M.J.L.F. Rodrigues, M. Belsley, E. de Matos Gomes, Nanostructured Electrospun Fibers with Self-

Assembled Cyclo-L-Tryptophan-L-Tyrosine Dipeptide as Piezoelectric Materials and Optical Second Harmonic Generators, Materials (Basel). 16 (2023) 4993. https://doi.org/10.3390/ma16144993.

[212] M. Orio, D.A. Pantazis, F. Neese, Density functional theory, Photosynth. Res. 102 (2009) 443–453. https://doi.org/10.1007/s11120-009-9404-8.

[213] D.S. Sholl, J.A. Steckel, Density Functional Theory, Wiley, 2009. https://doi.org/10.1002/9780470447710.

[214] M. te Vrugt, H. Löwen, R. Wittkowski, Classical dynamical density functional theory: from fundamentals to applications, Adv. Phys. 69 (2020) 121–247. https://doi.org/10.1080/00018732.2020.1854965.

[215] G. Kresse, J. Hafner, Ab initio molecular dynamics for liquid metals, Phys. Rev. B 47 (1993) 558–561. https://doi.org/10.1103/PhysRevB.47.558.

[216] G. Kresse, J. Furthmüller, Efficiency of ab-initio total energy calculations for metals and semiconductors using a plane-wave basis set, Comput. Mater. Sci. 6 (1996) 15–50. https://doi.org/10.1016/0927-0256(96)00008-0.

[217] A. Zunger, S.-H. Wei, L.G. Ferreira, J.E. Bernard, Special quasirandom structures, Phys. Rev. Lett. 65 (1990) 353–356. https://doi.org/10.1103/PhysRevLett.65.353.

[218] S.F. Matar, V. Eyert, A. Villesuzanne, M.-H. Whangbo, First-principles study of the electronic and magnetic structures of the tetragonal and orthorhombic phases of Ca3Mn2O7, Phys. Rev. B 76 (2007) 054403. https://doi.org/10.1103/PhysRevB.76.054403.

[219] C. Franchini, V. Bayer, R. Podloucky, J. Paier, G. Kresse, Density functional theory study of MnO by a hybrid functional approach, Phys. Rev. B 72 (2005) 045132. https://doi.org/10.1103/PhysRevB.72.045132.

[220] D. Bloch, R. Maury, Uniaxial Stress Experiments and Magnetoelastic Interactions in Manganese Oxide, Phys. Rev. B 7 (1973) 4883–4888. https://doi.org/10.1103/PhysRevB.7.4883.

[221] L. Cao, E. Sozontov, J. Zegenhagen, Cubic to Tetragonal Phase Transition of SrTiO3 under Epitaxial Stress: An X-Ray Backscattering Study, Phys. Status Solidi 181 (2000) 387–404. https://doi.org/10.1002/1521-396X(200010)181:2<387::AID-PSSA387>3.0.CO;2-5.

[222] R.K. Singh, N. Biunno, J. Narayan, Microstructural and compositional variations in laser-deposited superconducting thin films, Appl. Phys. Lett. 53 (1998) 1013. https://doi.org/10.1063/1.100653.

[223] R. Eason, Pulsed Laser Deposition of Thin Films: Applications-Led Growth of Functional Materials,

John Wiley and Sons Inc., 2007. https://doi.org/10.1002/9780470052129.

[224] T. Venkatesan, X.D. Wu, A. Inam, J.B. Wachtman, Observation of two distinct components during pulsed laser deposition of high Tc superconducting films, Appl. Phys. Lett. 52 (1998) 1193. https://doi.org/10.1063/1.99673.

[225] C. Araújo, B.G. Almeida, M. Aguiar, J.A. Mendes, Structural and magnetic properties of CoFe2O4 thin films deposited by laser ablation on Si (001) substrates, Vacuum 82 (2008) 1437–1440. https://doi.org/10.1016/j.vacuum.2008.03.014.

[226] I.T. Gomes, B.G. Almeida, A.M.L. Lopes, J.P. Araújo, J. Barbosa, J.A. Mendes, Structural and magnetic characterization of LaSrMnO3 thin films deposited by laser ablation on MgO substrates, J. Magn. Magn. Mater. 322 (2010) 1174–1177. https://doi.org/10.1016/j.jmmm.2009.06.072.

[227] M. Molinari, D.A. Tompsett, S.C. Parker, F. Azough, R. Freer, Structural, electronic and thermoelectric behaviour of CaMnO3 and CaMnO(3-δ), J. Mater. Chem. A 2 (2014) 14109–14117. https://doi.org/10.1039/c4ta01514b.

[228] C. Ablitt, A.A. Mostofi, N.C. Bristowe, M.S. Senn, Control of uniaxial negative thermal expansion in layered perovskites by Tuning layer thickness, Front. Chem. 6 (2018) 455. https://doi.org/10.3389/fchem.2018.00455.

[229] N. Guiblin, D. Grebille, H. Leligny, C. Martin, Ca3Mn2O7, Acta Crystallogr. Sect. C Cryst. Struct. Commun. 58 (2002). https://doi.org/10.1107/S0108270101018492.

[230] A. V. Ovchinnikov, O. V. Chefonov, E.D. Mishina, M.B. Agranat, Second harmonic generation in the bulk of silicon induced by an electric field of a high power terahertz pulse, Sci. Rep. 9 (2019) 9753. https://doi.org/10.1038/s41598-019-46284-8.

[231] V. Nalla, R. Medishetty, Y. Wang, Z. Bai, H. Sun, J. Wei, J.J. Vittal, Second harmonic generation from the `centrosymmetric' crystals, IUCrJ 2 (2015) 317–321. https://doi.org/10.1107/S2052252515002183.

[232] A.T. Raghavender, A.P. Samantilleke, P. Sa, B.G. Almeida, M.I. Vasilevskiy, N.H. Hong, Simple way to make Anatase TiO2 films on FTO glass for promising solar cells, Mater. Lett. 69 (2012) 59–62. https://doi.org/10.1016/J.MATLET.2011.11.067.

[233] S. Havriliak, S. Negami, A complex plane representation of dielectric and mechanical relaxation processes in some polymers, Polymer (Guildf). 8 (1967) 161–210. https://doi.org/10.1016/0032-3861(67)90021-3.

[234] P. Sahlot, G. Sharma, V. Sathe, A.K. Sinha, A.M. Awasthi, Interplay of spin, lattice, vibration, and

charge degrees of freedom: Magneto-dielectricity in Ca3Mn2O7, J. Am. Ceram. Soc. 103 (2020) 3238–3248. https://doi.org/10.1111/jace.17013.

[235] G. Kresse, J. Furthmüller, Efficient iterative schemes for ab initio total-energy calculations using a plane-wave basis set, Phys. Rev. B 54 (1996) 11169–11186. https://doi.org/10.1103/PhysRevB.54.11169.

[236] G. Kresse, D. Joubert, From ultrasoft pseudopotentials to the projector augmented-wave method, Phys. Rev. B 59 (1999) 1758–1775. https://doi.org/10.1103/PhysRevB.59.1758.

[237] J.P. Perdew, A. Ruzsinszky, G.I. Csonka, O.A. Vydrov, G.E. Scuseria, L.A. Constantin, X. Zhou, K. Burke, Restoring the Density-Gradient Expansion for Exchange in Solids and Surfaces, Phys. Rev. Lett. 100 (2008) 136406. https://doi.org/10.1103/PhysRevLett.100.136406.

[238] A. van de Walle, P. Tiwary, M. de Jong, D.L. Olmsted, M. Asta, A. Dick, D. Shin, Y. Wang, L.-Q. Chen, Z.-K. Liu, Efficient stochastic generation of special quasirandom structures, Calphad 42 (2013) 13–18. https://doi.org/10.1016/j.calphad.2013.06.006.

[239] A. van de Walle, M. Asta, G. Ceder, The alloy theoretic automated toolkit: A user guide, Calphad 26 (2002) 539–553. https://doi.org/10.1016/S0364-5916(02)80006-2.

[240] A.J. Logsdail, C.A. Downing, C.R.A. Catlow, A.A. Sokol, Magnetic coupling constants for MnO as calculated using hybrid density functional theory, Chem. Phys. Lett. 690 (2017) 47–53. https://doi.org/10.1016/j.cplett.2017.10.027.

[241] J.P. Perdew, M. Ernzerhof, K. Burke, Rationale for mixing exact exchange with density functional approximations, J. Chem. Phys. 105 (1996) 9982–9985. https://doi.org/10.1063/1.472933.

[242] M. Ernzerhof, G.E. Scuseria, Assessment of the Perdew–Burke–Ernzerhof exchange-correlation functional, J. Chem. Phys. 110 (1999) 5029–5036. https://doi.org/10.1063/1.478401.

[243] C. Adamo, V. Barone, Toward reliable density functional methods without adjustable parameters: The PBE0 model, J. Chem. Phys. 110 (1999) 6158–6170. https://doi.org/10.1063/1.478522.

[244] H.T. Stokes, D.M. Hatch, FINDSYM : program for identifying the space-group symmetry of a crystal, J. Appl. Crystallogr. 38 (2005) 237–238. https://doi.org/10.1107/S0021889804031528.

[245] K. Momma, F. Izumi, VESTA 3 for three-dimensional visualization of crystal, volumetric and morphology data, J. Appl. Crystallogr. 44 (2011) 1272–1276. https://doi.org/10.1107/S0021889811038970.

[246] J. Karczewski, B. Riegel, M. Gazda, P. Jasinski, B. Kusz, Electrical and structural properties of Nb-doped SrTiO3 ceramics, J. Electroceramics 24 (2010) 326–330.

https://doi.org/10.1007/s10832-009-9578-7.

[247] Z. Zhang, P. Qian, X. Yang, B. Wu, H.L. Cai, F.M. Zhang, X.S. Wu, Manipulating the carrier concentration and phase transition via Nb content in SrTiO3, Sci. Rep. 12 (2022) 2499. https://doi.org/10.1038/s41598-021-03199-7.

[248] M. Liu, Y. Zhang, L.F. Lin, L. Lin, S. Yang, X. Li, Y. Wang, S. Li, Z. Yan, X. Wang, X.G. Li, S. Dong, J.M. Liu, Direct observation of ferroelectricity in Ca3Mn2O7 and its prominent light absorption, Appl. Phys. Lett. 113 (2018) 022902. https://doi.org/10.1063/1.5037525.

[249] H.E. Stanley, V.K. Wong, Introduction to Phase Transitions and Critical Phenomena, Am. J. Phys. 40 (1972) 927–928. https://doi.org/10.1119/1.1986710.

[250] A. Deger, C. Flindt, Determination of universal critical exponents using Lee-Yang theory, Phys. Rev. Res. 1 (2019) 023004. https://doi.org/10.1103/PhysRevResearch.1.023004.

[251] E. Almahmoud, I. Kornev, L. Bellaiche, Critical Behavior in Ferroelectrics from First Principles, Phys. Rev. Lett. 102 (2009) 105701. https://doi.org/10.1103/PhysRevLett.102.105701.

[252] H. Nishimori, G. Ortiz, Elements of Phase Transitions and Critical Phenomena, Oxford University PressOxford, 2010. https://doi.org/10.1093/acprof:oso/9780199577224.001.0001.

[253] Y. Li, K. Baberschke, Dimensional crossover in ultrathin Ni(111) films on W(110), Phys. Rev. Lett. 68 (1992) 1208–1211. https://doi.org/10.1103/PhysRevLett.68.1208.

[254] J. Oliveira, B.M. Silva, T. Rebelo, P. V. Rodrigues, R.M.F. Baptista, M.J.L.F. Rodrigues, M. Belsley, N. Lekshmi, J.P. Araújo, J.A. Mendes, F.L. Deepak, B.G. Almeida, Structural, Magnetic, and Dielectric Properties of Laser-Ablated CoFe2O4/BaTiO3 Bilayers Deposited over Highly Doped Si(100), Materials (Basel). 17 (2024) 5707. https://doi.org/10.3390/ma17235707.

[255] E. Brézin, J. Zinn-Justin, Finite size effects in phase transitions, Nucl. Phys. B 257 (1985) 867–893. https://doi.org/10.1016/0550-3213(85)90379-7.

[256] X.T.P. Phu, V.T. Ngo, H.T. Diep, Critical behavior of magnetic thin films as a function of thickness, (2007). https://arxiv.org/pdf/0712.3181 (accessed July 1, 2025).